Structure and dynamics of symmetric diblok copolymers

Papadakis, Christine

Publication date:
1996

Document Version
Publisher's PDF, also known as Version of record

Citation for published version (APA):
Papadakis, C. (1996). *Structure and dynamics of symmetric diblok copolymers*. Roskilde Universitet. Tekster fra IMFUFA No. 323 http://milne.ruc.dk/ImfufaTekster/

TEKST NR 323 1996

Structure and Dynamics of Symmetric Diblock Copolymers

PhD Thesis

Christine Maria Papadakis

TEKSTER fra

IMFUFA ROSKILDE UNIVERSITETSCENTER
INSTITUT FOR STUDIET AF MATEMATIK OG FYSIK SAMT DERES FUNKTIONER I UNDERVISNING, FORSKNING OG ANVENDELSER

IMFUFA, Roskilde Universitetscenter, Postboks 260, 4000 Roskilde, Danmark

Structure and Dynamics of Symmetric Diblock Copolymers (PhD Thesis)
by: Christine Maria Papadakis
Advisors: Dorthe Posselt, Bent C. Jørgensen, Kristoffer Almdal (Risø National Laboratory)

IMFUFA-tekst nr. 323/96 209 pages ISSN 0106-6242

Abstract

Symmetric polystyrene-polybutadiene diblock copolymers in the bulk undergo a phase transition from a disordered melt to a lamellar structure upon variation of temperature or chain length. The interplay between structure and dynamics and the chain conformation has been studied using various scattering techniques.

A homologous series of ten symmetric polystyrene-polybutadiene diblock copolymers was synthesized using living anionic polymerization under inert atmosphere. The samples were characterized using NMR, DSC and chromatography and, among others, it was found that the samples have narrow molar-mass distributions. The order-disorder transition (ODT) temperatures of low molar-mass samples were determined in dynamic mechanical measurements. In this way, the Flory-Huggins segment-segment interaction parameter, χ, could be estimated.

Different sample preparation methods were used in order to test the existence of non-equilibrium structures in the ordered state: annealing, solvent-casting and shear alignment. No significant difference in the lamellar thickness according to the preparation method has been observed, indicating that the samples are in thermal equilibrium. The scaling of the characteristic lengthscale, D, with chain length, N, was studied using small-angle X-ray and neutron scattering. Model calculations of the scattering from lamellar structures were performed. In the strong-segregation limit ($\chi N \simeq 27 - 100$), the characteristic lengthscale scales like $D \propto N^{0.61}$. In the intermediate-segregation regime around the order-disorder transition ($\chi N \simeq 5 - 27$), $D \propto N^{0.82}$ was found. The finding of a crossover from the intermediate-segregation regime to the strong-segregation limit is in accordance with theories.

A temperature study of one sample around the ODT temperature using small-angle neutron scattering showed that the characteristic lengthscale does not change in a discontinuous way at the ODT temperature. In contrast, the height and width of the observed peak change discontinuously at the ODT temperature.

Using dynamic light scattering, the dynamic processes (modes) in three low molar-mass samples were studied. A new data analysis technique was applied in order to reveal modes of relatively low amplitude. Four modes have been identified in the disordered state close to the ODT: cluster diffusion, single-chain diffusion due to heterogeneity in composition from chain to chain, a mode related to chain stretching and orientation, and the segmental reorientational dynamics of the polystyrene blocks. The two latter processes give rise to depolarized scattering. In the ordered state, all modes give rise to depolarized scattering, which is attributed to the anisotropy of the lamellar structure. In the disordered state, the stretching mode was observed to vanish at $\chi N \simeq 5$. This is interpreted to be due to the transition from Gaussian to stretched chain conformation.

The main result of the Ph.D. work is that the intermediate-segregation regime is localized between $\chi N \simeq 5$ and 27.

This report is submitted in partial fulfillment of the requirements for a Ph.D. degree at Roskilde University. The supervisors are Dorthe Posselt and Bent C. Jørgensen at IMFUFA (Institute of Mathematics and Physics), Roskilde University and Kristoffer Almdal at Risø National Laboratory.

Sammenfatning

Symmetriske diblokcopolymerer i bulk undergår ved variation af temperatur eller kædelængde en faseovergang fra en ordnet lamellar struktur til en uordnet smelte. Ved hjælp af forskellige spredningsteknikker er sammenhængen mellem de strukturelle og dynamiske egenskaber og kædekonformation blevet undersøgt, og et nyt regime identificeret og karakteriseret.

En homolog serie bestående af ti symmetriske polystyren-polybutadien diblokcopolymerer er syntetiseret ved hjælp af anionisk polymerisation under inert atmosfære. Prøverne er blevet karakteriseret ved NMR, DSC og chromatografi og det er bl.a. blevet fundet at prøvernes molmassefordelingerne er snævre. Orden-uorden overgangs (ODT) temperaturerne af lavmolekylære prøver er bestemt med dynamisk mekaniske målinger, hvorved Flory-Huggins segment-segment vekselvirkningsparameteren, χ, kunne estimeres.

Forskellige prøvepræpareringsmetoder er anvendt for at teste eksistensen af uligevægtsstrukturer i den ordnede tilstand: annealing, solvent-casting og shear orientering. Der blev ikke observeret signifikant forskel i lameltykkelsen for de forskellige præpareringsmetoder, hvilket indikerer at prøverne er i termisk ligevægt. Ved hjælp af småvinkelrøntgen- og neutronspredning er det påvist, hvordan den karakteristiske længdeskala, D, skalerer med kædelængden, N. Modelberegninger af spredning fra lamellare strukturer er foretaget. I strong-segregation grænsen, ($\chi N \simeq 27 - 100$), skalerer den karakteristiske længdeskala som $D \propto N^{0.61}$. I intermediate-segregation regimet omkring ODT ($\chi N \simeq 5 - 27$) blev $D \propto N^{0.82}$ fundet. Crossover fra intermediate-segregation regime til strong-segregation grænsen er i overenstemmelse med teorierne.

Et temperaturstudie af en prøve omkring ODT temperaturen med småvinkelneutronspredning viste, at den karakteristiske afstand ikke ændrer sig diskontinuert ved orden-uorden overgangstemperaturen. Både højden og bredden af den observerede top ændrer sig derimod diskontinuert ved ODT temperaturen.

Ved hjælp af dynamisk lysspredning blev de dynamiske processer (modes) i tre lavmolekylære prøver studeret. En ny dataanalysemetode blev anvendt for at afsløre processer med relativ lav amplitude. Fire dynamiske processer blev identificeret i den uordnende fase tæt ved ODT temperaturen: diffusion af clustre, diffusion af enkelte polymerkæder på grund af uensartethed i polymersammensætningen, en proces relateret til kædestrækning og orientering, samt segmentreorientering i polystyrenblokken. De to sidstnævnte processer blev også observeret i målinger i depolariseret geometri. I den ordnede tilstand blev alle modes observeret i målinger i den depolariserede geometri, hvad der skyldes anisotropien af den lamellare struktur. I den uordnede tilstand blev det observeret, at den mode, der var relateret til kædestrækning, forsvandt ved $\chi N \simeq 5$. Dette tilskrives overgangen mellem den strakte og gaussiske kædekonformation.

Ph.d. arbejdets hovedresultat er således lokaliseringen af intermediate-segregation regimet mellem $\chi N \simeq 5$ og 27.

Denne rapport er indleveret som ph.d. afhandling ved Roskilde Universitetscenter. Vejledere er Dorthe Posselt og Bent C. Jørgensen fra IMFUFA (Institut for Matematik og Fysik), Roskilde Universitetscenter samt Kristoffer Almdal fra Forskningscenter Risø.

Contents

Preface and Acknowledgements

The present report is the result of a Ph.D.-work which was carried out at IMFUFA (Institute of Mathematics and Physics) at Roskilde University since august 1992. The advisors are Dorthe Posselt and Bent C. Jørgensen, IMFUFA and Kristoffer Almdal, Physics Department, Risø National Laboratory. The aim of the thesis is to explore the structural and dynamic properties of symmetric diblock copolymer systems, focusing on the relation between structure and dynamics and chain conformation. An intermediate-segregation regime around the order-disorder transition is identified and characterized.

The thesis is organized as follows: An introduction to block copolymers is given in Chapter 1. The synthesis of a homologous series of symmetric polystyrene-polybutadiene diblock copolymers, which was carried out at the Physics Department at Risø, is described in Chapter 2. The samples were characterized using various techniques at Risø and at the Department for Life Sciences and Chemistry at Roskilde University (Chapter 3). Careful sample preparation is prerequisite for studying equilibrium properties of block copolymer systems. The methods applied are presented and discussed in Chapter 4. Information about the scaling of the characteristic lengthscale with chain length is gained using small-angle scattering techniques (Chapter 5). Model calculations of the scattering of lamellar structures show how the scattering from different lamellar profiles can be distinguished. Small-angle X-ray scattering was carried out at IMFUFA using the Kratky-camera. These measurements gave information about the scaling behavior, but also about the shape of the lamellar density profile. In small-angle neutron scattering experiments, which were carried out at Risø, precise data on high-molar mass samples were obtained. In addition, it was studied, how the degree of orientation and the size of the lamellar domains depend on the preparation method. Combination of small-angle X-ray and neutron scattering data allowed us to identify the cross-over between the strong-segregation limit and the intermediate-segregation regime. A temperature study in a narrow region around the order-disorder transition was carried out using small-angle neutron scattering (Chapter 6). Dynamic information on symmetric diblock copolymer systems in the disordered and the ordered state was obtained using dynamic light scattering. These experiments were carried out during my six months stay at the Department of Physical Chemistry, Uppsala University. The method and the results are discussed in Chapter 7. In the Appendix, a vacuum oven which was designed for sample preparation, and a sledge for measurement of the beam profile of the Kratky-camera are described. A model calculation of the scattering intensity of a lamellar profile is presented. Small-angle X-ray experiments, which were carried out during a stay at the Service de Chimie Moléculaire, Centre de l'Energie Atomique at Saclay, are discussed.

Combination of different techniques is characteristic of the field of soft condensed matter. It has been very interesting to combine various chemical and physical techniques and concepts. Many people have been involved and I would like to thank all of them.

First of all, I would like to thank Dorthe Posselt for suggesting me to come to this nice country, introducing me to the fascinating field of soft condensed matter, and for being a good advisor. I learned a lot about small-angle scattering and data interpretation from her. Thanks for many discussions and for careful reading of manuscripts!

Kristoffer Almdal was courageous enough to let a physicist do synthesis in his lab. He taught me the art of anionic polymeriation and I learned a lot about polymer science from him. The invaluable help of Walther Batsberg Pedersen, Lotte Nielsen, Lene Hubert and Anne Bønke Nielsen from the polymer group at Risø with sample characterization is gratefully acknowledged. Kell Mortensen is thanked for his help with the SANS-experiments.

I would like to thank Mogens Brun Heefelt, Bent C. Jørgensen, Birthe Saltoft and Inger Grethe Christensen for doing their best to help me through the jungle of administration. I finished the thesis as an employee at IMFUFA and I thank my colleagues for giving me the freedom to write in peace. Thanks also for teaching me the art of teaching and of project work. Special thanks go to Niels Boye Olsen, Tage Christensen and Jeppe Dyre for good collaboration, many interesting seminars and study groups. Ib Høst Pedersen and Torben Steen Rasmussen are thanked for assisting with all kinds of technical problems. Mogens Holte Jensen, Jan-Ole Nielsen and Hans Wallin are thanked for making useable sample holders, vacuum ovens and sledges out of my drawings. The help of Morten Langgård, Poul Erik Hansen and Annelise Gudmundsson from the Department for Life Sciences and Chemistry with the NMR-analysis is gratefully acknowledged. Ritta Bitsch and Stine Bøggild made beautiful drawings for me.

I am grateful to Wyn Brown for giving me the opportunity to work as a member of his group at the Department of Physical Chemistry, Uppsala University, and for teaching me a lot about dynamic light scattering. Thanks to Bob Johnsen for his help with the data analysis. The other members of the light scattering group are thanked for creating a friendly and international atmosphere. The financing of my stay in Uppsala by the Danish Research Academy is gratefully acknowledged.

I spent two weeks with the X-ray scattering group at the Service de Chimie Moléculaire, Centre de l'Energie Atomique at Saclay and I would like to thank Thomas Zemb, Didier Gazeau and Frédéric Né for their hospitality. Lise Arleth is thanked for her help during my stay. A travel grant from Risø National Laboratory is gratefully acknowledged.

The rheology group consisting of scientists from the Copenhagen region provided a forum for discussing linear response functions, the rheological properties of yoghurt and even block copolymer phase behavior! Thanks also to John Ipsen and Bernd Dammann from the Department of Physical Chemistry at the Technical University for being enthusiastic about scaling concepts. Sokol Ndoni is thanked for many good discussions about anionic polymerization. Thanks to Otto Glatter from the University of Graz for giving an excellent summercourse on scattering techniques in soft materials science and for discussions about Kratky-cameras and data analysis. Thanks also to all the scientists from far and near for their interest in my work!

Finally, I would like to thank Bernd for sharing the adventure of living in Denmark and for all his support and friendship. Thanks also to my parents for providing us with Greek honey and German wine!

List of Publications

Christine M. Papadakis, Kristoffer Almdal, and Dorthe Posselt,
Molar-mass dependence of the lamellar thickness in symmetric diblock copolymers.
Il Nuovo Cimento **16D**, 835 (1994).

Sokol Ndoni, Christine M. Papadakis, Frank S. Bates, and Kristoffer Almdal,
Laboratory-scale setup for anionic polymerization under inert atmosphere.
Review of Scientific Instruments **66**, 1090 (1995).

Christine M. Papadakis, Wyn Brown, Robert M. Johnsen, Dorthe Posselt, and Kristoffer Almdal,
The dynamics of symmetric polystyrene-polybutadiene diblock copolymer melts studied above and below the order-disorder transition using dynamic light scattering.
Journal of Chemical Physics **104**, 1611 (1996).

Christine M. Papadakis, Kristoffer Almdal, Kell Mortensen, and Dorthe Posselt,
Identification of an intermediate-segregation regime in a diblock copolymer system.
Submitted to Europhysics Letters.

Christine M. Papadakis, Kristoffer Almdal, Kell Mortensen, and Dorthe Posselt,
A small-angle scattering study of the bulk structure of a symmetric diblock copolymer system.
Manuscript in preparation.

Chapter 1

An introduction to block copolymers

Block copolymers are macromolecules containing different species of monomers, which are arranged in blocks (Fig. 1.1). The monomers constituting the blocks are in most cases immiscible. Diblock copolymers consist of two different monomer species (A and B). Even though they represent a very simple architecture, they exhibit a rich phase behavior which is far from being understood [1]. According to the temperature and the chain length, diblock copolymers in the bulk (*i.e.* without solvent) form a disordered melt or an ordered structure. Symmetric diblock copolymers in the ordered state form a lamellar structure (Fig. 1.2). Even in the ordered state, the structure is amorphous locally, but the superstructure is ordered and is reminiscent of the crystal structure found in atomic crystals. The parameters governing block copolymer phase behavior are discussed in the next section.

Polymers may be considered as an example of soft materials, also termed complex fluids [2]. Other examples for soft materials are colloids, liquid crystals, micellar and biological systems. Common to all these materials are the weakness of enthalpic interactions (compared to traditionally studied solids, *e.g.* ionic crystals) and the important role of entropy, which is closely related to the mechanical softness. Even in the ordered state, block copolymers are amorphous, a large number of conformations is possible for each polymer. Self-organization on large lengthscales is characteristic of soft materials, one example being the lamellar structure formed in block copolymer systems. In fact, the morphologies found in block copolymers are reminiscent of those observed in liquid crystals [3]. Soft materials science is characterized by being interdisciplinary. A variety of chemical and physical methods are normally used for sample characterization, which also is the case in the present study.

The present study focuses on the chain conformation of symmetric diblock copolymers. In a first instant, we will review, how the chain conformation of simple homopolymers (linear chains) can be described. A linear, flexible chain (Fig. 1.3) can take up an enormous number of configurations. Therefore, statistical methods are used in order to describe the shape of a polymer. A good description of the global properties (*e.g.* the overall coil size) can be given, even though local properties, such as steric hindrances, are neglected. In a first instant, a linear chain molecule can be modelled as a chain of mass points, which

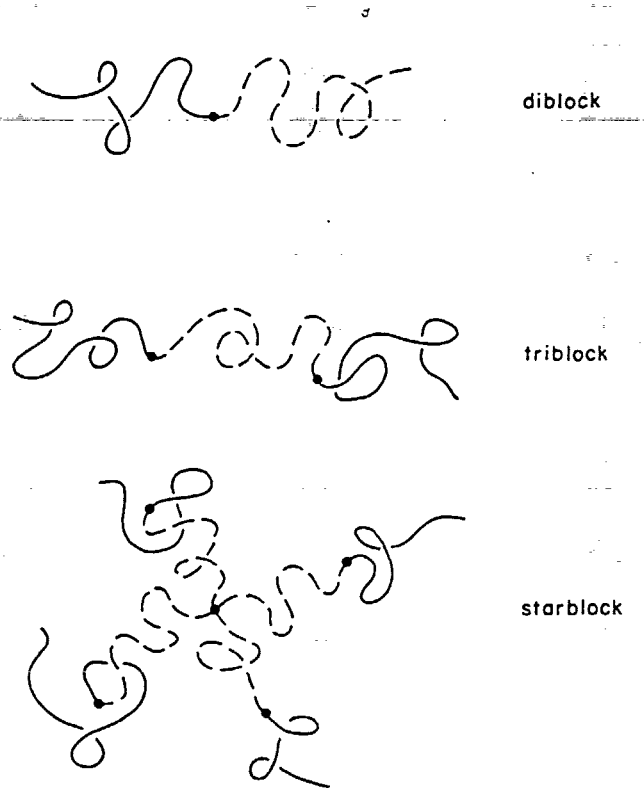

Figure 1.1: *Some polymer-polymer (dashed and solid curves) molecular architectures attainable through the polymerization of two distinct monomers. From [1].*

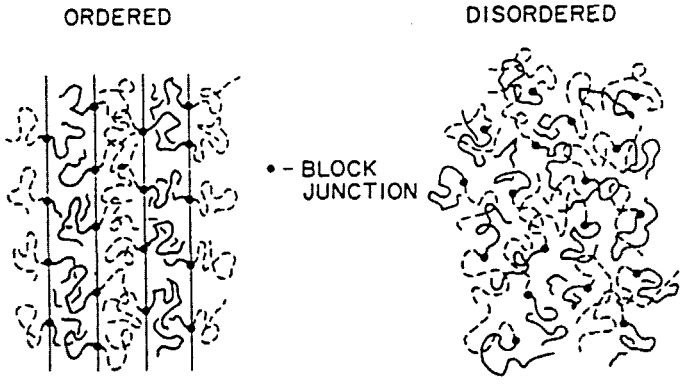

Figure 1.2: *Schematic representation of order and disorder in a symmetric diblock copolymer showing lamellar order. From [1].*

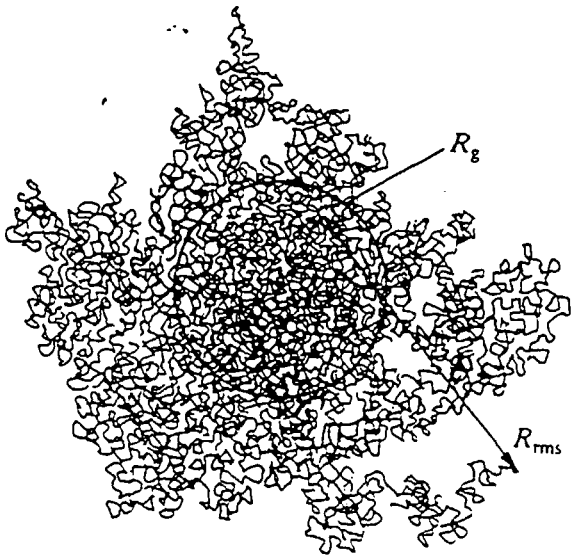

Figure 1.3: *A random coil in three dimensions. The number of steps, N, was ~ 4000. The end-to-end vector $\vec{R}_{rms}$ ($\vec{R}_{ee}$) and the radius of gyration R_g are indicated. From [4].*

are connected by bonds, all bond vectors $\vec{a}_i$, $i = 1, \ldots, N$, having the same length, a. This corresponds to a random flight in three dimensions: The direction of each step is independent of the previous one (Fig. 1.3). The average value of the squared end-to-end distance reads [5]

$$\langle R_{ee}^2 \rangle = \left\langle \sum_{i=1}^{N} \vec{a}_i \cdot \sum_{j=1}^{N} \vec{a}_j \right\rangle = Na^2 + 2 \sum_{1 \le i < j \le N} \langle \vec{a}_i \cdot \vec{a}_j \rangle \tag{1.1}$$

The last term is zero when the directions of the bond vectors are completely uncorrelated. In this case, the average end-to-end distance is given by [5]

$$\langle R_{ee}^2 \rangle^{1/2} = aN^{1/2} \tag{1.2}$$

where N denotes the number of steps. The chain conformation of a random flight is termed Gaussian, because the distribution of the end-to-end distance is a Gaussian distribution, centered at $R_{ee} = 0$ [5]. A measure of the size of a linear chain is the radius of gyration, R_g. It is defined as the root-mean-square distance of the collection of mass points from their common center of gravity (Fig. 1.3) [5]:

$$R_g^2 = \frac{1}{N+1} \sum_{i=0}^{N} s_i^2 \tag{1.3}$$

s_i denotes the distance from the ith mass point from the center of mass. It has been assumed that all $N + 1$ masses are equal. For random flights [5]

$$\langle R_g^2 \rangle = \langle R_{ee}^2 \rangle / 6 \tag{1.4}$$

Thus, the average radius of gyration of a Gaussian chain is given by

$$\langle R_g^2 \rangle^{1/2} = \frac{a}{6} N^{1/2} \tag{1.5}$$

Eq. 1.5 is only valid for long chains, *i.e.* large values of N. If N is sufficiently small, the radius of gyration is proportional to N [5].

Real polymer chains are self-avoiding. For self-avoiding random flights, the radius of gyration scales with a slightly higher exponent: $\langle R_g^2 \rangle^{1/2} \propto N^{\delta}$, $\delta \simeq 3/5$ [5]. This scaling behavior is observed with polymers in dilute solution in a good solvent. The chains are 'swollen'. In a dense melt of polymers, the random flight result $\langle R_g^2 \rangle^{1/2} \propto N^{1/2}$ is recovered. The reason is that the repulsive force created by the fact that polymers are self-avoiding, is screened by the other polymers present [6]. In the same way, scaling with an exponent of 1/2 may describe the polymer conformation in a solvent which is just between being good and poor. The chain conformation is neither swollen nor collapsed. Such solvents are termed Θ-solvents.

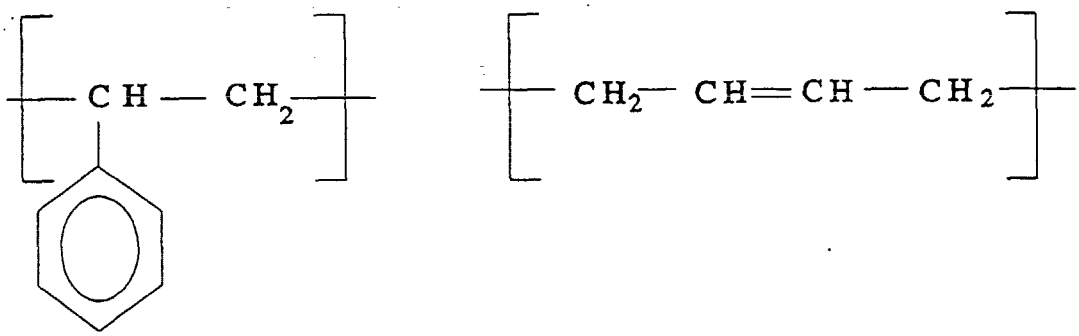

Figure 1.4: *Polystyrene (left figure) and polybutadiene monomer (right figure).*

In real polymers, there are local restrictions, such as restrictions of bond angles. Consider, for example, polystyrene or polybutadiene (Fig. 1.4). Polystyrene has bulky side-groups which hinder adjacent monomers of rotating freely around the backbone. Polybutadiene contains double bonds in the backbone which cannot rotate freely. Flory has shown that incorporation of these local effects does not change the exponents [5]; only the prefactors change. Therefore, a, which denotes the length of a statistically independent segment, may be much larger than the length of a chemical repeat unit (monomer). It can be determined by measuring the radius of gyration in dilute solution in a Θ-solvent [4]. Knowledge of the number of monomers, N, and the scaling exponent allows the determination of a.

In diblock copolymers, the situation is different in the disordered and in the ordered state. Deep in the disordered state, the repulsive interactions between different monomers are weak, and A- and B-monomers are evenly distributed. The chain conformation is close to Gaussian [7, 8]. In the ordered state, the two blocks are removed from each other. The

chains are dumbbell-like and stretched perpendicular to the interface. As will be reviewed in Chapter 5.1, the lamellar thickness has been predicted to scale like $R_g \propto N^{2/3}$ [9].[1] In Chapters 5 and 6, the chain conformation of diblock copolymers in a large region of phase space will be discussed.

As described above, many lengthscales are involved in polymer systems. Polymers are constituted of segments which consist of a group of atoms. Typical bond lengths are 1.45 Å for a carbon-carbon bond [10]. Typical segment lengths are several Ångstrøms, ~ 7 Å for the polystyrene segment. The segments form the chain which, according to the chain length, N, may have a radius of gyration of up to some thousand Ångstrøms. In a melt, the chain is intertwinned with many other polymers. This hierachical structure is reflected in the dynamics, because the lengthscales correspond to certain timescales: On a local scale, single segments may rotate or vibrate. These are fast processes. Another dynamic process are movements of parts of the polymer chain relatively to each other. These processes (termed internal chain modes) have been described by Rouse [11], considering the chain as a series of masses connected by springs. In addition, the chain as a whole may diffuse in its environment. The environment may be the solvent or, in the melt, the other chains. This process can be very slow, especially when the chains are very long and strongly entangled. In the latter case, a single chain reptates in the tube which is made up by the other polymers [6]. This movement is very slow. These complex dynamic properties on a large range of timescales are reflected in the special mechanical properties of polymeric materials [12]. On short timescales, polymer melts may appear elastic, whereas, on long timescales, they behave liquid-like.

In block copolymer systems in the bulk, the dynamic processes reflect the segregation due to the repulsive interactions: The segmental dynamics may have different relaxation times for the two blocks [13]. The repulsive interaction between different segments has also an influence on the internal chain relaxation processes and on the diffusion of single chains [14]. An interesting subject is the dynamics of block copolymer chains in the disordered state close to the ODT, where concentration fluctuations persist and the chains are stretched. Studying the dynamics of block copolymers in this region gives information about the chain conformation, *e.g.* the degree of chain stretching. In the lamellar state, diffusion of single block copolymer molecules is hindered: The chains diffuse mostly along the interfaces [15]. A survey of the dynamic processes encountered in block copolymer systems is given in Chapter 7.

1.1 The phase behavior

The phase behavior of A-B diblock copolymers can be described in terms of the overall degree of polymerization or chain length, N, the volume fraction of one block, f, and the Flory-Huggins segment-segment interaction parameter, χ. All three parameters can be controlled during the synthesis by the choice of monomers and by simple stoichiometry. In case of symmetric diblock copolymers, as considered here, $f = 0.5$.

The Flory-Huggins parameter, χ, describes the net interaction between different poly-

[1] In the following, we will use R_g instead of $\langle R_g^2 \rangle^{1/2}$.

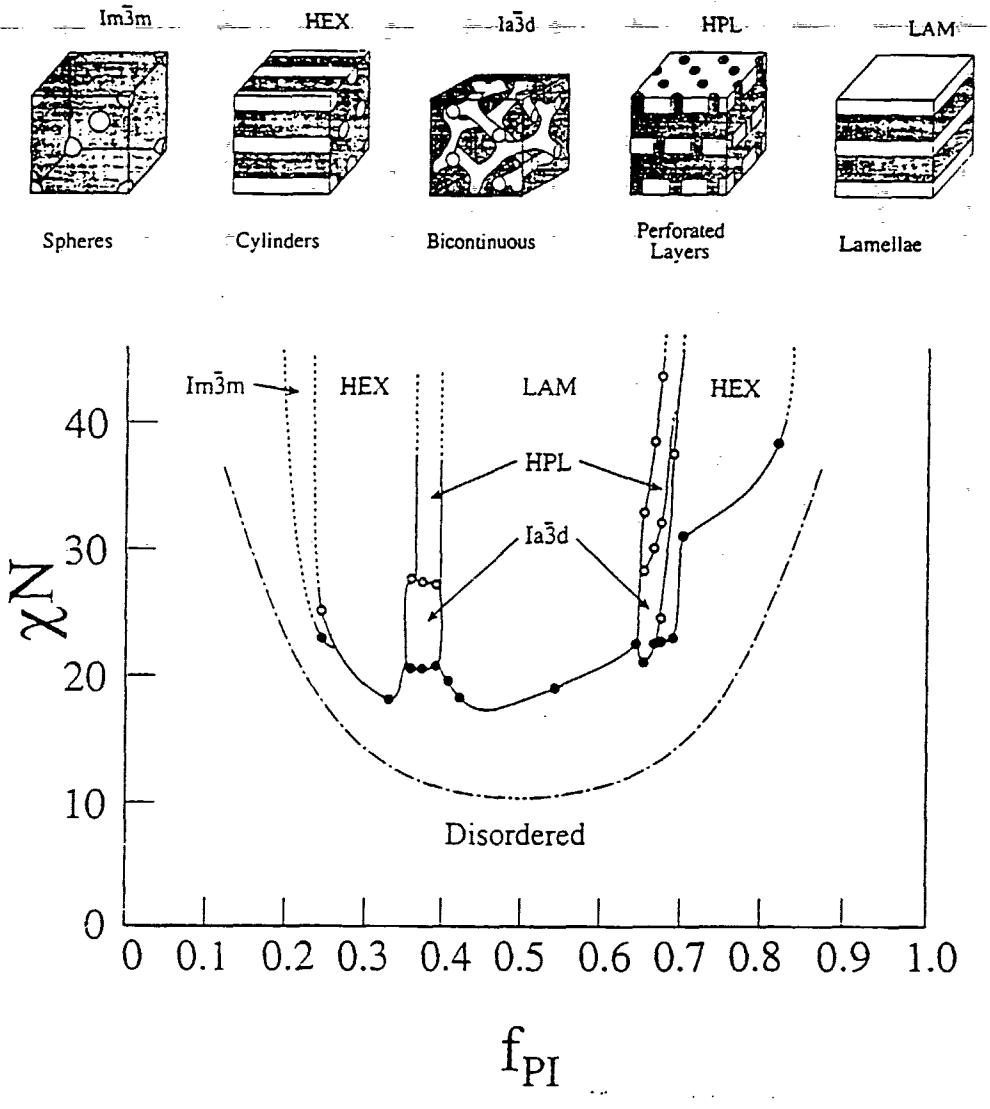

Figure 1.5: *Experimentally determined phase diagram of polystyrene-polyisoprene together with schematical drawings of the observed morphologies. The dash-dotted line is the mean-field prediction for the ODT. For explanations see text. From [16].*

mer segments (A and B) and is defined by [17]

$$\chi = \frac{1}{k_B T}\left[\epsilon_{AB} - \frac{1}{2}(\epsilon_{AA} + \epsilon_{BB})\right] \tag{1.6}$$

where ϵ_{ij} denotes the contact energy between i and j segments and k_B the Boltzmann constant. $k_B T\chi$ represents the change in enthalpy when bringing, say, an A-segment from a pure A-environment to a pure B-environment [18]. If χ is negative, mixing is favorable, this may be the case with hydrogen bonding; if χ is positive, the interaction between different segments is repulsive. The physical origin of the interaction between nonpolar monomers, such as the polystyrene or polybutadiene monomers, is the van der Waals-interaction, also termed 'dispersion forces' [19]. These forces arise from the fluctuating electric field created by the electrons oscillating around the nucleus in an atom, which may polarize nearby atoms. The resulting interaction between two equal atoms can be shown to be attractive [19]. Dispersion forces are at the origin of the crystallization of noble gases, for instance. The total intermolecular pair potential is obtained by adding the long-range attractive van-der-Waals-potential ($\propto 1/r^6$) and the repulsive hard-core potential, which is short-ranged ($\propto 1/r^{12}$). The simple picture valid for small spherical atoms has to be refined for anisotropic molecules, such as polymer segments, which may align each other upon mixing. An extra term containg these entropic contributions is therefore added to the interaction parameter between dissimilar species:

$$\chi = \frac{a}{T} + b \tag{1.7}$$

where a contains the enthalpic interactions described above (Eq. 1.6) and b the entropic effects of non-random segment packing. In principle, χ can be calculated; however, for most applications, it is determined experimentally. In this study, the interaction parameter of the styrene-butadiene pair was determined using the prediction $\chi N \simeq 10.5$ at the ODT, which is valid for symmetric diblock copolymers (Chapter 3).

A recent phase diagram for polystyrene-polyisoprene diblock copolymers, which was established experimentally [16] is shown in Fig. 1.5. Within mean-field theory, the phase behavior is described in terms of the combined parameter χN and the composition f. The use of χN as a combined parameter is a result of mean-field theory [7]. The ensemble of molecular configurations that leads to the minimum overall Gibbs free energy represents the equilibrium state [17]. At high temperatures, the interaction between dissimilar segments, χ, is small and the system forms a homogenous, disordered melt. As the temperature is lowered, the contact enthalpy increases, which is balanced by reducing the number of contacts. However, segregation is opposed by the associated loss in entropy. The system eventually orders and, according to the composition, f, forms one of the morphologies shown in Fig. 1.5. This phase transition is called the order-disorder transition (ODT) and has by fluctuation theory been predicted to be a weak first-order transition [20]. There are several differences between the experimentally determined phase diagram and the theoretical predictions: The experimentally determined phase line, $(\chi N)_{ODT}$, differs from the theoretically predicted line. In addition, several morphologies appear which were not predicted by theory, such as the Ia$\bar{3}$d and the HPL morphologies. The experimental phase diagram is not symmetric which is attributed to the conformational asymmetry of the two blocks, *i.e.* the difference of the length and the volume of the two segments. From this example, it can be concluded that the phase behavior of diblock copolymers in the bulk is far from being understood.

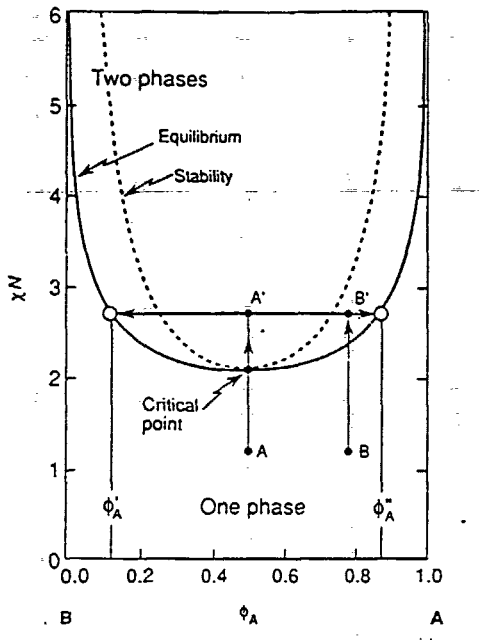

Figure 1.6: *Theoretical phase diagram of a symmetric polymer blend where both species have the same chain length. Parameters describing the phase behavior are the volume fraction of component A, ϕ_A and the product χN (see text). The dotted line represents the spinodal,* i.e. *the limit of stability. From [17].*

It is worthwhile to discuss the differences between binary mixtures of homopolymers and of diblock copolymers [17]. Binary mixtures of immiscible polymers often display an upper critical solution behavior: Upon cooling below a certain temperature, a homogeneous mixture becomes thermodynamically unstable and macroscopic demixing takes place. Parameters governing the phase behavior are the volume fraction of one component (A), ϕ_A, and, in the symmetric case (*i.e.* both components have the same chain length, $N_A = N_B = N$), the product χN. In this case, the critical point is located at $\chi N = 2$. A phase diagram of a symmetric binary polymer blend is shown in Fig. 1.6. Connecting the polymers pairwise by a covalent bond, which results in diblock copolymers, changes the behavior drastically: Diblock copolymers cannot demix macroscopically, but form ordered microphase-separated morphologies. In the disordered state between $\chi N \simeq 4$ ($N = N_A + N_B$) and the ODT ($\chi N \simeq 10$), the system can be considered as being frustrated [21]. The homopolymer blend would demix and form large domains, but diblock copolymers are prevented from demixing due to the bond. This frustration leads to important concentration fluctuations.

It should be noted that the term 'phase diagram' is not appropriate in a rigorous sense to the block copolymer diagrams shown here because χN and f are no intensive variables; however, the term will be used here for traditional reasons.

1.2 Structure and chain conformation

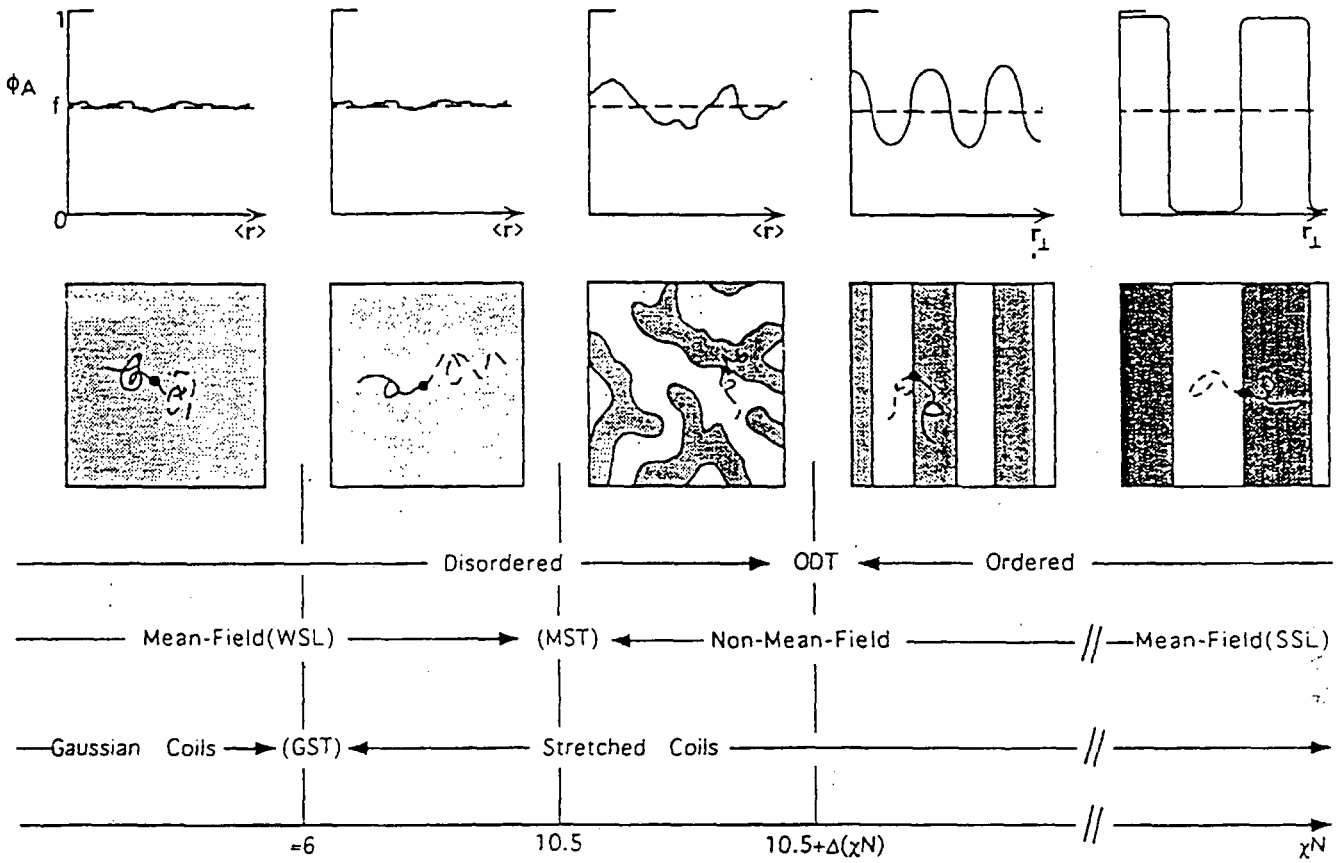

Figure 1.7: *Illustration of the five regimes for symmetric diblock copolymer melts. The upper figures of the local number density of A-segments, ϕ_A, provide a qualitative sense of the variation in the amplitude of the local composition as a function of χN. The lower figures depict the corresponding spatial patterns associated with each regime. From [22].*

The present study aims at describing the phase behavior of symmetric diblock copolymers, which form a lamellar structure for large values of χN. A schematic representation of the disordered and the lamellar state is shown in Fig. 1.2. A subject of fundamental interest is the interplay of structure and chain conformation. A schematic illustration is given in Fig. 1.7. Deep in the disordered state, the repulsive interaction between different segments is small and the melt is nearly homogeneous. The local number density of A-segments, ϕ_A, is similar to the stoichiometric number density, f_A, throughout the sample. In the homogeneous state, the chains are Gaussian [8] (Fig. 1.8).

Deep in the ordered state, the two blocks are confined in the lamellae and the chains are stretched. The interphases between A- and B-rich domains are narrow, *i.e.* the concen-

tration profile is close to rectangular. This regime is referred to as the strong-segregation limit, SSL. Mean-field theories predict a scaling of the lamellar thickness with chain length as $D \propto N^{2/3}$ [9] resp. $D \propto N^{0.643}$ [23]. These theories are reviewed in Chapter 5.

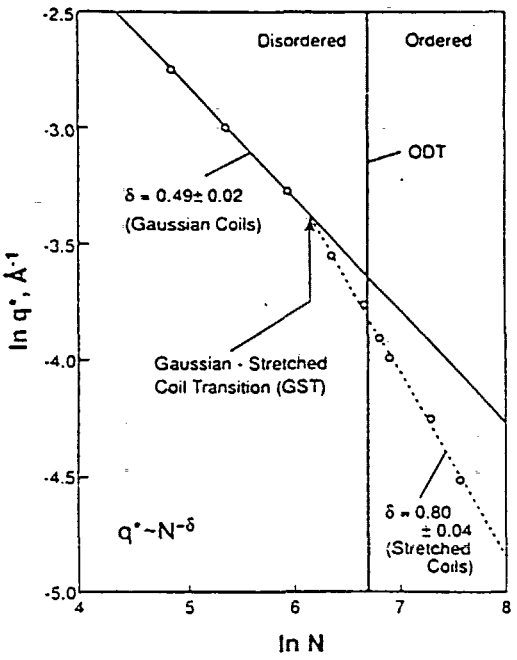

Figure 1.8: *Variation of the position of the maximum in scattered intensity with chain length, indicating the stretching of the chains prior to the ODT. The peak position is inversely proportional to the characteristic lengthscale in the system. From [8].*

The intermediate region around the ODT is more difficult to describe. Coming from the homogeneous state, composition fluctuations arise in the vicinity of the ODT, *i.e.* ϕ_A differs locally from f_A. The melt orders at $\chi N = 10.5 + \Delta(\chi N)$. $\chi N = 10.5$ is the mean-field prediction for symmetric diblock copolymer systems [7]. The correction term, $\Delta(\chi N)$, was found by taking fluctuations into account [20]. As fluctuations stabilize the disordered state, the ODT determined using fluctuation theory occurs at a lower temperature than predicted by mean-field theory. As shown in Fig. 1.8, deviations from the Gaussian scaling have been found in a region around the ODT [8]. As concentration fluctuations become important, the chains stretch, thus the centers of mass of the A- and B-blocks are separated slightly. This Gaussian- to stretched-coil transition has been identified to occur at $\chi N \simeq 6$ [22], thus quite deep in the disordered state. At the ODT, the chains were found to be stretched by 13% with respect to their unperturbed dimension. Interestingly, the exponent was higher than the values predicted for the SSL, $\delta = 2/3$ [9] and $\delta = 0.643$ [23]. The identification of a Gaussian- to stretched-coil transition coincides with the results from numerous Monte Carlo simulations [24, 25, 26] and from theory [27].

In the ordered state close to the ODT, the concentration profile has been shown to be

close to sinusoidal (Chapter 5.4). Some mixing of A- and B-monomers thus takes place in the interphase which has an influence on the balance of enthalpy and entropy. Up to $\chi N \simeq 33$, the same scaling behavior as in the disordered state close to the ODT was found: $\delta = 0.8$ [8].

The theories describing block copolymer phase behavior and the scaling of the characteristic lengthscale will be discussed in Chapter 5.1.

A comment seems appropriate on the classification of the different regimes. The term 'weak-segregation limit' (WSL) has traditionally been used for the region in the vicinity of the ODT. The shape of the density profile was assumed to be sinusoidal; and the chain conformation was assumed to be Gaussian. This regime was first described by Leibler [7]. However, experiments have shown that, at the ODT, the chains are stretched and become Gaussian only deep in the disordered state (Fig. 1.8, [8]). In Fig. 1.7, the WSL is therefore located at $\chi N < 10.5$. In the present work, we will not use the term WSL in order to avoid confusion. Instead, we will term the region deep in the disordered state 'homogeneous', the region around the ODT 'intermediate-segregation regime' (ISR) and the region deep in the ordered state 'strong-segregation limit' (SSL).

1.3 The present study

The present study focused on the intermediate-segregation regime around the ODT and on the crossover to the SSL.

A homologous series of ten symmetric polystyrene-polybutadiene diblock copolymer samples was synthesized [28]. Synthesis and characterization are described in Chapters 2 and 3 [29]. This particular block copolymer was chosen because the interaction parameter is relatively high; thus, a large region in phase space could be examined with polymers having moderate molar masses.

In order to identify the cross-over between the ISR and the SSL, the characteristic lengthscale was studied as a function of chain length at a fixed temperature (*i.e.* at a fixed value of χ). A region $\chi N \simeq 5 - 100$ was explored. Different sample preparation methods were applied in order to bring the samples into thermal equilibrium: annealing, shear alignment and solvent-casting. A combined small-angle X-ray (SAXS) [29] and neutron scattering (SANS) study was performed in order to cover a large range of scattering vectors. Model calculations show how different lamellar structures can be distinguished. The scattering experiments and the results are discussed in Chapter 5. A cross-over between the intermediate region and the strong-segregation limit is identified at $\chi N \simeq 27$. In the SSL ($\chi N > 27$), the characteristic lengthscale scales with chain length like $D \propto N^{0.61}$. The density profile has narrow interfaces. In the ISR ($\chi N < 27$), the characteristic lengthscale was found to scale like $D \propto N^{0.82}$. In this region, some mixing of segments takes place.

A temperature study with one sample around the ODT temperature was carried out using SANS in order to study the behavior of the characteristic lengthscale at the ODT (Chapter 6). No discontinuous change of the characteristic lengthscale was observed at the ODT temperature.

The dynamic properties of three low molar-mass samples were studied using dynamic light scattering (Chapter 7). Four dynamic processes were identified in the disordered state: cluster diffusion (long-range heterogeneities), single-chain diffusion, a mode related to chain stretching and orientation, and segmental re-orientational dynamics. With the lowest molar-mass sample, the stretching mode was observed to vanish at $\chi N \simeq 5$ which was interpreted as the Gaussian-to-stretched-coil transition. The intermediate-segregation regime is thus located between $\chi N \simeq 5$ and 27.

Chapter 2

Synthesis using anionic polymerization

(The synthesis was carried out in collaboration with Kristoffer Almdal, Risø National Laboratory.)

A homologous series of symmetric polystyrene-polybutadiene diblock copolymers was synthesized using anionic polymerization, which is a 'living' polymerization technique. A high degree of control over polymer chain architecture can be achieved [30]. Synthesis of tailor-made polymer systems, such as block copolymers, graft or star polymers or polymers with functional endgroups is possible. The molecular architecture depends on the choice of the functionality of the initiating molecule and on the way, the different monomer species are added during the polymerization reaction. In addition, living polymerization is the method of choice for synthesizing polymers with very narrow molar mass distributions. The technique is at present the only one allowing synthesis of block copolymers with controllable volume fractions. Synthesis of quantities of sample large enough for rheological and small-angle scattering studies is possible.

For the synthesis of polystyrene-polybutadiene diblock copolymers, a monofunctional initiator is chosen, and the different monomer species (styrene and butadiene) are added sequentially. As nearly 100% of the monomers are polymerized, the overall molar mass and the volume fraction of one block can be controlled by the amount of monomer and the amount of initiator, *i.e.* by simple stoichiometry. Due to the reactivity of the growing ends, the polymerization reaction must be conducted under dry and oxygen-free conditions which is crucial for obtaining narrow molar-mass distributions. This is achieved by purifying all reagents and flasks with great care and by carrying out the synthesis under clean conditions. Traditionally, anionic polymerization has been carried out under high vacuum. However, synthesis under a slight overpressure of purified inert gas, which was performed in the present study, offers comparable control over the molar-mass distribution and is easier and faster to run [28]. In this way, a homologous series of eleven polystyrene-polybutadiene diblock copolymers with molar masses between 9200 and 183000 g/mol having the same volume fraction, $f = 0.5$, was synthesized in batches between 25 and 120 g/mol.

In the following, the reaction kinetics, the set-up, the purification procedures, the way of controlling the molecular architecture, and the reaction process will be presented and discussed. The characteristics of the synthesized polymer samples will be given.

2.1 The mechanism of polymerization

The polymerization of a polystyrene-polybutadiene diblock copolymer follows a scheme with five steps: initiation (1), propagation of the styrene-block (2), crossing to the polymerization of butadiene (3), propagation of the butadiene-block (4), and termination with methanol (5):

$$
\begin{array}{lrcl}
(1) & \mathrm{S} + \mathrm{secBuLi} & \rightarrow & (\mathrm{Bu\ S})^{-}\mathrm{Li}^{+} \\
(2) & (\mathrm{Bu\ (S)}_{n})^{-}\mathrm{Li}^{+} + \mathrm{S} & \rightarrow & (\mathrm{Bu\ (S)}_{n+1})^{-}\mathrm{Li}^{+} \\
(3) & (\mathrm{Bu\ (S)}_{N_S})^{-}\mathrm{Li}^{+} + \mathrm{B} & \rightarrow & (\mathrm{Bu\ (S)}_{N_S}\ \mathrm{B})^{-}\mathrm{Li}^{+} \\
(4) & (\mathrm{Bu\ (S)}_{N_S}\mathrm{B}_{n})^{-}\mathrm{Li}^{+} + \mathrm{B} & \rightarrow & (\mathrm{Bu\ (S)}_{N_S}\ \mathrm{B}_{n+1})^{-}\mathrm{Li}^{+} \\
(5) & (\mathrm{Bu\ (S)}_{N_S}\ (\mathrm{B})_{N_B})^{-}\mathrm{Li}^{+} + \mathrm{CH_3OH} & \rightarrow & \mathrm{Bu\ (S)}_{N_S}\ (\mathrm{B})_{N_B}\ \mathrm{H} + \mathrm{CH_3OLi}
\end{array}
$$

where S stands for styrene, B for butadiene, Bu for butyl and secBuLi for *sec*-butyllithium. The overall number of monomers is $N = N_S + N_B$. It should be noted that this number is not the same as the chain length which is used below. The chain length is based on the polybutadiene monomer volume.

The distribution of molar mass is narrow because of the following reaction characteristics [30]: Virtually each initiator molecule starts a polymerization. The initiation reaction is fast compared to chain propagation. The polymerization is termination-free, *i.e.* the initiated polymers are all the time reactive enough to bind more monomers as long as there are monomers present. This is the reason for calling them 'living' polymers. In order to terminate the reaction (to 'kill the polymer'), some reagent (in this case methanol) has to be added. Chain transfer is considered to be negligible. Side-chain reactions can be avoided by the appropriate choice of reaction temperature.

Polymerization of polystyrene-polybutadiene diblock copolymers was carried out as follows: The reaction took place under an atmosphere of purified inert gas (here: argon) and in a nonpolar solvent, in the present case cyclohexane. Cyclohexane was chosen because it is a solvent for both styrene and butadiene. An organolithium compound (sec-butyllithium) was chosen as an initiator, which also is soluble in cyclohexane. First, an amount of styrene monomer was added to the solution of the initiator in cyclohexane. When the calculated reaction time for the styrene block had passed, an amount of butadiene monomer was added. After the reaction time for the butadiene block, methanol was added to stop the polymerization. The polymer sample was then precipitated, dried and treated further for structural analysis.

It is extremely important that all the reagents are as pure as possible because impurities can stop the polymerization and thus lead to a broadening of the molar mass distribution. Therefore, prior to synthesis, monomers were distilled with compounds removing water, air and other impurities and were kept under vacuum. The argon gas used was cleaned by passing it through substances which remove water and air. Cyclohexane was distilled under argon with polystyryllithium which reacts with impurities. Flasks were flamed and

the reactor was baked under vacuum in order to remove water from the inner glass walls. These purification procedures will be described in detail below.

The propagation reaction

$$(\mathrm{M_n})^-\mathrm{Li}^+ + \mathrm{M} \rightarrow (\mathrm{M_{n+1}})^-\mathrm{Li}^+ \tag{2.1}$$

where M stands for either the styrene or the butadiene monomer (the butyl ends are skipped here) can be described as follows [31]: The consumption of monomer is given by

$$\frac{\mathrm{d[M]}}{\mathrm{d}t} = -k_p^{(M)}\,[\mathrm{M_n^-Li^+}]\,[\mathrm{M}] \tag{2.2}$$

where $k_p^{(M)}$ is the rate constant of the propagation reaction. Square brackets denote the molar concentration in the solvent. It is assumed that every initiator molecule starts a polymerization process and that the number of growing chains is constant, thus $[\mathrm{M_n^-Li^+}] = \text{const}$. Eq. 2.2 can then be simplified to

$$\frac{\mathrm{d[M]}}{\mathrm{d}t} = -k_{app}^{(M)}\,[\mathrm{M}] \quad \Longleftrightarrow \quad [\mathrm{M}] = [\mathrm{M}]_0\,\exp(-k_{app}^{(M)}\mathrm{t}) \tag{2.3}$$

which corresponds to a first-order reaction with the apparent rate constant

$$k_{app}^{(M)} = k_p^{(M)}[\mathrm{M_n^-Li^+}] \tag{2.4}$$

The duration of a polymerization with $y\%$ conversion is given by

$$t_y = \frac{\ln(1-y)}{-k_{app}^{(M)}} \tag{2.5}$$

In practice, $y = 99.9\%$ was used. Calculation of the apparent rate constant, $k_{app}^{(M)}$, requires knowledge of the concentration of living chains, $[\mathrm{M_n^-Li^+}]$. It was verified experimentally that the propagation reaction is of order one-half or one-fourth in initiator concentration [30]. This has traditionally been explained in terms of a simple association model of the growing chains: the living anionic polystyryllithium (polybutadienelithium) chains aggregate in dimers (tetramers), in the same way as surfactants, and are only reactive in the dissociated state. As the growth rate of the chains is considered to be very high in the non-associated state, there is, on average, a certain propagation in reasonable time.[1] According to this simple picture, the association-dissociation equilibrium can be described in the following way:

$$(\mathrm{M_n^-Li^+})_x \rightleftharpoons x\,(\mathrm{M_n^-Li^+}) \tag{2.6}$$

where x takes the value 2 for polystyryllithium and 4 for polybutadienyllithium. This process is fast compared to the propagation reaction. Its equilibrium constant, $K_{eq}^{(M)}$, is given by

$$K_{eq}^{(M)} = \frac{[\mathrm{M_n^-Li^+}]^x}{[(\mathrm{M_n^-Li^+})_x]} \tag{2.7}$$

[1] There has been some debate in the literature about the values of the aggregation numbers 2 resp. 4. Only recently, a combined small-angle and light scattering study on living polystyryllithium and polybutadienyllithium solutions was published [32]. Both ions were found to aggregate in dimers and, simultaneously, in large micelles. No tetramers could be identified in case of polybutadienyllithium. The authors concluded that there is no simple relationship between reaction kinetics and aggregation behavior. In the following, the traditional way of describing propagation kinetics will be used. It describes the polymerization process quantitatively, even though the underlying picture is now known not to be correct.

where the number of aggregated chains is

$$x \cdot [(M_n^- Li^+)_x] = [\text{secBuLi}]_o - [M_n^- Li^+] \approx [\text{secBuLi}]_o \tag{2.8}$$

$[\text{secBuLi}]_o$ denotes the initiator concentration in the beginning. The concentration of free (growing) chains is, however, small compared to the number of aggregates and can therefore be neglected in the calculation of the rate constant. The concentration of aggregates can thus be written

$$[(M_n^- Li^+)_x] = \frac{[\text{secBuLi}]_o}{x} \tag{2.9}$$

Inserting $[M_n^- Li^+]$ into equations 2.7 and 2.4, the apparent rate constants of the polymerization of styrene and butadiene are found:

$$k_{app}^{(S)} = k_p^{(S)} \left(\frac{K_{eq}^{(S)} [\text{secBuLi}]_o}{2} \right)^{1/2} \tag{2.10}$$

$$k_{app}^{(B)} = k_p^{(B)} \left(\frac{K_{eq}^{(B)} [\text{secBuLi}]_o}{4} \right)^{1/4} \tag{2.11}$$

The duration of reaction can now be calculated taking into account the association process. The apparent rate constants at 40°C are only known in the following solvents [31]: $k_{app}^{(S)} = 3.5 \times 10^{-2} [\text{secBuLi}]_o^{1/2}$ for styrene in benzene and $k_{app}^{(B)} = 4.2 \times 10^{-4} [\text{secBuLi}]_o^{1/4}$ for butadiene in n-hexane. $k_{app}^{(S)}$ and $k_{app}^{(B)}$ are given in sec^{-1} and $[\text{secBuLi}]_o$ in mol per liter of cyclohexane. In cyclohexane, the polymerization of styrene is slightly slower than in benzene. The polymerization of butadiene in cyclohexane is a factor of ~ 1.5 faster than in n-hexane [33]. We multiplied therefore the rate constant $k_{app}^{(B)}$ (known for the reaction in benzene) by a factor of 1.5 before further use.

As the polymerization is very close to stoichiometric, the molar mass of, say, the polybutadiene block is given by

$$M_{PB} = \frac{m_B}{c_{secBuLi} \times V_{secBuLi}} \tag{2.12}$$

$c_{secBuLi}$ and $V_{secBuLi}$ denote the molar concentration and the volume of the sec-butyllithium solution added to the monomer solution. The overall molar mass is then $M_{total} = M_{PS} + M_{PB}$, M_{PS} being calculated in the same way as M_{PB}. The precision of M_{total} is estimated from the uncertainties in $V_{secBuLi}$, $c_{secBuLi}$ and the monomer masses. $V_{secBuLi}$ was controlled within 0.5%, the concentration of the initiator solution was determined by titration within 0.5%. The monomer masses (typically between 10 and 50 g) were controlled by weighing the ampoules containing monomer, and subtracting the mass of the empty, evacuated ampoules, which was done with a precision of 0.1 g. This means that the overall mass of the polymer, M_{total}, is determined within 1.5%.

The volume fraction of the styrene block in the diblock copolymer, f_{PS}, is given by the masses of the monomer species and the densities of the polymer blocks, ρ_{PS} and ρ_{PB}:

$$f_{PS} = \frac{V_{PS}}{V_{PS} + V_{PB}} = \frac{m_S/\rho_{PS}}{m_B/\rho_{PB} + m_S/\rho_{PS}} \tag{2.13}$$

The following values were used: $\rho_{PS} = 1.05$ g/cm^3 [34] and $\rho_{PB} = 0.886$ g/cm^3 [33]. The volume fraction is controlled within 1% if the uncertainties in density are assumed to be

0.01 g/ml and if the volume of mixing is zero. The weight fraction of polystyrene was determined using NMR (Chapter 3).

Under the reaction conditions described above, polystyrene is expected to be atactic, *i.e.* crystallization is hindered. Polybutadiene is expected to be a random copolymer consisting of 43% 1,4-cis-, 50% 1,4-trans- and 7% 1,2-addition ([34], p.IV-4, polymerization in hexane, or [30], p. 150). The content of 1,2-addition was determined using nuclear magnetic resonance spectroscopy (Chapter 3).

2.2 The set-up

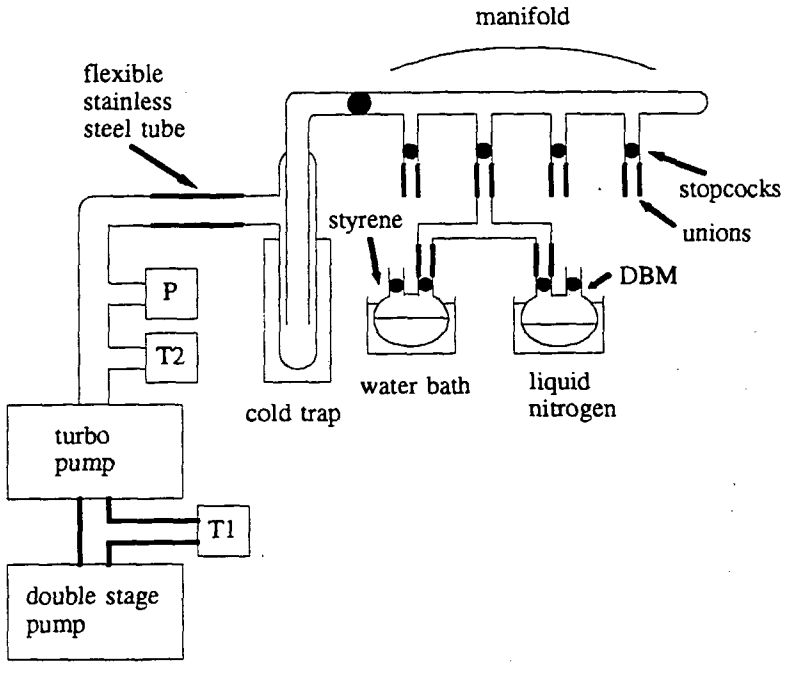

Figure 2.1: *Schematic drawing of the high vacuum distribution manifold. Thin lines represent glass and thick lines flexible stainless steel tubes. T1, T2 and P denote pressure gauges. In addition, the distillation of styrene to dibutylmagnesium, DBM, is shown.*

The set-up consisted of a high-vacuum distribution manifold, which was used for monomer distillation, and of a combined argon/vacuum distribution manifold, which was used for solvent distillation and during polymerization. Flasks, the reactor and others were connected to these two manifolds by means of unions and flexible stainless steel tubes.

For monomer distillation, a manifold connected to a high vacuum-system is used. Fig. 2.1 shows a schematic drawing. The design of the pumping system is described in detail in [31]. The pumping system consisted of a Baltzers turbo molecular pump TPH 050, driven by a TCP 040 electronic drive unit and cooled by air, together with an Edwards double stage rotary vane pump model EDM 8. Pressure was monitored with a Leybold-Heraeus Combitron CM330 pressure measuring system, equipped with two 2 thermocouple

gauges TR 201 (T1 and T2 in Fig. 2.1), and one cold cathode ionization gauge model PR31 (P in Fig. 2.1). A pressure range between atmospheric pressure and 10^{-7}mbar could be monitored. The base pressure in the high vacuum manifold was approximatively 10^{-6}mbar. The manifold was constructed from 1/2" medium or heavy wall glass tubing. Young teflon stopcocks were used. They could be used without vacuum grease. Different parts of the glassware were connected by Cajon 1/2" Ultratorr unions made from stainless steel or brass. In these connections, the sealing was obtained by pressing a Viton O-ring against the glass.

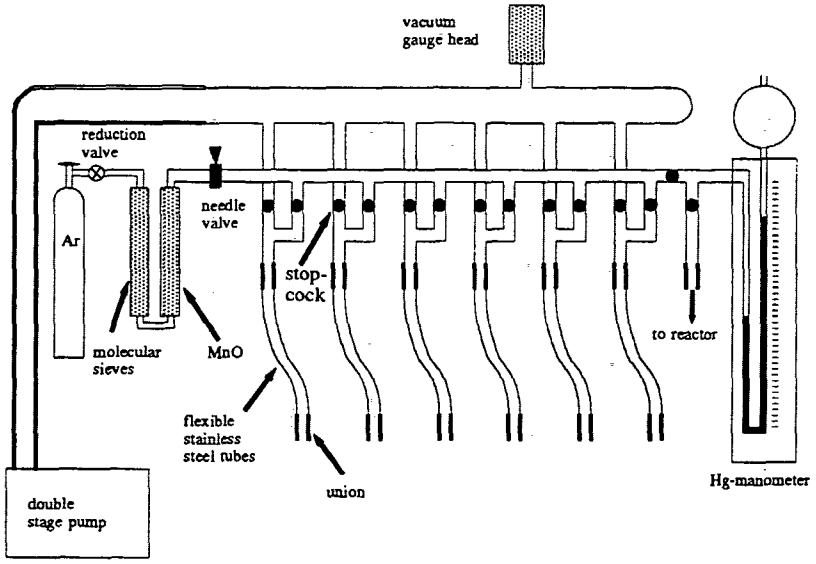

Figure 2.2: *Schematic drawing of the argon/vacuum distribution manifold.*

For solvent distillation and during polymerization, a combined argon/vacuum distribution manifold was used. Fig. 2.2 shows a schematic drawing. The argon used during solvent distillation and polymerization and for the purging of flasks must be free from water, air or other impurities. Before entering the manifold, it was purified by passing it through one column filled with molecular sieves (Aldrich, 5 Å, 8-12 mesh), which removes water, and one filled with manganese(II)oxide, which removes oxygen ($[O_2] < 1$ppm) [35]. The flow of purified argon into the manifold was controlled by means of a needle valve in a range between some ml/sec and 100 ml/sec. In the manifold, the maximum argon pressure was around 1.3 atmospheres. In order to monitor the pressure above atmospheric pressure, a mercury manometer was connected to the argon manifold or to the reactor which also served as a security valve during the polymerization. An Edwards double stage rotary vane pump model E2M8 was used for evacuating the vacuum manifold to a base pressure of 10 mTorr. The pressure in the vacuum manifold was monitored by a Varian 0531 gauge in a range from atmospheric pressure down to 1 mTorr. 3/8" heavy wall glassware was used. Young stopcocks were used. Flasks and others were attached by means of Cajon 1/2" and 3/8" Ultratorr unions made from stainless steel or brass.

The reactor was a 1 l or 3 l round bottom flask with 6 necks (Fig. 2.3) having glass threads (ACE Glass Inc.), to which monomer ampoules, a glass tube with rubber mem-

branes, a glass tube containing a thermocouple, and the connections to the solvent flask and to the manifold were connected. Conections were made by means of ACE nylon threads with Viton O-rings and, possibly, with flexible stainless steel tubes.

2.3 Purifications

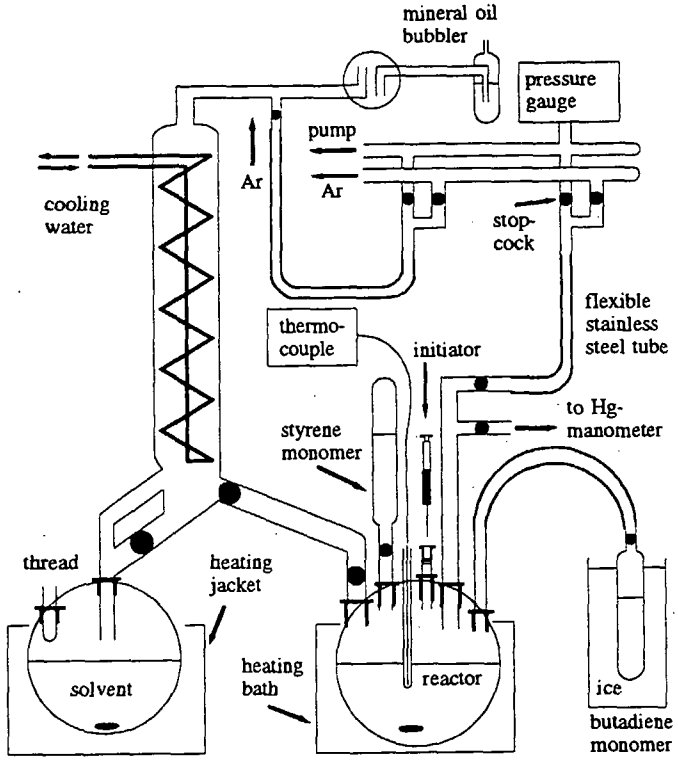

Figure 2.3: *Schematic drawing of the set-up for solvent distillation and polymerization which was connected to the argon/vauum manifold.*

Monomer flasks (Fig. 2.1), the solvent flask, and flasks used during titration of initiator were cleaned by evacuating and filling them with argon several times. Monomer ampoules were evacuated and flamed in order to remove water from the inner surface which was crucial as the purified, unstabilized monomer was kept in them before polymerization. The reactor was allowed to relax in an oven at 500°C for some hours in order to clean the surfaces and to remove tensions. Before polymerization, it was connected to the argon/vacuum manifold, evacuated and baked overnight at 250°C. During baking, a teflon-coated stirring bar was held on top of the reactor in order to avoid melting of the teflon. Whenever opening the solvent flask or the reactor, a stream of argon gas was maintained in order to avoid contamination with air. Hamilton syringes were flushed with argon several times before use.

Cyclohexane (Aldrich, 99%) was purified by keeping it on sulphuric acid (Merck, 95-97%, 100 ml per liter) for some days. In this way, unsaturated impurities were converted to sulphates which dissolved in the sulphuric acid layer at the bottom of the flask. 2 l of

the such purified cyclohexane were poured into the clean solvent flask and were refluxed under an argon atmosphere in order to remove air and other volatile impurities (Fig. 2.3). It was refluxed once more under argon with a small amount of 2.0 M n-butyllithium (2.5 ml per liter; Aldrich, 2.0 M in cyclohexane) and styrene (2 ml per liter; Aldrich, 99%), which leads to the formation of polystyryllithium reacting with remaining impurities. The persisting orange color of living polystyrylanions is an indication of solvent purity. New batches of purified cyclohexane were added together with styrene and n-butyllithium as long as the orange colour persisted. Distilling cyclohexane from this flask into the reactor leads to highly purified solvent.

1 l of styrene (Aldrich, 99%) was purified by stirring it with finely ground calciumhydride (Merck, GR) under vacuum for half an hour and then distilling the mixture, which removes inhibitor and water. A standard distillation kit was used together with a water pump. Such purified styrene monomer was kept in the freezer in order to prevent it from polymerizing. A batch of 250 ml of styrene was then filled into a monomer flask (Fig. 2.1) which was fitted to the high-vacuum manifold. Styrene was degassed by freezing it with liquid nitrogen and then pumping off the remaining gas phase. Then, styrene was thawed in a bath with hot water from the tap. Experience shows that the flasks tend to break when allowed to thaw slowly at room temperature [33]. After several freeze-thaw cycles, styrene was distilled from dibutylmagnesium, DBM. DBM initiates a slow polymerization of styrene. For this purpose, 10 ml of dibutylmagnesium (Alfa, 0.5 M in heptane) was given into another monomer flask in an argon-filled glovebox. The heptane was pumped off at the high-vacuum mainfold. Then, styrene was distilled into this flask (Fig. 2.1) by heating the styrene flask in a 30 – 35°C water bath and freezing the dibutylmagnesium-flask with liquid nitrogen. The mixture was kept at room temperature for some time. This leads to a yellow precipitation indicating a slow polymerization of styrene. The living polymers formed react with remaining impurities.

1,3-butadiene was purified by distillation with dibutylmagnesium and, in some runs, also with n-butyllithium in order to remove remaining impurities. Great care was necessary when working with butadiene, because it boils at −4.4°C and is very flammable. At room temperature, it has a vapor pressure of approximately 2.5 atmospheres, which is more than a standard laboratory flask can withstand. Therefore, it was kept on dry-ice/isopropanol or on ice-water all the time. The purification was carried out as follows: Butadiene gas (Aldrich, inhibited with p-tert-butylcatechol) was left to condense in a monomer flask containing vacuum-dried dibutylmagnesium (12 ml of stock solution) which was frozen with liquid nitrogen. The flask was then frozen thoroughly and the gasphase was pumped off. The flask was kept on ice-water for at least some hours before distilling butadiene into the monomer ampoule (see below) in order to make the formation of living polybutadienyllithium possible. In some runs, butadiene was distilled once more with n-butyllithium in order to improve the purity. For this purpose, butadiene, which had been kept on dibutylmagnesium, was distilled into another monomer flask. This flask contained some ml of vacuum-dried n-butyllithium (some ml of stock solution). During the distillation, the butadiene flask was kept on ice and the other flask on liquid nitrogen. The mixture was kept on ice for some time. However, we did not observe any effect of this purification step on the molar mass distribution of the resulting polystyrene-polybutadiene block copolymer, which is why this step was skipped again.

2.4 Control of chain architecture

The concentration of the sec-butyllithium solution, (Aldrich, 12% solution in cyclohexane/isopentane 92/8, $\sim$ 1.4 M), $c_{secBuLi}$, was determined following the Gilman double titration method [36, 37]. In the solution also other lithium compounds are present, such as lithium butoxide, lithium hydroxide, lithium hydride, and lithium oxide. Two batches of solution were titrated: one which was hydrolyzed and one where the sec-butyllithium compound had been destroyed by adding 1,2-dibromoethane (Aldrich, 99+%) before hydrolysis. As water reacts with all the compounds present forming lithiumhydroxide, the total amount of Li-compounds can be determined by titrating the hydrolyzed solution. By titrating the other batch, the concentration of basic impurities was determined. The difference between the two concentrations yields the concentration of sec-butyllithium. The titration was carried out as follows: 2 ml of distilled water were introduced through a rubber septum (Aldrich) into a cleaned flask (which was filled with argon) by means of a gastight syringe. Into another flask, 2 ml of dibromoethane were introduced in the same way. (Dibromoethane was kept on molecular sieves under argon.) To both flasks, 1.00 ml of sec-butyllithium solution was added by means of a gastight Hamilton syringe. Both solutions were hydrolyzed with $10-20$ ml of distilled water and titrated with 0.1 M hydrochloric acid using phenolphtalein as an indicator. The difference in concentrations determines $c_{secBuLi}$ which was typically 1.4 mol/l. As the other lithium compounds are unable to initiate the polymerization of styrene or butadiene, it was not necessary to purge the solution, but stock solution could be used for initiation.

The amounts of monomer were controlled in the following way: An amount of purified butadiene was distilled into a pre-weighed ampoule made from 25 or 100 ml graduated cylinders (Fig. 2.3). The necessary amount of styrene as calculated from Eq. 2.13 (which reduces to $m_S = m_B \times \rho_{PS}/\rho_{PB}$ in case of symmetric diblock copolymers) was distilled into another monomer ampoule. Excess styrene was distilled into the cold trap. Both flasks were connected to the high-vacuum manifold and kept on dry-ice/isopropanol until polymerization.

2.5 Polymerization

Monomer ampoules were fitted onto the baked reactor under a stream of argon. Then, the reactor was evacuated and flushed with argon at least five times. During polymerization, the temperature was controlled by immersing the reactor in a water bath. The bath was heated to 40°C by a copper tube through which thermostated water was pumped.

Cyclohexane was refluxed with polystyryllithium under argon and, according to the reactor used, an amount of 0.5 respectively 1.5 l of cyclohexane was distilled into the reactor. The solvent volume was chosen such, that the mass concentration of the polymer during the polymerization did not exceed 20%, in order to prevent the living polymer solution from becoming too viscous. An overpressure of approximately 50 mm Hg of argon was created in the reactor in order to avoid air from penetrating into the reactor. The connection to the argon distribution manifold was closed in order to monitor the reactor pressure using the mercury manometer.

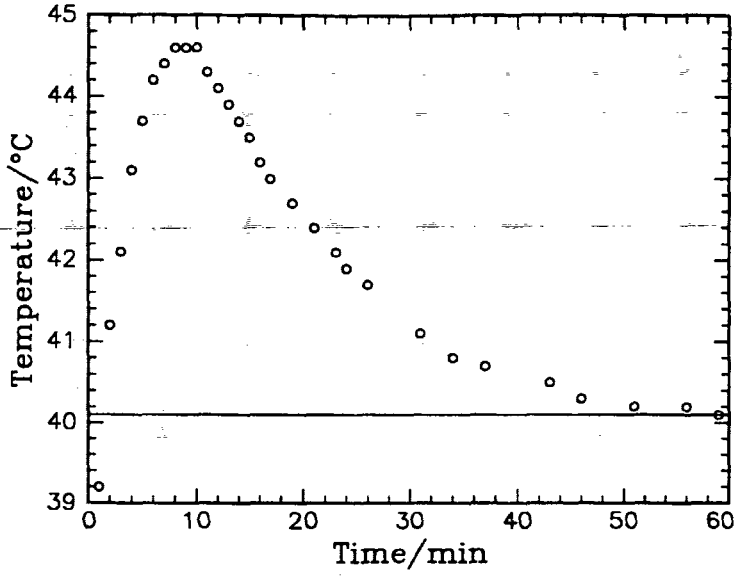

Figure 2.4: *Temperature in the reactor during the polymerization of polystyrene (SB08). M_{PS}=12000 g/mol, m_S=17.8 g, V_{CHx}=0.5 l, [RLi]=2.98 mmol/l. Before polymerization, the temperature was 40.1°C, was indicated by the horizontal line.*

The calculated amount of sec-butyllithium solution was introduced into the reactor through the teflon-coated rubber septa (Supelco) by means of a gastight syringe (Fig. 2.3). Styrene monomer was let to flow into the reactor. The solution turned yellow indicating the presence of polystyryllithium. The temperature increased with some degrees and typically reached a maximum after 10 to 15 minutes (Fig. 2.4). If a polymer with low molar mass ($M_{total} \leq 10000$ g/mol) was synthesized, styrene was added to the reactor in small amounts in order to avoid a large, sudden rise in temperature. The polymerization of styrene blocks between 3000 and 100000 g/mol took between 30 min and 3 hours depending on the concentration. When the calculated reaction time for polystyrene had elapsed (Eq. 2.5), butadiene momomer, which had been kept on ice during the polymerization of styrene, was added to the reactor. The solution lost color indicating the termination of the styrene polymerization. If the polystyryllithium solution is very viscous, butadiene gas is only slowly miscible and the pressure in the reactor may rise considerably. Therefore, butadiene was added in small amounts (5 to 10 ml), watching the pressure in the reactor which should not exceed 1 atmosphere of overpressure. During the polymerization, the pressure dropped continuously (Fig. 2.5) which allowed to estimate the rate constant. It was assumed that the vapor pressure of butadiene in the reactor is proportional to butadiene monomer concentration in the solution, *i.e.* the vapor pressure of the other species present in the reactor was assumed to be constant during polymerization. The following equation was used to estimate the rate constant by fitting it to the data:

$$p = p_{end} + (p_0 - p_{end}) \exp(-k_{app}^{(B)} t) \tag{2.14}$$

where p_0 is the pressure before the polymerization and p_{end} the pressure when all monomer has reacted. Using the pressure values measured during the polymerization of butadiene for SB07, we obtained $k_{app}^{(B)} = (1.13 \pm 0.05) \times 10^{-4} s^{-1}$ from the fit which is of the same

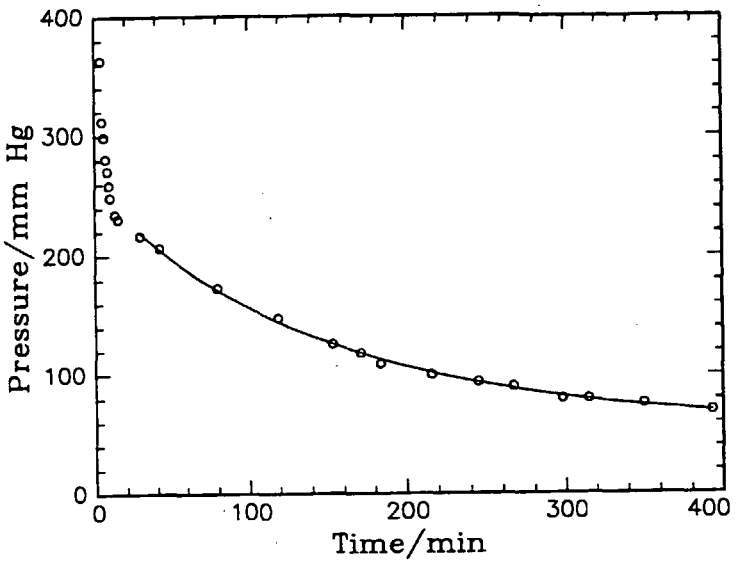

Figure 2.5: *Pressure in the reactor during the polymerization of butadiene (SB07).* M_{PB} = 67900 *g/mol,* m_S = 32.9 *g,* V_{CHx} = 1.5 *l,* $[RLi]$ = 0.325 *mmol/l,* T = 39.3°*C. Before polymerization, the pressure was 50 mm Hg. During the first 20 minutes, the pressure dropped fastly because butadiene monomer was dissolved in cyclohexane. The line is a fit of Eq. 2.14.*

order of magnitude as the predicted value, $k_{app}^{(B)} = 8.5 \times 10^{-5}\text{sec}^{-1}$. The polymerization of polybutadiene blocks between 4000 and 85000 g/mol took between 4 and 22 hours. A problem with high molar mass polymers was that the viscosity increased significantly during polymerization, making the stirrer bar get stuck. Both the growing polymers and the aggregates formed contributed to this rise.

The polymerization was stopped with methanol. For this purpose, 50 ml of methanol were degassed during several freeze-thaw cycles and were kept under argon. With a gastight syringe, 5 ml (*i.e.* an excess amount) were added to the reactor when the reaction time for the polybutadiene block had elapsed. The viscosity dropped immediately because the association processes of the living polymers were stopped.

The polymer samples were isolated by dripping the solution into the three-fold volume of a 2:1 methanol/isopropanol mixture. The solvent was poured off and the polymer sample was dried in a vacuum oven, which made the sample foam. After some days at a pressure of approximately 1 mbar samples were stored in the freezer (−30°C).

In Table 2.1, the samples together with the respective reaction conditions are given. The values of the yield (polymer mass obtained after drying divided by monomer mass) are higher than 95% for most of the samples which were used for further investigations. Keeping in mind that typically 1 g was lost during isolation and drying, the calculated molar mass values, $\bar{M}_N^{stoich}$, are accurate within some percent. Only the yield values of the low molar-mass samples SB05, SB14, and SB11 are lower than 95%, which is due to their partial solubility in the solvent mixture cyclohexane/methanol/isopropanol.

To summarize, a homologous series of symmetric polystyrene-polybutadiene has been carried out using anionic polymerization under inert atmosphere.

sample	$\bar{M}_n$ g/mol	monomer mass / g	yield %	[secBuLi]$_o$ mmol/l	reaction time/h PS	PB
SB01	18500	23.9	95	2.58	2.0	14
SB02[a]	54500	25.1	98	0.614	3.0	21
SB03[a]	5550	30.4	97	7.35	2.0	21
SB04[a,b]	165000	31.8	88	3.86	3.0	22
SB05	9200	83.8	94	18.2	1.1	4
SB06	91900	81.3	95	1.77	0.75	16
SB07[a]	148000	71.9	98	0.323	3.0	21
SB08	22600	32.7	(d)	2.89	1.0	17
SB09[b]	73400	71.9	99	0.653	2.0	16
SB10[c]	183000	120.1	99	0.438	2.5	20
SB11[c]	18300	65.8	93	2.40	1.0	10.5
SB12	22100	85.3	(d)	7.73	0.75	19.5
SB13[b]	13900	41.7	87	6.01	0.75	20.5
SB14	13900	28.0	65	1.34	1.6	17.0
SB15	69900	24.8	(d)	0.238	3.4	19.5

Table 2.1: *Reaction conditions of the polystyrene-polybutadiene samples. Given are the stoichiometric molar mass, the overall monomer mass used, the yield, the initiator concentration and the reaction times for each block. (a) Polybutadiene was polymerized first, (b) leakage during polymerization, (c) butadiene was distilled with dibutylmagnesium and with n-butyllithium, (d) not known.*

Chapter 3

Sample characterization

The samples synthesized as described in the previous chapter were characterized using various methods. Using size exclusion chromatography, the molar mass distributions were determined. The microstructure, *i.e.* the weight fraction of polystyrene and the content of 1,2-addition in the polybutadiene block was determined using nuclear magnetic resonance (NMR) spectroscopy. In dynamic mechanical experiments, the order-disorder transition temperatures were measured, thus making it possible to estimate the Flory-Huggins segment-segment interaction parameter. The glass temperatures of five low molar-mass sample were estimated using differential scanning calorimetry.

3.1 The molar-mass distributions

(Size exclusion chromatography was carried out in collaboration with Lotte Nielsen, Risø National Laboratory.)

The molar mass of the polymers synthesized by anionic polymerization is a Poisson distribution, because of the statistical nature of monomer addition [30]. However, impurities may terminate growing polymers. Chain transfer and side reactions may occur, leading to additional broadening of the distribution. In some polymerization runs, a leakage occured in the reactor when butadiene was added to the solution of living polystyrene, due to the rise in pressure. It was doubtful if these polymers samples could be used for further investigations. Therefore, the molar mass distributions of all polymers synthesized were measured using size exclusion chromatography.

Size exclusion chromatography is a separation method for polymers [40] and is used to determine the distribution of molar mass of the synthesized polymers. The separation process takes place in a chromatographic column filled with beads of a rigid porous material, *e.g.* cross-linked polystyrene. The pores are approximately of the same size as the dimensions of the polymer molecules to be separated. The separation process is started by injecting a sample of a dilute polymer solution into the solvent stream flowing through the column. This is the task of the injection unit (Fig. 3.1). As the dissolved polymer molecules flow past the porous beads, they can diffuse into the pores of the packing material to an extent depending on their size and the size distribution of the pores. The

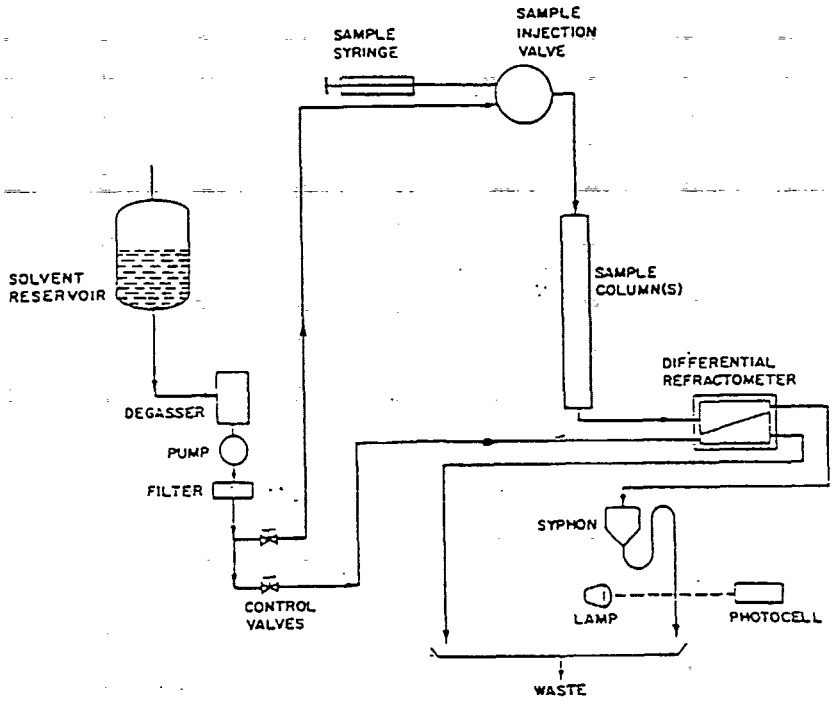

Figure 3.1: *Schematic set-up for size exclusion chromatography. For explanation see text. From [38]. The original is from [39].*

larger the hydrodynamic radius of the molecules dissolved, the smaller is the fraction of the accessible pore volume which is the reason why large molecules leave the column first. The weigth fraction of polymers having a certain hydrodynamic radius is determined by measuring the differential refractive index of the solution leaving the column, *i.e.* the difference of the refractive index of the solution and the pure solvent. A syphon having a known volume together with an optical detection system provides a direct measure of the elution volume, *i.e.* the volume of the column accessible to the polymers.

A Knauer system equipped with a HPLC pump FR-30, a PL-precolumn 20 μ, a 100 cm Shodex A-80M column, and a high temperature differential refractometer as detector was used in the present study. The column temperature was stabilized at 30°C. Stabilized tetrahydrofurane was used as a solvent. In order to determine the distribution of molar mass of the polymers, the system was calibrated with a dilute solution of different commercially available polystyrene samples having known molar masses and narrow molar mass distributions (Table 3.1). A typical calibration curve is shown in Fig. 3.2. The logarithm of the polystyrene molar mass is plotted versus the elution volume, i.e. the volume of solvent that has flowed through the column before the sample was detected.

Polystyrene-polybutadiene samples were diluted in toluene to concentrations between 0.75 and 1.30 mg/ml. Some chromatograms are shown in Fig. 3.3. Elution volumes ranged between 27 and 37 ml. The chromatograms were analyzed by means of a computer program [31] which fitted a third-order polynomial to the calibration data (Fig. 3.2). The

$\bar{M}_N$ [g/mol]	brand
12250000	Polymer Lab
655000	Waters
110000	Waters
17050	TSK F-2
1000	TSK 1000

Table 3.1: *Polystyrene samples in the standard solution used for calibration of the chromatography system.*

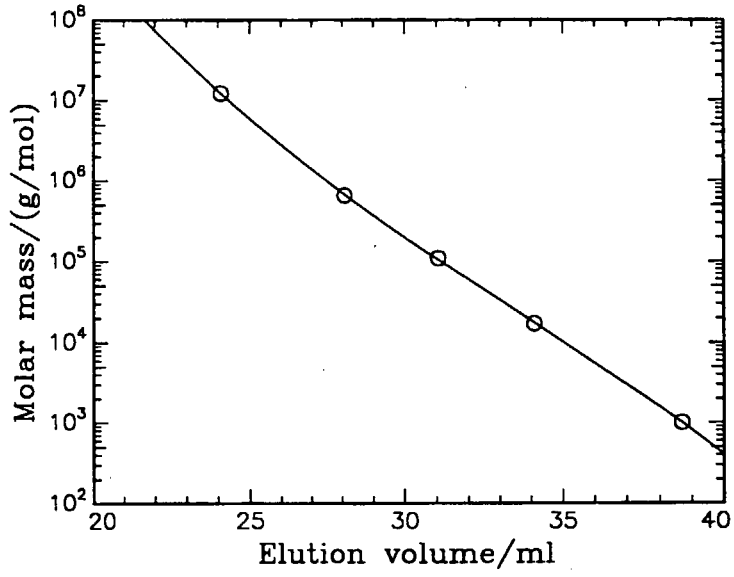

Figure 3.2: *Typical calibration curve of the column using polystyrene standards. The line is a fit of a third-order polynomial.*

chromatograms of the samples were approximated by a histogram from which the number-average molar mass, $\bar{M}_N = \sum_i N_i M_i / \sum_i N_i$, the weight-average, $\bar{M}_W = \sum_i N_i M_i^2 / \sum_i N_i M_i$ (where N_i is the number of molecules having molar mass M_i) and the polydispersity index $\bar{M}_W/\bar{M}_N$ were calculated. $\bar{M}_W/\bar{M}_N$ provides a measure of the width of the molar-mass distribution; for single species, $\bar{M}_W/\bar{M}_N = 1$. As the system was calibrated with polystyrene and not with polystyrene-polybutadiene, the absolute molar masses of the polystyrene-polybutadiene samples could not be determined, because the hydrodynamic radii of polybutadiene and polystyrene having the same molar mass are different. However, the $\bar{M}_W/\bar{M}_N$-values are considered to be approximately correct. The main interest of the study was to verify that the distributions of the polystyrene-polybutadiene samples were monomodal and as narrow as the ones of the polystyrene standard samples. In Table 3.2, the results are given together with the number of segments, N, which is based on the butadiene monomer volume ($v_{PB} = M_B/\rho_{PB} = 101$ Å^3). The polydispersity values represent upper limits because of the finite resolution of the system. The peaks of

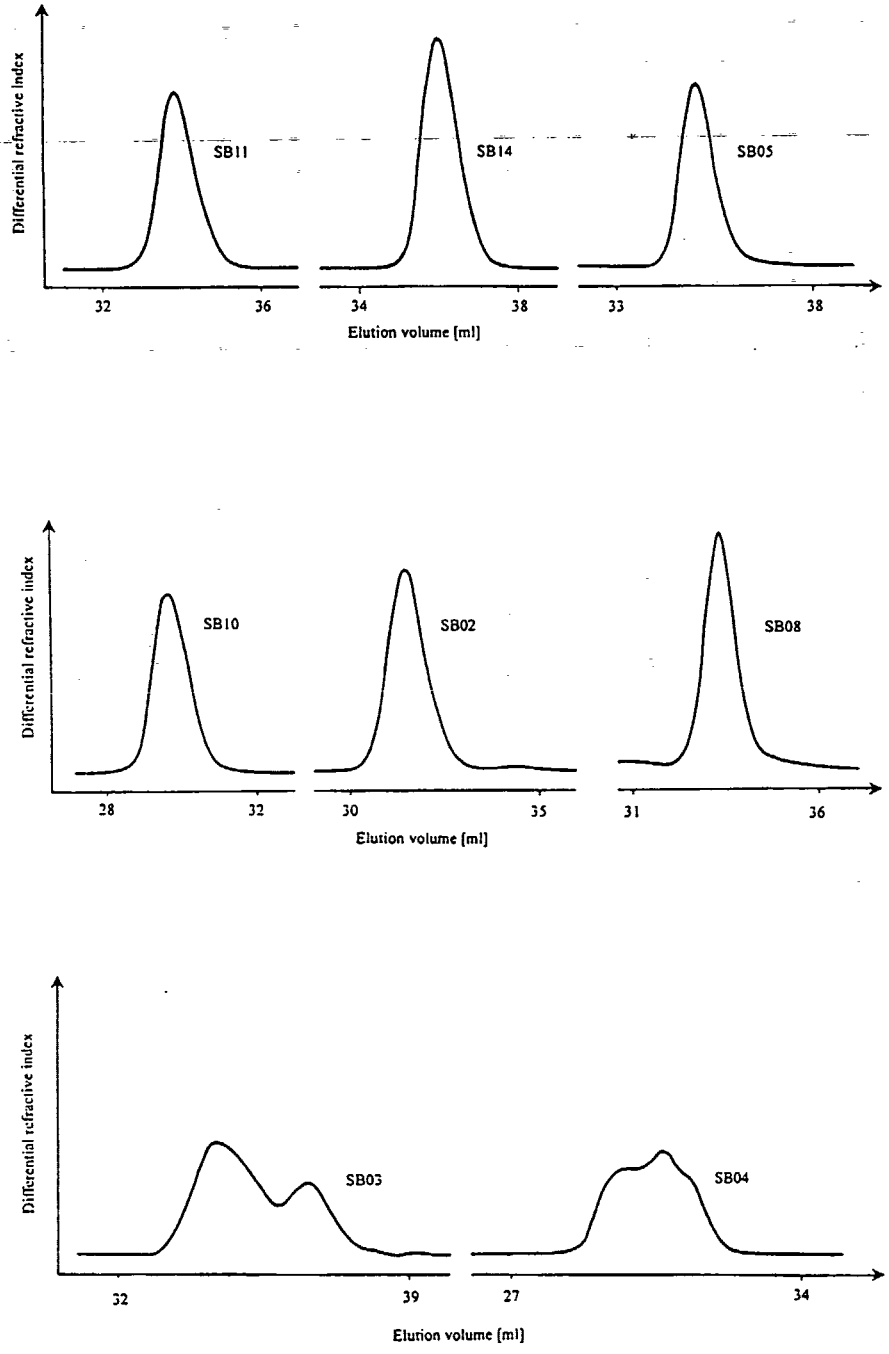

Figure 3.3: *Upper and middle figure: Chromatograms of polystyrene-polybutadiene diblock copolymers which were used for further investigations. Lower figure: Chromatograms of two samples having non-monomodal molar-mass distributions. These samples were not used for further investigations. For the corresponding values of* $\bar{M}_W/\bar{M}_N$ *see Table 3.2.*

polystyrene-polybutadiene samples (except those of SB03, SB04 and SB09) were of the same width as the commercial polystyrene samples.

sample	M_N^{stoich} [g/mol]	N	$\bar{M}_W/\bar{M}_N$
SB03	5550	94	1.51[a,b]
SB05	9200	156	1.09
SB13	13900	236	–[b]
SB14	13900	236	1.07
SB11	18300	310	1.05
SB01	18500	313	1.09
SB12	22100	374	1.05
SB08	22600	383	1.13
SB02	54500	921	1.07
SB15	69900	1182	1.08
SB09	73400	1241	1.22[a,b]
SB06	91900	1555	1.11
SB07	148000	2511	1.18
SB04	165000	2789	1.23[a,b]
SB10	183000	3090	1.10

Table 3.2: *Size exclusion chromatography results of the polystyrene-polybutadiene samples. Given are the overall stoichiometric molar mass, the number of segments based on the polybutadiene monomer volume and the polydipersity index. (a) Bimodal distribution, (b) not used for further investigations.*

3.2 The microstructure

(NMR-spectroscopy was carried out at the Department for Life Sciences and Chemistry, Roskilde University in collaboration with Morten Langgård, Annelise Gudmundsson and Poul Erik Hansen.)

The microstructure of the polystyrene-polybutadiene diblock copolymers synthesized, *i.e.* the weight fraction of styrene, w_{PS}, and the content of 1,2- and 1,4-addition in the polybutadiene block, $f_{1,2}$, was determined using nuclear magnetic resonance (NMR) spectroscopy.

NMR is a widely used technique for investigating the microstructure of polymers and other samples. The principle of the method is the following [41]: A high magnetic field is applied to the sample which makes the nuclear spins precess around the field axis with a certain frequency, the so-called Larmor frequency. In addition, a small, rotating magnetic field is applied perpendicular to the magnetic field. A resonance condition is achieved when the rotation rate of the field equals the Larmor frequency. However, the magnetic field experienced by a given nucleus depends on its surroundings. Thus, resonance is achieved at a frequency which is shifted with respect to a hypothetic isolated nucleus.

This 'chemical shift' allows thus to quantify the number fraction of nuclei with a given surrounding (double bonds, phenyl rings etc.) and to study the microstructure of polymers. Using proton NMR, the number of aliphatic and vinylic protons and of protons belonging to the phenyl ring was measured, which allows determination of the content of polystyrene and of 1,4- and 1,2-added polybutadiene monomers.

The volume fraction of styrene in the diblock copolymer, f_{PS}, is an important factor for the phase behaviour of the block copolymers. During synthesis, the weight fraction

$$w_{PS} = \frac{M_{PS}}{M_{PS} + M_{PB}} \tag{3.1}$$

is controlled by choosing the appropriate amounts of monomer species and by bringing the polymerization as good as possible to completion. M_{PS} and M_{PB} denote the molar masses of the polystyrene and the polybutadiene blocks, respectively. The volume fraction is related to the weight fraction by

$$f_{PS} = \left(1 + \frac{1 - w_{PS}}{w_{PS}} \times \frac{\rho_{PS}}{\rho_{PB}}\right)^{-1} \tag{3.2}$$

From stoichiometry, the weight fractions of styrene were estimated to be $w_{PS} = 0.54$ corresponding to $f_{PS} = 0.50$. NMR provides an independent measure of w_{PS}.

Knowledge of the content of 1,2- and 1,4-addition in the polybutadiene block is important because, among others, the Flory-Huggins interaction parameter of the styrene-butadiene monomer pair (which governs phase behavior) and the glass transition temperature of the polybutadiene block depend on the microstructure of the polybutadiene block [34]. During synthesis, the microstructure of polybutadiene is controlled through temperature, polarity of solvent and choice of initiator. Synthesis was carried out in a non-polar solvent (cyclohexane) at 40°C and *sec*-butyllithium was used an initiator. Under these conditions, a content of ca. 7% of 1,2-addition is expected (ref. 7 in Chapter 15 of [30]).

3.2.1 Experimental

Samples were dried in a vacuum oven (Appendix A) at $120-130$°C for ca. 2 hours in order to remove traces of solvent and were then dissolved in deuterated chloroform (99.8% D, Fluorochem Limited). The polymer concentrations were between 25.8 and 34.7 mg/ml. The solutions were filled into ultra precision NMR sample tubes (Dr. Glaser AG, 5 mm outer diameter, 178 mm long). A Bruker AC-250 MHz NMR-instrument was used for proton NMR measurements. With this instrument, a rotating magnetic field was applied during a short time and then, the decay of signal was measured in a period of time. A delay time of at least 10 sec between the pulses was found to be crucial for exact determination of the relative peak intensities because of the slow relaxation processes occuring in polymer solutions. However, the longer the delay, the stronger the signal from water which is present in chloroform. The water signal is located in the region of peak 4 (see below). The sample temperature in the spectrometer was stabilized at 23°C. The apparatus was locked on the signal of d-chloroform. The zero of the scale corresponds to the signal of tetramethylsilane.

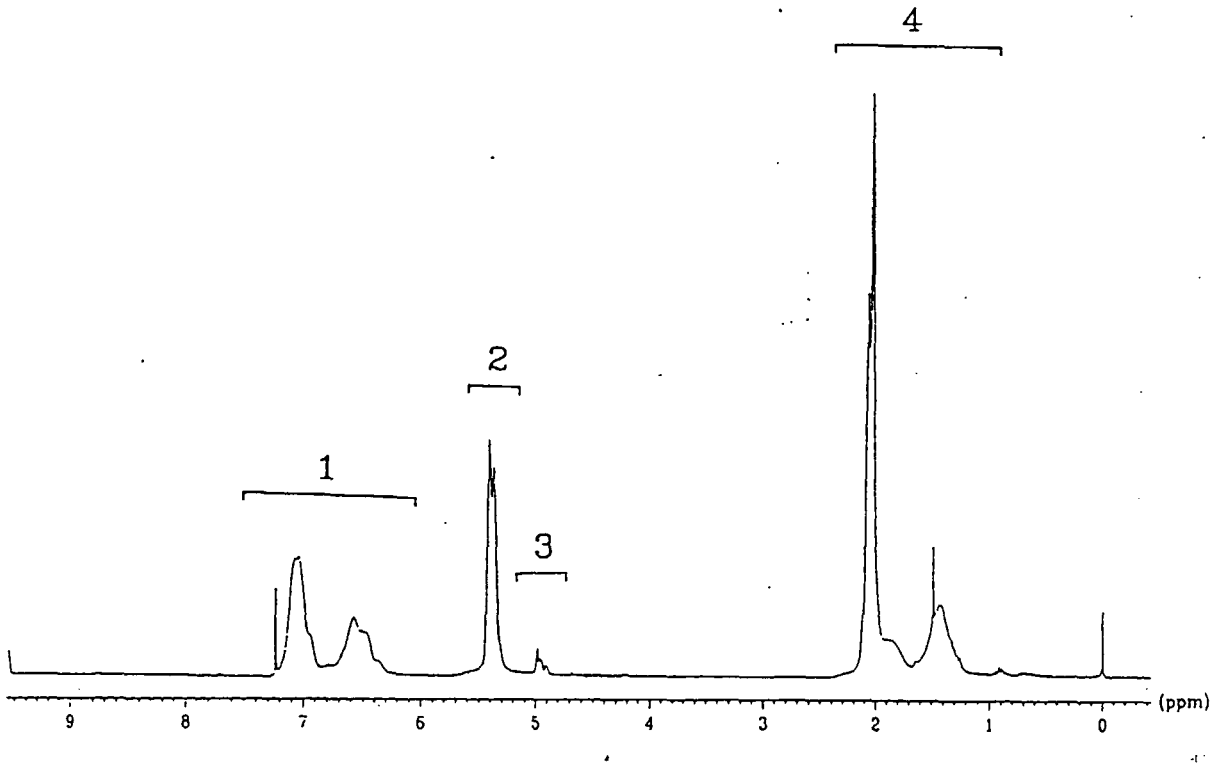

Figure 3.4: *NMR-spectrum of SB11 in d-chloroform.*

3.2.2 Data analysis

The NMR-spectrum of a polystyrene-polybutadiene samples shows four groups of peaks which are labelled 1,..., 4 (Fig. 3.4). The different types of monomer addition are shown in Fig. 3.5 where the protons are marked with letters $A, \ldots, I$. Peak 1 is due to signals from protons in the phenyl ring of styrene (A, B, C in Fig. 3.5), peaks 2 and 3 to vinylic protons (F, H, I) and peak 4 to aliphatic protons (D, E, G). The peak intensities are written as a function of N_S (the number of styrene monomers) and of $N_B^{1,2}$ and $N_B^{1,4}$ (the number of 1,2- resp. 1,4-added butadiene monomers):

$$\begin{aligned} I_1 &= 2I_A + 2I_B + I_C = 5cN_S \\ I_2 &= 2I_F + I_H = 2cN_B^{1,4} + cN_B^{1,2} \\ I_3 &= 2I_I = 2cN_B^{1,2} \\ I_4 &= I_D + 8I_E + I_G = 3cN_S + 4cN_B^{1,4} + 3cN_B^{1,2} \end{aligned}$$

where c denotes the signal strength per proton. For the determination of w_{PS} and $f_{1,2}$ only signals from the protons in the phenyl ring and from vinylic protons are used. The reasons are the contamination of peak 4 with the water signal and that the signal strength of aliphatic protons might be different from the signal strength of ring- and vinylic protons. Thus, using the expressions for I_1, I_2, and I_3, N_S and $N_B = N_B^{1,2} + N_B^{1,4}$ are given by

$$N_S = c^{-1} \times 0.2I_1 \quad (3.3)$$

$$N_B^{1,2} = c^{-1} \times 0.5I_3 \quad (3.4)$$

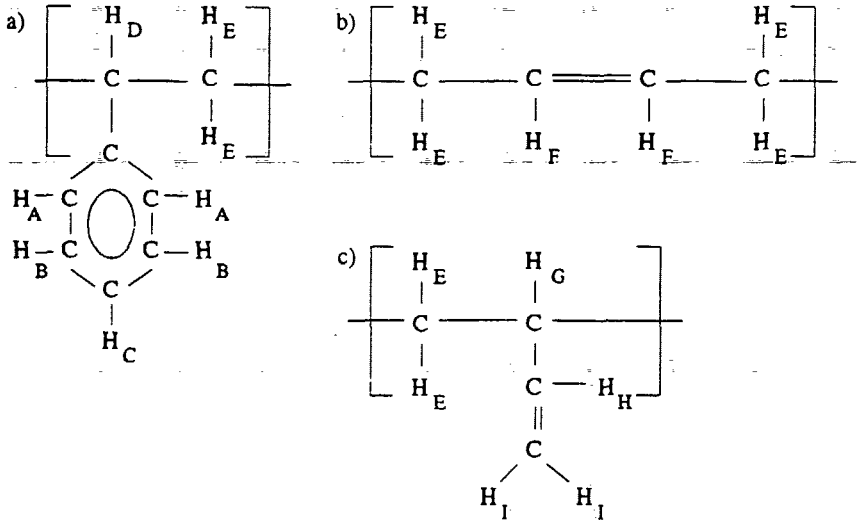

Figure 3.5: *A polystyrene monomer (a), a 1,4- (b) and a 1,2-added polybutadiene monomer (c).*

$$N_B^{1,4} = c^{-1}(0.5I_2 - 0.25I_3) \tag{3.5}$$
$$\Longrightarrow N_B = c^{-1}(0.5I_2 + 0.25I_3) \tag{3.6}$$

w_{PS} and $f_{1,2}$ are defined as

$$w_{PS} = \frac{M_{PS}}{M_{PS} + M_{PB}} = \left(1 + \frac{N_B}{N_S}\frac{M_B}{M_S}\right)^{-1}, \quad f_{1,2} = \frac{N_B^{1,2}}{N_B^{1,2} + N_B^{1,4}} \tag{3.7}$$

where $M_{PS} = 104.2$ g/mol and $M_{PB} = 54.1$ g/mol are the stoichiometric molar masses of the styrene and the butadiene block. Thus,

$$w_{PS}^{(1)} = \left(1 + \frac{0.5I_2 + 0.25I_3}{0.2I_1}\frac{M_B}{M_S}\right)^{-1}, \quad f_{1,2} = \frac{I_3}{I_2 + 0.5I_3} \tag{3.8}$$

3.2.3 Results and discussion

The integrated peak intensities $I_1 - I_4$ together with the values of w_{PS} and $f_{1,2}$ are given in Table 3.3. As only intensity ratios are used, the results are independent of measuring time and concentration. In order to facilitate comparison, the value of I_1 is set to 1.000 for all samples. The weight fractions of styrene determined using NMR are between 0.54 and 0.56. These values do not differ more than by 0.02 or 4% from the stoichiometric values. NMR thus confirms the values calculated from stoichiometry. Possible reasons for the slight discrepancy are loss of monomer during the synthesis and incomplete reactions. The integrated peak intensities may be too high because of biased baselines which cause errors, especially for broad peaks, *e.g.* for I_1. There is also a large difference in intensity between I_2 and I_3 (a factor of approx. 10) which may cause errors in the determination of w_{PS}.

sample	m_S [g]	m_B [g]	w_{PS} stoich.	I_1	I_2	I_3	I_4	w_{PS} NMR	$f_{1,2}$% NMR
SB05	45.5	38.3	0.55	1.000	0.609	0.0637	1.97	0.55	9.9
SB11	35.7	30.1	0.54	1.000	0.586	0.0427	1.90	0.56	7.0
SB01	12.9	11.0	0.54	1.000	0.625	0.0555	2.02	0.54	8.5
SB12	46.1	39.2	0.54	1.000	0.616	0.0582	1.98	0.55	9.0
SB08	17.8	14.9	0.54	1.000	0.577	0.0553	1.83	0.56	9.2
SB02	13.7	11.4	0.55	1.000	0.600	0.0603	1.88	0.55	9.6
SB06	44.2	37.1	0.54	1.000	0.623	0.0665	1.85	0.54	10.1
SB07	39.0	32.9	0.54	1.000	0.631	0.0612	2.09	0.54	9.3
SB10	65.2	54.9	0.54	1.000	0.614	0.0542	2.04	0.55	8.5

Table 3.3: *Comparison of stoichiometric and NMR results. Given are the monomer masses used, m_S and m_B, and the weight fraction $w_{PS} = m_S/(m_S + m_B)$. Furthermore, the integrated peak intensities from NMR, the calculated values of the weight fractions of polystyrene and the percentages of 1,2-addition in polybutadiene. I_1 was set to 1.000.*

However, the values determined using NMR confirm the stoichiometric values. Assuming polymer densities $\rho_{PS} = 1.05$ g/cm^3 [34] and $\rho_{PB} = 0.886$ g/cm^3 [33], NMR gives volume fractions of polystyrene $f_{PS} = 0.51 \pm 0.01$ whereas the values from stoichiometry are centered around 0.50. Our experience is that the delay time of 10 sec was necessary to obtain satisfactory results. In summary, the diblock copolymers synthesized are very close to being symmetric.

The content of 1,2-addition in the polybutadiene blocks was found to be 9.0 ± 0.9%. The high spread of the data is due to the small values of I_3 in comparison to I_2. Nearly all values are higher than literature values for similar polymerization conditions (7%) [30]. The difference is probably due to traces of polar molecules in the monomer species and in the solvent which has an influence on the polybutadiene microstructure.

3.3 The order-disorder transition temperatures

(The dynamic mechanical measurements were carried out at Risø National Laboratory in collaboration with Lene Hubert and Kristoffer Almdal.)

The rheological behavior of diblock copolymers is known to be very complex, especially in the ordered state, and is still a subject of intensive investigations (*e.g.* [22, 42, 43]). The time-temperature superposition principle which has been used succesfully for homopolymers [44], does not apply in the ordered state. No comprehensive theory explaining the rheological response on a molecular basis exists so far. In this study, we only use the results from dynamic mechanical measurements on low molar-mass samples for determination of the ODT temperatures. The ODT has by fluctuation theory been shown to be a weak first-order transition [20]. Therefore, the dynamic elastic and loss modulus are expected to drop discontinuously at the ODT temperature, which allows determination of the transition temperatures. The Flory-Huggins segment-segment interaction parameter can be determined using the mean-field prediction for symmetric diblock copolymers, that

$\chi N \simeq 10.5$ at the ODT [7] and assuming that $\chi = a/T + b$ [45]. Knowledge of the ODT temperatures of samples with different chain lengths, N, then allows one to determine the parameters a and b. This makes it possible to calculate χN for all block copolymers studied and to locate them in the phase diagram.

3.3.1 Experimental

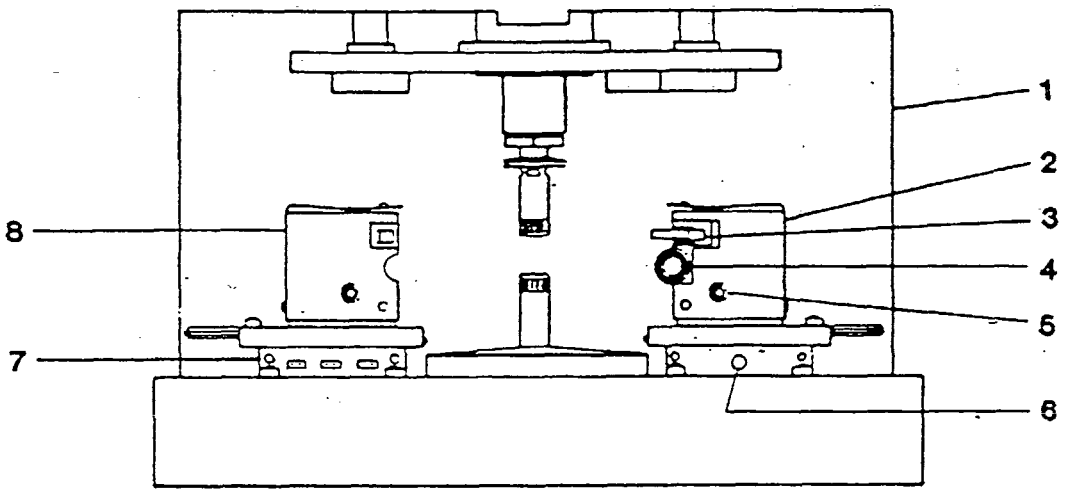

Figure 3.6: *Schematic drawing of the RMS-800 rheometer. Shown is the parallel plate geometry, where the lower plate oscillates around the vertical axis and the upper plate is coupled to a force transducer monitoring the transmitted torque. During the measurements, the upper plate is lowered, the oven is closed and a stream of nitrogen gas is maintained to heat the sample. From [46].*

An RMS-800 rheometer [46] was used in the parallel-plate geometry with plates having a diameter of 50 mm. A schematic drawing of the instrument is shown in Fig. 3.6. Pills of 1 mm thickness were pressed and mounted between the plates. The samples were thermally equilibrated in a stream of nitrogen gas.

3.3.2 The ODT temperatures

The frequency behavior of diblock copolymers is known to change drastically at the ODT temperature. Above the ODT temperature, a liquidlike response has been observed: in the terminal region (*i.e.* at low frequencies), the dynamic elastic modulus, G', has been found to be proportional to ω^2 and the loss modulus $G'' \propto \omega$ [47]. Below the ODT temperature, the elastic and the loss modulus were found to depend more weakly on frequency: $G' \propto \omega^{0.5}$ and $G'' \propto \omega^{0.7}$ were observed for poly(ethylene propylene)-poly(ethyl ethylene) in the terminal region [47]. In this regime, the existence of lamellar domains leads to a higher

elasticity and viscosity. However, above a certain frequency, the rheological response has not been found to be affected by the ODT. This might be attributed to the fact that, at high frequencies, lengthscales smaller than the lamellar thickness are probed. This behavior could also be observed with polystyrene-polybutadiene diblock copolymers. In Fig. 3.7, the dynamic elastic and loss modulus are shown for temperatures below and above the ODT temperature. The curves measured below the ODT temperature are nearly equal. A linear fit to data measured at 167°C gives $G' \propto \omega^{0.4}$ and $G'' \propto \omega^{0.6}$. Both exponents are lower than the ones given by Rosedale *et al.* [47] which certainly is due to the fact that the terminal region has not been reached. In addition, the fitting range is very small. Measurements at lower frequencies could not be carried out because of a low signal. At the ODT (181°C), both the elastic and the loss modulus display a stronger frequency dependence in the terminal region than above. Due to the small signal, measurements could not be made at lower frequencies and thus, no fit could be performed.

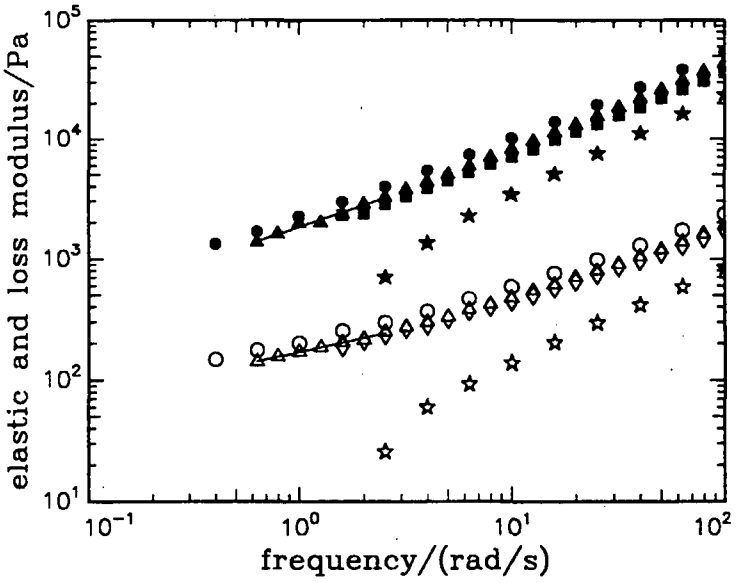

Figure 3.7: *The dynamic elastic and loss modulus of sample SB12 at 162°C (G': open circles, G'': filled circles), 167°C (G': open triangles, G'': filled triangles), 173°C (G': diamonds, G'': filled boxes), 181°C (G': open stars, G'': filled stars). Data of the loss modulus were shifted upwards by one decade. The strain amplitude was 2%, except at 162°C where it was 1%. Lines are linear fits to data at 167°C.*

The ODT temperatures were determined in temperature sweeps (Fig. 3.8). The parameters used are summarized in Table 3.4. One might suspect that 1°C/min was too high a heating rate; however, as can be seen with sample SB11, the width of the transition is approximately 2°C. This is partly due to the time needed to heat the whole sample above the ODT temperature and partly to the intrinsic width of the transition, which might be due to polydispersity. A difference of 4°C between the temperature where the signal dropped upon heating and increased upon cooling was found with sample SB11. However, an uncertainty of ±2°C is not considered to have a large effect on the value of the Flory-Huggins parameter (see below).

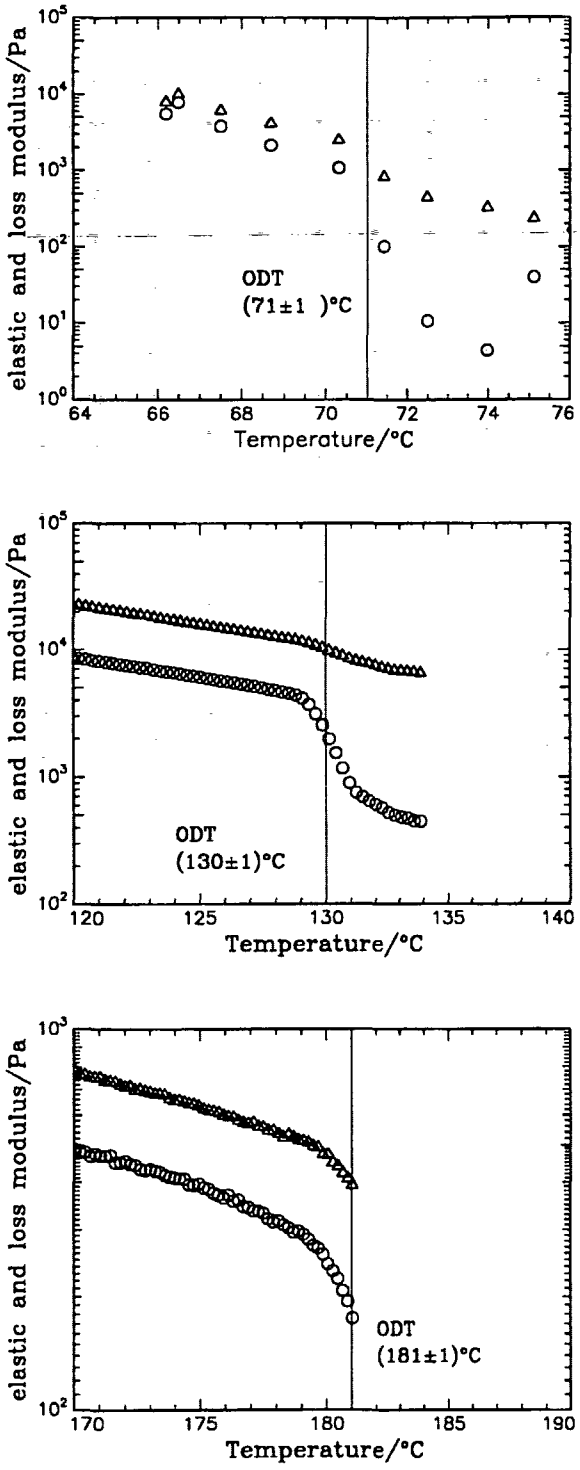

Figure 3.8: *Dynamic elastic (o) and loss (△) modulus as a function of temperature for three low molar mass samples. Upper figure: Sample SB14. The strain amplitude was 5%, the frequency 0.02 rad/s and the heating rate 0.1°C/min. Middle figure: Sample SB11. The strain amplitude was 2%, the frequency 10 rad/s and the heating rate 1.0°C/min. Every second point is shown. Lower figure: Sample SB12. The strain amplitude was 2%, the frequency 10 rad/s and the heating rate 1.0°C/min.*

The question may arise if the ODT temperatures of quenched, lamellar samples containing a lot of imperfections, are the same as the ones determined from macroscopically oriented samples, similar to single crystals. Imperfections might promote the disordering process such that the ODT temperatures determined in the way described above are too low [48]. The hypothesis may be tested by preparing oriented samples, which can be done by shear alignment (Chapter 4), and then determining their ODT temperatures in the same way as described above. The ODT temperature of one shear aligned sample (SB12) was found to be 186°C, in contrast to the value of 181°C found as described above. It could be worthwhile to study the effect in detail. For the present purpose, namely the determination of the Flory-Huggins parameter, the difference is not significant.

sample	N	shear amplitude/%	shear rate [rad/s]	heating rate °C/min	T_{ODT} [°C]
SB14	236	5	0.02	0.1	71 ± 1
SB11	310	2	10.0	1.0	130 ± 1
SB01	313	5	40.0	0.5	145.5 ± 1
SB12	374	2	10.0	1.0	181 ± 1
SB08	383	5	40.0	3.0	204 ± 1

Table 3.4: *Parameters used for determination of the ODT temperatures, T_{ODT}.*

3.3.3 The Flory-Huggins segment-segment interaction parameter

Knowledge of the ODT temperatures makes it possible to estimate the Flory-Huggins segment-segment interaction parameter, χ. By mean-field theory, it has been predicted that $(\chi N)_{ODT} = 10.5$ for symmetric diblock copolymers [7]. Combination with the Flory-Huggins expression $\chi = a/T + b$ [45] leads to the expression

$$T_{ODT} = \frac{aN}{10.5 - bN} \tag{3.9}$$

A fit of this expression to the ODT temperatures (Table 3.4) gives

$$a = (21.6 \pm 2.1)\text{K}, \qquad b = -0.019 \pm 0.005 \tag{3.10}$$

Fluctuation theory predicts that the value of χN at the ODT is not constant, but depends on chain length, N:

$$(\chi N)_{ODT} = 10.5 + 41.0 \left(\frac{\bar{a}^6}{v^2} N \right)^{-1/3} \tag{3.11}$$

where $\bar{a}$ is the average statistical segment length and v the segment volume [20]. In order to test the influence of the correction term on the value of the χ-parameter, we tentatively used the following relation:

$$T_{ODT} = \frac{aN}{10.5 - bN + 41.0(N\bar{a}^6/v^2)^{-1/3}} \tag{3.12}$$

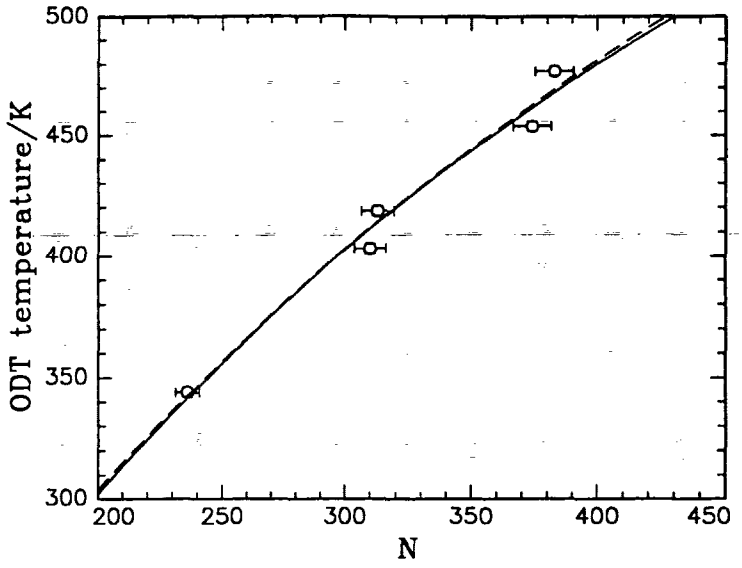

Figure 3.9: *ODT temperature as a function of chain length (based on the polybutadiene monomer volume). An error of 2 K for the temperature and of 2% for the chain length is shown. The broken line is a fit of the mean-field expression given in Eq. 3.9 and the full line a fit of expression 3.12.*

The average segment length was estimated to be 6.9 Å by fitting a Leibler structure factor to the peaks observed in small-angle scattering spectra (Chapter 5). The segment volume is given by $v = M_B/\rho_{PB} = 101$ Å^3 where M_B is the molar mass of butadiene and ρ_{PB} the density of polybutadiene. Fit of Eq. 3.12 to the data gives

$$a = (29.2 \pm 3.0)\text{K}, \qquad b = -0.028 \pm 0.007 \tag{3.13}$$

The values found differ from the mean-field result; however, the fitted curve cannot be discerned from the mean-field result in the range of the plot (Fig. 3.9). Using the a- and b-values from Eq. 3.13, the χN-values determined at the ODT temperatures are found to be $(\chi N)_{ODT} \simeq 13 - 14$, thus higher than the results from mean-field theory $(\chi N)_{ODT} \simeq 10.5$ which is imposed by fluctuation theory: As fluctuations stabilize the disordered state, the ODT occurs at a temperature which is lower than predicted by mean-field theory.

In the study of the lamellar thickness as a function of chain length, which is presented in Chapter 5, a fixed temperature of $T = 150$°C was chosen for the measurements. Using the χ-values as determined above, the range in phase space explored by varying the chain length can be estimated. Using mean-field theory, we find a range between $\chi N = 5 \pm 1$ and $\chi N = 100 \pm 22$. Using the result from fluctuation theory, values between 6 ± 2 and 126 ± 32 are found. The latter values are higher but still equal to the mean-field results within the errorbars. In the following, the mean-field values for a and b are used. Then, $N_{ODT} = 323$ at 150°C.

3.4 The glass transitions

(DSC-mesurements were carried out by Anne Bønke Nielsen, Risø National Laboratory.)

Differential Scanning Calorimetry (DSC) is a method which allows to monitor thermal events, such as crystallization, vaporization, or glass transitions by measuring changes in the specific heat at constant pressure, c_p. In the case of glass transitions, the change in c_p is due to the fact that the specific volume changes its temperature behavior. Below the glass transition, the specific volume is very low, thus many degrees of freedom are frozen in. At the glass transition, the specific volume increases and many more modes of movement are activated. Thus, the specific heat rises when heating through the glass transition [49]. Heat flow DSC is frequently used to detect glass transitions. A small amount of sample is mounted in a cell which, together with a reference cell, is heated such that sample and reference cell are at the same temperature throughout the measurement [50]. The energy difference in the independent supplies to the sample and the reference cell is recorded against temperature and is proportional to the specific heat. In order to obtain detectable signals, high heating rates (in the present study 40°C/min) are applied. This technique is not well-suited to follow details of the transition, because, due to the large heating rate, the sample is not necessarily in thermal equilibrium. However, DSC gives the transition temperature and the information, if the transition is endo- or exothermic. Glass transitions are endothermic.

In microphase-separated block copolymer systems, two glass transitions are expected, both being close to the glass transition of the homopolymers, which the block copolymer consists of [51, 52]. In case of polystyrene-polybutadiene, a transition at $T_g^{PS} = 100°C - 1.0 \times 10^5/M$ (M is the molar mass in g/mol) is expected for the polystyrene block and $T_g^{PB} = -107$ to $-83°C$ for the polybutadiene block (for a high content of 1,4-addition [34]). In the fully homogeneous state far above the ODT temperature, the empirical 'mixing rule'

$$\frac{1}{T_g} = \frac{\phi_S}{T_g^{PS}} + \frac{1-\phi_S}{T_g^{PB}} \tag{3.14}$$

is assumed to apply [33]. ϕ_S is the local volume fraction of polystyrene.

3.4.1 Experimental

In the present study, the glass transitions of six low molar-mass samples were determined. Samples were dried under vacuum at 120 – 130°C in order to evaporate traces of solvent. If solvent evaporates during the DSC scan, the signal might interfere with the upper glass transition of the block copolymer. Sample amounts of 20.5 – 30.3 mg were used for DSC studies. A Perkin-Elmer DSC-4 instrument was used at temperatures between −130 and 150°C. Before the measurements, the samples were heated to 150°C with a rate of 40°C/min and cooled down to −130°C with a rate of −2°C/min in order to release tensions.

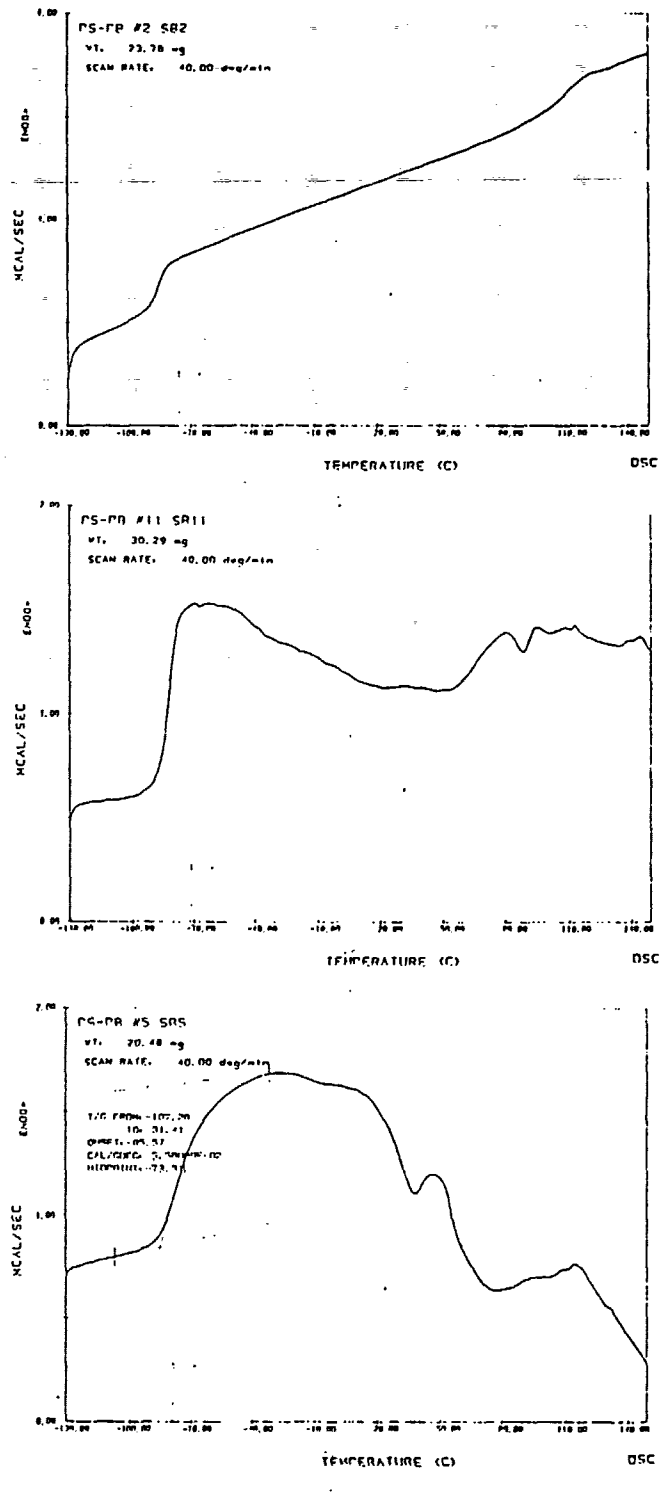

Figure 3.10: *DSC scans of (from top to bottom) sample SB02, SB11 and SB05. The temperature axes range from* -135 *to* $140°C$.

3.4.2 Results

sample	M_N^{stoich} [g/mol]	M_{PS}^{stoich} [g/mol]	T_g^{PS} °C	T_{ODT} °C	T_{g1} °C	T_{g2} °C
SB05	9200	5000	80	-21 ± 10^a	-78	–
SB11	18300	9900	90	130 ± 2	-88	–
SB01	18500	10000	90	145.5 ± 2	-89	–
SB12	22100	11900	92	181 ± 2	-89	76
SB02	54500	29700	97	204 ± 2	-91	102

Table 3.5: *Results from DSC measurements. Given are the overall molar mass, the molar mass of the polystyrene blocks, the glass temperature of pure polystyrene having the same molar mass as the polystyrene block, the ODT temperature of the block copolymer, and the glass temperatures as determined by DSC. (a) The ODT temperature was estimated.*

Curves from three low molar-mass samples are shown in Fig. 3.10. The scan of sample SB02 shows two transitions, the transition temperatures (−91 and 102°C) being close to the values expected for pure polystyrene and polybutadiene. The ODT temperature (204°C) is far above the temperature range studied and the results corroborate the notion of a lamellar state with nearly pure polystyrene and polybutadiene domains. The results are summarized in Table 3.5.

The scan of sample SB11 ($T_{ODT} = 130$°C) shows a change of signal at −88°C which is close to the glass temperature of pure polybutadiene which indicates the existence of nearly pure polybutadiene domains. The glass transition of polystyrene domains could not be resolved which is attributed to an interplay with the disordering process. In the ordered state in the vicinity of the ODT temperature, the density profile becomes close to sinusoidal and partial mixing takes place (Chapter 5.4). This might be the reason for the strange signals at high temperatures. At 130°C, the ODT temperature, no characteristic change in signal is seen. This might be due to the fact that, locally, the density profile is similar just above and just below the ODT temperature. Thus, the degree of mixing does not change in a discontinuous way at the ODT. Therefore, DSC is not well-suited for determining ODT temperatures of low molar-mass polystyrene-polybutadiene diblock copolymers.

The scan of sample SB05 is similar to the one of SB11. A change of signal is observed at −78°C which is attributed to the glass transition of the polybutadiene block. Above −10°C, the curve displays a strange shape, which might be related to the interplay between concentration fluctuations and the glass transition of the polystyrene block. The latter is, corresponding to the molar mass of the polystyrene block estimated to occur at 80°C in a pure polystyrene environment (Table 3.5). In case of homogeneous mixing ($\phi_{PS} = 0.5$), a single glass transition at −26°C (found using Eq. 3.14) would be expected. The discrepancy indicates that there are no pure polybutadiene domains, but that these domains contain polystyrene. This corroborates the value of the ODT temperature which was estimated to be −21°C.

3.5 Conclusion

A homologous series of fifteen symmetric polystyrene-polybutadiene diblock copolymers having molar masses between 9200 and 183000 g/mol has been synthesized using anionic polymerization under an inert gas atmosphere.

The molar mass distributions, as measured with size exclusion chromatography, were found to be monomodal and as narrow as the standard samples for eleven of the synthesized samples. These samples were used for further investigations.

Using proton NMR, it could be confirmed that the weight fraction of styrene was approximately 0.55 for all samples, which corresponds to a volume fraction $f_{PS} = 0.51$. The content of 1,2-added polybutadiene monomers was found to be ~9%, thus somewhat higher than values reported in literature, which may be due to nonpolar impurities present during polymerization.

The rheological response of low molar-mass samples was found to be consistent with what had been reported: The behavior was close to liquidlike in the disordered state but more complex in the ordered state. At the ODT temperature, the dynamic elastic and loss modulus drop drastically. This was used for determining the ODT temperatures of five low molar-mass samples. Knowledge of the ODT tenperatures allowed us to estimate the parameters a and b in the expression for the Flory-Huggins segment-segment interaction parameter, $\chi = a/T + b$. Predictions for $(\chi N)_{ODT}$ from both mean-field and fluctuation theory were used and were found to give similar results.

Differential scanning calorimetry was used to determine the glass transition temperatures of several low molar-mass samples. Only with samples which were ordered in the temperature range studied, two glass transitions (of the polystyrene and the polybutadiene block) could be resolved which indicated that the samples were microphase-separated. With lower molar-mass samples, only one transition close to the one of pure polybutadiene was observed. At the ODT temperatures, no change of signal in the DSC scans was observed, probably because the local density profile does not change drastically at the ODT.

Chapter 4

Sample preparation

(Walther Batsberg helped with the stabilization, Kristoffer Almdal and Lene Hubert with the shear alignment and Lotte Nielsen with the size exclusion chromatography (all Risø National Laboratory).)

Samples for small-angle studies were prepared using different techniques (melting, annealing, solvent-casting and shear alignment) in order to ensure thermal equilibrium. The reason is the following: As described in Chapter 2, the synthesis was carried out in solution. In order to precipitate the polymer sample, the polymer solution was dripped into a poor solvent after termination. The chains thus collapsed very quickly. The sample obtained was dried at room temperature, thus below the glass temperature of the polystyrene blocks ($\sim$ 100°C). It was not sure that thermal equilibrium has been obtained. Therefore, further preparation above the glass temperature was necessary after drying. In order to minimize the effect of crosslinking during preparation at high temperatures, antioxidant was added to stabilize the polymers.

4.1 Stabilization

Thermal degradation of polymers is a well-known problem which is reviewed in [53]. The degradation process starts with the formation of radicals, which may result in chain scission or crosslinking. Especially under prolonged annealing and when oxygen is present, degradation and/or oxidation may occur. Both chain scission and crosslinking cause severe problems in determining the structural properties of block copolymers as a function of chain length because the chain length of degraded polymers is not well-defined. In case of chain scission, the molar-mass distribution becomes broader and the average molar mass decreases. Crosslinking of two or more polymers also leads to broadening of the molar-mass distribution, but the average molar mass increases. In the worst case, a network is formed. In addition, reptation of the chains towards equilibrium is hindered by crosslinking. The effect of crosslinking is most severe for high molar-mass polymers: one crosslink prevents two long chains from reptating freely. In low molar-mass polymer samples, only a smaller volume fraction of the sample is affected by a crosslink.

As becomes evident from the size exclusion chromatograms shown below, crosslinking

is the prevalent mechanism in polystyrene-polybutadiene. Polystyrene is a relatively stable polymer due to the shielding effect of the phenyle ring. Polybutadiene is more unstable; here, the α-protons (which are adjacent to the carbon-atoms forming the double bond, Fig. 4.1) are most reactive. The crosslinks formed between two polybutadiene chains in absence or presence of oxygen are shown in Fig. 4.1.

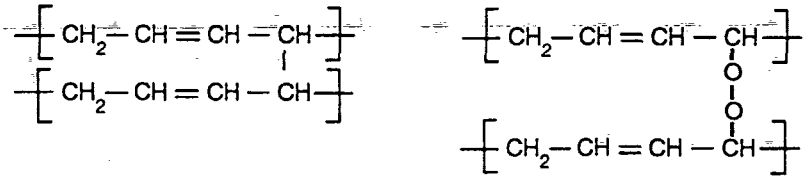

Figure 4.1: *Crosslink formed by the α-protons in polybutadiene chains in the absence (left figure) and in the presence of oxygen (right figure).*

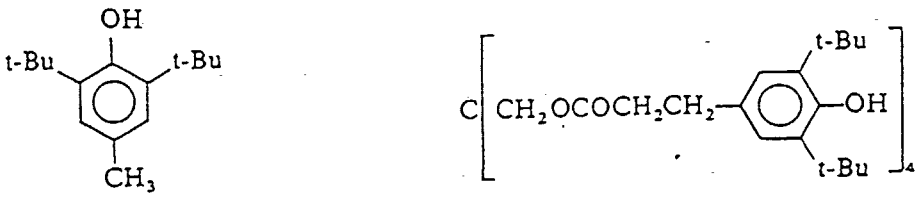

Figure 4.2: *Structure of the antioxidant molecules butylated hydroxytoluene, BHT (left), and of Irganox 1010 (right) [54].*

Addition of small amounts of antioxidant (typically 0.05 – 1.0 weight-%) stabilizes the polymers and prevents their crosslinking [54]. In this work, the antioxidant Irganox 1010 was used (Fig. 4.2). It is characterized by the butylated hydroxytoluene groups. In a reaction with a radical, this group acts as a donor and transfers a hydrogen atom to the radical which is thus 'repaired':

$$\mathrm{P}\cdot + \mathrm{AH} \rightarrow \mathrm{PH} + \mathrm{A}\cdot$$
$$\mathrm{PO_2}\cdot + \mathrm{AH} \rightarrow \mathrm{POOH} + \mathrm{A}\cdot$$

where P denotes the polymer chain and A the antioxidant molecule. After the reaction, the antioxidant molecule (A) has become a radical, but, in contrast to the polymer radical, it is very stable because of the phenyle ring and the *tert*-butyl groups.

During the course of this work, it turned out that the unstabilized polymer samples were crosslinked after some days of annealing at 150°C under vacuum. The polymers had formed macroscopic pieces of gels and could not be dissolved anymore. In a first test, the antioxidant BHT (butylated hydroxy toluene, see Fig. 4.2, left part), which is commonly used for stabilizing polystyrene-polyisoprene (*e.g.* [55]) was tried. Even though 3.5 weight-% (antioxidant/polymer) were used, gels had formed after one week of annealing at 150°C under vacuum. This was probably due to evaporation of BHT during annealing.

Therefore, the antioxidant Irganox 1010 (Ciba-Geigy, Fig. 4.2, right part) was used. It is a larger molecule than BHT and has a higher boiling point. 0.1 resp. 0.5 wt-% was added

to the polymer by dissolving polymer and Irganox in benzene (polymer concentrations between 100 and 200 mg/ml) and stirring the solution overnight. Then, the solutions were left to dry at room temperature for 3 days and were further dried at 100°C, *i.e.* above benzene's boiling point (80°C at atmospheric pressure) at a pressure of 0.07 mbar for 2 hours. As will be shown below, the samples were effectively stabilized by Irganox 1010.

The question may arise if the presence of antioxidant has an influence on the lamellar structure. There is one molecule of Irganox 1010 per 20000 segments, when 0.1 wt-% were added, and one molecule per 4000 segments, when 0.5 wt-% were added. These amounts are considered to be negligible.

4.2 Methods for sample preparation

In order to bring the stabilized samples into an equilibrium state after drying, four different methods of sample preparation were used: Melting, annealing, solvent-casting and shear alignment. For the sake of consistency, both preparation and measurements were carried out at 150°C. This temperature was chosen because it is well above the glass temperature of the polystyrene blocks (80 – 100°C depending on molar mass, Chapter 3) but still below the degradation temperature (ca. 180°C). As the relaxation times of polymer segments are very long below and in the vicinity of the glass transition, equilibrium can on a laboratory time scale only be achieved above the glass temperature. The samples together with the preparation method used are listed in Table 4.1. 'SBI' stands for 'polystyrene-polybutadiene with Irganox 1010', the number is related to the molar mass, and the last letter is related to the preparation method. In the following, the different methods will be described.

4.2.1 Melting

Some of the samples have ODT temperatures below 150°C and are thus molten (*i.e.* in the disordered state). In order to obtain bubble-free samples, pills of ca. 1 mm thickness were pressed in a teflon-coated press (diameter 2.5 cm) using a hydraulic press and were heated above the ODT temperature just before the small-angle scattering experiments.

4.2.2 Quenching

Samples having ODT temperatures above 150°C, but below the degradation temperature can be molten and cooled down again into the ordered state. The resulting structure is expected to be 'polycrystalline', *i.e.* consisting of many lamellar domains which are randomly oriented. This technique was only applied to one sample (Chapter 6).

4.2.3 Annealing

For samples having ODT temperatures above 150°C, equilibrium may be achieved during long annealing above the glass temperature of the polystyrene blocks. For this purpose, a vacuum oven was constructed which is described in Appendix A. Pills of ca. 1 mm

sample	N	ODT °C	antioxidant content [wt-%]	preparation method	parameters during shear alignment[a]
SBI05B	156	-21 ± 10	0.1	molten at 150°C	
SBI14B	236	71 ± 1	0.1	molten at 150°C	
SBI11B	310	130 ± 1	0.1	molten at 150°C	
SBI11C			0.1	molten at 150°C	
SBI12A	374	181 ± 1	0.1	solvent-cast	
SBI12C			0.1	shear aligned	4000 s: 1.0 rad/s, 70%
SBI12F			0.1	annealed	
SBI08A	383	205 ± 1	0.1	solvent-cast	
SBI08C			0.1	shear aligned	4000 s: 1.0 rad/s, 20%
SBI08F			0.1	annealed	
SBI02D	921		0.1	shear aligned	4000 s: 1.0 rad/s, 100%
SBI02F			0.1	annealed	
SBI02G			0.1	solvent-cast	
SBI15A	1182		0.1	solvent-cast	
SBI15E			0.1	shear aligned	3600 s: 1.0 rad/s, 100%, 3600 s: 1.0 rad/s, 70%
SBI15F			0.1	annealed	
SBI06A	1555		0.1	solvent-cast	
SBI06D			0.1	shear aligned	500 s: 1.0 rad/s, 99%, 3300 s: 1.0 rad/s, 70%, 1600 s: 1.0 rad/s, 30%, 1200 s: 1.0 rad/s, 70%
SBI06G			0.5	solvent-cast	
SBI06H			0.5	annealed	
SBI06K			0.5	shear aligned	15000 s: 0.02 rad/s, 20%
SBI06L			0.5	solvent-cast (CHx)	
SBI07G	2511		0.5	solvent-cast	
SBI07H			0.5	annealed	
SBI07K			0.5	shear aligned	15000 s: 0.02 rad/s, 20%
SBI07L			0.5	solvent-cast (CHx)	
SBI10A	3090		0.1	solvent-cast	
SBI10D			0.1	shear aligned	14000 s: 1.0 rad/s, 30%
SBI10F			0.1	annealed	
SBI10G			0.5	solvent-cast	
SBI10H			0.5	annealed	
SBI10K			0.5	shear aligned	15000 s: 0.02 rad/s, 20%

Table 4.1: *Sample preparation carried out at 150°C. (a) Parameters given are: duration, shear rate, and amplitude. If not stated otherwise, the samples were solvent-cast from benzene. CHx stands for cyclohexane. Details about the preparation methods are given in the text.*

height were pressed as described above. They were annealed between two teflon platelets under vacuum (0.07 mbar) at 150°C for two days. Longer annealing times were avoided in order to minimize the risk of crosslinking. The structure obtained is a 'polycrystalline' lamellar structure (Fig. 4.3, left part), giving rise to isotropic small-angle scattering with diffraction rings (Chapter 5.5).

4.2.4 Solvent-casting

Solvent-casting is a widely used method to obtain oriented samples (*e.g.* [56, 57, 58, 59]). The alignment is induced by the film surfaces to air respectively the support; thus, the lamellar interfaces align parallel to the film surface. The thinner the film the higher is the degree of orientation. This technique was, like annealing, applied for samples having ODT temperatures above 180°C. A problem with this technique might be that a certain degree of order is achieved while solvent is still present [59]. Especially when solvent-casting below the glass temperature of the polymers, a non-equilibrium state may freeze in, and it is not sure that a bulk equilibrium state can be achieved during later annealing. The problem might be especially severe for long chains. As will be established below, the samples used in this study show the same lamellar spacings as the ones prepared by annealing and shear alignment.

In this study, the polymer samples were dissolved in benzene ($c = 39 - 90$ mg/ml) which is a good solvent for both blocks. In order to study if the selectivity of the solvent plays a role in the ordering process, two samples (SBI06L, SBI07L) were solvent-cast from cyclohexane (CHx) which is a selective solvent. CHx is a marginal solvent for polystyrene (the Θ-temperature is 35°C) and a good solvent for polybutadiene. The solutions were left to dry in teflon beakers (diameter 50 mm) at room temperature for some days resulting in films of 0.6 ± 0.1 mm height. Finally, the films were annealed for two days at 150° C under vacuum (0.07 mbar).

4.2.5 Shear alignment

The third method used in this study to bring ordered block copolymer samples into equilibrium was shear alignment. This method gives oriented samples and was applied for the first time to block copolymers by Hadziioannou *et al.* [60]. The sample is mounted between two plates and is subject to oscillatory or simple shear at a temperature below the ODT temperature. The shear field leads to orientation of the lamellar grains. Three orientations can, in principle, be obtained as shown in Fig. 4.3.

The mechanisms leading to alignment of polycrystalline domains are still under discussion. Key parameters seem to be the shear rate and amplitude together with the temperature relative to the ODT [61, 62, 63, 64]. It has not been clarified yet which mechanisms lead to alignment of 'polycrystalline' lamellar samples to form a 'single crystal'. However, the method has been used for the preparation of oriented samples in order to identify complex morphologies [65, 66, 67]. There is so far only one study on the scaling of the lamellar thickness with chain length where shear aligned samples were used [68].

In this work, shear alignment was used as an alternative method for bringing samples into equilibrium. In a first attempt, shear alignment of low molar-mass samples was carried

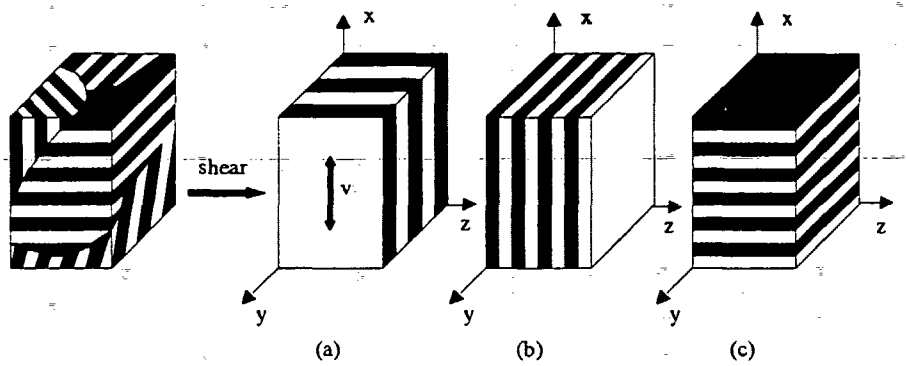

Figure 4.3: *Three possible lamellar orientations can be obtained by shearing a 'polycrystalline' sample (left): the parallel (a), the perpendicular (b) and the transverse (c) orientation. The x-axis is parallel to the shear direction of velocity $\vec{v}$, the y-axis is parallel to the shear gradient. Only (a) and (b) are considered to be equilibrium structures [61].*

out using the RMS-800 rheometer described in Chapter 3. The rheometer was operated in a parallel-plate geometry with plates having a diameter of 50 mm. The pill height was chosen to be 1 mm. As an example, results from sample SB11 are presented. The sample was heated to a temperature just above the ODT temperature (130°C) under a stream of nitrogen gas. Then, it was cooled down to 118°C, and, after some time, the dynamic elastic and loss modulus were measured applying a shear amplitude of 2% as a function of frequency (Fig. 4.4). After the rate sweep, the sample was subject to shear for 155 min at the same temperature with shear amplitudes in the non-linear regime (between 50 and 200%) and a frequency of 1.0 rad/s (Fig. 4.4). While shearing, the moduli were monitored. As the shear amplitude was not in the linear regime, the values obtained for the dynamic elastic and shear modulus are probably too low. However, changes in the moduli could be detected. Both moduli decreased strongly during the first couple of minutes and then reached plateau values indicating that the sample was oriented. The reason for the decrease of the elastic modulus is considered to be the following: In a polycrystalline sample, there are domains having the lamellar interfaces not parallel to the shear direction (Fig. 4.3a). Shearing these domains means pulling A-blocks into the B-part of the lamellae and *vice versa*. A restoring force arises which has its origin in the repulsive interaction of the different segments. During alignment, the domains orient such that the lamellar interfaces become parallel to the shear direction and the elastic modulus related to this process decreases with increasing degree of orientation. In order to study how the frequency-dependence of the dynamic elastic and loss modulus changes during the alignment, the shear alignment was stopped several times and the elastic and the loss modulus were measured with a low strain amplitude. In Fig. 4.4, data measured before the alignment, after 35 min and after 155 min of alignment are shown. The dynamic elastic modulus decreases, the longer the sample is aligned. The slope in the terminal region increases slightly $(0.4 - 0.6)$. The loss modulus gets steeper in the terminal region during alignment: The slope increases from 0.59 ± 0.01 before alignment to 0.74 ± 0.01 after 35 min and further to 0.92 ± 0.02 after 155 min. For homopolymers, the typical behavior is $G'' \propto \omega^1$ [44]. We conclude that the samples become more and more liquidlike during the

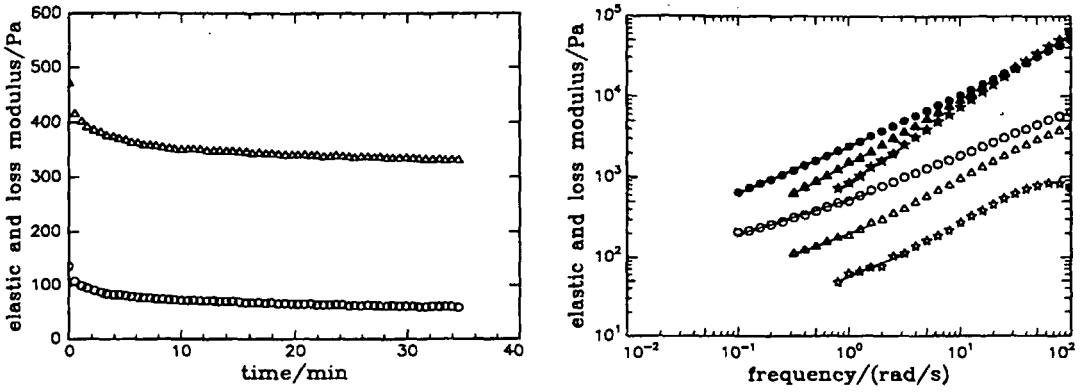

Figure 4.4: *Left figure: The first 35 min of shear alignment of sample SB11B at 118°C. The strain amplitude was 50% and the strain rate 1.0 rad/s. (○) dynamic elastic modulus, (△) dynamic loss modulus. Every second point is shown. Right figure: Dynamic elastic (open symbols) and loss modulus (filled symbols) of sample SB11B at 118°C. Data of the loss modulus (log(G″)) are shifted upwards by half a decade. Circles: measured before alignment, triangles: after 35 min of alignment with a shear amplitude of 50% and a shear rate of 1.0 rad/s, stars: after 155 min of alignment with amplitudes of 50 – 200% and a rate of 1.0 rad/s. During the frequency sweeps shown her, the strain amplitude was 2%. Lines are linear fits.*

alignment procedure, because the interfaces align parallel to the shear direction.

However, it was not possible to shear align higher molar-mass samples in the RMS-800 rheometer. Samples which are deep in the ordered state, *i.e.* strongly segregated, appear mechanically hard. This was the case for samples with molar masses larger than ~50000 g/mol. With these samples, it was difficult to establish good contact between the pills and the plates of the rheometer. The upper plate of the rheometer was coupled to the force transducer which is very sensitive to axial stress. Lowering the upper plate onto the sample in order to squeeze it between the plates caused the transducer to switch off. Measurement of the rheological response or shear alignment was thus not possible using this rheometer. Therefore, we decided to use the RSA II rheometer (Rheometrics Solids Analyzer) together with a shear sandwich fixture (Fig. 4.5) [69] for dynamically shearing the samples. For consistency, all samples used for small-angle scattering investigations were shear aligned using the RSA II rheometer. In the shear sandwich geometry, pills are mounted pairwise between the insert and the jaws. The advantage of the RSA II instrument is that the contact between the sample and the plates is established by fastening the front screw, such pressing the jars together. Thus, no load is put onto the force transducer when mounting the sample. Oscillatory shear in the vertical direction is applied by the actuator which is connected to the jaws whereas the response of the samples is monitored by the force transducer connected to the insert.

Shear alignment was carried out as follows: Platelets of 0.5 mm thickness (12.5×16 mm large) were cut from the pressed pills and mounted pairwise between the insert and the jaws. The samples were sheared at 150°C in the nonlinear regime (shear amplitudes of 20 – 100%) for 1 – 4 hours at frequencies of 0.02 (high molar-mass samples) or 1.0 rad/sec. As shown by small-angle scattering (see below), all samples were oriented parallel to the

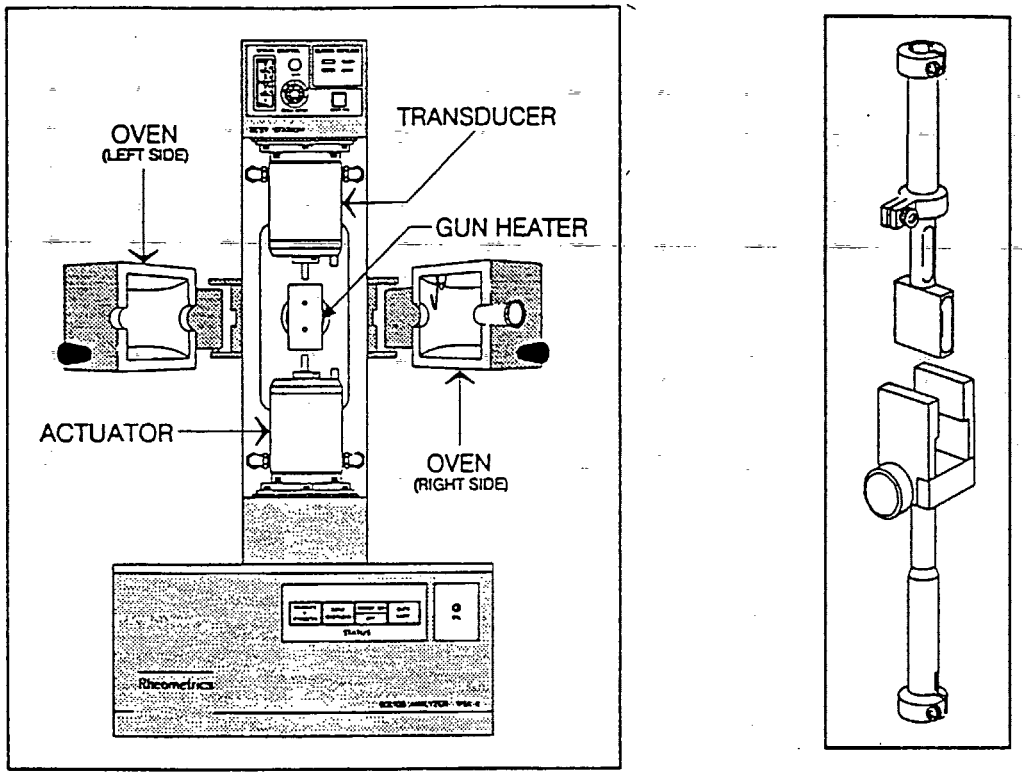

Figure 4.5: *The test station of the RSA II rheometer (left part) and the shear sandwich fixture (right part) [69]. The sample is mounted in front of the gun heater. Before mounting the samples, the insert (upper part) is lowered such that it is located between the jaws (lower part).*

shear velocity (Fig. 4.3a). Before and after shearing, frequency sweeps using low shear amplitudes were measured in order to monitor the effect of the alignment on the mechanical properties (Fig. 4.6). No significant differences were observed which might be due to the fact that changes only appear at rates lower than the shear rate. No measurements were made at these frequencies. Only at high rates, a change in the signal is observed. The reason of this change is still unclear. During the shearing process, the dynamic elastic and loss modulus were recorded. As the obtained values were measured in the nonlinear regime, they were only used to monitor a possible change of the signal with time. With most samples (SBI12C, SBI02D, SBI15E, SBI06D, SBI07K), it was observed that the moduli decreased during the first minutes and then remained constant or rose smoothly (Fig. 4.6). The fact that plateau values were reached was interpreted to mean that all 'crystallites' were oriented. With two samples (SBI08C and SBI10K) no change of the signal was observed during alignment. However, both samples were found to be oriented (Chapters 5.4 and 5.5).

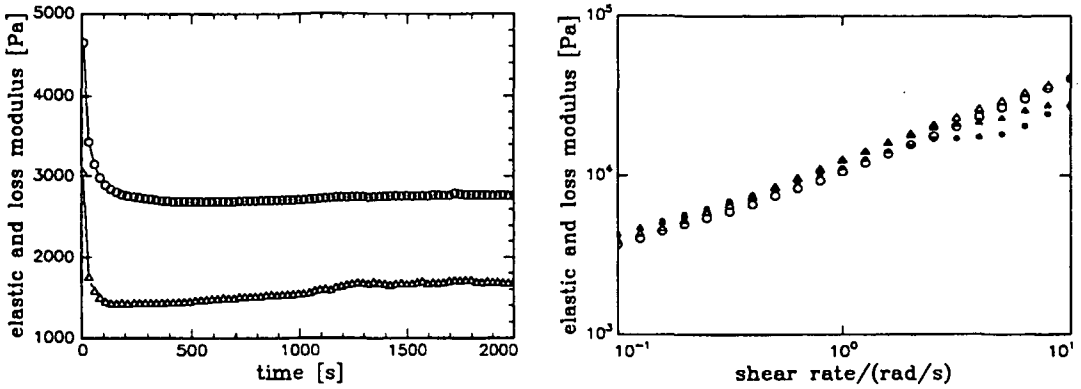

Figure 4.6: *Left figure: Dynamic elastic (o) and loss (△) modulus of sample SBI15E during shear alignment at 150°C. The shear rate was 0.02 rad/s and the amplitude 20%. Every fifth datapoint is shown. Right figure: Dynamic elastic (o) and loss (△) modulus of sample SBI15E before (open symbols) and after (filled symbols) shear alignment. The shear amplitude was 2% and the temperature 150°C.*

4.3 Molar-mass distributions after preparation

In order to make sure that the molar-mass distributions of the samples had not broadened too much (*i.e.* that the chain length was still well-defined) during the preparation, size exclusion chromatography (SEC) was carried out both on untreated samples (containing Irganox 1010, after drying) and on prepared (annealed, solvent-cast and shear aligned) samples. For a description of the technique see Chapter 3. The SEC system consisted of a Knauer HPLC pump FR-30 together with a Knauer high-temperature differential refractometer and the following set of columns: a PL gel precolumn and two 50 cm columns filled with Shodex A-80M. The system was run at a speed of 1 ml/min. The sample volume was 200 μl. The column temperature was stabilized at 30°. Stabilized tetrahydrofuran was used as an eluent, and the system was calibrated with polystyrene standard samples having known molar masses and narrow molar-mass distributions ($\sim$ 1.06). The polystyrene-polybutadiene samples were dissolved in toluene to 4 – 20 mg/ml and further in THF to 1.0 mg/ml.

The results are summarized in Table 4.2. Fig. 4.7 shows that annealing, solvent-casting and shear alignment lead to flat shoulders on the high molar-mass sides indicating some crosslinking of the polymers. The arrows indicate the elution volume of dimers (two polymers crosslinked) and trimers. It can be seen that small amounts of dimers and trimers have formed during preparation. The molar-mass distributions were affected less by shear alignment than by the other techniques (solvent-casting and annealing) because, during shear alignment, the samples are at high temperature (150°C) for much shorter time (some hours) than during solvent-casting and annealing (two days).

The effect of heat treatment on the molar-mass distributions was found to depend on the chain length: Both samples shown in Fig. 4.8 contained 0.1 wt-% Irganox 1010 and were solvent-cast from benzene. The shoulder in the chromatogram of the lower molar-mass sample (SBI12A, 22100 g/mol) is much less pronounced than the one of SBI06A

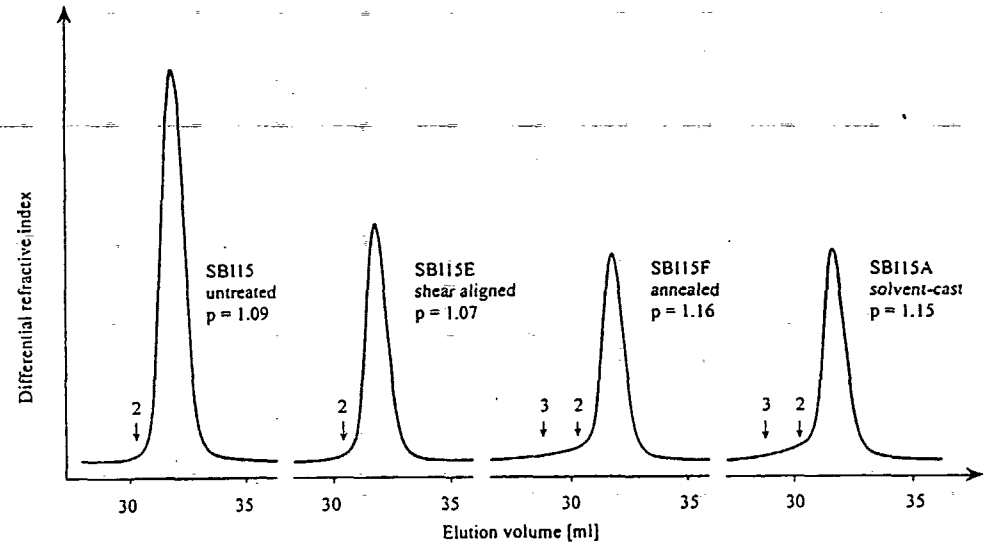

Figure 4.7: *Size exclusion chromatograms of SBI15 containing 0.1 wt-% Irganox 1010: from left to right: untreated material, SBI15E (shear-aligned), SBI15F (annealed), and SBI15A (solvent-cast from benzene).* $p = \bar{M}_W/\bar{M}_N$ *denotes the polydispersity index. Arrows indicate the elution volume of two or three times the peak molar mass.*

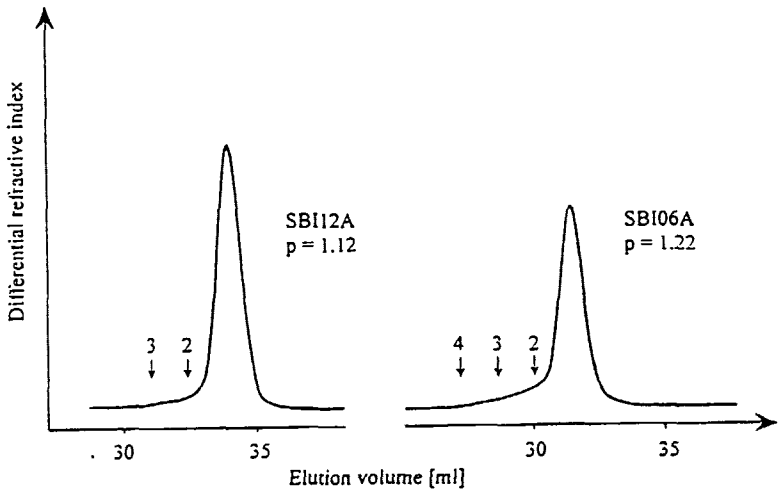

Figure 4.8: *Size exclusion chromatograms of two samples with different molar masses containing the same amount of Irganox 1010. Left: SBI12A (22100 g/mol), right: SBI06A (91900 g/mol). Both samples were solvent-cast from benzene.* $p = \bar{M}_W/\bar{M}_N$ *denotes the polydispersity index. Arrows indicate the elution volume of two, three or four times the peak molar mass.*

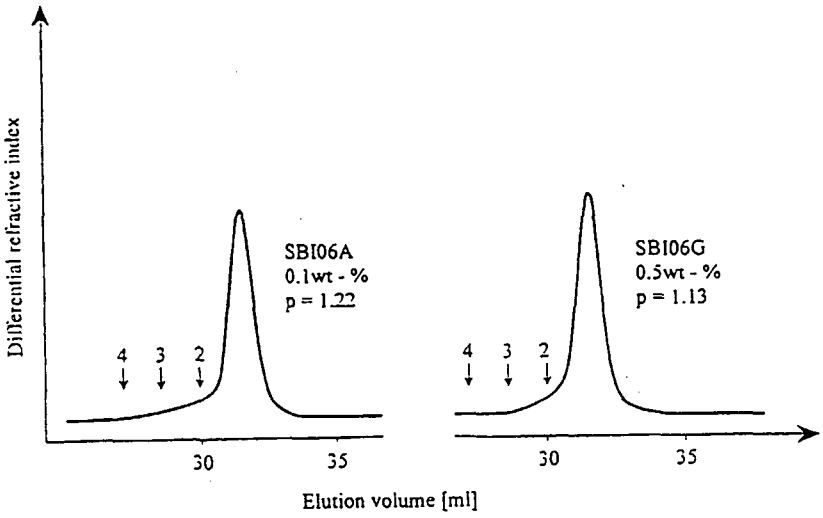

Figure 4.9: *Size exclusion chromatograms of two samples of SBI06 (91900 g/mol) containing different amounts of Irganox 1010. Left: SBI06A (0.1 wt-%), right: SBI06G (0.5 wt-%). Both samples are solvent-cast from benzene.* $p = \bar{M}_W/\bar{M}_N$ *denotes the polydispersity index. Arrows indicate the elution volume of two, three or four times the peak molar mass.*

(91900 g/mol) because the amount of crosslinked material per crosslink increases with chain length. Thus, the higher the molar mass of the polymers, the more sensitive are their molar-mass distributions to crosslinking. Therefore, the amount of antioxidant in high molar mass samples was increased to 0.5% (Tables 4.1 and 4.2). The effect is shown in Fig. 4.9. The shoulder in the chromatogram is much less pronounced for SBI06G (0.5 wt-%) than for SBI06A (0.1 wt-%). For further structural studies, only samples with $p \leq 1.3$ were used. This corresponds to ~15% of crosslinked polymers in the case of sample SBI10H as estimated from the areas under the peaks in the chromatogram. However, for the majority of samples, the degree of crosslinking is much lower (5 – 7 %). The samples used for small-angle studies are marked with an asterisk in Table 4.2.

N	antioxidant content [wt-%]	$\bar{M}_W/\bar{M}_N$ untreated	annealed	solvent-cast	shear aligned
374	0.1	1.07	*SBI12F: 1.14	*SBI12A: 1.12	*SBI12C: (a)
383	0.1	1.07	*SBI08F: 1.09	*SBI08A: 1.16	*SBI08C: (a)
921	0.1	1.11	*SBI02F: 1.20	*SBI02G: 1.27	*SBI02D: 1.10
1182	0.1	1.09	*SBI15F: 1.16	*SBI15A: 1.15	*SBI15E: 1.07
1555	0.1	1.08		*SBI06A: 1.22	*SBI06D: 1.09
	0.5	1.08	*SBI06H: 1.12	*SBI06G: 1.13 *SBI06L: 1.12[b]	
2511	0.5	1.09	*SBI07H: 1.26	*SBI07G: 1.18 *SBI07L: 1.23[b]	*SBI07K: 1.16
3090	0.1	1.08	SBI10F: 1.35	SBI10A: 1.45	SBI10D: 1.35
	0.5	1.07	*SBI10H: 1.31	*SBI10G: 1.27	*SBI10K: 1.16

Table 4.2: *Change of the width of the molar-mass distributions, $\bar{M}_W/\bar{M}_N$, during sample preparation. The error of $\bar{M}_W/\bar{M}_N$ is ~ 0.05, as could be seen from repeated measurements. (a) not determined, (b) solvent-cast from cyclohexane. Samples marked with an asterisk were used for small-angle scattering studies.*

Chapter 5

Scaling behavior of the characteristic lengthscale with chain length

As discussed in Chapter 1, the overall structure and the chain conformation are closely linked in block copolymer systems in the bulk: Deep in the disordered state, the chains are Gaussian. In the Gaussian regime, the characteristic lengthscale, D, scales with chain length, N, like $D \propto N^{1/2}$ [7, 8]. However, when approaching the ODT, interchain interactions become important and the chains stretch, becoming dumbbell-like. It was found experimentally that the characteristic lengthscale scales like $D \propto N^{0.80}$ for $\chi N \simeq 6 - 33$ [8]. This study was carried out using a homologous series of poly(ethylene propylene)-poly(ethylethylene) covering a range of $\chi N \simeq 2 - 33$. Deep in the ordered state (in the strong-segregation limit), the lamellar thickness has been predicted to scale like $D \propto N^{0.643}$ [23] or $D \propto N^{2/3}$ [70], respectively. It has not been clarified yet if the exponent of 0.8 is found also in the strong-segregation limit, or if there is a crossover from an intermediate regime around the ODT where $D \propto N^{0.8}$ to a regime deep in the ordered state where the exponents 2/3 or 0.643 are recovered. Such a crossover has been predicted theoretically (see below) but has not been verified experimentally.

The aim of the present study is to reconcile the different predictions and experimental findings by studying the scaling behavior of the characteristic lengthscale with chain length in a large range of phase space ($\chi N = 5 - 100$). In particular, we are interested in establishing if a crossover exists from the intermediate regime to the strong segregation limit and where it is located. For this purpose, a homologous series of symmetric polystyrene-polybutadiene diblock copolymers is used. This block copolymer has the advantage of having a large segment-segment interaction parameter, χ, such that a large range in χN could be explored with polymers of moderate molar mass. The characteristic lengthscales were determined in a combined small-angle X-ray and neutron study.

In the next section, the theoretical and experimental background for the present study is reviewed. Former experimental studies of the scaling behavior are presented and discussed. The scattering from ordered, lamellar block copolymer systems is calculated by means of simple models and the scattering from disordered block copolymers as described

by the Leibler structure factor is reviewed. Small-angle X-ray and neutron scattering results are presented. The scaling behavior of the characteristic lengthscale is established. We find that the characteristic lengthscale scales like $D \propto N^{0.82}$ for $\chi N \simeq 5 - 30$, in accordance with [8]. Between $\chi N \simeq 30$ and 100, a scaling like $D \propto N^{0.61}$ is observed. This region is the strong-segregation limit. Thus, a crossover from an intermediate region to the strong-segregation limit is identified at $\chi N \simeq 30$. A modified phase diagram is presented.

5.1 The background

In spite of more than 20 years of theoretical interest in the field of diblock copolymer phase behavior, no unified theory describing all regions in the phase diagram exists (Chapter 1). However, the strong-segregation limit (SSL) and the disordered state can be described reasonably well by mean-field theories. The reason is that, in the SSL, the interfaces can be considered as narrow. Gibb's free energy can be written in terms of few enthalpic and entropic contributions. The mean-field theories by Helfand and Wasserman [23] (which is reviewed in [18]) and by Semenov [9] are reviewed below. Deep in the disordered state, the melt can be considered completely homogeneous, *i.e.* concentration fluctuations are low in amplitude. The chains can thus assumed to be Gaussian. Leibler made a Landau expansion of the free energy [7], one result being the structure factor of block copolymer melts in the disordered state. Leibler's approach is dicussed below.

In the vicinity of the ODT, the behavior is more complicated. Coming from the disordered state, concentration fluctuations arise when cooling towards the ODT. Domains start to form where the local density of A-segments deviates from average. The chains start to stretch as A- and B-blocks start to separate from each other. A scaling behavior different from Gaussian can thus be expected, even though the melt is still disordered. At the ODT, the melt eventually orders. However, the concentration profile is close to sinusoidal, thus, some mixing still takes place. The chains are stretched, but not as strongly as deep in the ordered state. One should note that when going from the disordered to the ordered state, long-range order is established; however, locally, the concentration profile does not necessarily change drastically at the ODT.

Several theoretical attempts have been made to address the intermediate region around the ODT [27, 71, 72, 73, 74, 75]. The assumptions and the results are reviewed below.

Finally, the experimental studies which have been performed in order to establish the scaling behavior of the characteristic lengthscale with chain length are presented. Only in one study, the exponent 2/3 is found to fit the data [57]. In other studies, different exponents were identified [8, 58, 59, 68]. The experimental conditions and the results of these studies are briefly discussed.

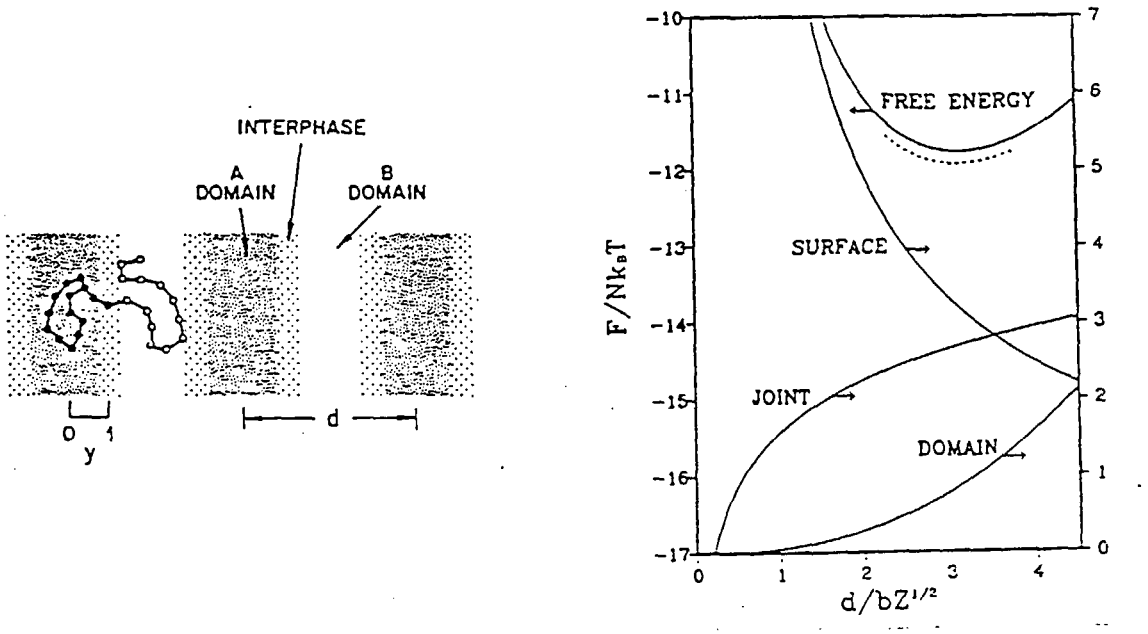

Figure 5.1: *Left figure: Schematic diagram of a lamellar microdomain structure in a block copolymer system. Right figure: The free energy per chain as a function of repeat distance d. The curves labelled 'surface', 'joint', and 'domain' correspond to H_{int}, ΔS_J, and ΔS_s, respectively. b is the average segment length and Z the chain length. Both figures are from [23].*

5.1.1 Theoretical approaches

The strong-segregation limit

Helfand and Wasserman [23] have studied the SSL and have given an expression of the difference of Gibb's free energy per chain deep in the ordered state and in the fully homogeneous state. Deep in the ordered state, the interphases between the A- and B-part of the lamella (or another microstructure) are assumed to be narrow compared to the repeat distance of the lattice, D. The assumed structure is sketched for the case of lamellae in Fig. 5.1. In the following, the lamellar state is referred to as an example of an ordered morphology; however, the calculations of Helfand and Wasserman are valid for all morphologies. The lamellar thickness obtained is the result of a balance between enthalpic terms favoring a large value of the lamellar thickness and entropic terms favoring a small thickness. Several enthalpic and entropic contributions are considered:

The enthalpy in the homogeneous state is the product of the Flory-Huggins segment-segment interaction parameter, χ, and the number of contacts between A- and B-segments [23]. In the homogeneous state, the latter can be written $f_A f_B$ where

$$f_A = \frac{N_A/\rho_A}{N_A/\rho_A + N_B/\rho_B} \tag{5.1}$$

is the volume fraction of the A-block and $f_B = 1 - f_A$. N_A and N_B denote the number of segments per block and ρ_A and ρ_B the number density of segments. N_A/ρ_A, for instance,

represents the volume of the A-block. The enthalpy per chain in the disordered state in units of k_BT, where k_B is the Boltzmann-factor and T the temperature, is given by [23]

$$\frac{H_{dis}}{N_c k_B T} = \chi\rho_o \times \frac{(N_A/\rho_A)(N_B/\rho_B)}{N_A/\rho_A + N_B/\rho_B} \tag{5.2}$$

where N_c is the number of chains and $\rho_o = (N_A/\rho_A + N_B/\rho_B)^{-1}$ the number density of chains.

In the strongly segregated structure, the only contributions to the enthalpy arise from interactions in the interphase. The interfacial enthalpy per chain is given by the interfacial tension, γ, times the interfacial area per chain. γ has by Helfand and Wasserman been predicted to be proportional to $\sqrt{\chi}$ [23]. The interfacial area per chain is given by twice the chain volume divided by the lamellar thickness, D (there are two lamellar interfaces per lamella). In summary, the interfacial enthalpy per chain is given by [23]

$$\frac{H_{int}}{N_c k_B T} = \frac{2\gamma}{k_B T} \times \frac{N_A/\rho_A + N_B/\rho_B}{D} \tag{5.3}$$

The enthalpy in the ordered state is minimized by maximizing the lamellar thickness, thus favoring large values of the lamellar thickness.

In the ordered state, the joints between A- and B-blocks are localized in the interphase which can be thought of as a layer of thickness a_J between the A- and the B-part of the lamella. The volume fraction available to the joints is $2a_J/D$ (there are two interphases per lamella), thus the loss of entropy with respect to the homogeneous state is [23]

$$\frac{\Delta S_J}{N_c k_B T} = -\frac{1}{T} \ln\left(\frac{D}{2a_J}\right) \tag{5.4}$$

In order to minimize the entropy loss by localizing the joints, the system tends to minimize the lamellar thickness relatively to the interphase width. This term thus favors small values of the lamellar thickness. However, it depends only weakly on D.

Lamellar ordering implies a certain loss of entropy for the blocks. The chains have to fill the lamellae in such a way that the density is constant inside the two lamellar parts as depicted in Fig. 5.1.[1] The number of possibilities for a chain to reach out from one part of the lamella to the other part is lower than in the homogeneous state where the ends are free. This restricts the number of possible conformations to a large degree. In a simple picture, one chain can be imagined as a spring having an unperturbed length given by the end-to-end distance (Fig. 1.3), $R_{ee} = aN^{1/2}$ [5], where a is the average segment length and $N = N_A + N_B$ the total chain length. Stretching the chain to a length $D/2$ (Fig. 1.2), leads to an entropy loss, ΔS. In case of an ideal spring, this entropy loss is given by $\Delta S \propto (D/(2R_{ee}))^2 \propto (D/(2N^{1/2}))^2$ [4]. (Here, the chain is assumed to have freely rotating bonds.) Helfand and Wasserman showed numerically that the dependence is slightly stronger, namely $\Delta S \propto (D/N^{1/2})^{2.5}$ [23]. In summary, the entropy loss caused

[1] The fact that the polymer density is nearly constant is related to the fact that the bulk modulus of polymers typically is large compared to the shear modulus. The reason is that the potential well (*e.g.* of a Lenard-Jones potential with a repulsive and an attractive part) between two segments is steep, thus the energy required for segments to change the mutual distance is high. Therefore, the mutual distance does not fluctuate significantly and the density is close to being constant.

by chain stretching due to the requirement of constant density is given by [23]

$$\frac{\Delta S_s}{N_c k_B T} = -c_s \left[\left(\frac{D_A}{a_A N_A^{1/2}} \right)^{2.5} + \left(\frac{D_B}{a_B N_B^{1/2}} \right)^{2.5} \right] \tag{5.5}$$

where c_s is a numerically determined constant and where D_A and D_B denote the thicknesses of the A- and the B-part of the lamellae. This entropic contribution favors small values of the lamellar thickness.

Assembling all terms, the difference in Gibb's free energy per chain between the ordered and disordered state is obtained [23]:

$$\frac{\Delta G}{N_c k_B T} = \frac{G_{ordered} - G_{disordered}}{N_c k_B T} \tag{5.6}$$

$$= \frac{H_{int}}{N_c k_B T} - T\frac{\Delta S_J}{N_c k_B T} - T\frac{\Delta S_s}{N_c k_B T} - \frac{H_{dis}}{N_c k_B T} \tag{5.7}$$

$$= c_{int}\frac{N}{D} + c_J \ln(D) + c'_J + c'_s \left(\frac{D}{N^{1/2}} \right)^{2.5} - c_{dis} \tag{5.8}$$

where the c's are constants independent of N and D, except the last one, c_{dis} which depends on N. The constants are temperature-dependent. In their further calculations, Helfand and Wasserman considered completely symmetric diblock copolymers: $\rho_A = \rho_B = \rho$, $a_A = a_B = a$, and $D_A = D_B = D/2$ [23].[2] In fact, only the latter assumption is met in the present experiment with symmetric diblock copolymers ($f_A = 0.5$) and it cannot be excluded that the results depend on the choice of these parameters. The dependence of the three first terms on the lamellar thickness for fixed temperature is shown schematically in Fig. 5.1. The enthalpy term H_{int} decreases strongly with rising D, thus favoring large values of D. This term is counterbalanced by the rise of the two entropy terms ΔS_J and ΔS_s. The sum of these terms, the free energy, displays a minimum at a certain lamellar thickness which represents the equilibrium thickness. Finding the minimum of $\Delta G/(N_c k_B T)$ with respect to D leads to

$$D \propto N^{9/14} = N^{0.643} \tag{5.9}$$

as a limiting behavior for large values of the chain length. In this case, the logarithmic term can be neglected.

Semenov [9] was able to give an analytical result of the free energy related to chain stretching. This contribution was found to scale with $(D/(aN^{1/2}))^2$, thus like in the case of Gaussian chains, even though the chains were assumed to be strongly stretched, the chains ends being distributed at excess in the middle of the lamella parts. Semenov gives the following expression for the lamellar thickness:

$$D = 4\left(\frac{3}{\pi^2}\right)^{1/3} a N^{2/3} \chi^{1/6} \tag{5.10}$$

The exponent found by Semenov for the scaling of the lamellar thickness with chain length ($D \propto N^{2/3}$) is slightly higher than the result from Helfand and Wasserman ($D \propto N^{0.643}$).

[2] In case of polystyrene-polybutadiene, there are slight differences: the densities are $\rho_{PS} = 1.05$ g/cm^3 and $\rho_{PB} = 0.886$ g/cm^3 (Chapter 2). The segment lengths are both ~ 6.9 Å [76, 77].

Another mean-field theory describing the ordered state has been published by Ohta and Kawasaki [78]. These authors use the random-phase approximation which treats the chains as Gaussian. Rigorously, this assumption is only valid in the disordered state and in the vicinity of the ODT. However, an exponent of 2/3 was identified.

As will be established below, we find an exponent of 0.61 ± 0.01 for $\chi N \simeq 27 - 100$ which is slightly lower than the predictions reviewed here.

The disordered state

We now turn to the description of the disordered state where the mean-field theory of Leibler [7] has proven successful. This formalism has later been used as a starting point to describe the intermediate region (see below). Leibler could predict the phase transitions from the disordered state into ordered states with different morphologies. In addition, he calculated the structure factor in the disordered state. In the following, we only review the characteristics of the theory as far as relevant for the present study.

Leibler made a Landau expansion of the free energy of block copolymer melts where the deviation of the local number density of A-monomers from the mean density served as an order parameter, ψ:

$$\psi(\vec{r}) = \langle \tilde{\rho}_A(\vec{r}) - f_A \rangle \tag{5.11}$$

where $\tilde{\rho}_A(\vec{r}) = \rho_A(\vec{r})/\rho_{av}$ is the normalized density. The average number density ρ_{av} is in each point $\vec{r}$ given by $\rho_{av} = \rho_A(\vec{r}) + \rho_B(\vec{r})$ and f_A is the volume fraction of the A-block. This approach has proven successful in the vicinity of second-order and weak first-order phase transitions where the amplitude of the order parameter is small. Assuming incompressibility of the block copolymer melt, the density ρ_{av} can be considered to be constant throughout the sample.[3] The order parameter $\psi(\vec{r})$ is zero throughout the sample deep in the disordered state and different from zero in the ordered state. In order to calculate the free energy of block copolymer melts, Leibler used a random phase approximation: The response to the potentials was calculated as if the chains were Gaussian (as in homopolymer melts). However, when calculating the external fields conjugated to the order parameter, the interaction potentials between monomers were included. By calculating the free energy for different morphologies (disordered, cubic, hexagonal, lamellar), Leibler determined the phase diagram in the vicinity of the ODT.[4] The phase transitions were shown to be weak first-order for asymmetric diblock copolymers. A critical point was predicted for symmetric diblock copolymers at $\chi N = 10.495$. Here, a second-order (continuous) phase transition from the disordered to the lamellar phase was predicted. In this case, the order parameter (*i.e.* the amplitude of the lamellar profile) should rise continuously starting from zero at the ODT. Fluctuation theory (see below) showed that the transition is weakly first-order for all values of the volume fraction, f, also for $f = 0.5$.

Another result of Leibler's theory is the structure factor in the disordered state as a function of the radius of gyration, R_g, the chain length N, the Flory-Huggins interaction

[3] It has later been shown by McMullen and Freed [79] and by Tang and Freed [80] that releasing the incompressibility constraint changes the shape of the structure factor. However, in the case $N_A = N_B = 100$ and $\chi = 0.05$ which is comparable to the samples studied in this work, the peak position does not vary significantly upon introducing a finite compressibility [80].

[4] This region used to be termed the 'weak-segregation limit'. As it is not unambiguously defined (Chapter 1, we will not use this term.

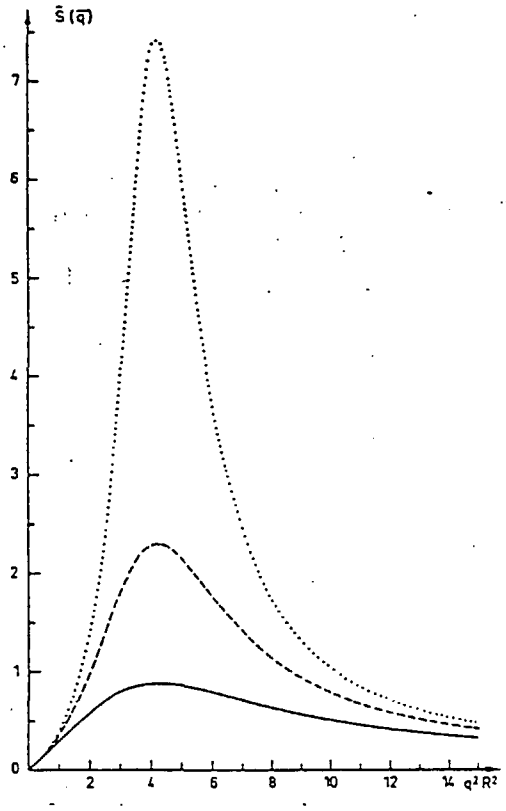

Figure 5.2: *Leibler's structure factor in arbitrary units of a diblock copolymer melt ($f = 0.25$) as a function of $x = q^2R_g^2$. Dotted line: $\chi N = 17.5$, dashed line: $\chi N = 16.0$, full line: $\chi N = 12.5$. For $f = 0.25$, the χN-value at the ODT is ~18. From [7].*

parameter χ and the scattering vector q:

$$S(q) = \frac{N}{F(x) - 2\chi N} \tag{5.12}$$

where $x = q^2R_g^2$ and where

$$F(x) = \frac{g(1,x)}{g(f,x)g(1-f,x) - \frac{1}{4}[g(1,x) - g(f,x) - g(1-f,x)]^2} \tag{5.13}$$

with

$$g(f,x) = \frac{2}{x^2}[fx + e^{-fx} - 1] \tag{5.14}$$

is the Debye function giving the formfactor of one block. Even in the athermal limit ($\chi = 0$) the structure factor is non-vanishing. In this case, the structure factor only describes the correlation hole: in the vicinity of an A-monomer, the probability of finding an A-monomer belonging to another chain chain is lowered because the chain to which the reference monomer belongs already occupies a certain volume [6]. The structure factor displays a broad peak (Fig. 5.2). As the chains are assumed to be Gaussian, the

peak position, q^*, which is inversely proportional to the radius of gyration of the block copolymer, scales like [7]

$$q^* \propto R_g^{-1} \propto N^{-1/2} \tag{5.15}$$

The characteristic lengthscale, defined in terms of a Bragg reflection, $D = 2\pi/q^*$, scales thus with

$$D \propto R_g \propto N^{1/2} \tag{5.16}$$

The variation of the characteristic lengthscale with temperature or chain length depends thus only on the behavior of the radius of gyration, *i.e.* for Gaussian chains:

$$D \propto N^{1/2} \tag{5.17}$$

In summary, according to mean-field theories we would expect the following scaling of the lamellar thickness with chain length:

$$D \propto N^{\delta} \text{ where } \begin{cases} \delta = 1/2 & \text{deep in the disordered state} \\ \delta = 0.643 \text{ or } 2/3 & \text{deep in the ordered state} \end{cases} \tag{5.18}$$

The intermediate region

As the present study focuses on the intermediate region and the crossover to the SSL, some of the theoretical approaches dealing with this region will be reviewed. They can be classified into mean-field theories [71, 72, 73, 74, 75] and theories incorporating fluctuations [27]. In the following, we will sketch the assumptions, methods and results of the different approaches.

By means of a density functional theory, Melenkevitz and Muthukumar [71] identified three scaling regimes, all of them in the ordered, lamellar state (Fig. 5.3): a region in the vicinity of the ODT: $\chi N = 10.5 - 12.5$, where $D \propto N^{0.5}$, an intermediate region: $\chi N = 12.5 - 95$, where $D \propto N^{0.72}\chi^{0.22}$, and the SSL: $\chi N > 95$, where $D \propto N^{0.67}\chi^{0.17}$.

Tang and Freed [72] assumed Gaussian statistics for each block and used an expression for the free-energy functional given by Ohta and Kawasaki [78]. Their expression for the free energy density contains two terms: a stretching term $\propto (D/N)^2$ and an interfacial term $\propto (\chi - C(f)/N)^{1/2}/D$ where $C(f) = 3.6$ for $f = 0.5$. The second term is different from the one given by Helfand and Wasserman [23] and is due to a smooth density profile implying a certain degree of mixing. The authors found that the characteristic lengthscale, D, varies as follows for a symmetric diblock copolymer system:

$$D \propto \left(\chi - \frac{C(f)}{N}\right)^{1/6} N^{2/3} a \tag{5.19}$$

where a is the average segment length. This expression converges to $D \propto N^{2/3}$ for large N. The authors evaluated the peak position, q^*, as a function of χN in a range of $\chi N = 10-24$ and found an exponent $\delta = 0.72$, thus higher than the mean-field predictions in the SSL. We plotted the expression given in Eq. 5.19 for our case, where $\chi = 0.0325$ at the working temperature, 150°C, and in the N-range studied, $N = 156 - 3090$ (not shown). Linear fits for low and high values of N give exponents $\delta_{low} = 0.73$ and $\delta_{high} = 0.68$. The exponent is thus higher in the vicinity of the ODT than in the SSL. A crossover is found at $\chi N \simeq 25$.

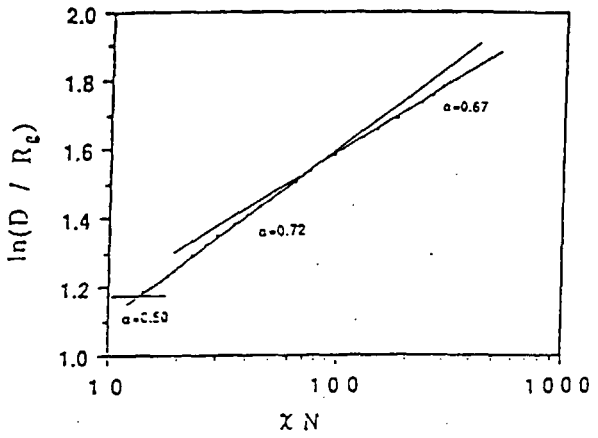

Figure 5.3: $\ln(D/R_g)$ *(where* $R_g \propto N^{1/2}$*) as a function of* $\ln(\chi N)$ *for* f*=0.5. From Melenkevitz and Muthukumar [71].*

However, the authors do not mention the existence of a crossover. The model fails in describing the disordered state where $\chi N < C(f)$.

Vavasour and Whitmore [73] used self-consistent field theory and found for symmetric diblock copolymers that the lamellar thickness, D, scales with chain length like

$$D \propto a(\chi N)^p N^{1/2} \tag{5.20}$$

where a is the average segment length and $p \simeq 0.2$ in the SSL, *i.e.* $D \propto N^{0.7}$. As the system approaches the ODT, $p \to 1/2$, *i.e.* $D \propto N^1$. For $\chi = 0.05$, the value being closest to the one in the present study, a crossover is identified at $N \simeq 300$, *i.e.* at $\chi N \simeq 15$.

McMullen [74] used a density-functional approach which is similar to the random phase approximation used by Leibler [7]. The influence of higher-order terms (up to fourth order) was evaluated and the dependence of D/R_g (where R_g is the unperturbed radius of gyration, $R_g \propto N^{1/2}$) on χN was determined. The result in the ordered state is shown in Fig. 5.4. The fourth-order expansion yields a curve having a steep rise between $\chi N \simeq 10.5$ and 12.5. In the region $\chi N \simeq 12.5 - 30$ the curve is flatter and an exponent of 1.0 can be read off. At very high values of χN (> 100), the curve reaches the 2/3-behavior. Extrapolating the lines in the log-log-plot, a crossover can be identified at $\chi N \simeq 55$.

Sones *et al.* [75] studied a mean-field model similar to that by Helfand and Wasserman between $\chi N = 10$ and 120 assuming the density profile to be sinusoidal. Numerical calculations lead to the identification of an intermediate regime ($\chi N < 17 - 18$) where

$$D = 0.844 R_g (\chi N)^{0.571} = 0.141 a^2 N^{1.071} \chi^{0.571} \tag{5.21}$$

Surprisingly, the exponent in this regime was found to be larger than unity. For higher values of χN, the SSL exponent 2/3 is regained (Fig. 5.5).

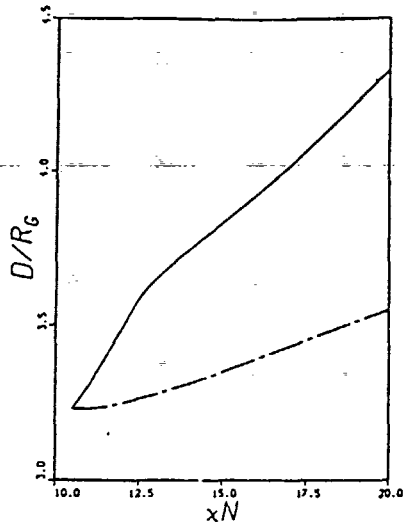

Figure 5.4: *Lamellar thickness, D, divided by the unperturbed radius of gyration ($R_g \propto N^{1/2}$) as a function of χN. From McMullen [74]. The full line is the result of the fourth-order expansion, the dash-dotted line from second-order.*

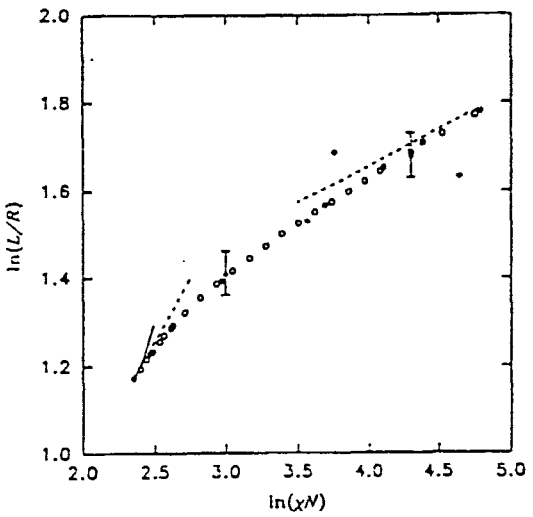

Figure 5.5: $\ln(D/R_g)$ *(where $R_g \propto N^{1/2}$) as a function of* $\ln(\chi N)$ *for f=0.5. Circles are numerical results, dashed lines are analytic predictions for the weak (Eq. 5.21) and the strong segregation limits ($D \propto N^{2/3}$). From Sones* et al. *[75].*

Fredrickson and Helfand [20] studied the influence of fluctuations on the phase behavior in the vicinity of the ODT. In this way, the Leibler theory [7] was improved. It was shown that the Hamiltonian describing the block copolymer system belonged to the same universality class as the Brazovskii Hamiltonian [81]. The latter describes phase transitions from isotropic to anisotropic states, as is also the case with block copolymer systems. The phase transition described by the Brazovskii Hamiltonian is of first order, even for $f = 0.5$ and not of second order, as predicted by Leibler. The most severe change compared to Leibler's results is the location of the ODT, $(\chi N)_{ODT}$ which in the Fredrickson-Helfand theory is dependent on chain length. For symmetric diblock copolymers, the ODT is located at $(\chi N)_{ODT} = 10.495 + 41.022\bar{N}^{-1/3}$ where $\bar{N} = N(\bar{a}^6/v^2)$ ($\bar{a}$ denotes the average segment length and v the specific segment volume). Thus, the smaller the chain length, N, the lower the ODT temperature. For $N \rightarrow \infty$, the mean-field result, $(\chi N)_{ODT} = 10.495$, is recovered. As the value of the characteristic lengthscale was kept fixed in this approch, no predictions could be made about the scaling behavior of the characteristic lengthscale.

The approach of Barrat and Fredrickson [27] takes the fluctuation theory of Fredrickson and Helfand [20] as a starting point. Barrat and Fredrickson released the characteristic lengthscale and evaluated $q^*R_g = q^*(Na^2/6)^{1/2}$ as a function of χN for different values of N. The curves are horizontal for low values of χN (*i.e.* $q^* \propto N^{1/2}$), but at larger χN-values, q^*R_g decreases with rising χN, indicating the onset of chain stretching. The theoretical curve could be shown to fit experimental data ([8], see Fig. 1.8) quantitatively. However, the authors state that their approach cannot easily be extended further into the ordered state.

In summary, several theoretical approaches to the region between the fully homogeneous state and the SSL have been made. In this intermediate region, exponents higher than the exponent predicted for the SSL (2/3) have been found. The difference in scaling between the intermediate region and the SSL is closely related to the shape of the density profile which, in the intermediate region, is close to sinusoidal whereas it has sharp interfaces in the SSL. A crossover from an intermediate regime with an exponent higher than 2/3 to the SSL has been predicted. As will be established below, we have identified a crossover from a region where $D \propto N^{0.82}$ ($\chi N \simeq 5 - 30$) to the SSL where $D \propto N^{0.61}$.

5.1.2 Experimental studies

Several experimental studies of the scaling of the lamellar thickness with chain length have been carried out during the past 16 years. The characteristics of some of these studies will be outlined in chronological order.

An electron microscopy and small-angle X-ray scattering (SAXS) study of six polystyrene-polyisoprene diblock copolymers was carried out by Hashimoto *et al.* [57]. Samples had molar masses between 21000 and 102000 g/mol and were nearly symmetric in composition. They were solvent-cast from toluene and were left to dry at 30°C and at room temperature under vacuum for several days. The samples were found to be well-oriented, the lamellae being parallel to the film surfaces, and the lamellar thickness scaled at room temperature like $D = 0.24$ Å $M_n^{2/3}$ where M_n denotes the number-average molar mass.

Hadziioannou and Skoulios [68] studied a homologous series of nine nearly symmetric polystyrene-polyisoprene diblock copolymers having molar masses between 8500 and

205000 g/mol of which eight were ordered. Samples were subjected to oscillatory shear (which aligns the lamellar domains) and were annealed above the glass temperature of the polystyrene blocks. The lamellar thickness, as determined at room temperature using SAXS, scaled like $D = 0.06$ Å $M_n^{0.79\pm0.02}$. This exponent is substantially higher than 2/3. Also the prefactor is very different from the one found by Hashimoto *et al.* [57]. It might be that the difference compared to Hashimoto's study lies in the way of preparing samples: here, the samples were shear aligned instead of solvent-cast. In addition, a larger molar-mass range was studied by Hadziioannou and Skoulios.

Richards and Thomason [59] studied (among other samples) six polystyrene-polyisoprene diblock copolymers having molar masses between 37770 and 178100 g/mol using electron microscopy and small-angle neutron scattering (SANS). The weight fractions of the polystyrene blocks were $0.514 - 0.728$, *i.e.* the polymers were not really symmetric. All samples studied were ordered. Samples were solvent-cast from toluene and left to dry at room temperature for two weeks (one week under vacuum). They found $D = 0.997$ Å $M^{0.56}$ (M denotes the overall molar mass) for the 'interdomain separation', D (which corresponds to the lamellar thickness) and $L = 0.22$ Å $M_D^{0.66}$ where L denotes the thickness of the polystyrene part of the lamella and M_D the molar mass of the polystyrene block. It should be noted that there are discrepancies between the values found with electron microscopy and with SANS. The authors express their surprise about the different exponents found for D and L, which they attribute to the fact that the preparation conditions probably did not lead to equilibrium states.

Matsushita *et al.* [58] studied a homologous series of ten polystyrene-poly(2-vinylpyridine) diblock copolymers. The molar masses ranged between 38000 and 739000 g/mol and were thus much higher than the samples studied in the investigations described above. Samples were solvent-cast at room temperature from toluene and studied by SAXS (also at room temperature). The samples were found to be well oriented. A scaling relation $D = 0.33$ Å $M_n^{0.64\pm0.03}$ was found, which corroborates the prediction of Helfand and Wasserman [23].

Almdal *et al.* [8] studied nine poly(ethylene propylene)-poly(ethyl ethylene) samples having chain lengths in the range $N = 125 - 1890$. Five of the samples were disordered. An advantage of these samples, compared to block copolymers having a polystyrene block, is their low glass temperature (below $-50°$). The samples were annealed just by keeping them at room temperature. An exponent δ=0.80 ± 0.04 was found in a region around the ODT: $0.57\,N_{ODT} < N < 2.4\,N_{ODT}$ at 23°C, which corresponds to $\chi N \simeq 2 - 33$. A crossover to the Gaussian regime was identified at $\chi N \simeq 6$ [22] (Fig. 1.8).

To summarize, different values of the exponent δ have been obtained experimentally, lying between 0.56 and 0.80. This large span might be due to the fact that chemically different polymers were studied. Another reason might be that different regions in the phase diagram were studied, *e.g.* the region around the ODT [8] or the region deep in the ordered state [58]. Also, different preparation methods were used: solvent-casting at room temperature, shear alignment above the glass temperature and annealing above the glass temperature.

In the present study, we attempt to reconcile the different results obtained so far, especially to establish the link between the intermediate region and the SSL. A region $\chi N \simeq 5 - 100$ is studied using a homologous series of symmetric polystyrene-polybutadiene

diblock copolymers. In order to study the influence of the preparation method chosen on the lamellar thickness, annealing, solvent-casting and shear alignment were used (Chapter 4). Before preparation, samples were stabilized against degradation by adding antioxidant and only samples with $\bar{M}_W/\bar{M}_N < 1.3$ after preparation were used. We have also studied the influence of the selectivity of the solvent used for solvent-casting. For consistency and in order to avoid non-equilibrium effects, preparation and examination were carried out at the same temperature (150°C) which was chosen to be above the glass temperature of the polystyrene block ($\simeq$ 100°C), but below the degradation temperature of the polymers (degradation is estimated to become a severe problem above ca. 180°C). A combined SAXS and SANS-study was performed in order to cover a large range of scattering vectors and to determine the peak positions as precisely as possible.

5.2 Small-angle scattering – the technique

Small-angle X-ray (SAXS) and neutron (SANS) scattering are powerful tools for structural investigations on a lengthscale between ~10 and 1000 Å and have been widely used for studying very different samples, *e.g.* colloidal and macromolecular solutions, polymeric systems, porous glasses, alloys and ceramic materials. The technique has been extensively reviewed in [82, 83], for instance. A survey and a comparison of SAXS and SANS is given in [84]. Recent developments in small-angle scattering of soft condensed matter are studies of samples under shear and time-resolved studies using synchrotron radiation. These and other topics were discussed at the NATO Advanced Study Institute in 1993 which dealt with the 'Modern Aspects of Small-Angle Scattering' [85].

An X-ray or neutron beam penetrates the sample under investigation and the angular dependence of the intensity of the scattered radiation is recorded. The difference of X-ray and neutron scattering lies in the way the beam and the sample interact: in X-ray scattering, the photons interact with the electrons in the material, thus, it is the electron density that is probed; in neutron scattering, the neutrons interact with the nuclei in the sample via nuclear forces, thus probing the scattering length density.

In this section, the review given in [84] is followed. A general scattering experiment is shown in Fig. 5.6. The incoming beam is considered a plane wave having a wavevector $\vec{k}$ with the length $|\vec{k}| = 2\pi/\lambda$, λ being the wavelength. Each scatterer emits a spherical wave having a wavevector $\vec{k}'$. The scattering vector is then defined as

$$\vec{q} = \vec{k} - \vec{k}' \tag{5.22}$$

From the scattering triangle (Fig. 5.6) which is valid in the case of elastic scattering ($|\vec{k}| = |\vec{k}'|$), the relation

$$q = \frac{4\pi}{\lambda} \sin\left(\frac{\theta}{2}\right) \tag{5.23}$$

is found. The scattering amplitudes from an extended sample containing many scatterers, each contributing a spherical wavelet, are added:

$$A(\vec{q}) = \int_V d\vec{r}\rho(\vec{r}) \exp(i\vec{q}\cdot\vec{r}) \tag{5.24}$$

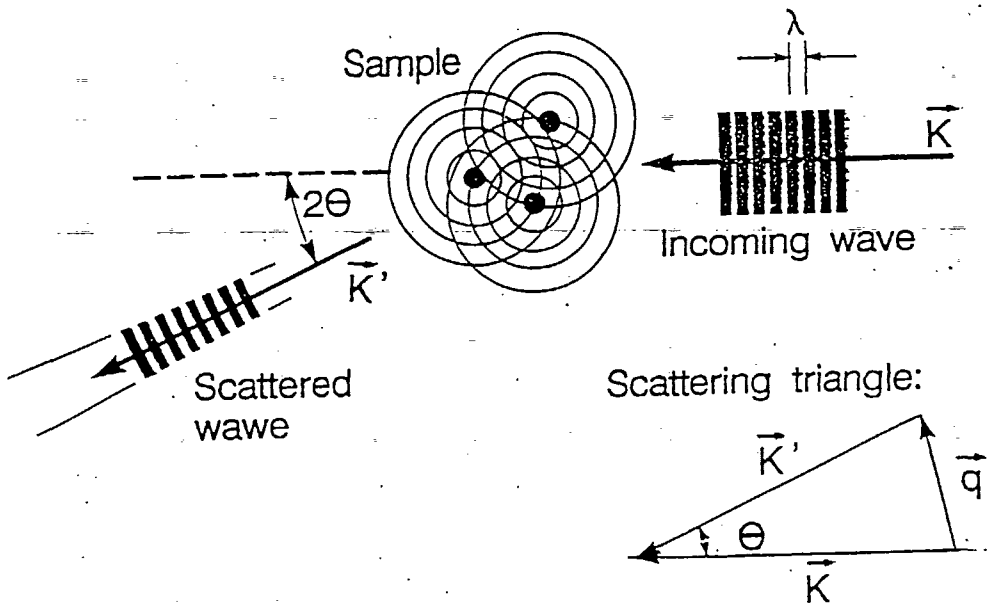

Figure 5.6: *General scattering experiment with the scattering triangle. From [84].*

where $\rho(\vec{r})$ denotes the density of scatterers and V the scattering volume. Then, the intensity is proportional to[5]

$$I(\vec{q}) = A(\vec{q})A^*(\vec{q}) \tag{5.25}$$

$$= \int_V d\vec{r}_1 \int_V d\vec{r}_2 \rho(\vec{r}_1) \exp(i\vec{q}\cdot\vec{r}_1)\rho(\vec{r}_2)\exp(-i\vec{q}\cdot\vec{r}_2) \tag{5.26}$$

$$\tag{5.27}$$

Transforming the coordinates according to $\vec{r} = \vec{r}_1 - \vec{r}_2$ and $\vec{r}' = \vec{r}_2$ and rearranging the integrals leads to

$$I(\vec{q}) = \int_v d\vec{r}\exp(i\vec{q}\cdot\vec{r}) \int_V d\vec{r}'\rho(\vec{r}')\rho(\vec{r}+\vec{r}') \tag{5.28}$$

Thus, the scattering intensity is a measure of the density distribution in the sample. The latter integral is proportional to the pair correlation function:

$$G(\vec{r}) = \frac{1}{N}\int_V d\vec{r}'\langle\rho(\vec{r}')\rangle\langle\rho(\vec{r}+\vec{r}')\rangle \tag{5.29}$$

where N denotes the number of scatterers. The brackets denote an ensemble average which, in ergodic systems, is equal to the time average.

Structures on large lengthscales compared to the probing wavelength give rise to scattering at small angles. The maximum lengthscale, r, that can be explored in a scattering

[5]Here, the Thomson factor, the incoming flux, geometrical factors and other prefactors are omitted [86]. Nevertheless, we use the equality symbol for simplicity.

experiment is thus related to the minimum q-value attainable, q_{min}. r is given by [87]

$$r = \frac{\pi}{q_{min}} \tag{5.30}$$

The value of q_{min} is determined by the width of the primary beam. The minimum length-scale that can be investigated is $r_{min} \approx \lambda/2$, corresponding to backscattering. Most small-angle scattering instruments have a maximum scattering vector of $q_{max} \simeq 1$ Å^{-1} corresponding to a minimum dimension of ca. 10 Å.

Other methods for structural investigations are electron microscopy and light scattering. With electron microscopy, approximately the same lengthscales as in small-angle scattering can be studied, but the technique has the advantage of giving a real-space picture. However, electrically isolating samples have to be stained with metal oxides which can lead to artifacts and, as microscopy is a surface technique, it has to be used very carefully. In order to get a picture of the bulk, samples have to be microtomed, *i.e.* cut into very thin slices. In addition, electron microscopy is only a local probe. In light scattering, the wavelengths used are much larger than in X-ray or neutron scattering, typically some hundred nanometers. The q-range accessible is typically $\sim 0.001 - 0.004$ Å^{-1}, *i.e.* much larger objects can be studied than with small-angle scattering.

5.3 Models for scattering from block copolymer systems

In order to model the scattered intensity as a function of the scattering vector, a model for the density profile of the block copolymer samples is taken as a starting point. The density profile of the A-block, ϕ_A, of symmetric diblock copolymers in the disordered and in the ordered state and in the vicinity of the ODT is sketched in Fig. 1.7. Deep in the ordered state, symmetric diblock copolymers have a lamellar structure and the interfaces are sharp. Approaching the ODT, the interfaces become more diffuse and, eventually, the density profile is close to sinusoidal. In the disordered state close to the ODT, there are still concentration fluctuations even though the structure is disordered. Deep in the disordered state, the melt is homogenous and the Leibler structure factor [7] is a good approximation to describe the correlations between A- and B-segments.

In the following, the scattering intensity of a symmetric diblock copolymer system deep in the ordered state is calculated by means of a simple lamellar model. Then, the scattering from a sample having a sinusoidal density profile is given and the Leibler structure factor is reviewed.

5.3.1 The strongly segregated state

In case of lamellar diblock copolymer systems in the strong-segregation limit, a simple, one-dimensional model for the density can be applied. The density is assumed to vary along the z-axis as shown in Fig. 5.7, *i.e.*

$$\rho(z) = \begin{cases} \rho_1 & \text{if} \quad (n+\phi)D < z < (n+1)D \\ \rho_2 & \text{if} \quad nD < z < (n+\phi)D \end{cases} \tag{5.31}$$

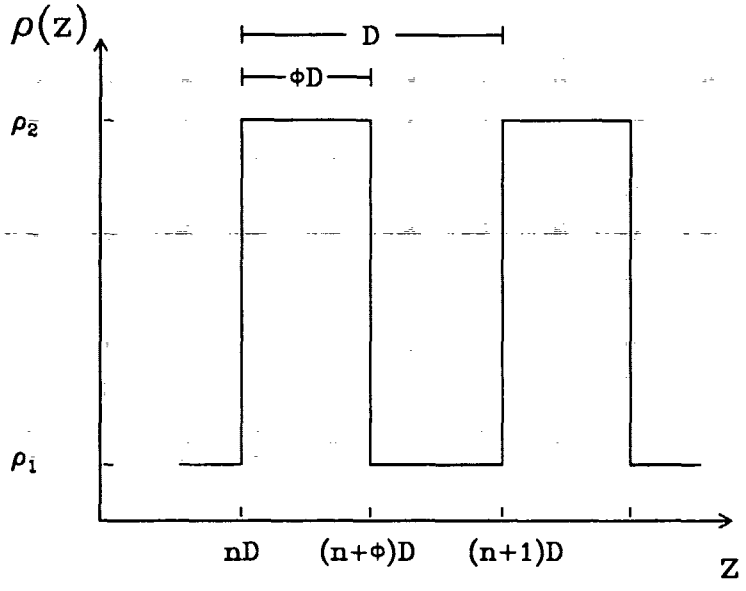

Figure 5.7: *Simple model for the density profile in a lamellar block copolymer system. For symbols see text.*

D is the lamellar thickness. ϕD is the part of the lamella where $\rho(z) = \rho_1$. $0 \leq \phi \leq 1$. $0 \leq n \leq N-1$ is an integer. The height of the lamellar stack, ND, is analagous to the volume in three dimensions. In the two other dimensions (x and y), the density is assumed to be constant. The model describes a single-crystal. Density fluctuations on the lengthscale of single polymer segments give rise to scattering at much higher angles which is why the crude model can be successfully applied.

The intensity is split up into a form- and a structure factor where the formfactor describes a single lamella and the structure factor the regular array of lamellae. For this purpose, the density profile of a stack of N lamellae is written as the convolution product of one lamella of thickness D and a lattice peak function of a regular one-dimensional lattice [86]. This approach is analogous to the basis and lattice formalism in crystallography and is valid if the structure consists of lattice cells containing the same density profile. The basis thus corresponds to a single lamella:

$$\rho_s(z) = \begin{cases} \Delta\rho & \text{if} \quad 0 < z < \phi D \\ 0 & \text{if} \quad \phi D < z < D \end{cases} \tag{5.32}$$

where $\Delta\rho = \rho_2 - \rho_1$. The subscript s refers to a single lamella. ρ_1 is set to zero because the scattering is measured relative to ρ_1. The lattice peak function describing the position of lamellae is a sum of delta functions

$$\rho_l(z) = \sum_{n=0}^{N-1} \delta(z - nD) \tag{5.33}$$

where the subscript l refers to the lattice. The scattering intensity is proportional[6] to the product of a formfactor $F(q)$ (describing the scattering of a single lamella) and of a

[6] Again, prefactors are omitted [86].

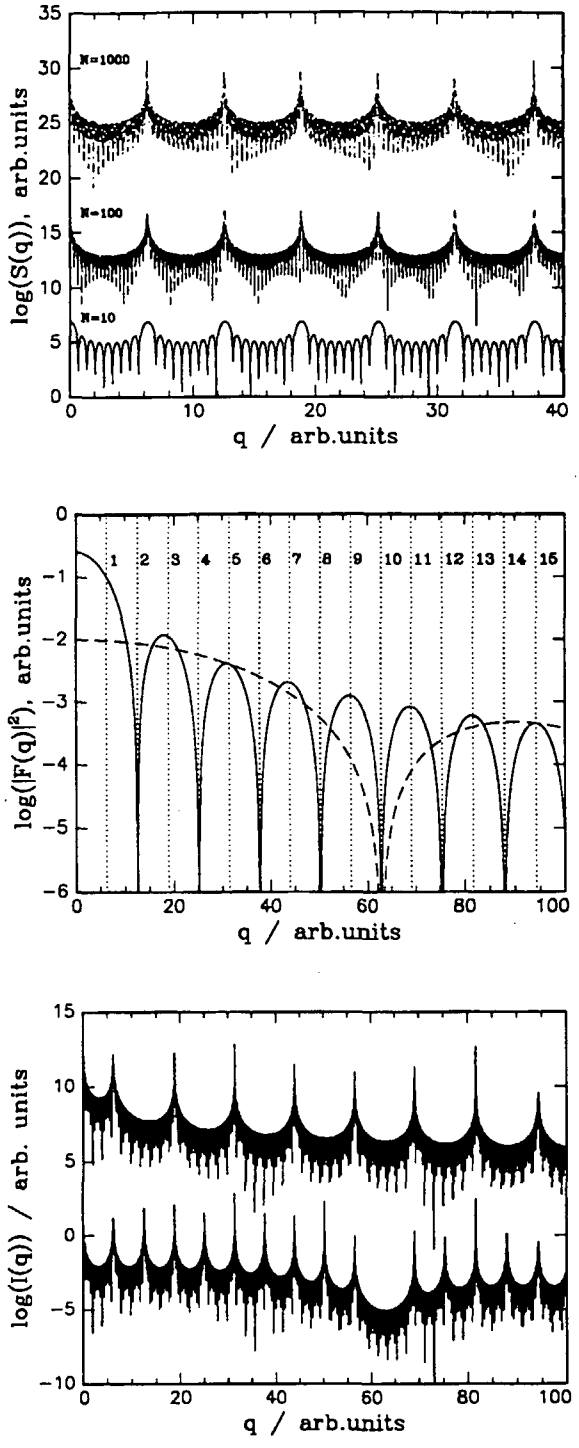

Figure 5.8: *Upper figure: Structure factor for symmetric lamellae, ϕ=0.5, and for different values of N. The lamellar thickness was set to $D = 1$. Middle figure: Formfactor for symmetric lamellae, $\phi = 0.5$ (full line) and for asymmetric lamellae, $\phi = 0.1$ (broken line). $D = 1$ and $\Delta\rho = 1$ were used for both curves. The dotted lines represent the positions of the Bragg peaks of the lattice peak function, $q = 2\pi k/D$. Lower figure: Scattering intensity. The following parameters were used: $N = 1000$, $D = 1$, $\Delta\rho = 1$. Upper curve: $\phi = 0.5$, lower curve: $\phi = 0.1$.*

structure factor $S(q)$ (describing the scattering of the lattice):

$$I(q) = |F(q)|^2 S(q) \tag{5.34}$$

where $F(q)$ is the Fourier transform of $\rho_s(z)$

$$F(q) = \int dz\, \rho_s(z) e^{iqz} \tag{5.35}$$

and $S(q)$ is the modulus squared of the Fourier transform of the lattice function $\rho_l(z)$. The formfactor is given by

$$|F(q)|^2 = \frac{4(\Delta\rho)^2}{q^2} \sin^2\left(\frac{qD}{2}\phi\right) \tag{5.36}$$

and the structure factor by

$$S(q) = \left|\sum_{n=0}^{N-1} e^{iqnD}\right|^2 = \left|\frac{1 - e^{iqDN}}{1 - e^{iqD}}\right|^2 = \frac{\sin^2(qDN/2)}{\sin^2(qD/2)} \tag{5.37}$$

The structure factor has maxima at $q = 2\pi k/D$ (k being an integer). Using l'Hospital's rule, $S(q)$ can be shown to converge to N^2 at the peak positions ($q = 2\pi k/D$). Combining the form- and the structure factor gives the scattering intensity:

$$I(q) = \frac{4(\Delta\rho)^2}{q^2} \sin^2\left(\frac{qD}{2}\phi\right) \frac{\sin^2(qDN/2)}{\sin^2(qD/2)} \tag{5.38}$$

The peak height is given by

$$I\left(\frac{2\pi}{D}k\right) = \frac{(ND)^2(\Delta\rho)^2}{\pi^2 k^2} \sin^2(\pi k\phi) \tag{5.39}$$

We will now examine the structure and the formfactor in more detail. The structure factor for symmetric lamellae (Eq. 5.37) is shown in Fig. 5.8 for different values of N. The larger N, the sharper are the diffraction peaks and the lower is the background compared to the peak height because of interference effects. Plotting the formfactor $|F(q)|^2$ (Eq. 5.36) for symmetric ($\phi = 0.5$) and strongly asymmetric lamellae ($\phi = 0.1$)[7], it is found for symmetric polymers that the even order peaks are suppressed (Fig. 5.8) and that for $\phi = 0.1$, every tenth peak is suppressed. As the formfactor is proportional to $\sin^2(qD\phi/2)/q^2$ (Eq. 5.36), the envelope of the formfactor decreases with q like $1/q^2$. (The peak height of the structure factor is q-independent.) For symmetric lamellae, the height of the first diffraction maxima (up to fifth order) falls strongly with rising order of diffraction whereas it is relatively constant for the first five orders of diffraction for asymmetric lamellae. This is the reason why only a limited number of Bragg reflections is observed in case of symmetric lamellae (Chapter 5.4): The formfactor 'kills' the structure factor.

In Fig. 5.9, the first order Bragg peak is shown for different values of N. The intensities are divided by N^2. The smaller N, the broader the peaks and the higher are the sidemaxima compared to the peak. We now attempt at deriving the relationship between the half

[7]The latter structure is not observed in diblock copolymer melts

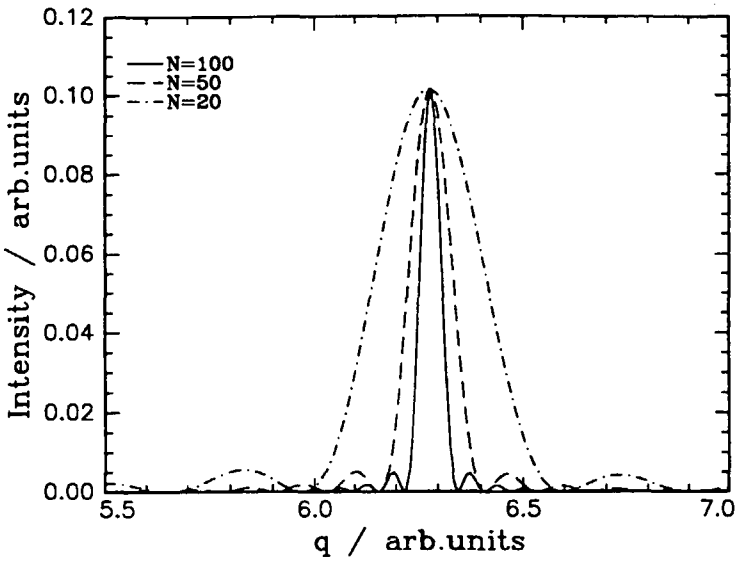

Figure 5.9: *First order Bragg reflection of symmetric lamellae for $D = 1$, $\Delta\rho = 1$ and for different values of N. The intensities are divided by N^2.*

width at half maximum, $HWHM$, and the stack height, ND. The $HWHM$ is calculated by regarding the intensity around $q = 0$ [88]. This can be done because the zeroth and first order peak are of approximately the same width.[8] From Eq. 5.38, it follows that

$$I(q = 0) = (\Delta\rho)^2(ND)^2\phi^2 \tag{5.40}$$

This expression has been found by approximating $\sin(qD\phi/2) \approx qD\phi/2$ and $\sin(qD/2) \approx qD/2$. It has also been used that $\sin(x)/x \to 1$ for $x \to 0$. The HWHM, q_H, is determined by $I(q_H) = I(0)/2$. Using the same kind of approximations, one arrives at

$$\frac{\sin^2(q_H ND/2)}{(q_H ND/2)^2} = \frac{1}{2} \tag{5.41}$$

This equation is transzendental and is approximately solved by

$$\frac{q_H ND}{2} \simeq 1.3916 \tag{5.42}$$

The $HWHM$ is thus given by

$$HWHM = q_H \simeq \frac{2.783}{ND} \tag{5.43}$$

This result is used for analysis of SANS-spectra where Lorentz-functions were fitted to the Bragg reflections (Chapter 5.5):

$$I(q) = \frac{I_o}{1 + (q - q^*)^2\xi^2} \tag{5.44}$$

[8] In the analysis of our SANS-spectra, we used the first order peaks (Chapter 5.5).

The half width at half maximum of this function is $1/\xi$. Combination of these expressions leads to

$$\xi \simeq \frac{ND}{2.783} \tag{5.45}$$

which allows us to estimate the average number of lamellae stacked per grain, N. The lamellar thickness, D, is deduced from the peak position.

The scattering intensity is shown in Fig. 5.8 for symmetric and asymmetric lamellae and shows the characteristics discussed above. If the intensity of the single-crystal is divided by the Lorentz factor for polycrystals, *i.e.* for randomly oriented grains [89], the intensity of a polycrystalline lamellar structure is obtained:

$$I_p(q) = \frac{I_s(q)}{4\pi q^2} \tag{5.46}$$

where the subscripts s and p stand for single- and polycrystalline. This leads to the following peak height:

$$I_p\left(\frac{2\pi k}{D}\right) = \frac{N^2 D^4 \Delta\rho^2}{16\pi^5 k^4} \sin^2(\pi k\phi) \tag{5.47}$$

The envelope of $I_p(q)$ decreases with k^{-4}. This scaling is consistent with the Porod law which states that the intensity of an isotropic structure with sharp interfaces scales with q^{-4} at large scattering angles [90].

To conclude, spectra of symmetric lamellar systems are expected to have the following characteristics: Bragg peaks appear at $q^* = 2\pi k/D$ where D is the lamellar thickness and k an odd integer. The peak height decreases strongly with rising order: $I_{peak} \propto k^{-2}$ for oriented lamellae and $I_{peak} \propto k^{-4}$ for 'polycrystalline' systems.

Another way of calculating the scattering intensity is to write the intensity as the modulus squared of the scattering amplitude. This approach gives the same result as found here. The calculation is given in Appendix B.

The crude model of the lamellar state assuming sharp interfaces and constant density within the A- and the B-part of the lamellae has been improved (for a review see [91]) to include both diffuse boundaries and density fluctuations within the lamellae. Both effects lead to deviations from the Porod law which states that $I(q) \propto q^{-4}$ for large values of q [91].

5.3.2 The ordered state close to the ODT

Close to the ODT, the density profile can be assumed to be close to sinusoidal, *i.e.* the concept of narrow interfaces cannot be applied anymore. In case of symmetric diblock copolymers, the density profile of a single lamella is approximated by

$$\rho_s = \Delta\rho \sin\left(2\pi \frac{z}{D}\right) \tag{5.48}$$

The formfactor then reads (Eq. 5.35)

$$|F(q)|^2 = \frac{16\pi^2(\Delta\rho)^2 D^2}{(4\pi^2 - q^2D^2)^2} \sin^2\left(\frac{qD}{2}\right) \tag{5.49}$$

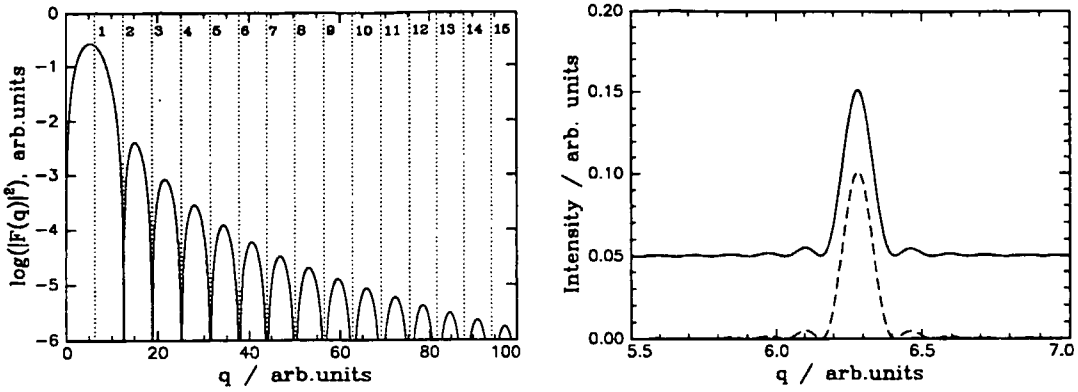

Figure 5.10: *Left figure: Formfactor for symmetric lamellae having a sinusoidal density profile, $\phi = 0.5$. $D = 1$ and $\Delta\rho = 1$. The dotted lines represent the positions of the Bragg peaks from the lattice, $q_k = 2\pi k/D$. Right figure: First order Bragg peak calculated for $N = 50$, using $D = 1$, $\Delta\rho = 1$ for the rectangular profile (full line, Eq. 5.38) and $\Delta\rho = 2/\pi$ (see text) for the sinusoidal profile (dashed line, Eq. 5.49). The intensities were divided by N^2. The curve for the rectangular profile is shifted by 0.05.*

$|F(q)|^2$ vanishes at $q = 2\pi k/D$ for all k except $k = 1$ (Fig. 5.10, left figure). This means that all Bragg peaks except the first one are suppressed and only the first-order Bragg peak is observed in the spectra. The absence of higher order peaks is thus characteristic for a sinusoidal profile. We observed this behavior with two samples which were close to the ODT (Chapter 5.5).

Comparing the peak shape as deduced from a rectangular and a sinusoidal profile, no difference in width is observed (Fig. 5.10, right figure). The amplitude of the sinusoidal profile was multiplied by $2/\pi$ in order to obtain the same peak height as for the rectangular profile. We conclude that the shape of the profile does not have an influence on the peak width.

5.3.3 The disordered state

Disordered diblock copolymer systems deep in the disordered state can be described by the Leibler structure factor [7] which is given above (Eq. 5.12 and Fig. 5.2). The structure factor goes to zero at zero scattering angle which reflects the incompressibility because the forward scattering is proportional to the isothermal compressibility [7]. The smaller χN, the deeper the sample is in the disordered state and the flatter the structure factor. The peak positions are shifted according to the chain length As has been shown by Leibler and Benoit [92], it is important to include polydispersity corrections in order to obtain correct values of χ and R from the experimental data. The Leibler structure factor without corrections was tentatively fitted to SAXS-spectra from disordered samples (Chapter 5.4). In the peak region, the Leibler structure factor can be fairly well approximated by a Lorentzian (Chapter 5.4):

$$S(q) = \frac{S(q^*)}{1 + (q - q^*)^2 \xi^2} \tag{5.50}$$

To summarize, symmetric diblock copolymers in the ordered, lamellar state give rise to Bragg peaks at

$$q_k^* = \frac{2\pi k}{D} \tag{5.51}$$

where k is an odd integer. From the peak positions, the lamellar thickness, D, can be deduced. The peak width gives information about the average stack height in the lamellar grains: $HWHM \simeq 2.783/(ND)$ (Eq. 5.43). The presence of higher order reflections indicates that the density profile is close to rectangular. If the profile is sinusoidal, only the first order Bragg peak is non-vanishing. In the disordered state, the Leibler structure factor is widely used (*e.g.* [77]). However, corrections for polydispersity and compressibility are prerequisite for obtaining good fits. In order to get a measure for the peak position and width and to maintain consistency with the ordered state, the peaks observed in the disordered state were fitted to Lorentz-functions.

5.4 Small-angle X-ray scattering

(The SAXS-study was carried out in collaboration with Dorthe Posselt, IMFUFA.)

This section is an extended and revised version of [29].

5.4.1 The Kratky-camera

SAXS spectra were recorded using the Kratky compact-camera (MBraun Graz Optical Systems) at IMFUFA which is a widely used 'table-top' instrument for structural investigations by small-angle X-ray scattering. The Kratky-camera (Fig. 5.11) was developed by Otto Kratky in the fifties [93, 94, 95, 96]. The main difficulty lies in data handling where one has to correct for the slit smearing induced by the line-shaped beam. A recent description of the instrument can be found in [97].

The X-ray source used at IMFUFA is a copper anode operated between 500 and 1600 W using a Philips PW 1729 generator. The generated radiation is mainly Cu K_α ($\lambda = 1.54$ Å) and Cu-K_β radiation ($\lambda = 1.39$ Å). The K_β radiation, however, is damped to a large extent by a nickel filter mounted in front of the focus. A long fine focus (12 mm $\times$ 0.4 mm) was used. The camera was installed on top of the X-ray tube under an angle of 3° leading to an effective focus size of 12 mm $\times$ 0.02 mm. The Kratky *compact*-camera is mounted directly on the X-ray tube. The take-off angle, the height of the camera head and the horizontal tilt angle can be adjusted by means of a fluorescent screen. All components (collimation block, sample holder, filter unit) are mounted in an evacuated housing ($p \leq 0.4$ Torr). Good mechanical and thermal stability are thus ensured and scattering by air is minimized.

The characteristic feature of the Kratky-camera is the collimation block (Fig. 5.12) giving a line shaped beam (typical dimensions: $1 - 2$ cm length $\times$ $10 - 40$ μm width). This geometry is often chosen together with a conventional X-ray generator in order to maximize the incoming beam intensity. It has the disadvantage of introducing a smearing effect which has to be corrected for numerically. The advantages of the Kratky collimation block are its mechanical solidity and the elimination of parasitic scattering above the main

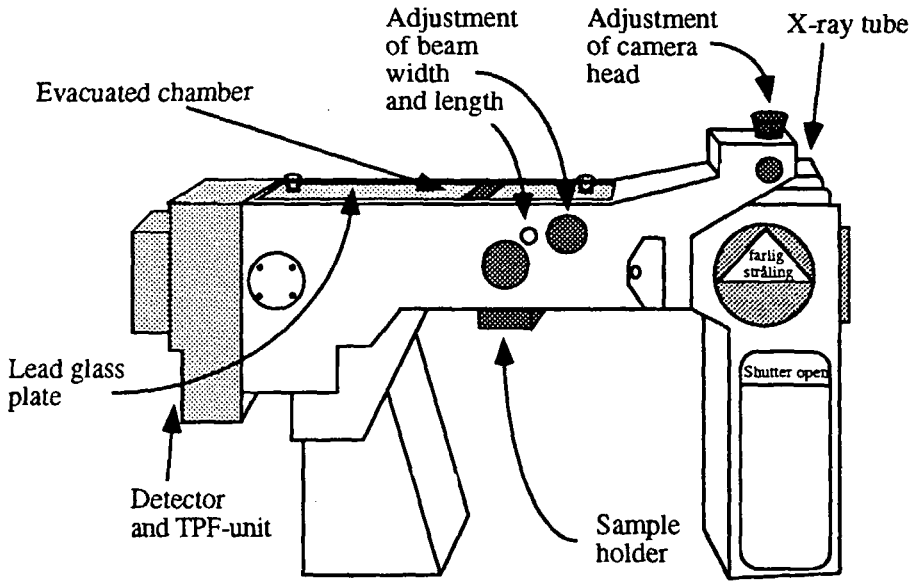

Figure 5.11: *Schematic drawing of the Kratky compact-camera. From [98].*

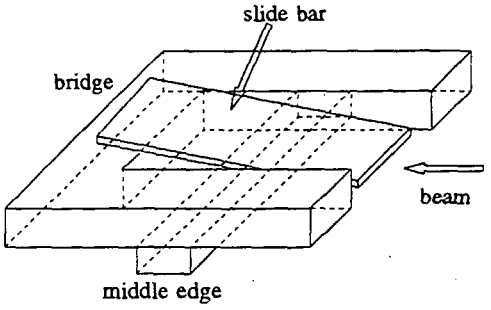

Figure 5.12: *Schematic drawing of the collimation block. The beam width (vertical direction) can be varied by moving the slide bar.*

section because rays scattered by the middle edge are absorbed by the bridge (Fig. 5.13). Spectra are measured in x-direction above the main section. The width profile, $Q(x)$, has thus the shape of a triangle, the side towards the main section being steeper than the lower one. The beam width (height) can be varied by moving the slide bar up and down; the beam length is determined by the beam length delimiters right behind the collimation. In the beam length direction (t) which is perpendicular to the direction of detection, the beam has a trapezoidal shape, $P(t)$.

Samples are mounted in different holders specially designed for liquids, solids or powders. In this work, a home-built holder was used (see below). It is specifically designed for studies of 'sticky' polymer samples at high temperatures and is mounted on the support of the standard Kratky sample holders. It is made of copper which has a high heat conductivity and is teflon-coated because the polystyrene-polybutadiene samples tend to stick to metal surfaces. The beam enters the holder via a slit (20 mm long and 2 mm high) which is kept as small as possible in order to minimize temperature gradients by

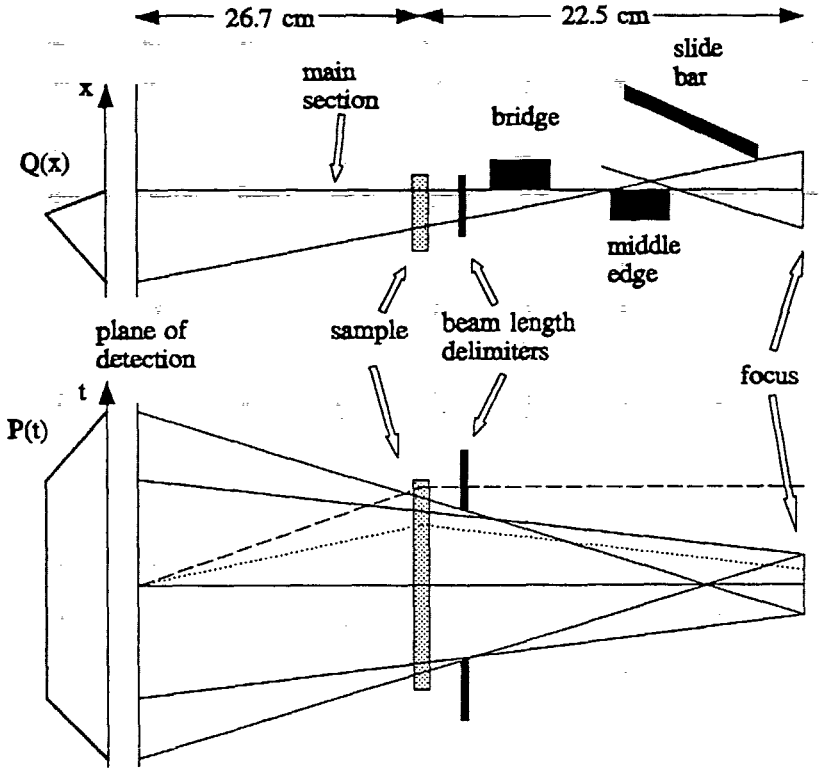

Figure 5.13: *Upper figure: Collimation seen from the side together with the beam width profile $Q(x)$. Note that the vertical dimensions are exaggerated. Spectra are measured in x-direction above the main section. Lower figure: Collimation seen from above together with the beam length profile $P(t)$. For the dashed and the dotted line see text.*

radiation losses. Samples are clamped between the two copper blocks. The holder can be heated to temperatures between 50 and 160°C by a heating wire mounted in a ceramic tube in the lower part of the block. The temperature is measured by a Pt 100 resistance mounted in the block right below the sample. The temperature is regulated by a temperature controller leading to a stability of ±0.1°C. A temperature calibration using a Fe-CuNi thermocouple mounted at the sample's place in the holder showed that between 65 and 155°C, the sample temperature, T_{sample}, is given by

$$T_{sample}[°C] = 0.992\, T_{set}[°C] - 1.30°C \tag{5.52}$$

A set temperature of 150°C leads thus to a sample temperature of 147.5°C. This deviation is, however, not critical for the present study where all measurements were performed at the same temperature (150°C). The holder can be adjusted in the vertical direction with a precision of 0.05 mm which is especially important when studying thin solvent-cast films edge on. In addition, the holder can be tilted around the beam axis. In order to avoid that the camera walls heat up when the sample holder is at high temperature, a flow of cooling water is maintained through the support.

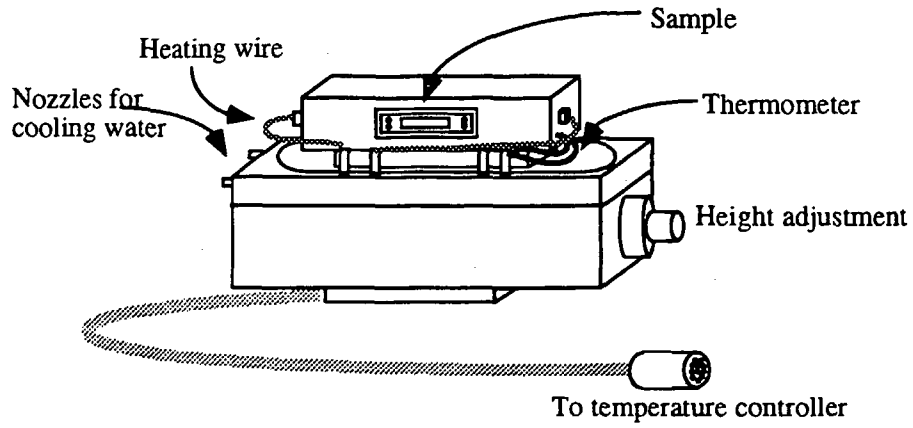

Figure 5.14: *Schematic drawing of the sample holder. The sample is clamped between the two copper blocks. The support was purchased from MBraun Graz Optical Systems, whereas the upper part was home-built,. The beam enters the holder from behind through a slit. From [98].*

Spectra are recorded with a one-dimensional position-sensitive detector (OED 50M, MBraun Graz Optical Systems) having an entrance window of ca. 6 cm height (x-direction) $\times$ 1 cm width (t-direction) which is mounted at a distance of 26.7 cm from the sample. The positional information is obtained using a copper cathode [99]. The detector rear wall which constitutes the cathode is divided into two parts consisting of triangles which are 'dovetailed' like a game of backgammon. The charge created by the ionizing radiation is divided into two fractions depending on the height of the impact. A platinum wire is used as the anode. A voltage of 3.6 kV is applied between the wire and the wall. The nominal detector resolution is ca. 60 μm. The detector is operated at 7-8 bar with a 90/10 % mixture of argon and methane. A gas flow of 0.5 l/h is maintained to renew the detector gas. Our experience is that countrates of more than 70 cts/s/channel for some hours lead to a reduction of the sensitivity of some percent. Therefore, great care must be taken when studying samples leading to Bragg peaks. The overall countrate should not exceed 10^4 cts/s. As the camera was operated without monochromator and thus the bremsspectrum was not eliminated, it was necessary to use the energy discrimination of the readout electronics. The energy spectrum displays a broad peak around which the energy limits can be set.

The TPF-unit (transparent primary filter) prevents the direct beam from hitting the detector. It consists of a tungsten filter (1 mm thick), absorbing the beam completely, and a nickel filter (also 1 mm thick) which is semitransparent. The latter makes measurements of the beam position and profile possible. Both filters can be moved in the vertical direction in order to cover as much of the detector as desired (total travel ca. 8 mm). Their position is controlled by a Heidenhain monitor with micrometer precision. In addition, the filters can be tilted around the beam axis such that their upper edges are parallel to the beam. Precise adjustment of the filters makes measurements at low angles possible. In order to measure the beam length profile, a sledge was designed making the sidewards movement of the detector possible. The sledge (described in Appendix C) is mounted between the camera housing and the TPF-unit, resulting in a sample-detector distance of 28.5 cm. Alternatively, the beam length profile was recorded with the detector mounted horizontally

(Fig. 5.16).

Beam profiles can also be measured using a nickel attenuator (thickness 1.00±0.02 mm, Goodfellow) which is installed between focus and collimation. The filter is then moved to the lowest possible position. This setup has the advantage that radiation scattered by the attenuator cannot penetrate the collimation in contrast to scattered radiation by the nickel filter right in front of the detector. However, it is important to use good quality nickel platelets having a thickness as homogeneous as possible. So far, we have not observed any difference in the width profile, when using the nickel attenuator or the nickel filter, respectively. This means that scattering from the nickel filter is negligible.

The q-range of the 'RUC-SAXS' instrument is $\sim 0.007 - 0.55$ Å^{-1}.

5.4.2 The experiment

The camera was aligned such that the take-off angle was 3° which is the case when the lead glass plate is horizontal, *i.e.* adjustment is possible with a level. The take-off angle was adjusted by lifting or lowering the rear end. By tilting the camera around its long axis, the camera was adjusted such that the collimation was parallel to the focus of the camera. This was checked by means of a fluorescent screen mounted in the camera body right in front of the detector: When the entrance slit was lowered, the image of the beam should vanish equally over the whole length. The camera head and the rear end were aligned sidewards such that the intensity at the detector was maximum. However, the sidewards alignment was not found to have a large influence on the intensity obtained. When the beam width was set, the height of the camera head was adjusted such that the intensity was maximum. This was done by means of a screw on top of the camera head.

Samples were mounted in the sample holder between kapton foil. Kapton diplays a peak at ~ 0.4 Å^{-1} which is far above the q-region where the polystyrene-polybutadiene samples show Bragg-peaks. Samples to be melted were mounted in a brass frame onto which pieces of kapton foil were glued with epoxy resin. The reason is that these samples tend to foam under vacuum and to flow out of the holder at higher temperatures. Annealed samples were mounted between kapton in a teflon frame such that the beam passed perpendicular to the pill surface ('through'). Oriented samples (solvent-cast or shear aligned) were glued onto a brass stripe such that the beam passed parallel ('edge on') resp. perpendicular to the pill surface (Fig. 5.15). In this way, it could be established in which direction shear aligned samples were oriented — parallel to the shear plane or perpendiular.

The spectra were measured in three series. Each series comprised the following steps: choice of beam length and width, measurement of beam profiles, measurement of sample and background spectra, determination of the sample and background and sample transmissions, measurement of the detector sensitivity, and calibration of the q-range. The procedure is described in the following.

When measuring sample spectra, care was taken not to exceed countrates of 70 cts/s/channel in order to avoid damage of the detector wire. This is especially critical for spectra from oriented samples showing sharp peaks. Therefore, the beam size was chosen to be relatively small: The beam length was chosen to be 8 mm, the width between 12.5 and 15 μm (Fig. 5.16).

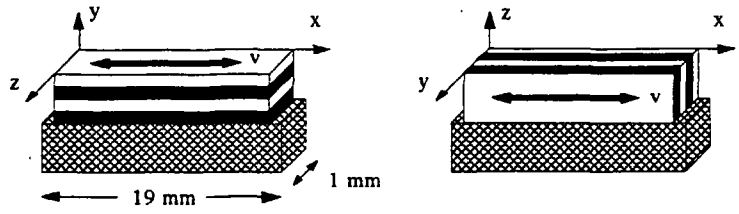

Figure 5.15: *The way of mounting oriented samples on a brass stripe: 'edge on' (left part) and 'through' direction (right part). The beam is perpendicular to the plane of paper having its long dimension in x-direction. The sample shown has the lamellar orientation parallel to the shear plane.*

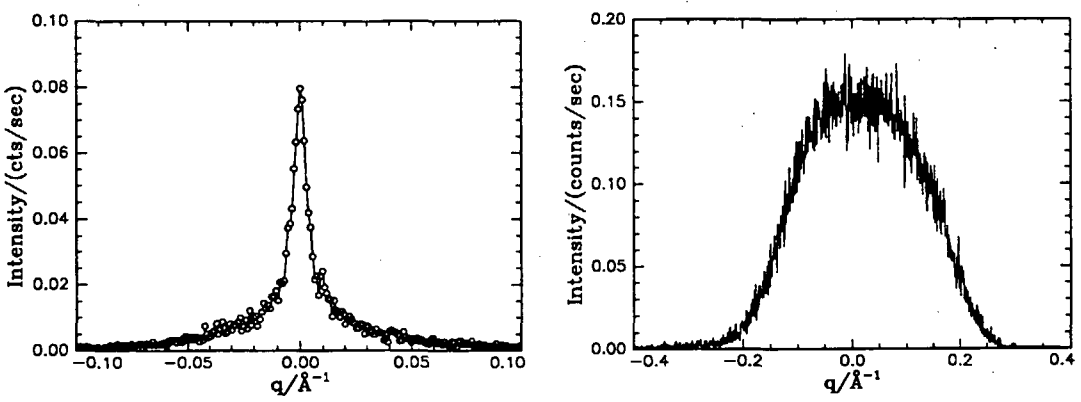

Figure 5.16: *Left figure: Beam width profile. The line guides the eye. Right figure: Beam length profile measured with the detector installed horizontally. Both profiles were measured using the nickel attenuator. The beam width was 15 μm and the beam length 8 mm.*

The beam width profiles used for desmearing (see below) were measured using the nickel attenuator (Fig. 5.16). These profiles also served for the determination of $q = 0$. Lines were fitted to both sides of the width profile. The channel where these lines cross was taken as zero. The beam length profiles were measured using the same attenuator and either the sledge or the detector mounted horizontally. As expected, the length profiles have trapezoidal shape (Fig. 5.16). A beam length profile measured using the sledge is shown in Appendix C. The question may arise why the beam profile measured in the detector plane is used for desmearing and not the one measured in the sample plane. The reason is that the beam is divergent in the horizontal direction (Fig. 5.13, lower part). This effect is not included in the desmearing routine (Eq. 5.54, see below). Using the profile measured in the detector plane, the correct distribution of scattering angles is obtained. Consider, for instance, the dotted ray in Fig. 5.13. It is divergent before hitting the sample. A photon following the dashed line hits the detector at the same point and has been scattered under the same scattering angle. However, the dashed ray is non-divergent before being scattered. Thus, using the beam profile measured in the detector plane and assuming that the incoming beam is non-divergent, the same distribution of scattering angles is obtained as with a divergent beam.

Sample spectra were measured as follows: When the desired temperature (150°C) was reached, four or more spectra of 500 or 1000 s duration were measured. The spectra were averaged if they looked equal indicating that thermal equilibrium was reached. A typical sample spectrum is shown in Fig. 5.17. For background measurements, only kapton foil (25.4 μm thick, Dupont) was installed in the beam. The same settings were used as for sample measurements. A typical background spectrum is given in Fig. 5.17.

The transmission of a sample installed in the beam is proportional to the area of the direct beam. These areas were tentatively determined using the nickel attenuator both for kapton (A_k) and for the sample mounted between kapton (A_{k+s}). The transmission ratios T_{s+bg}/T_{bg} such obtained (bg and s stand for background and sample, respectively) were always too high. Therefore, they had to be determined numerically using a trial and error method (see below).

The detector sensitivity was measured using a radioactive iron-55 source (0.1 mC, Amersham) mounted on a sample holder. The intensity was reduced in those channels where the detector wire was damaged. The wire was changed when the reduction in sensitivity exceeded a few percent.

The q-range was calibrated using silver behenate (98%, Rose Chemicals) which has a lamellar spacing of 58.380 Å [100]. In the angular range of the camera, five equidistant peaks were observed. When the sledge was not installed, the sample-detector distance was 26.7 cm and a value of $(0.879 \pm 0.005) \times 10^{-3}\text{Å}^{-1}$/channel was obtained. When the sledge was mounted, the sample-detector distance was 28.5 cm and $(0.821 \pm 0.004) \times 10^{-3}\text{Å}^{-1}$/channel was obtained.

5.4.3 Data analysis

Data were analyzed using Otto Glatter's (University of Graz) software package, especially the programs PDH (Primary Data Handling) for background subtraction and ITR (Indirect Transformation in Reciprocal Space) for desmearing [101]. The following procedure was applied.

The spectra were divided by the measuring time and averaged. The resulting spectrum was divided point by point by the iron-55 spectrum in order to account for detector efficiency and channels were converted to q-values. The equally treated background spectrum was subtracted leading to

$$I_s(q) \propto I_{s+bg}(q) - \frac{T_{s+bg}}{T_{bg}} I_{bg}(q) \tag{5.53}$$

where s and bg stand for sample and background, respectively. I denotes the intensity and T the transmission. The ratio of transmissions was determined when subtracting the background: It was adjusted such that the resulting spectrum was flat in the region of the kapton peak (~ 0.4 Å^{-1}), which can be done with a precision of 10%. Typical values for the transmission range between 0.4 and 0.8. A typical sample spectrum together with a background spectrum and a sample spectrum corrected according to Eq. 5.53 is shown in Fig. 5.17. A value of 0.5 was chosen for T_{s+bg}/T_{bg}.

The smeared intensity, *i.e.* the instrument-broadened, measured intensity, $\tilde{I}(q)$, can in case of slit collimation be calculated from the theoretical intensity, $I(q)$, the beam width

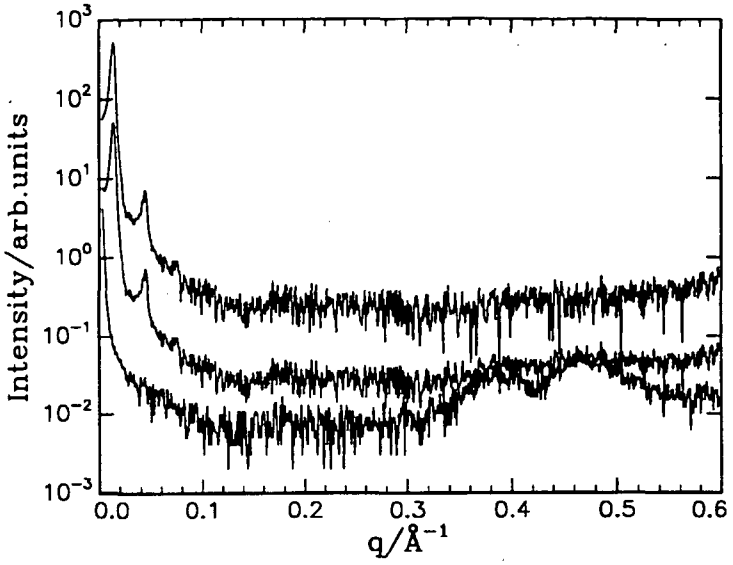

Figure 5.17: *Lower curve: Background spectrum. Kapton was installed in the beam. Middle curve: Sample spectrum. The sample (SBI02G, see Chapter 5.4) was installed between kapton. Upper curve: Same as the middle curve, but the background was subtracted, using* $T_{s+bg}/T_{bg} = 0.5$. *For clarity, the curve was shifted upwards by one decade.*

profile, $Q(x)$, and the beam length profile, $P(t)$ (Fig. 5.18) [82]:

$$\tilde{I}(m) = 2 \int_{-\infty}^{\infty} dx \int_{0}^{\infty} dt\, Q(x) P(t) I\{[(m-x)^2 + t^2]^{1/2}\} \tag{5.54}$$

Wavelength smearing can be neglected in case of nickel filtered Cu K_α radiation. m has the dimension of a length and is proportional to the scattering vector: $m = \lambda d q / 2\pi$ where d is the sample-detector distance. It has been assumed that the width profile has the same shape over the whole beam length. The effect of finite spatial resolution of the detector is already included if the beam profiles are measured in the same way as the spectra. This is the case when using the sledge instead of turning the detector. However, beam length profiles measured in either way did not show significant differences. The length smearing effect on an isotropic spectrum can be seen in Fig. 5.19. Consider a polycrystalline sample. A thin stripe of the sample is illuminated. This results in a superposition of diffraction rings. The peak observed with a one-dimensional detector is not sharp but there are contributions on the low-q-side of the nominal peak position. The peak becomes asymmetric because there is an enhanced contribution at lower angles (Fig. 5.20). This effect is absent for single crystals (Fig. 5.19) which show peaks along the detector axis (*e.g.* an oriented, lamellar sample mounted as shown in Fig. 5.15, left figure). As these spectra are not subject to beam length smearing, only the integral over the beam width profile is performed. As will be discussed below, spectra from disordered samples were desmeared for the beam width and length effect. Spectra from annealed samples were desmeared for the beam length effect. Spectra from solvent-cast and shear aligned samples were not desmeared.

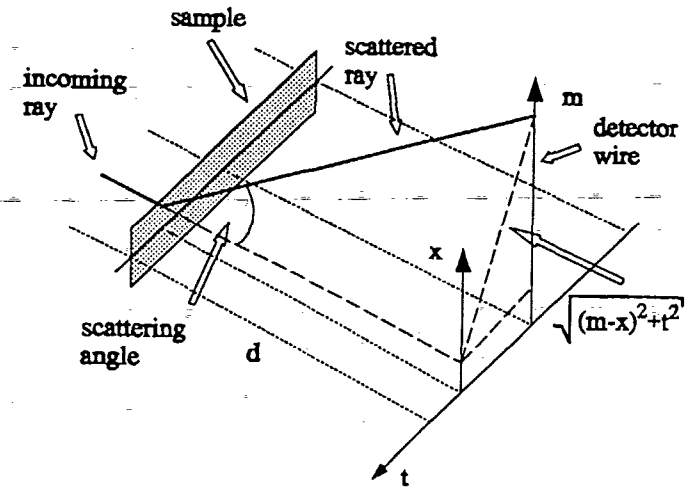

Figure 5.18: *Slit length and width smearing using slit collimation. The shaded area represents the cross-section of the incoming beam in the sample plane. The thick line represents a ray being scattered in an arbitrary point of the sample. The scattering angle corresponding to the scattering event shown is* $\arctan(\sqrt{(m-x)^2+t^2}/d)$, *where* d *is the sample-detector distance.*

Inversion of the integral given in Eq. 5.54 in order to determine the unsmeared intensity, $I(m)$, is an ill-posed problem because of the limited q-range of the measured scattering curve and because of noise in the data. Therefore, indirect methods must be used, one of them being the routine ITR. The desmearing routine ITR works as follows [101, 102]. The program starts with a linear combination of N functions $\phi_k(q)$ (cubic B-splines) representing an approximation of the theoretical intensity :

$$I(q) = \sum_{k=1}^{N} c_k \phi_k(q) \tag{5.55}$$

Cubic B-splines have the advantage of being smooth functions which are zero outside a certain q-range. Smearing $I(q)$ according to Eq. 5.54 yields $\sum_{k=1}^{N} c_k \psi_k(q)$ where ψ_k are the smeared cubic B-splines. Then, $\sum_{k=1}^{N} c_k \psi_k(q)$ is fitted to the experimental data by a weighted least-squares routine. In this way, the coefficients c_k are determined, and the desmeared intensity is calculated (Eq. 5.55). Stability problems due to the statistical noise are overcome by using a Lagrange parameter, λ. The routine minimizes the sum

$$\sum_{i=1}^{M} \left[I_{exp}(q_i) - \sum_{k=1}^{N} c_k \psi_k(q_i) \right]^2 \Big/ \sigma^2(q_i)$$
$$+\lambda \sum_{k=1}^{N-1} (c_{k+1} - c_k)^2 = \text{minimum}$$

where M is the number of datapoints, N the number of splines and $\sigma^2(q_i)$ the variance of the intensity $I_{exp}(q_i)$. Solutions where adjacent amplitudes c_k are very different are thus

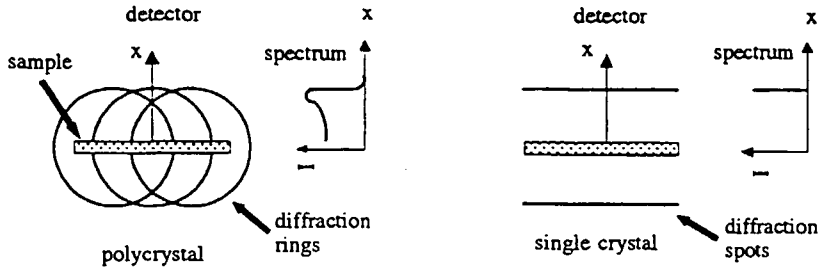

Figure 5.19: *Left figure: Length smearing effect on a diffraction ring from a polycrystalline sample. The detector wire is vertical. The resulting spectrum is shown schematically. Right figure: Beam length smearing effect on a spectrum from an oriented sample.*

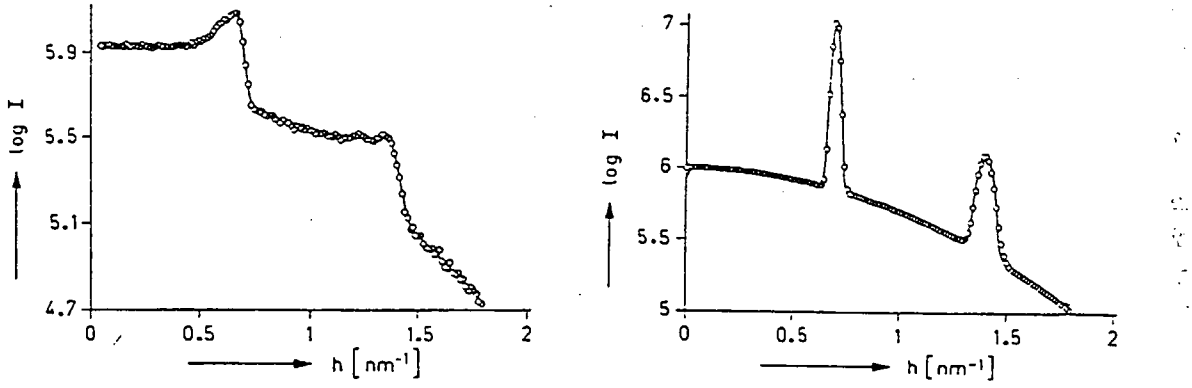

Figure 5.20: *Simulated smeared scattering curve (left figure) with two Gaussian peaks on a background and desmeared curve (right figure). The curve was desmeared according to slit length and to a wavelength distribution corresponding to the K_α and K_β part of unfiltered copper radiation using the routine ITR. From [101].*

suppressed. The optimum value of λ is chosen such that the mean square deviation of the fitted curve and the experimental data is minimum. In addition, $\sum_{k=1}^{N-1}(c_{k+1} - c_k)^2$ must show a plateau when plotted as a function of λ. However, when desmearing spectra displaying sharp peaks, it is necessary to stabilize the solution in a different way in peak- and interpeak-regions in order to avoid getting overdamped solutions in the peakregions or oscillations between the peaks. Therefore, the experimental spectrum is funneled using a peak recognition program before using ITR such that all datapoints are used in peak regions, but only few points between the peaks. The number of splines per q-interval is then chosen proportional to the number of datapoints per q-interval. During the desmearing process, the user can adjust the following parameters: The number of data points in

peak- and interpeak-regions, the absolute number of spline functions (N) and the value of the Lagrange parameter. Criteria for a good desmearing are that the peaks in the desmeared spectrum are not steeper on the left peak side than on the right peak side (see the section about solvent-cast samples) and that the approximated curve, $\sum_{k=1}^{N} c_k \psi_k(q)$, fits the experimental data well.

In order to determine the peak positions, q^*, Lorentz-functions were fitted to the desmeared peaks:

$$I(q) = \frac{I_o}{1 + (q - q^*)^2 \xi^2} + B \tag{5.56}$$

where I_o is the peak intensity, ξ the correlation length which is related to the peak width (the half-width at half maximum is $HWHM = 1/\xi$), and B a background. When fitting to smeared spectra (solvent-cast and shear aligned samples), a slanted background was added in some cases:

$$I(q) = \frac{I_o}{1 + (q - q^*)^2 \xi^2} + B + s\,q \tag{5.57}$$

where s is the background slope. The error in determining the peak position is estimated to be ± 1 channel for the broad peaks from disordered samples and ± 0.5 channels for the sharp peaks obtained with ordered samples. The choice of Lorentz-functions is somewhat arbitrary, however, they were found suitable to fit the experimental data. In order to apply the same procedure both in the disordered and in the ordered state, Lorentz-functions were fitted in both regimes. The only parameter used from the fits to SAXS-spectra is the peak position q^*. Peak intensity I_o and correlation length ξ were not used because of the large uncertainty introduced by the desmearing routine. In addition, the spectra from ordered samples were not desmeared for the beam width effect. This leads to values for ξ which are underestimated.

5.4.4 Results

SAXS-results obtained from disordered, annealed, solvent-cast and shear aligned samples will be presented separately first and then the values of the characteristic lengthscale will be compared. The scaling behavior of the characteristic lengthscale with chain length will only be discussed together with the results from SANS.

Disordered samples

Spectra from disordered samples show broad peaks of low intensity (Fig. 5.21). The smaller the chain length, the higher the peak position and the flatter and broader the peaks. This is consistent with the picture of a decreasing amplitude of concentration fluctuations the deeper the samples are in the disordered state. These spectra were desmeared for both beam length and width (Fig. 5.21). The peak position changes significantly upon desmearing and the peaks become sharper. Oscillations were in some cases induced by desmearing on both sides of the peak, probably due to statistical noise in the raw spectra, but the peak regions were nicely resolved. In order to determine the peak positions with better precision, Lorentz-functions were fitted to the peaks in the desmeared spectra. The resulting peak positions are given in Table 5.1. For a discussion of the scaling behavior see Chapter 5.6.

chain length N	sample	preparation method	$q_1^*/\text{Å}^{-1}$	$q_3^*/\text{Å}^{-1}$	q_3^*/q_1^*	$q^*/\text{Å}^{-1}$ value used
156	SBI05B	disordered	6.20×10^{-2}			$(6.20 \pm 0.09) \times 10^{-2}$
236	SBI14B	disordered	4.55×10^{-2}			$(4.55 \pm 0.09) \times 10^{-2}$
310	SBI11C	disordered	3.98×10^{-2}			$(3.98 \pm 0.09) \times 10^{-2}$
374	SBI12F	annealed	3.33×10^{-2}			$(3.33 \pm 0.04) \times 10^{-2}$
	SBI12A	solvent-cast	3.33×10^{-2}			$(3.33 \pm 0.04) \times 10^{-2}$
	SBI12C	shear aligned	3.28×10^{-2}	9.95×10^{-2}(*)	3.0	$(3.32 \pm 0.02) \times 10^{-2}$
383	SBI08F	annealed	3.18×10^{-2}			$(3.18 \pm 0.04) \times 10^{-2}$
	SBI08A	solvent-cast	3.13×10^{-2}			$(3.13 \pm 0.04) \times 10^{-2}$
	SBI08C	shear aligned	3.12×10^{-2}			$(3.12 \pm 0.04) \times 10^{-2}$
921	SBI02F	annealed	1.49×10^{-2}	4.62×10^{-2}(*)	3.1	$(1.54 \pm 0.02) \times 10^{-2}$
	SBI02G	solvent-cast	1.41×10^{-2}	4.43×10^{-2}(*)	3.1	$(1.48 \pm 0.02) \times 10^{-2}$
	SBI02D	shear aligned	1.47×10^{-2}	4.54×10^{-2}(*)	3.1	$(1.51 \pm 0.02) \times 10^{-2}$
1182	SBI15F	annealed	1.33×10^{-2}	4.10×10^{-2}(*)	3.1	$(1.37 \pm 0.02) \times 10^{-2}$
	SBI15A	solvent-cast	1.28×10^{-2}	3.99×10^{-2}(*)	3.1	$(1.33 \pm 0.02) \times 10^{-2}$
	SBI15E	shear aligned	1.30×10^{-2}	4.02×10^{-2}(*)	3.1	$(1.34 \pm 0.02) \times 10^{-2}$
1555	SBI06H	annealed	1.17×10^{-2}	3.58×10^{-2}(*)	3.1	$(1.19 \pm 0.02) \times 10^{-2}$
	SBI06G	solvent-cast	1.18×10^{-2}	3.57×10^{-2}(*)	3.0	$(1.19 \pm 0.02) \times 10^{-2}$
	SBI06A	solvent-cast[a]	1.09×10^{-2}	3.45×10^{-2}	3.2	$(1.15 \pm 0.02) \times 10^{-2}$
	SBI06L	solvent-cast[b]	1.12×10^{-2}	3.45×10^{-2}	3.0	$(1.15 \pm 0.02) \times 10^{-2}$
	SBI06D	shear aligned	1.13×10^{-2}	3.51×10^{-2}(*)	3.1	$(1.17 \pm 0.02) \times 10^{-2}$

Table 5.1: *Peak positions as determined with SAXS at 150°C. If not stated otherwise, samples were solvent-cast from benzene. (a) 0.1% Irganox 1010, (b) solvent-cast from cyclohexane. The errors on q_1^* and q_3^* are estimated to be $0.88 \times 10^{-3}\text{Å}^{-1}$ in the disordered state and $0.44 \times 10^{-3}\text{Å}^{-1}$ in the ordered state. Asterisks mark the data where the third order Bragg peak was used for analysis of the scaling behavior. The q^*-values used (either q_1^* or $q_3^*/3$) for determination of the lamellar thickness ($D = 2\pi/q^*$) are given in the last column.*

In order to obtain an estimate of the average statistical segment length of polystyrene-polybutadiene and to see if the peak position obtained is different from the one determined by fitting a Lorentz-function, a Leibler structure factor (Eq. 5.12) was fitted to the peaks of the three disordered samples. The amplitude of the structure factor was adjusted by multiplication with a factor and by adding a constant background. The fits are shown in Fig. 5.22. At 150°C, the Flory-Huggins segment-segment interaction parameter, as determined from the ODT temperatures (Chapter 3), has the value $\chi = 0.033 \pm 0.007$ (Eq. 3.10). Keeping the interaction parameter fixed at $\chi = 0.033$ gave poor agreement, especially with the two samples with lowest molar mass. Releasing χ, gave satisfactory results provided the fitting range was kept narrow. The resulting χ-values deviate significantly from $\chi = 0.033 \pm 0.007$ which probably is due to distorsions in peak shape arising during desmearing. The peak positions determined using the Kratky-camera are assumed to be correct because we obtained very similar values using a Huxley-Holmes camera (Appendix D) and in SANS-experiments. Another reason for the disparity might be the polydispersity in chain length and composition which has not been taken into account in

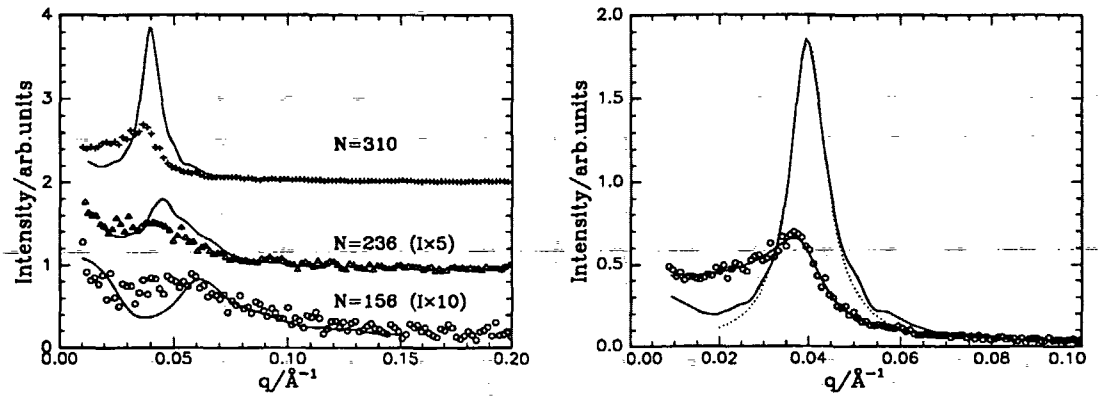

Figure 5.21: *Left figure: SAXS-spectra from SBI05B (○), SBI14B (△) and SBI11C (+) at 150°C. For clarity, only every second point is shown. The intensities of the spectra from SBI05B and of SBI14B where multiplied by a factor of 10 and 5, respectively. The intensities were shifted. Full lines are the desmeared curves. Right figure: Spectrum from SBI11C (○) together with the desmeared and approximated curve (full lines). The dotted line is the fit of a Lorentz-curve to the desmeared spectrum.*

N	sample	fitting range/Å^{-1}	χ	R_g/Å	a/Å	q^*/Å^{-1}
156	SBI05B	0.040 – 0.080	0.0603 ± 0.0002	31.54 ± 0.07	6.2	0.0617
236	SBI14B	0.035 – 0.050	0.0412 ± 0.0001	43.37 ± 0.08	6.9	0.0449
310	SBI11C	0.032 – 0.047	0.0331 ± 0.0001	49.01 ± 0.03	6.8	0.0397

Table 5.2: *Fitting parameters obtained from fitting a Leibler structure factor to SAXS-spectra from disordered samples measured at 150°C. χ denotes the Flory-Huggins segment-segment interaction parameter, R_g the radius of gyration, a the average segment length derived from $R_g = a\sqrt{N/6}$. q^* is the maximum position of the fitted function. χ and R_g are fitting parameters.*

the Leibler structure factor. Polydispersity in chain length has been shown to change the peak shape and position [92]. We have not attempted to include the polydispersity because the peak shape of desmeared spectra is not well-determined. The fitting parameters obtained with χ as a free fitting parameter are compiled in Table 5.2. The average segment length, a, as estimated from $R_g = a\sqrt{N/6}$ [6],[9] takes values between 6 and 7 Å which is consistent with the values of 6.9 Å [76] and 6.6 – 7.2 Å [77, 103] reported for polybutadiene and polystyrene, resp. The peak positions obtained from the fitted structure factor, q^*, agree with those obtained from fitting Lorentz-functions (Table 5.1) within 2%. In the following, we will use the peak positions as determined fitting Lorentz-functions.

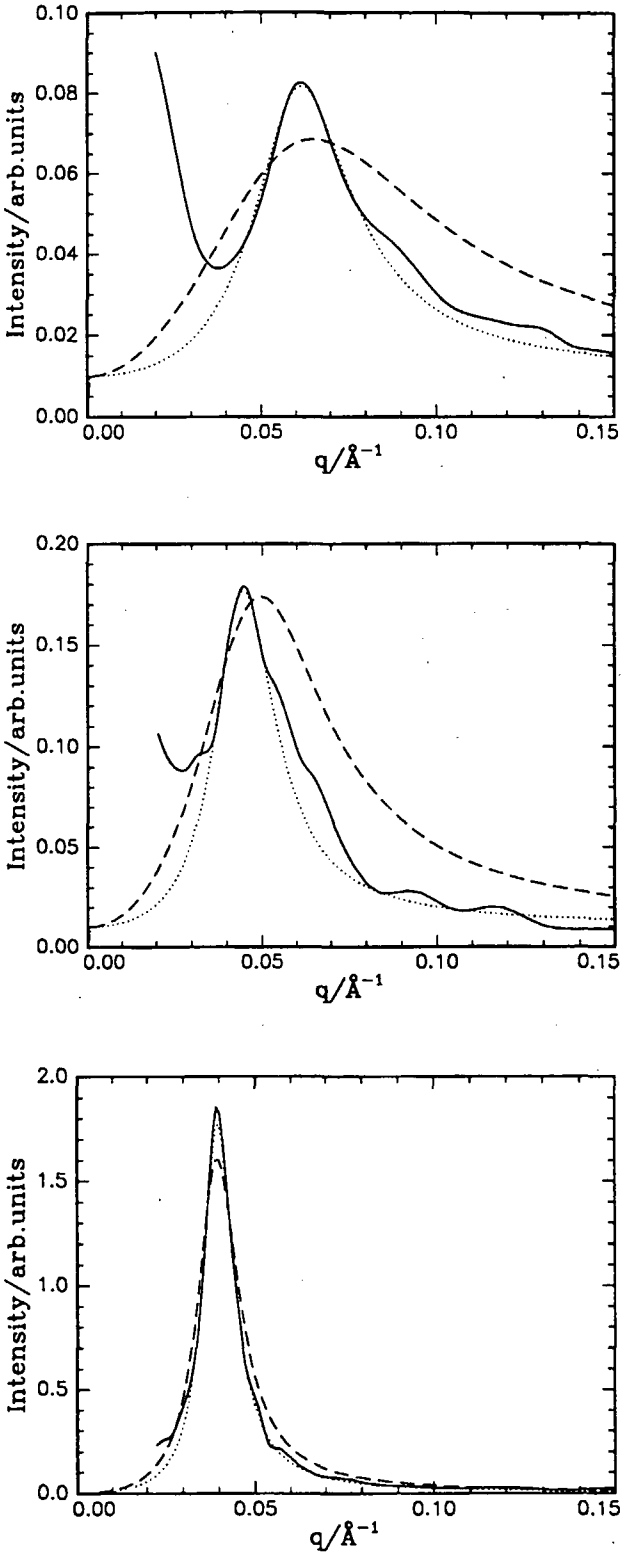

Figure 5.22: *Desmeared SAXS-spectra from disordered samples at 150°C together with fits of the Leibler stucture factor. Upper figure: SBI05B, middle figure: SBI14B, lower figure: SBI11C. Full lines: desmeared spectra, broken lines: fits keeping $\chi = 0.0325$ fixed, dotted lines: fits with χ being a free fitting parameter.*

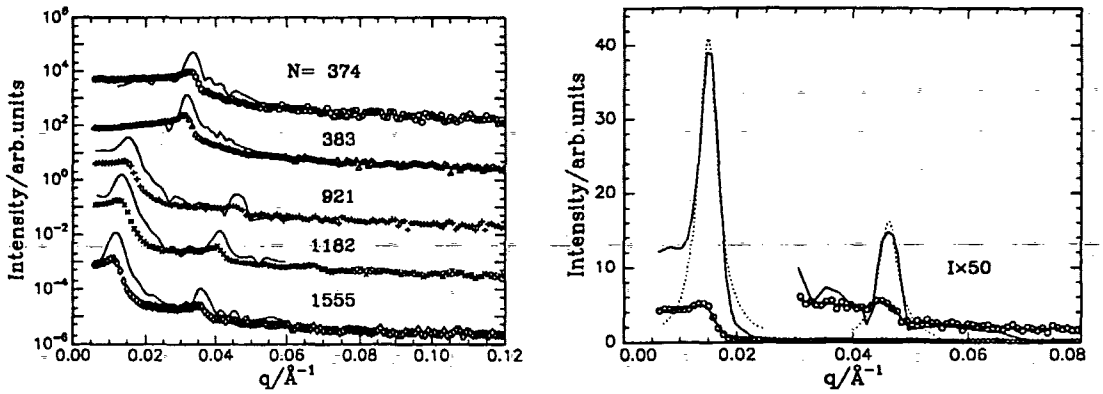

Figure 5.23: *Left figure: SAXS-spectra from annealed samples at 150°C. (○) SBI12F, (△) SBI08F, (+) SBI02F, (×) SBI15F, (◇) SBI06H. Lines are the desmeared spectra. For clarity, the curves were shifted by two decades. Right figure: Spectrum from SBI02F (annealed) at 150°C. Shown are the experimental data (○), the approximated and the desmeared curve (full lines) and the fit of a Lorentz-function to the desmeared curve (dotted line). Intensities for $q > 0.03$ Å^{-1} are multiplied with a factor of 50 to reveal the third order Bragg peak.*

Annealed samples

Spectra from annealed samples measured in 'through'-direction are shown in Fig. 5.23. They display Bragg peaks due to the lamellar structure. The peak positions depend on chain length. The larger the chain length the more Bragg peaks are seen. This reflects the fact that, close to the ODT, the density profile is close to sinusoidal, whereas it is close to rectangular in the strong-segregation limit. As model calculations show (Chapter 5.3), only the first order Bragg peak is non-vanishing in spectra from samples having a sinusoidal profile. For profiles with sharp interfaces, higher order Bragg peaks are observed. Fig. 5.23 shows that samples with higher molar masses than SBI06 are difficult to study using the Kratky-camera because the first order peak is very close to the filter edge. The peaks in spectra from annealed samples (Fig. 5.23) are observed to be steeper on the high q-side than on the low q-side. This is attributed to the fact that the samples are polycrystalline and therefore give rise to diffraction rings, which are subject to lengthsmearing (Fig. 5.19). In SANS-experiments, spectra from annealed samples are also observed to be isotropic (Fig. 5.33). Desmearing of the SAXS-spectra for the beam length effect results in sharp peaks (Fig. 5.23) which are comparable in width with the direct beam (Fig. 5.16). Simultaneous width desmearing gave numerical problems which is why it was not performed. In addition, width smearing does not change the peak positions as is the case with length smearing. Lorentz-functions were fitted to the peaks in order to determine the peak positions (Fig. 5.23, right figure). The resulting peak positions are given in Table 5.1. It was observed that desmearing for the beam length effect shifted the peak positions of the first order peaks by $3 - 9$ % to higher values. The positions of the third order peaks did not change to the same extent during desmearing, only by $1 - 3$ %, which is attributed to the observation that the effect of beam length smearing

[9]Here, Gaussian chain conformation has been assumed.

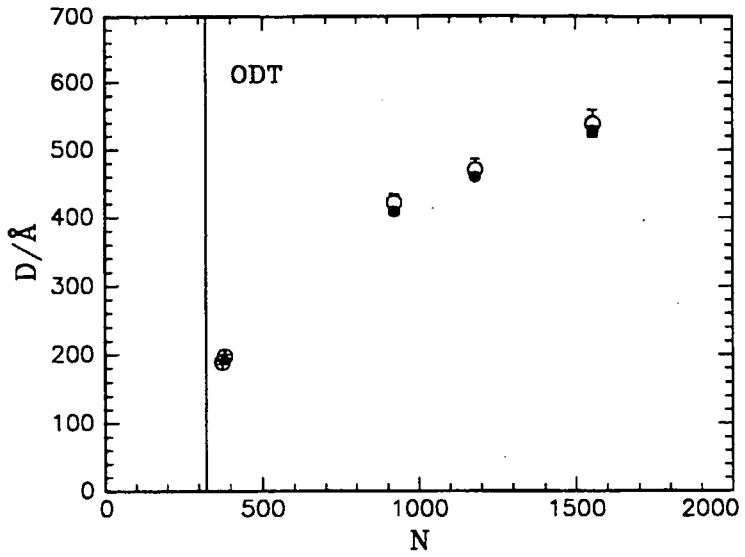

Figure 5.24: *Lamellar thickness of annealed samples as a function of chain length. The values were determined in SAXS-experiments at 150°C The vertical line indicates the ODT. (○) $D = 2\pi/q_1^*$, (●) $D = 3 \times 2\pi/q_3^*$. The errorbars correspond to ±0.5 channels.*

decreases with increasing scattering vector [104]. The ratio q_3^*/q_1^* which should equal 3.0 for a lamellar structure was 3.06 – 3.10 after desmearing. The influence of this slight difference on the scaling behavior can be seen in Fig. 5.24. The lamellar thickness calculated from $D = 2\pi/(q_3^*/3)$ is slightly smaller than $D = 2\pi/q_1^*$ but the values are still within the errorbars. In the following analysis we will use the lamellar thickness determined from q_3^* if third order peaks exist, because the relative errors on q_3^* are smaller than the ones on q_1^*. Assuming an error of ±0.5 channels, which corresponds to $\pm 0.44 \times 10^{-3}$Å, the errors on q_1^* were typically 1 – 4 %, whereas the errors on q_3^* only were 1 – 2 %. In Table 5.1, samples where the third order Bragg peak was used for further analysis, are marked with an asterisk .

Solvent-cast samples

Solvent-cast samples were expected to have the lamellar interfaces oriented parallel to the film surface. Spectra from samples solvent-cast from benzene and measured 'edge on' are shown in Fig. 5.25. The number of peaks which can be discerned from the background increases with chain length indicating the change of density profile from being close to sinusoidal in the vicinity of the ODT to being close to rectangular in the strong-segregation limit. Spectra from SBI08A, SBI02G and SBI15A display nearly symmetric peaks. This means that the smearing effect due to the length effect is weak (Fig. 5.19). Therefore, the samples are assumed to be macroscopically oriented. The peaks in the spectra from SBI12A and SBI06G look asymmetric. This is attributed to the fact that the samples were 'polycrystalline' like the annealed samples. Therefore, an attempt was made to desmear these spectra for the beam length effect. This could satisfactorily be done for SBI06G and the desmeared spectrum was used for the determination of the peak position. For

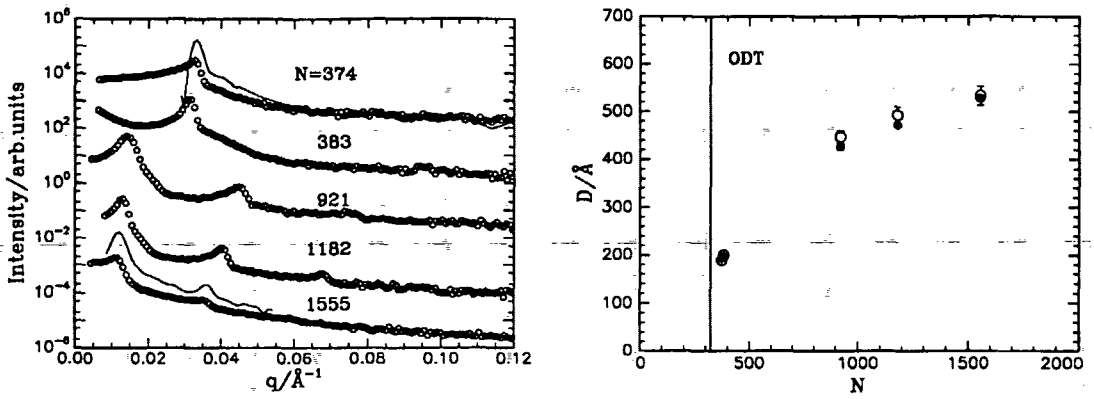

Figure 5.25: *Left figure: SAXS-spectra from samples solvent-cast from benzene and measured at 150°C. From above: SBI12A, SBI08A, SBI02G, SBI15A, and SBI06G. All spectra were measured in the 'edge on' direction. Lines are spectra desmeared for the length effect. For clarity, the spectra were shifted by two decades. Right figure: Lamellar thickness of samples solvent-cast from benzene as a function of chain length. The values were obtained in SAXS-experiments at 150°C. The vertical line indicates the ODT. (○) $D = 2\pi/q_1^*$, (●) $D = 3 \times 2\pi/q_3^*$. The errorbars correspond to ±0.5 channels.*

SBI12A, the result was less satisfactory: The desmeared spectrum is extremely steep on the left side of the peak. This effect is attributed to the fact that the scattering is not completely isotropic. The lamellae are probably not oriented perfectly, but there is some texture in the sample. In SANS-experiments (Fig. 5.33), solvent-cast samples gave rise to spectra containing diffraction peaks on top of a diffraction ring. It is not straightforward to desmear SAXS-spectra from partially oriented samples. Therefore, the smeared spectra were used for determining the peak position for all samples except SBI06G. As the background rises smoothly towards low q-values (Fig. 5.28), the expression given in Eq. 5.57 was fitted to the peaks. This background scattering is observed even though the background spectrum was subtracted as described in the data analysis section (Fig. 5.17). An alternative way of treating the spectra would have been to subtract the remaining background from the spectra. The origin of the remaining background is still unclear. It might be due to voids or to scattering from lamellar domains.

The values of the lamellar thickness obtained from first order and third order Bragg peaks are shown and in Fig. 5.25. They are observed to be very similar. For the peak positions see Table 5.1. Those samples are marked with an asterisk, where the third order Bragg peaks are used for further analysis. The peak positions determined as described above coincide nicely with the peak positions from SANS (Chapter 5.5).

In order to establish if solvent selectivity has an influence on the obtained structure, one sample (SBI06L) was solvent-cast from cyclohexane instead of benzene. At room temperature, cyclohexane is a marginal solvent for polystyrene (the Θ-temperature is 35°C) but a good solvent for polybutadiene whereas benzene is nearly equally good for both blocks. As can be seen from Fig. 5.26 and Table 5.1, no significant difference in structure between sample SBI06G (solvent-cast from benzene) and SBI06L is observed. The ratio of peak positions of sample SBI06L is $q_5^* : q_3^* : q_1^* = 5.3 : 3.1 : 1$ which indicates

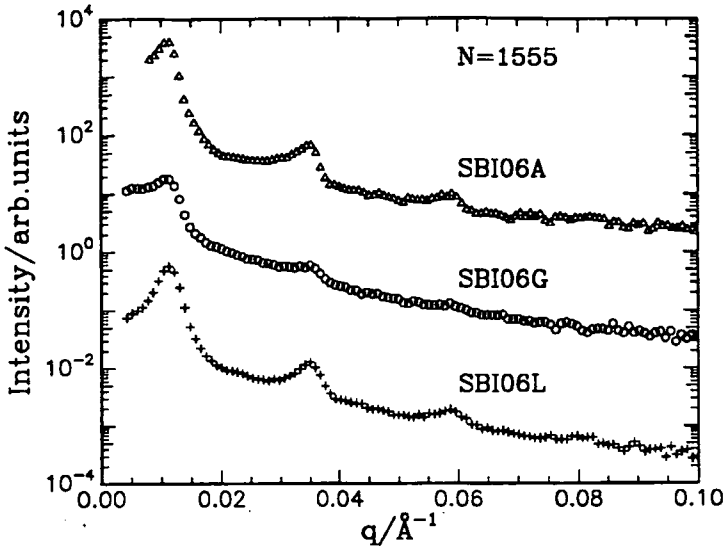

Figure 5.26: *SAXS-spectra from sample SBI06 at 150°C: (o) SBI06G, 0.5 wt-% Irganox, $p = 1.13$, solvent-cast from benzene, (△) SBI06A, 0.1 wt-% Irganox, $p = 1.22$, solvent-cast from benzene, (+) SBI06L, 0.5 wt-% Irganox, $p = 1.12$, solvent-cast from cyclohexane. All spectra were measured in the 'edge on' direction. For clarity, the intensities were shifted by two decades.*

that a lamellar structure was formed. The deviation from the ratio 5 : 3 : 1 is attributed to a residual beam length smearing effect. The peak positions of SBI06G ($q_1^* = 0.0118$ Å^{-1}) and SBI06L ($q_1^* = 0.0112$ Å^{-1}) differ by 5%. The spectra from SBI06G differs from the two other spectra shown in Fig. 5.26 at low q: The spectrum from SBI06G rises towards low q and the peaks are relatively asymmetric. It seems that the sample is not very well aligned and that lamellar domains persist which give rise to enhanced scattering at low q. The peaks in the spectra from SBI06A and SBI06L are close to symmetric which indicates good alignment. In these spectra, the intensity decreases towards low q which indicates that the domains are very large. Scattering from very large domains would be expected at very low q which cannot be resolved. We conclude that sample SBI06G is not as well aligned as the two other samples. A reason might be that, during solvent-casting, the film thickness of sample SBI06G was higher than the film thickness of the other samples.

The effect of crosslinking was studied using a sample (SBI06A) prepared in the same way as SBI06G (solvent-cast from benzene) but containing less antioxidant (only 0.1 wt-%). The polydispersity of SBI06A was $\bar{M}_W/\bar{M}_N = 1.22$, thus larger than the value obtained with SBI06G ($\bar{M}_W/\bar{M}_N = 1.13$) (Fig. 4.9 and Table 4.2) which means that the degree of crosslinking in SBI06A is higher than in SBI06G. The ratio of peak positions is $q_5^* : q_3^* : q_1^* = 5.4 : 3.2 : 1$. The reason for the deviation from the ration 5 : 3 : 1 might be a residual smearing effect. The values of the lamellar thickness as derived from the first order peaks differ by 8%, sample SBI06A having a larger lamellar thickness than SBI06G. It should be noted that the difference in peak positions corresponds to only one channel which is at the limit of detection. The positions of the third order Bragg peaks which are determined more precisely, differ only by 3% or 1.5 channels. It can thus not be resolved

unambiguously if a slight change in the degree of crosslinking, as is the case here, has an effect on the lamellar thickness. If so, then an explanation might be that crosslinking happens while the chains are still swollen, and that therefore the lamellar thickness is higher than in equilibrium.

Shear aligned samples

Spectra from shear-aligned samples were measured with the sample mounted in two different ways as explained above (Fig. 5.15). In this way, information is gained about the direction of lamellar orientation. Fig. 5.27 shows that spectra measured in 'edge on' direction display more pronounced and more symmetric peaks than spectra measured in 'through' direction which is interpreted to mean that all samples showed the parallel orientation (Fig. 4.3a). As with annealed and solvent-cast samples, the number of peaks observed in the 'edge on' direction increases with chain length from two to four peaks (corresponding to seventh order!). This means that the profile changes from being close to sinusoidal in the vicinity of the ODT to being more rectangular deeper in the ordered state. In 'through' direction, peaks were observed which resembled spectra from annealed samples in what concerns peak shape. This was interpreted as being due to unoriented lamellar domains. Scattering in the 'edge on' direction is mainly affected by beam width smearing. As the peaks were as narrow as the direct beam we used the smeared 'edge on' spectra for determination of the peak positions by fitting Lorentz-functions. As with solvent-cast samples, the expression from Eq. 5.57 was fitted to spectra with asymmetric peaks (Fig. 5.28). The results are given in Table 5.1.

The lamellar thickness of shear aligned samples as a function of chain length is shown in Fig. 5.29. Again, slight differences ($3-4$ %) between values derived from first and third order Bragg peaks are observed. For the reasons cited above, third order peaks were used if existing.

Results

In order to establish whether the lamellar thickness is dependent on the preparation method, data from the ordered state were plotted together in Fig. 5.30. No significant difference in lamellar thickness according to the preparation method is found, indicating that the samples prepared are in thermal equlibrium. The values are equal within 4 %. No difference between a sample solvent-cast from benzene and one solvent-cast from cyclohexane is observed. Only sample SBI06A which has a slightly higher degree of crosslinking is found to have a slightly higher lamellar thickness than the other samples with the same chain length. The data from this sample as well as the data from SBI06L (solvent-cast from cyclohexane) were not used for further analysis. The scaling behavior of the characteristic lengthscale will be established after the analysis of data from high molar-mass samples which were studied using SANS.

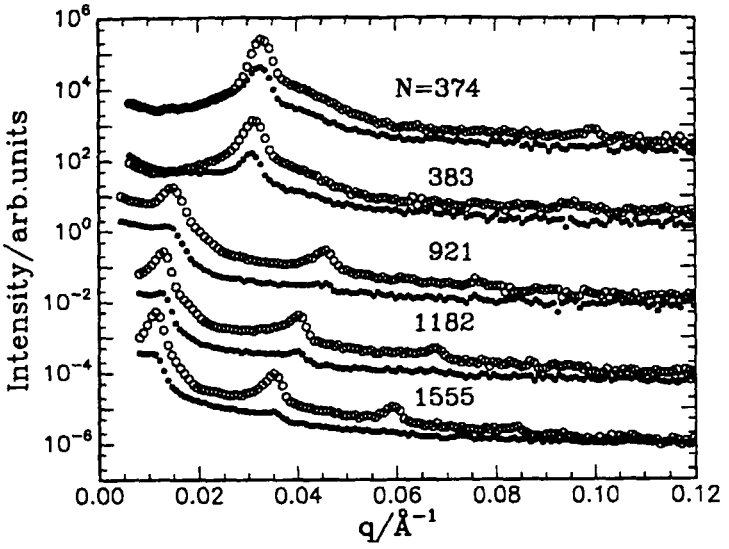

Figure 5.27: *SAXS-spectra from shear aligned samples at 150°C. From above: SBI12C, SBI08C, SBI02D, SBI15E, and SBI06D. (○) measured in the 'edge on' direction, (●) measured in the 'through' direction. For clarity, the spectra were shifted by arbitrary amounts.*

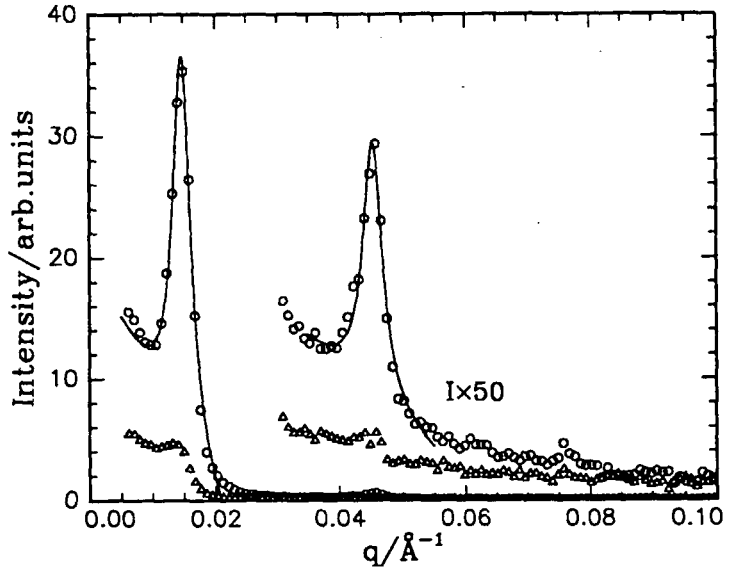

Figure 5.28: *SAXS-spectra from sample SBI02D at 150°C. The beam is parallel (○) or perpendicular (△) to the shear plane. The sharp peaks in parallel direction and the weak peaks in perpendicular direction show that the sample is oriented. Intensities for $q > 0.03$ Å^{-1} were multiplied with a factor of 50 in order to reveal the third order Bragg peak. Lines are fits of Lorentz-functions on a slanted background to the peaks.*

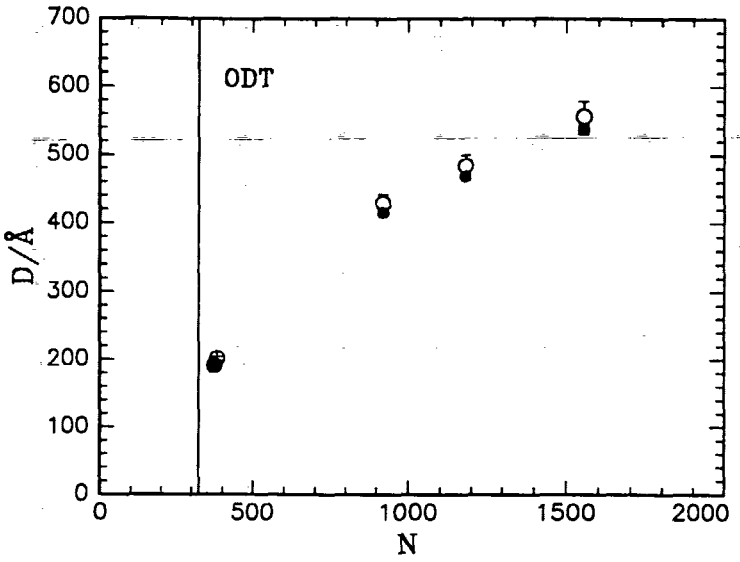

Figure 5.29: *Lamellar thickness of shear aligned samples as a function of chain length. The values were obtained in SAXS-experiments at 150°C. The vertical line indicates the ODT. (○) $D = 2\pi/q_1^*$, (●) $D = 3 \times 2\pi/q_3^*$. The errorbars correspond to ±0.5 channels.*

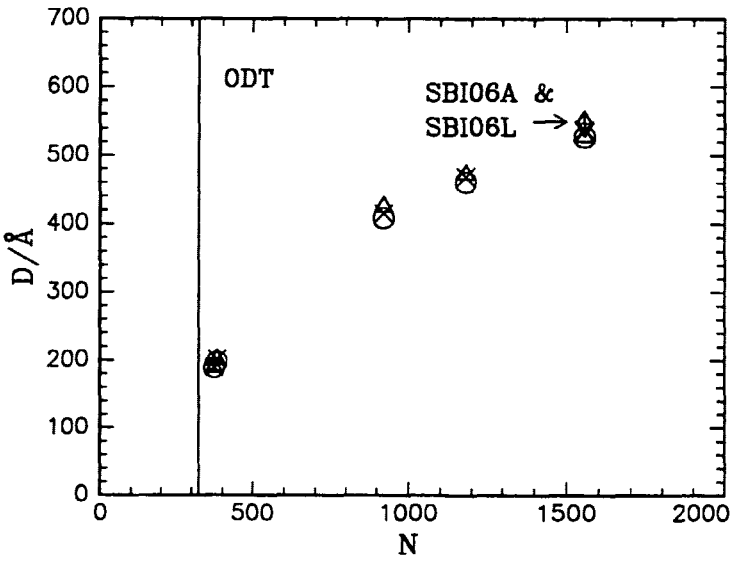

Figure 5.30: *Lamellar thickness of ordered samples as a function of chain length. The values were determined using SAXS at 150°C. The vertical line represents the ODT. (○) annealed, (△) solvent-cast from benzene, (×) shear aligned, (+) SBI06L (solvent-cast from cyclohexane), (◇) SBI06A (0.1% Irganox, solvent-cast from benzene).*

5.5 Small-angle neutron scattering

(The SANS-study was carried out in collaboration with Dorthe Posselt, IMFUFA, and Kristoffer Almdal and Kell Mortensen, Risø National Laboratory.)

Small-angle neutron scattering (SANS) experiments were carried out in order to determine the peak positions of high molar-mass samples. Using the Kratky-camera, the precise determination of the first-order Bragg peaks from these samples was difficult because they were at the lower limit of the q-range of the Kratky-camera. In first test experiments, it turned out that the polystyrene-polybutadiene samples had reasonable neutron contrast even though they were not deuterated. The peak positions of high molar-mass samples were determined in small-angle neutron scattering experiments at Risø National Laboratory. This instrument has a pinhole geometry and a two-dimensional detector. Using large wavelengths and large sample detector distances, measurements at small q-values were carried out and the peak positions of high molar-mass samples could be determined. The degree of orientation of oriented (solvent-cast and shear aligned) samples was estimated. From the peak width, the domain sizes were estimated. Using the results from the model calculations presented in Chapter 5.3, the average number of lamellae per domain could be estimated. In the following, the instrument, the experiment and the way of analyzing the spectra will be presented. The results will be discussed for disordered, annealed, solvent-cast and shear aligned samples separately. Then, the characteristic lengthscales obtained from the different methods will be compared.

5.5.1 The instrument

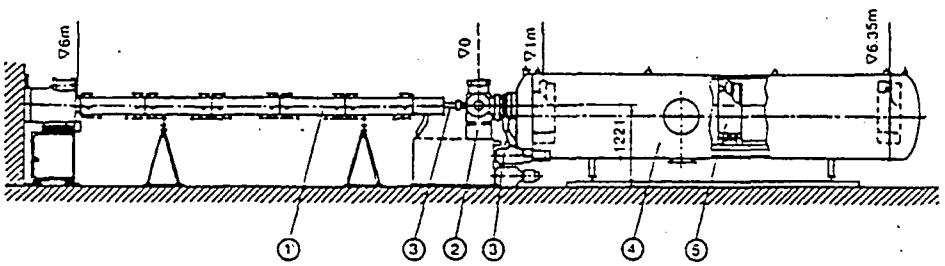

Figure 5.31: *Layout of the Risø SANS instrument. (1) collimator, (2) sample chamber, (3) valves/windows, (4) detector tank, (5) area sensitive detector. From [105], original from [106].*

The SANS facility at Risø (Fig. 5.31) is a variable instrument which is described in detail in [84]. The overall length is 12 m; both the collimation section and the sample-detector distance can be varied between 1 and 6 m. Wavelengths in a range of $2 - 20$ Å can be selected using a mechanical velocity selector, consisting of a rotating drum with helical blades of a neutron absorbing material. The spread of the wavelength can be set to values between 9 and 20%. Collimation of the beam can be performed over a distance of $1 - 6$ m. The source point is defined at the position of the source aperture (diameter 16 mm).

The sample chamber is very flexible. In our case, an oven specially designed for polymer studies was installed (see below). The detector is an area sensitive multiwire detector and can be installed at distances from the sample of $1 - 6$ m. The detector has a diameter of 60 cm, and the q-range is $0.002 - 0.55$ Å^{-1}. The positional information is divided into 128×128 pixels which gives a pixel size of ca. 7 mm. Both the collimation section and the detector tank are evacuated whereas the sample chamber was at ambient pressure during our experiments. The operation of the instrument and data acquisition is computer controlled via a dedicated micro VAX.

5.5.2 The experiment

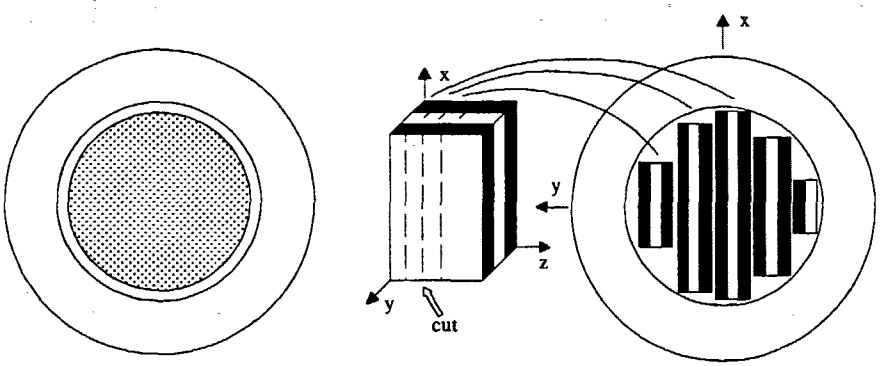

Figure 5.32: *The way of mounting isotropic (left) and anisotropic samples (right). The beam is perpendicular to the plane of paper.*

Polystyrene-polybutadiene samples were mounted in holders made of brass rings (thickness 1.5 mm, inner diameter 11.5 mm, outer diameter 25.5 mm) onto which aluminum foil (heavy duty) was glued using epoxy resin. The samples were mounted in two different ways (Fig. 5.32): Isotropic samples (disordered or annealed) were mounted such that the beam impinged perpendicular on the pill surface. Anisotropic samples (solvent-cast or shear aligned) were mounted such that the beam passed parallel to the pill surface The samples were mounted in this way, because, using SAXS, the lamellar orientation was found to be parallel to the pill surfaces (Fig. 4.3a). The orientation in the beam was such that peaks were expected on the left and right side of the direct beam (on the detector). In order to mount a reasonable amount of sample in the beam, stripes were cut from the pills and were stacked. In this way, the brass rings were 'filled' as good as possible. In order to minimize the risk of crosslinking during the measurements, the holders were thoroughly flushed with nitrogen before sealing. (Measurements were carried out at high temperatures.) The brass holders were mounted in an oven made from copper and heated by two heating wires. The temperature was measured very close to the sample by means of a thermocouple. In order to optimize the temperature stability, a shielding, which was heated to the same temperature as the oven, was mounted around the oven. The temperature regulation was computer-controlled. The beam passed through aluminum windows in the shielding and the oven. Two pinholes were mounted: one having a diameter of 10 mm at the end of the collimation section and one having a diameter of 7 mm right behind the sample. The latter one determines the smearing effect due to the beam size

(see below). In order to determine peak positions of high molar-mass samples as precisely as possible, the largest possible sample-detector distance (6 m) was chosen together with large wavelengths (14.8 and 7.67 Å) and the smallest possible wavelength spread (9%). For the lower molar-mass samples, a sample-detector distance of 3 m was used together with a wavelength of 5.58 Å. The settings were chosen such that the first-order Bragg peaks were approximately in the middle of the q-range. In contrast to the SAXS-experiments (Chapter 5.4), the q-range chosen in the SANS-experiments did not allow detection of higher order peaks. The settings used together with the q-range obtained are summarized in Table 5.3. Measuring times were between 1 hour at $\lambda = 14.8$ Å, where the neutron flux is low, and few minutes at $\lambda = 5.58$ Å.

Background measurements were made using an empty sample holder. Furthermore, spectra with boronated plastic at the sample position were recorded to estimate the detector dark current background. ^{11}B has a high neutron absorbing cross section and a piece of boronated plastic at the sample position prevents the beam from passing on directly to the detector. The transmission of the samples was measured by damping the beam with a Cd-plate with small holes in front of the collimation section. The beamstop was removed, and the integrated intensity over a small area ($\sim 10 \times 10$ pixels) was taken as a measure of the transmission.

samples	setting	q-range [Å^{-1}]
SBI10G, 10H, 10K SBI07G, 07H, 07K, 07L SBI06H	6m/6m/14.8Å	0.003 – 0.02
SBI06A, 06D, 06G, 06H, 06L SBI15A, 15E, 15F SBI02D, 02F, 02G SBI08A	6m/6m/7.67Å	0.006 – 0.38
SBI08A, 08F SBI12A, 12F SBI11C	3m/3m/5.58Å	0.05 – 0.10

Table 5.3: *Settings used for SANS measurements: collimation length, sample-detector distance, wavelength ($\Delta\lambda/\lambda = 0.09$) and the q-range obtained.*

Fig. 5.33 shows typical spectra displaying first-order diffraction peaks or rings. Spectra from annealed samples were typically isotropic (except for the highest molar-mass sample, SBI10H, which is attributed to mechanical stresses in the sample), whereas spectra from solvent-cast samples showed some degree of orientation, *i.e.* two peaks on top of a ring. The peaks are due to oriented lamellar grains whereas the ring arises from unoriented material. Spectra from shear aligned samples show typically two peaks which are curved. This curving has been attributed to texture of the lamellar grains [22].

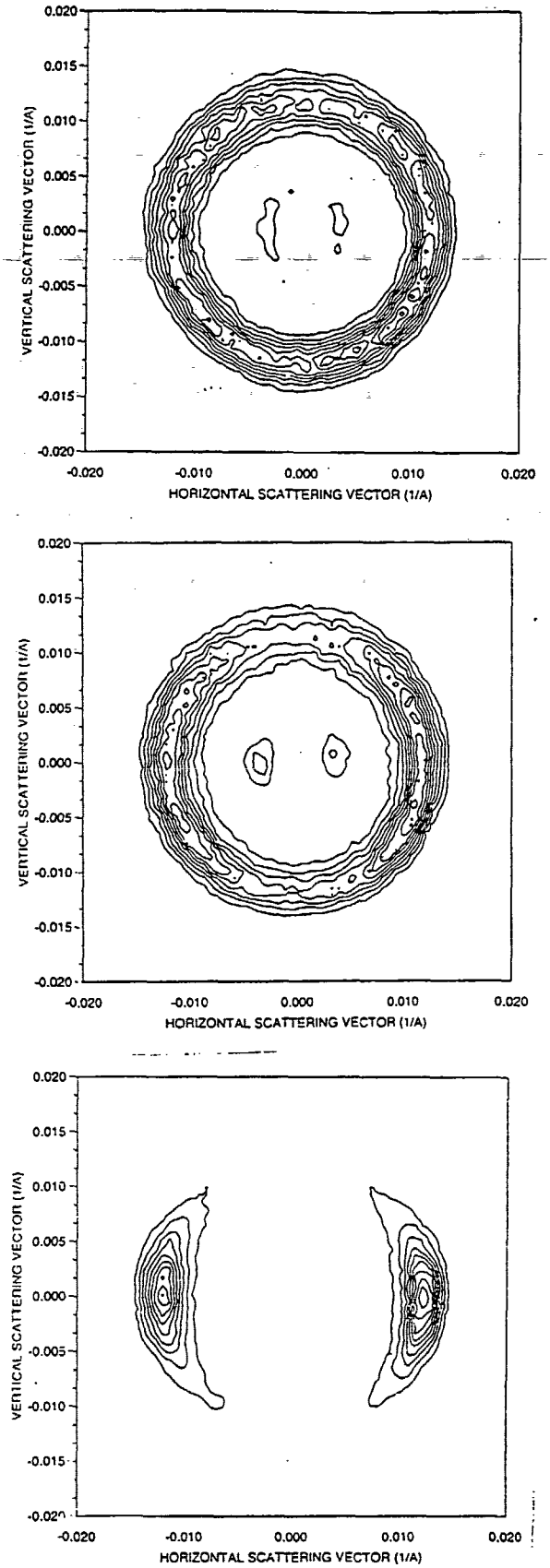

Figure 5.33: *Two-dimensional SANS-spectra from an annealed (SBI06H), a solvent-cast (SBI06A) and a shear aligned sample (SBI06D). The isointensity lines are spaced linearly.*

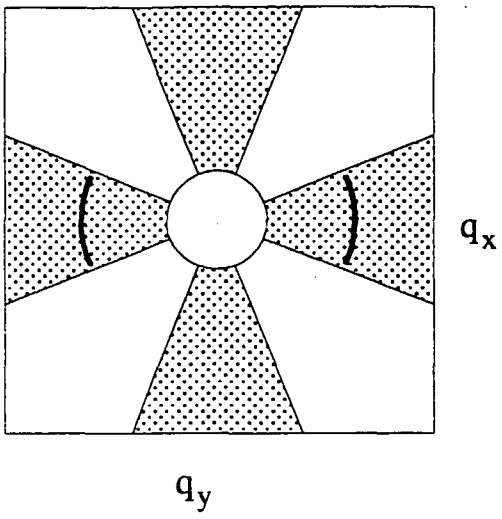

Figure 5.34: *Sector masks used for analysis of spectra from solvent-cast and shear aligned samples. The opening angle is 30°. The arcs indicate the diffraction peaks. The circle in the middle indicates the beamstop which also is masked.*

5.5.3 Data Analysis

Data analysis was performed using standard Risø SANS software [107]. Raw spectra were normalized to incoming beam flux. Spectra from isotropic (disordered and annealed) samples were azimuthally averaged with the beamstop masked away. Anisotropic spectra (from solvent-cast and shear aligned samples) were averaged using horizontal and vertical sector masks with an opening angle of 30° (Fig. 5.34). Sectors having this angle covered the regions of the peaks where the intensity was high (in horizontal direction). Due to slight misalignment of the samples, the peaks did not always lie exactly on a horizontal line. Therefore, the sector masks were aligned such that the centerline passed through the pixels having maximum intensity. The vertical sector mask was chosen perpendicular to the horizontal mask. Background spectra treated in the same way were subtracted from azimuthally averaged sample spectra:

$$I_s^{cor} = \frac{I_s}{M_s} - \frac{T_s}{T_b}\frac{I_b}{M_b} - \left(1 - \frac{T_s}{T_b}\right)\frac{I_{bpl}}{M_{bpl}} \tag{5.58}$$

where the indices s, b, and bpl stand for sample, background, and boronated plastic. I is the measured intensity, T the transmission and M a measure of the incoming beam flux. In contrast to the SAXS-spectra described in Chapter 5.4, the SANS-spectra were not desmeared, but a model function was smeared according to the beam size effect and the wavelength distribution, and this smeared function was fitted to the data. For a description of the smearing routine see [107]. This combined smearing and fitting was performed using standard Risø software. The following parameters were used for smearing: the collimation length and the sample-detector distance (both given in Table 5.3), the radius of the pinhole at the entrance of the collimation section, 8 mm, the radius of the pinhole at the sample position, 3.5 mm, and the width of the wavelength distribution, $\Delta\lambda/\lambda = 0.09$. We chose to use Lorentz-functions (Eq. 5.56) which were smeared and fitted

to the peaks. The peak positions, q^*, were found to be nearly uncorrelated with the other fitting parameters and nearly independent of the fitting range. The errors in determining peak positions were estimated to be half the pixel size. In order to estimate the internal calibration of the instrument, two samples were measured at two of the settings used: SBI08A was measured at 6m/6m/7.67Å and 3m/3m/5.58Å and SBI06H at 6m/6m/7.67Å and 6m/6m/14.8Å. In both cases, the peak position changed with 3% when changing setting (see Table 5.4). However, as the values are equal within the errors, no adjustment of peak positions measured with different settings was made. Even though the incoherent background was not subtracted, the background scattering was found to be negliglible compared to the peak height. When fitting Lorentz-functions to the peaks, the background B was set to zero in most cases.

5.5.4 Results

Disordered and annealed samples

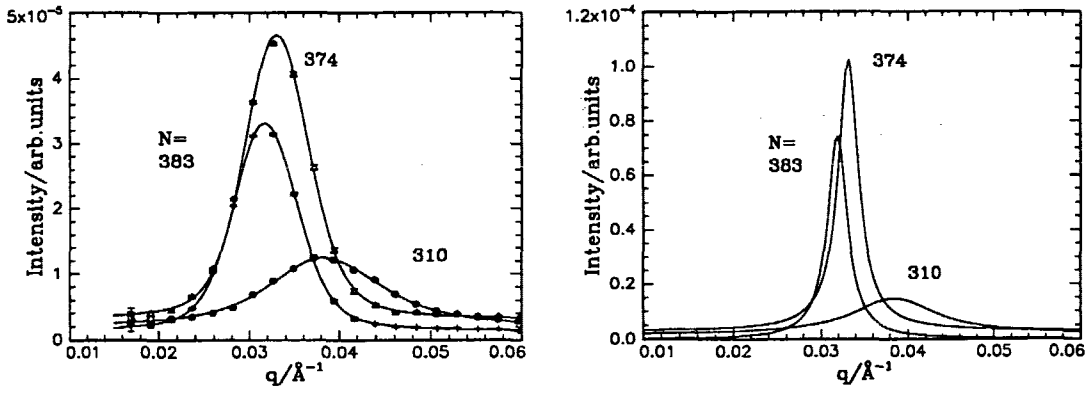

Figure 5.35: *Azimuthally averaged SANS-spectra from low molar-mass disordered and annealed samples measured at 150 °C together with fits of smeared Lorentz-functions (left figure). From left to right: SBI08F, SBI12F, and SBI11C. The spectra were measured with different settings (Table 5.3). The corresponding Lorentz-functions are shown in the right figure.*

As described above, spectra from disordered and from annealed samples were centrosymmetric and therefore averaged azimuthally, only the beamstop being masked away. The results from fits using azimuthally averaged spectra are summarized in Table 5.4. Experimental data with fits of smeared Lorentz-functions together with the Lorentz-functions are shown in Fig. 5.35 and 5.36.

In principle, spectra from 'polycrystalline' samples should be multiplied with the Lorentz-factor for polycrystalline samples [89]. This was not done in the present analysis. Normally, the procedure is as follows [89]: The background, if existing, is subtracted from the azimuthally averaged and desmeared intensity, I_p. The such obtained spectrum is multiplied by $4\pi q^2$ in order to get the single-crystal intensity, I_s:

$$I_s(q) = 4\pi q^2 I_p(q) \tag{5.59}$$

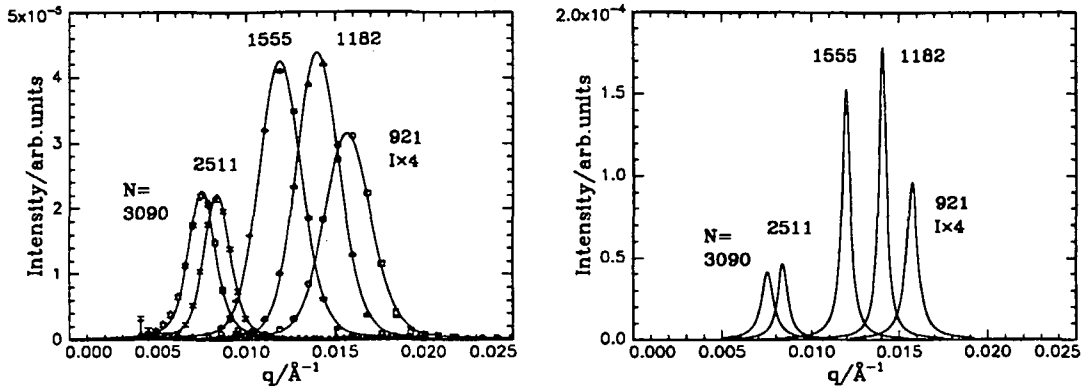

Figure 5.36: *Azimuthally averaged SANS-spectra from high molar-mass annealed samples measured at 150 °C together with fits of smeared Lorentz-functions (left figure). From left to right: SBI10H, SBI07H, SBI06H, SBI15F, and SBI02F. The spectra were measured with different settings (Table 5.3). The corresponding Lorentz-functions are shown in the right figure.*

sample	N	setting	$q^*/\text{Å}^{-1}$	$\xi/\text{Å}$	N_s
SBI11C	310	(a)	$(3.85 \pm 0.11)10^{-2}$	180 ± 10	
SBI12F	374	(a)	$(3.32 \pm 0.11)10^{-2}$	690 ± 30	10 ± 1
SBI08F	383	(a)	$(3.19 \pm 0.11)10^{-2}$	730 ± 30	10 ± 1
SBI02F	921	(b)	$(1.57 \pm 0.04)10^{-2}$	2680 ± 350	19 ± 3
SBI15F	1182	(b)	$(1.41 \pm 0.04)10^{-2}$	3940 ± 660	25 ± 4
SBI06H	1555	(b)	$(1.20 \pm 0.04)10^{-2}$	3500 ± 420	19 ± 2
		(c)	$(1.24 \pm 0.02)10^{-2}$	3270 ± 220	18 ± 1
SBI07H	2511	(c)	$(8.39 \pm 0.22)10^{-3}$	2990 ± 230	11 ± 1
SBI10H	3090	(c)	$(7.53 \pm 0.22)10^{-3}$	2440 ± 240	8 ± 1

Table 5.4: *Fit parameters of disordered and annealed samples at 150°C. The data were obtained from azimuthal averaging Given are the setting (collimator length, sample detector distance, wavelength), the peak positions, q^*, the peak intensities, I, the correlation lengths, ξ, and the average number of lamellae per stack, N_s. (a) 3m/3m/5.58Å, (b) 6m/6m/7.67Å, (c) 6m/6m/14.8Å. Sample SBI11C is disordered, the other samples are annealed.*

In the present analysis, Lorentz-functions were fitted directly to $I_p(q)$. We now attempt to estimate the error in peak position. The difference in peak position of the single-crystal spectrum, $I_s(q)$, and the isotropic spectrum, $I_p(q)$, as found by minimizing $I_s(q)$ with respect to q, reads

$$q_s^* = q_p^* + \frac{1}{\xi^2 q_p^*} \tag{5.60}$$

where q_s^* and q_p^* denote the peak positions of the single-crystal spectrum and the isotropic spectrum, respectively. Using the ξ-values from Table 5.4 and setting $q_p^* = q^*$, the shifts in peak position were found to be smaller than 0.2% and were thus considered to be negligible.

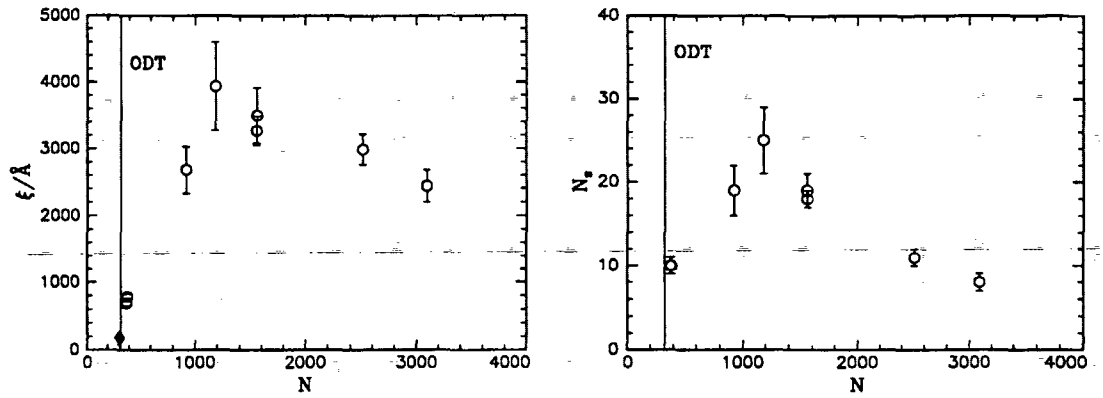

Figure 5.37: *Left figure: Correlation lengths of disordered and annealed samples as a function of chain length at 150°C. The vertical line represents the ODT. Error bars are errors from the fit. Right figure: Average number of lamellae per stack, N_s, for annealed samples as a function of chain length at 150°C.*

Analysis of the peak width gives information about the average number of lamellae stacked in one 'grain' provided that the distribution of lamellar thicknesses is narrow (Chapter 5.3). The correlation length is related to the half width at half maximum by $\xi = 1/(HWHM)$. A plot of the correlation length ξ as obtained from the Lorentz-fits is shown in the left graph of Fig. 5.37. The correlation length has its maximum value of 2000 – 4000 Å for samples with chain length larger than 1000. Below $N = 1000$, ξ is much smaller, below 1000 Å. Due to the smearing effect, the errors in determining the correlation length are relatively large. As described in Chapter 5.3, the average number of lamellae per stack, N_s, can be determined from the peak width using Eq. 5.45

$$\xi \simeq \frac{N_s D}{2.783} = \frac{2\pi N_s}{2.783\, q^*} \qquad \Longrightarrow \qquad N_s \simeq 0.443\, \xi q^* \tag{5.61}$$

The average number of lamellae per grain of annealed samples is shown in Fig. 5.37. N_s takes values between 8 and 25 for all samples. The average number of lamellae per grain is maximum for middle molar-mass samples ($N = 921 - 1555$). The average number of lamellae of the two highest molar-mass samples is only 8 – 11. A reason might be that it takes a very long time for these samples to form grains of a certain size. The chains are very long, *i.e.* the diffusion constants are low and entanglement effects play an important role. For samples close to the ODT, N_s is relatively small. The fact that the profile is close to sinusoidal (as shown using SAXS, Fig. 5.23) should not give rise to a smaller correlation length than for a rectangular profile (Fig. 5.10). Thus, it may be that, close to the ODT, the average number of lamellae per stack is smaller than for samples deeper in the ordered state or that the distribution of lamellar thicknesses is larger.

Solvent-cast samples

Solvent-cast and shear aligned samples were mounted as shown in Fig. 5.32. Peaks were expected on the left and right side of the direct beam (q_y-direction). Anisotropic spectra (from solvent-cast and shear aligned samples) were azimuthally averaged using horizontal

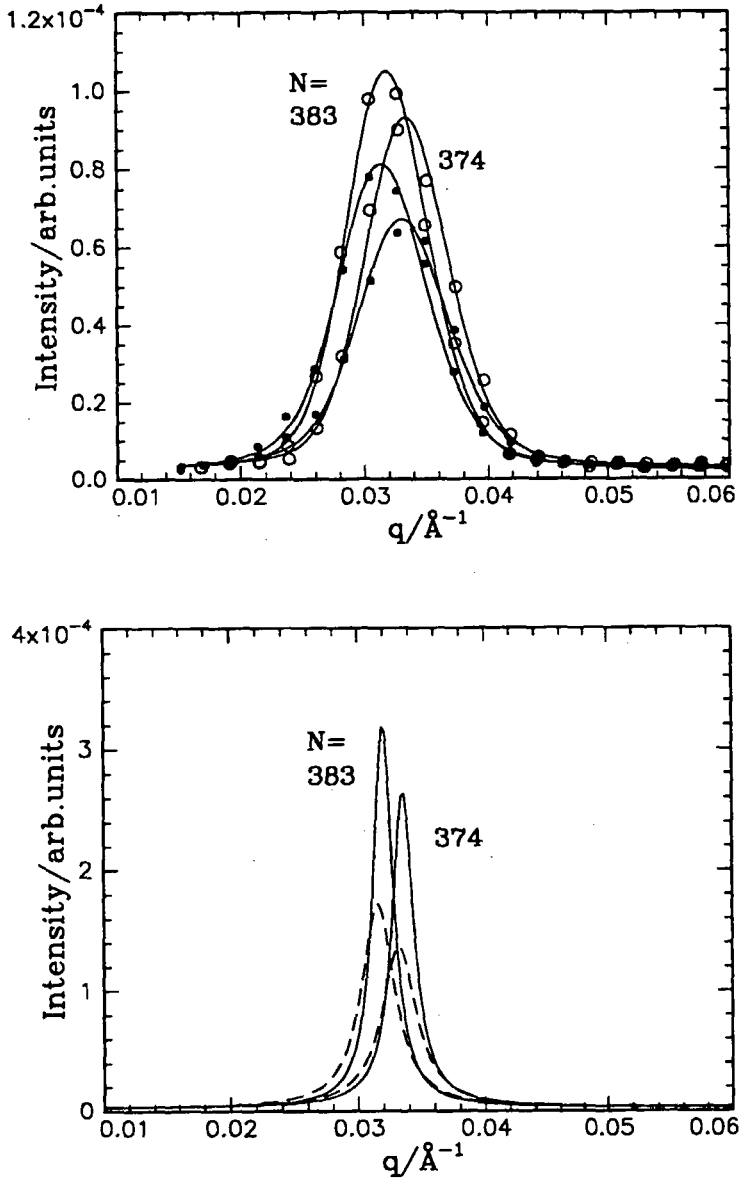

Figure 5.38: *Upper figure: Horizontal (q_y, ○) and vertical (q_x, •) spectra at 150°C from low molar-mass samples solvent-cast from benzene. Lines are fits of smeared Lorentz-functions. Left curves: SBI08A, right curves: SBI12A. Both spectra were measured at 3m/3m/5.58Å. The corresponding Lorentz-functions are shown in the lower graph.*

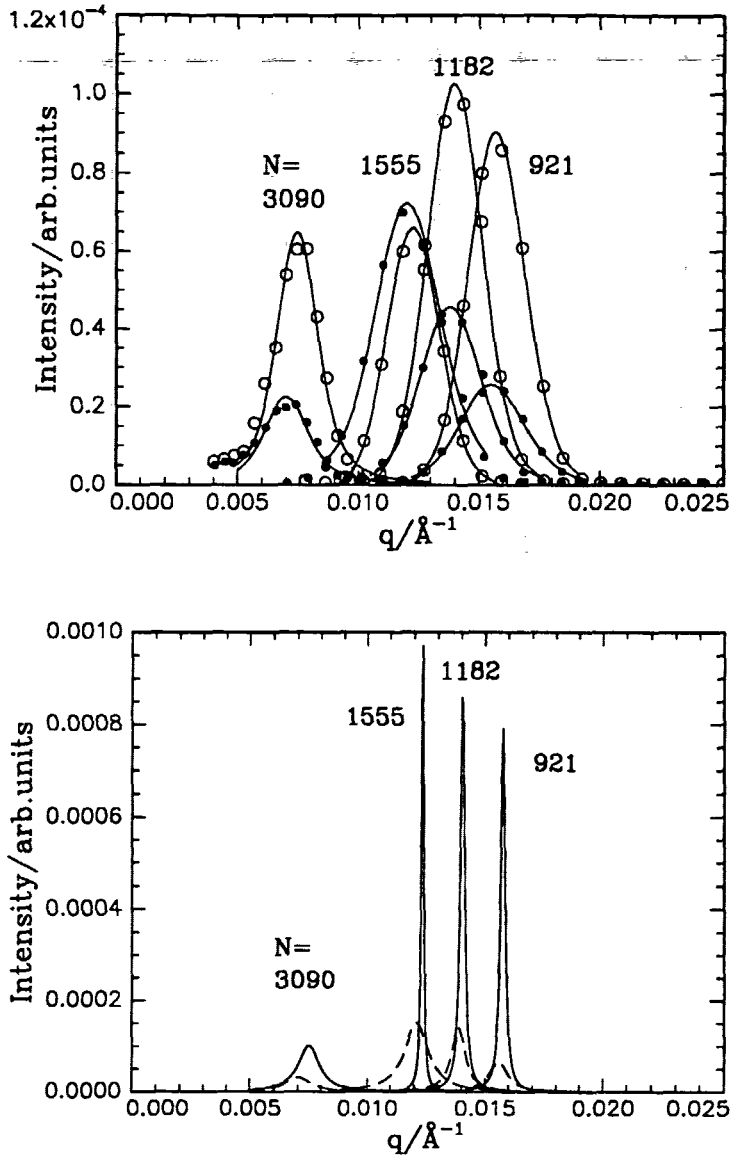

Figure 5.39: *Upper figure: Horizontal (q_y, ○) and vertical (q_x, ●) SANS-spectra at 150°C from high molar-mass samples solvent-cast from benzene. Lines are fits of smeared Lorentz-functions. From left to right: SBI10G, SBI06G, SBI15A, and SBI02G. The corresponding Lorentz-functions are shown in the lower graph.*

and vertical sector masks (Fig. 5.34), thus giving information on the peaks and the underlying diffraction ring, if existing. The horizontal sectors correspond to q_y and the vertical sectors to q_x. Spectra from solvent-cast samples averaged in this way together with fits of smeared Lorentz-functions and the corresponding Lorentz-functions are shown in Fig. 5.38 and 5.39. The peak positions, q_x^*, q_y^*, the peak intensities, I_x, I_y, and correlation lengths, ξ_x, ξ_y for solvent-cast samples found in q_y- and in q_x-direction are given in Table 5.5. The peak positions in q_x- and q_y-direction do not differ more than 2% with the exception of the highest molar-mass sample (SBI10G) where a difference of 6% is found which is attributed to mechanical stresses. One sample (SBI08A) was measured with two settings. The peak positions obtained in q_y-direction differ by 3%. However, the peak width changes by a factor of 3 upon changing the setting (Table 5.5). A reason might be an instability of the fitting routine which leads to a high error on ξ.

sample	N	setting	peak positions q_y^*, q_x^*/Å^{-1}	peak intensities I_y, I_x/arb.units	ratio I_y/I_x	correlation lengths ξ_y, ξ_x/Å	N_s
SBI12A	374	(a)	$(3.35 \pm 0.11)10^{-2}$	$(2.6 \pm 0.2)10^{-4}$		970 ± 100	14 ± 2
			$(3.32 \pm 0.11)10^{-2}$	$(1.3 \pm 0.1)10^{-4}$	2.0	600 ± 60	9 ± 1
SBI08A	383	(a)	$(3.20 \pm 0.11)10^{-2}$	$(3.2 \pm 0.2)10^{-4}$		1070 ± 90	15 ± 1
			$(3.15 \pm 0.11)10^{-2}$	$(1.7 \pm 0.1)10^{-4}$	1.9	640 ± 50	9 ± 1
		(b)	$(3.31 \pm 0.04)10^{-2}$	$(2.7 \pm 1.4)10^{-5}$		2700 ± 1600	40 ± 24
			$(3.29 \pm 0.04)10^{-2}$	$(7.5 \pm 1.0)10^{-6}$	3.6	700 ± 130	10 ± 2
SBI02G	921	(b)	$(1.58 \pm 0.04)10^{-2}$	$(7.9 \pm 1.3)10^{-4}$		9100 ± 1600	64 ± 11
			$(1.56 \pm 0.04)10^{-2}$	$(6.6 \pm 0.6)10^{-5}$	12	2150 ± 210	15 ± 2
SBI15A	1182	(b)	$(1.40 \pm 0.04)10^{-2}$	$(8.7 \pm 1.9)10^{-4}$		9100 ± 200	56 ± 2
			$(1.39 \pm 0.04)10^{-2}$	$(1.4 \pm 0.2)10^{-4}$	6.1	2820 ± 490	17 ± 3
SBI06A	1555	(b)	$(1.18 \pm 0.04)10^{-2}$	$(3.9 \pm 1.0)10^{-4}$		3900 ± 1100	18 ± 5
			$(1.18 \pm 0.04)10^{-2}$	$(1.2 \pm 0.2)10^{-4}$	3.3	2160 ± 440	11 ± 2
SBI06G	1555	(b)	$(1.23 \pm 0.04)10^{-2}$	$(1.0 \pm 0.3)10^{-3}$(d)		18100 ± 6200(d)	–
			$(1.21 \pm 0.04)10^{-2}$	$(1.5 \pm 0.1)10^{-4}$	6.9	1660 ± 170	9 ± 1
SBI06L	1555	(b)	$(1.23 \pm 0.04)10^{-2}$	$(3.6 \pm 0.6)10^{-3}$		15900 ± 2900	87 ± 16
			$(1.21 \pm 0.04)10^{-2}$	$(4.6 \pm 0.5)10^{-5}$	78	2010 ± 220	11 ± 1
SBI07G	2511	(c)	$(8.32 \pm 0.22)10^{-3}$	$(1.8 \pm 0.2)10^{-4}$		5540 ± 590	20 ± 2
			$(8.33 \pm 0.22)10^{-3}$	$(9.7 \pm 0.5)10^{-5}$	1.8	4180 ± 260	15 ± 1
SBI07L	2511	(c)	$(8.38 \pm 0.22)10^{-3}$	$(7.1 \pm 0.4)10^{-5}$		1540 ± 100	6 ± 1
			$(8.26 \pm 0.22)10^{-3}$	$(3.0 \pm 0.2)10^{-5}$	2.4	1320 ± 90	5 ± 1
SBI10G	3090	(c)	$(7.47 \pm 0.22)10^{-3}$	$(1.0 \pm 0.1)10^{-4}$		1970 ± 180	7 ± 1
			$(7.03 \pm 0.22)10^{-3}$	$(3.2 \pm 0.3)10^{-5}$	3.2	1500 ± 170	5 ± 1

Table 5.5: *Fit parameters of solvent-cast samples at 150°C. The data were obtained from azimuthal averaging using sector masks in horizontal (upper values) and vertical direction (lower values). Given are the the setting (collimator length, sample detector distance, wavelength), the peak positions, q_y^*, q_x^*, the peak intensities, I_y, I_x, the correlation lengths, ξ_y, ξ_x, and the average number of lamellae per stack, N_s, in y- and x-direction. (a) 3m/3m/5.58Å, (b) 6m/6m/7.67Å, (c) 6m/6m/14.8Å. (d) Due to an instability in the fitting routine, this value is probably too high.*

The degree of orientation is estimated from the peak height ratio, I_y/I_x, and from the difference in correlation length in q_x- and q_y-direction. The peak height ratios, I_y/I_x, vary

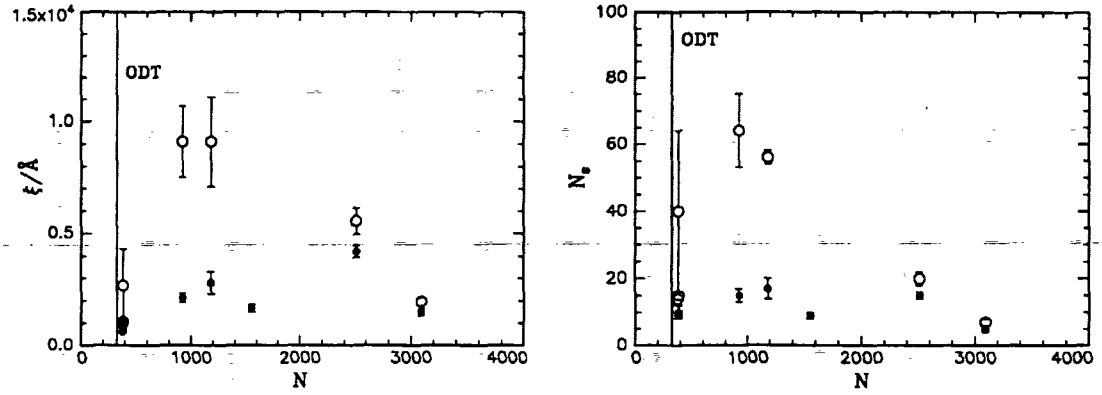

Figure 5.40: *Left figure: Correlation lengths of samples solvent-cast from benzene as a function of chain length at 150°C. (○) Horizontal (q_x), (●) vertical (q_y) direction. The vertical line represents the ODT. Error bars are errors from the fit. Right figure: Average number of lamellae per stack, N_s, as a function of chain length at 150°C.*

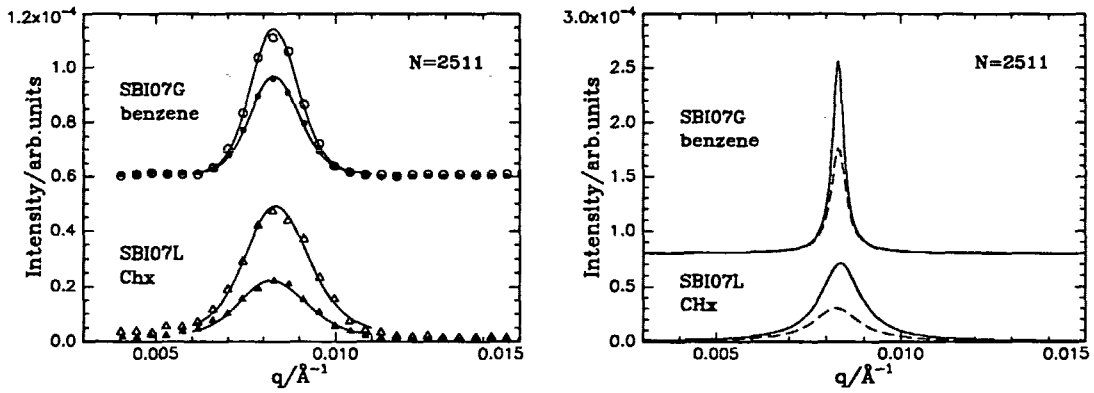

Figure 5.41: *Left figure: Horizontal (q_y, ○) and vertical (q_x, ●) SANS-spectra at 150°C from SBI07G (solvent-cast from benzene) and from SBI07L (solvent-cast from cyclohexane). Lines are fits of smeared Lorentz-functions. The intensities are shifted. The corresponding Lorentz-functions are shown in the right figure.*

a lot from sample to sample and are subject to large errors. For most samples the ratio is found to be $2-3$ meaning that the samples are oriented parallel to the film surface to a certain degree. The correlation length as a function of chain length and the average number of lamellae per stack are shown in Fig. 5.40. One should not put too much weight on the exact values obtained, as values above $\sim$ 3000 Å normally cannot be resolved [108]. The average number of lamellae in q_y-direction, is found to take values between 6 and 87. In q_x-direction, values between 5 and 17 are found which are similar to the ones found with annealed samples (Table 5.4 and Fig. 5.37). Especially for low and middle molar-mass samples, the number of lamellae per grain is thus larger normal to the film surface than parallel to the film surface. In general, the degree of alignment is smaller than what is obtained using shear alignment (see below). The degree of alignment depends strongly on the film thickness, because lamellar ordering is induced at the surfaces. A film thickness

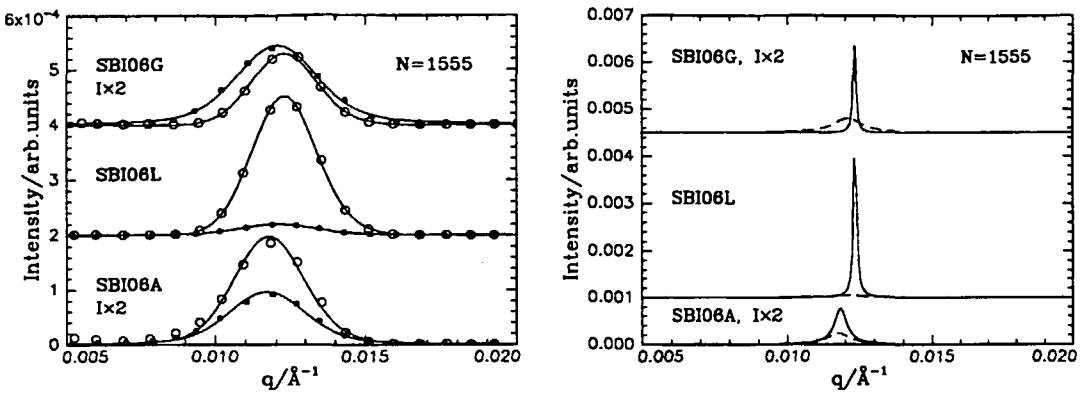

Figure 5.42: *Left figure: Horizontal (q_y, ○) and vertical (q_x, ●) spectra at 150°C from SBI06G (solvent-cast from benzene, $p = 1.13$), SBI06L (solvent-cast from cyclohexane, $\bar{M}_W/\bar{M}_N = 1.12$) and SBI06A (solvent-cast from benzene, $\bar{M}_W/\bar{M}_N = 1.22$). The intensities are shifted. Lines are fits of smeared Lorentz-functions. The corresponding Lorentz-functions are shown in the right graph. The fact that the Lorentz-function in horizontal direction is so sharp compared to the curve in vertical direction, is attributed to an instability of the fitting routine.*

of 0.6 mm, as chosen here[10], is probably too high for obtaining good alignment. For films of 0.1 mm thickness, good alignment has been reported [109].

We now attempt at establishing if there is a difference in lamellar thickness according to the solvent chosen and to the degree of crosslinking. Samples SBI07L and SBI06L are solvent-cast from cyclohexane which, at room temperature, is a marginal solvent for polystyrene and a good solvent for polybutadiene. The results from these samples are compared with the results from samples SBI07G and SBI06G which both were solvent-cast from benzene, a good solvent for both blocks. Comparing the peak positions from SBI07G and SBI07L, a difference of only 0.7% (horizontal direction) is found which is considered negligible. The experimental data together with the fits are shown in Fig. 5.41. No difference is found in the peak positions of SBI06G and for SBI06L (Fig. 5.42 and Table 5.5). However, comparing SBI06A and SBI06G which are both solvent-cast from benzene, but contain different amounts of the antioxidant Irganox 1010 (SBI06A: 0.1 wt-%, $\bar{M}_W/\bar{M}_N = 1.22$, SBI06G: 0.5 wt-%, $\bar{M}_W/\bar{M}_N = 1.13$), a slight difference in peak positions is found. The slightly larger degree of crosslinking of SBI06A leads to a lamellar thickness which is 4% higher than the one of SBI06G which corroborates the SAXS-result (Fig. 5.26 and Table 5.1). It is concluded that crosslinking occurs during solvent-casting, in a state where the chains are still swollen. Great care is thus necessary when preparing polystyrene-polybutadiene samples for determination of the lamellar thickness.

To summarize, solvent-casting under the conditions used (using benzene, a good, non-selective solvent, a film thickness of 0.6 mm and subsequent annealing at 150°C) leads to a certain degree of alignment, as seen from the intensity ratio and the difference in stack height. No difference in peak position is found using different solvents. However, crosslinking during the solvent-casting process has a slight influence on the lamellar thickness.

[10] A relatively high value of the film thickness was chosen in order to get tractable samples.

Shear aligned samples

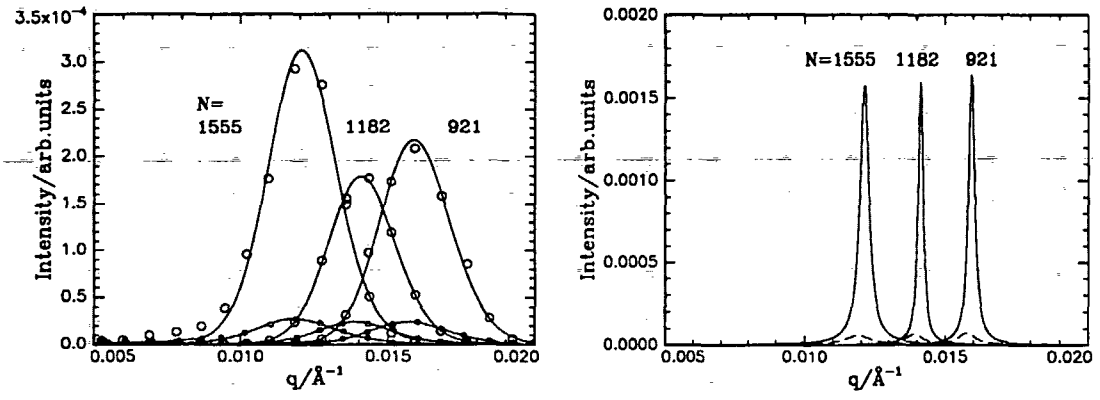

Figure 5.43: *Left figure: Horizontal (q_y, ○) and vertical (q_x, •) spectra from shear aligned samples at 150°C. From left to right: SBI06D, SBI15E, and SBI02D. Lines are fits of smeared Lorentz-functions. The corresponding Lorentz-functions are shown in the right graph. Full line: q_y, broken line: q_x.*

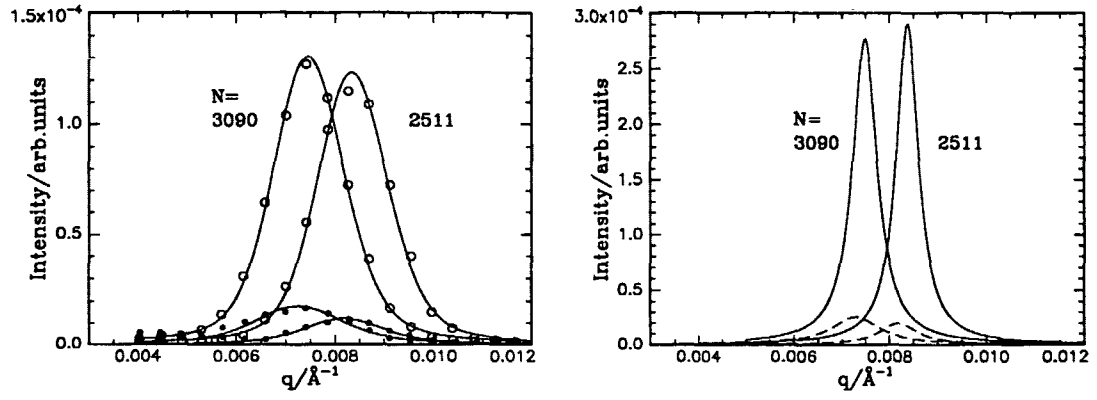

Figure 5.44: *Left figure: Horizontal (q_y, ○) and vertical (q_x, •) spectra from SBI10K (left curves) and SBI07K (right curves) which were shear aligned. The spectra were measured at 150°C. Lines are fits of smeared Lorentz-functions. The corresponding Lorentz-functions are shown in the right graph. Full line: q_y, broken line: q_x.*

Spectra from shear aligned samples were treated in the same way as solvent-cast samples. The such obtained spectra together with fits of resolution smeared Lorentz-functions are shown in Fig. 5.44 and 5.43. The peak positions, peak intensities and correlation lengths found are given in Table 5.6. As stated above, values of the correlation length above $\sim$ 3000 Å cannot be determined precisely by the fitting routine [108]. However, the overall picture concerning the degree of alignment is consistent, as will be established below. The peak positions found in the q_y- and q_x-directions are nearly equal. The values of the peak height in the q_y- and q_x-direction are very different ($I_y/I_x = 11 - 28$) which means that the samples are well-aligned. As established in SAXS-experiments, all samples were found to be aligned in the parallel direction (Fig. 5.27). This finding is corroborated

sample	N	setting	peak positions q_y^*, $q_x^*/\text{Å}^{-1}$	peak intensities I_y, I_x/arb.units	ratio I_y/I_x	correlation lengths ξ_y, $\xi_x/\text{Å}$	N_s
SBI02D	921	(a)	$(1.59 \pm 0.04)10^{-2}$	$(1.7 \pm 0.5)10^{-3}$		7800 ± 2000	55 ± 14
			$(1.58 \pm 0.04)10^{-2}$	$(7.4 \pm 1.0)10^{-5}$	22	2680 ± 390	19 ± 3
SBI15E	1182	(a)	$(1.41 \pm 0.04)10^{-2}$	$(1.6 \pm 0.2)10^{-3}$		9600 ± 1100	60 ± 7
			$(1.39 \pm 0.04)10^{-2}$	$(6.7 \pm 0.6)10^{-5}$	24	2480 ± 230	15 ± 1
SBI06D	1555	(a)	$(1.21 \pm 0.04)10^{-2}$	$(1.6 \pm 0.5)10^{-3}$		5300 ± 1800	28 ± 10
			$(1.19 \pm 0.04)10^{-2}$	$(5.8 \pm 0.9)10^{-5}$	28	1720 ± 290	9 ± 2
SBI07K	2511	(b)	$(8.37 \pm 0.22)10^{-3}$	$(2.9 \pm 0.2)10^{-4}$		3600 ± 310	13 ± 1
			$(8.19 \pm 0.22)10^{-3}$	$(2.0 \pm 0.2)10^{-5}$	15	2070 ± 250	8 ± 1
SBI10K	3090	(b)	$(7.48 \pm 0.22)10^{-3}$	$(2.8 \pm 0.2)10^{-4}$		3170 ± 290	11 ± 1
			$(7.29 \pm 0.22)10^{-3}$	$(2.6 \pm 0.2)10^{-5}$	11	1590 ± 200	5 ± 1

Table 5.6: *Fit parameters of shear aligned samples at 150°C. The data were obtained from azimuthal averaging using sector masks in horizontal (upper values) and vertical direction (lower values). Given are the the setting (collimator length, sample detector distance, wavelength), the peak positions, q_y^*, q_x^*, the peak intensities, I_y, I_x, the correlation lengths, ξ_y, ξ_x, and the average number of lamellae per stack, N_s, in y- and x-direction. (a) 6m/6m/7.67Å, (b) 6m/6m/14.8Å.*

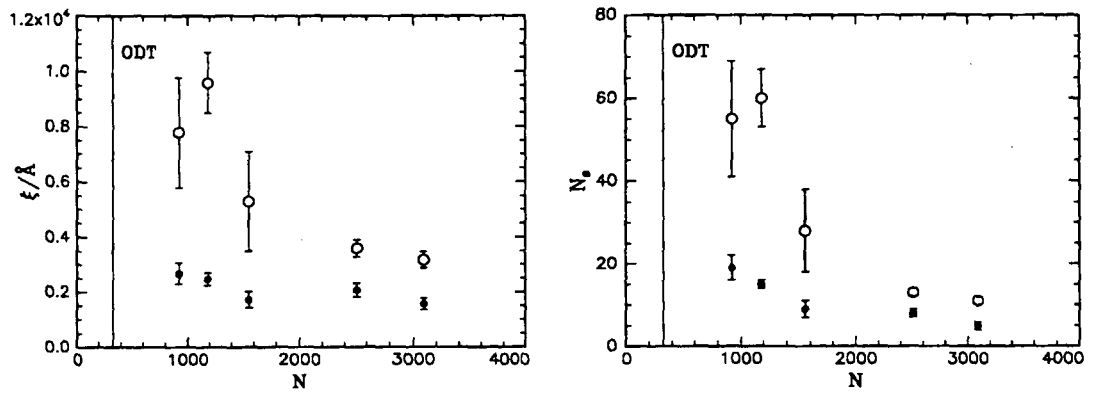

Figure 5.45: *Left figure: Correlation lengths of shear aligned samples as a function of chain length at 150°C. (○) horizontal (q_x), (●) vertical (q_y). The vertical line represents the ODT. Error bars are errors from the fit. Right figure: Average number of lamellae per stack, N_s, as a function of chain length at 150°C.*

by the difference in correlation length ξ as shown in Fig. 5.45 and in the resulting average number of lamellae per stack. Especially for samples having intermediate molar masses ($N = 921 - 1555$), up to ~ 60 lamellae are stacked parallel to the shear plane (q_y-direction) whereas domains oriented perpendicular to the shear direction only contain $\sim 5 - 19$ lamellae on average. The latter value is similar to the results from annealed samples (Table 5.4). The difference is not quite as high for the two highest molar mass samples which might be due to the difficulty of aligning entangled, high molar-mass samples.

Comparison of different preparation methods

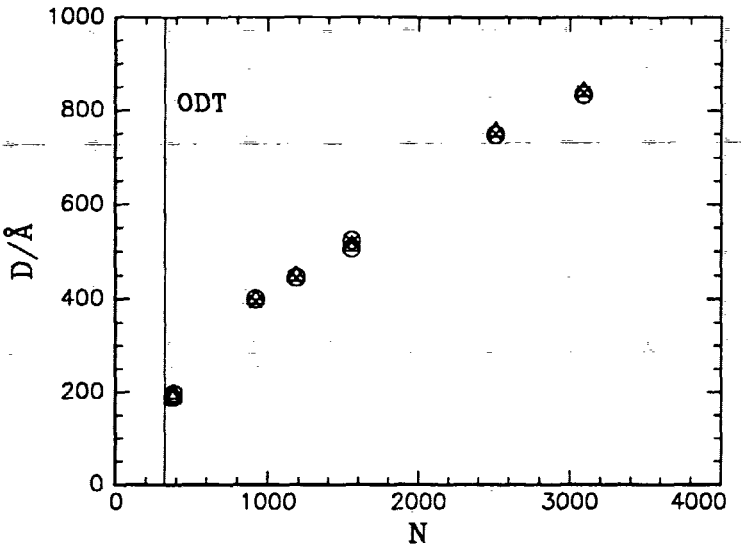

Figure 5.46: *Lamellar thickness of samples prepared in different ways as a function of chain length at 150°C. The values were determined using SANS. (◇) disordered, (○) annealed, (△) solvent-cast from benzene, data found in q_y-direction, (×) shear-aligned, data found in q_y-direction. The vertical line represents the ODT.*

In Fig. 5.46, the lamellar thickness found for disordered, annealed, solvent-cast and shear aligned samples are shown. Values in q_y-direction were used for solvent-cast and shear aligned samples. As with SAXS, no significant differences are seen according to the preparation method which indicates that the samples are in thermal equilibrium.

5.6 Results and discussion

In this section, data from samples prepared in different ways and studied using small-angle X-ray and neutron scattering are compiled and discussed. First, the peak positions as obtained with SAXS and SANS are compared for the three preparation methods separately. Second, results from samples prepared in different ways are compared. No significant differences in the values of the lamellar thickness are observed which indicates that the samples are in thermal equilibrium. Third, a more thorough analysis of the scaling behavior in different regions of phase space is made using data from all samples. An intermediate regime is identified and discussed in relation to results reported in the literature.

The peak positions as determined from SAXS and SANS are given in Table 5.7. For disordered samples, the differences are smaller than 3%. Two samples (SB05F and SB11B) were additionally studied using a Huxley-Holmes camera. These experiments are described in Appendix D. The results coincide nicely with the data from the Kratky-camera and from SANS. The characteristic lengthscale in the disordered state, $D = 2\pi/q^*$, defined in terms of a Bragg reflection, is shown as a function of chain length in Fig. 5.47. The peak

N	sample	$q^*/\text{Å}^{-1}$ SAXS	$q^*/\text{Å}^{-1}$ SANS	q^*_{SAXS}/q^*_{SANS}
156	SBI05B	$(6.20 \pm 0.09)10^{-2}$		
	SB05F	$(6.10 \pm 0.17)10^{-2}$(a)		
236	SBI14B	$(4.55 \pm 0.09)10^{-2}$		
310	SBI11C	$(3.98 \pm 0.09)10^{-2}$	$(3.85 \pm 0.11)10^{-2}$	1.03
	SB11B	$(3.93 \pm 0.17)10^{-2}$(a)		1.02
374	SBI12F	$(3.33 \pm 0.04)10^{-2}$	$(3.32 \pm 0.11)10^{-2}$	1.00
383	SBI08F	$(3.18 \pm 0.04)10^{-2}$	$(3.19 \pm 0.11)10^{-2}$	1.00
921	SBI02F	$(1.54 \pm 0.02)10^{-2}$(b)	$(1.57 \pm 0.04)10^{-2}$	0.98
1182	SBI15F	$(1.37 \pm 0.02)10^{-2}$(b)	$(1.41 \pm 0.04)10^{-2}$	0.97
1555	SBI06H	$(1.19 \pm 0.02)10^{-2}$(b)	$(1.20 \pm 0.04)10^{-2}$(c)	0.99
			$(1.24 \pm 0.02)10^{-2}$(c)	0.96
2511	SBI07H		$(8.39 \pm 0.22)10^{-3}$	
3090	SBI10H		$(7.53 \pm 0.22)10^{-3}$	
374	SBI12A	$(3.33 \pm 0.04)10^{-2}$	$(3.35 \pm 0.11)10^{-2}$	0.99
383	SBI08A	$(3.13 \pm 0.04)10^{-2}$	$(3.20 \pm 0.11)10^{-2}$(c)	0.98
			$(3.31 \pm 0.04)10^{-2}$(c)	0.95
921	SBI02G	$(1.48 \pm 0.02)10^{-2}$(b)	$(1.58 \pm 0.04)10^{-2}$	0.94
1182	SBI15A	$(1.33 \pm 0.02)10^{-2}$(b)	$(1.40 \pm 0.04)10^{-2}$	0.95
1555	SBI06G	$(1.19 \pm 0.02)10^{-2}$(b)	$(1.23 \pm 0.04)10^{-2}$	0.97
2511	SBI07G		$(8.32 \pm 0.22)10^{-3}$	
3090	SBI10G		$(7.47 \pm 0.22)10^{-3}$	
374	SBI12C	$(3.32 \pm 0.02)10^{-2}$(b)		
383	SBI08C	$(3.12 \pm 0.03)10^{-2}$		
921	SBI02D	$(1.51 \pm 0.02)10^{-2}$(b)	$(1.59 \pm 0.04)10^{-2}$	0.95
1182	SBI15E	$(1.34 \pm 0.02)10^{-2}$(b)	$(1.41 \pm 0.04)10^{-2}$	0.95
1555	SBI06D	$(1.17 \pm 0.02)10^{-2}$(b)	$(1.21 \pm 0.04)10^{-2}$	0.97
2511	SBI07K		$(8.37 \pm 0.22)10^{-3}$	
3090	SBI10K		$(7.48 \pm 0.22)10^{-3}$	

Table 5.7: *Peak positions of disordered, annealed, solvent-cast and shear aligned samples, determined at 150°C in SAXS- and SANS experiments. (a) measured using the Huxley-Holmes camera at Saclay. All other SAXS-data were measured using the Kratky-camera. (b) determined using the third order Bragg peak, (c) measured at different settings.*

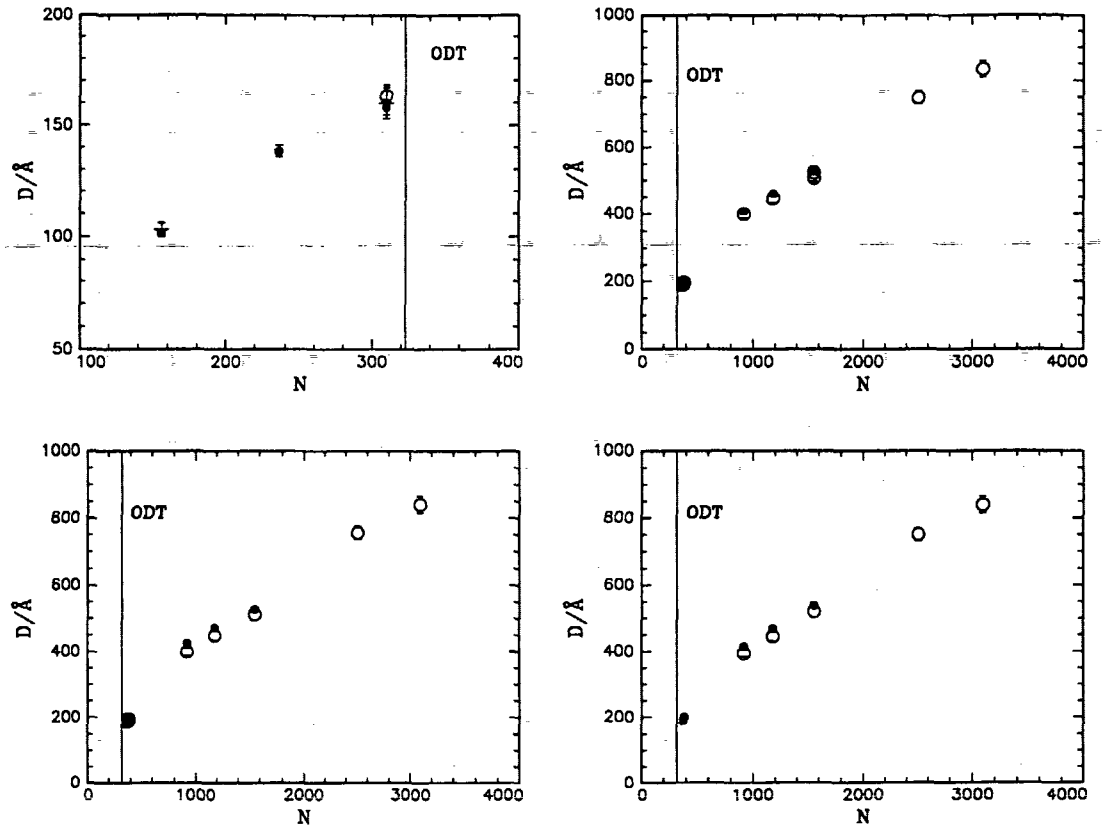

Figure 5.47: *Lamellar thickness of disordered (upper left), annealed (upper right), solvent-cast (lower left) and shear aligned samples (lower right) versus chainlength at 150°C as obtained with SAXS (•) and with SANS (o). The vertical line indicates the ODT.*

positions from annealed samples do not differ more than 4%. For solvent-cast and shear aligned samples, the differences between SAXS- and SANS-results are slightly higher: 6 and 5%, respectively (Fig. 5.47). As the SAXS-spectra from solvent-cast and from shear aligned samples were not desmeared (except the spectrum of SBI06G), the differences might be due to a residual beam length smearing effect. However, as in most cases the values are equal within the error bars, the data are used without further adjustments.

The reason for using different preparation methods (annealing, solvent-casting from a good, non-selective solvent, and shear alignment) was to test the existence of non-equilibrium states. The influence of solvent quality and of polydispersity in chain length on the lamellar thickness have been discussed in Sections 5.4 and 5.5; no differences were observed for samples solvent-cast from benzene (a good solvent) and from cyclohexane (a solvent good for polybutadiene and marginal for polystyrene), but the lamellar thickness was found to depend on the width of the molar-mass distributions. For consistency, the samples solvent-cast from cyclohexane and those with a broader molar-mass distribution will be excluded from further analysis. The values of the characteristic lengthscale, $D = 2\pi/q^*$, as obtained from samples prepared in different ways are plotted in Fig. 5.48. No significant differences in peak position according to the preparation method are observed, which indicates that the samples are close to thermal equilibrium. This allows us to

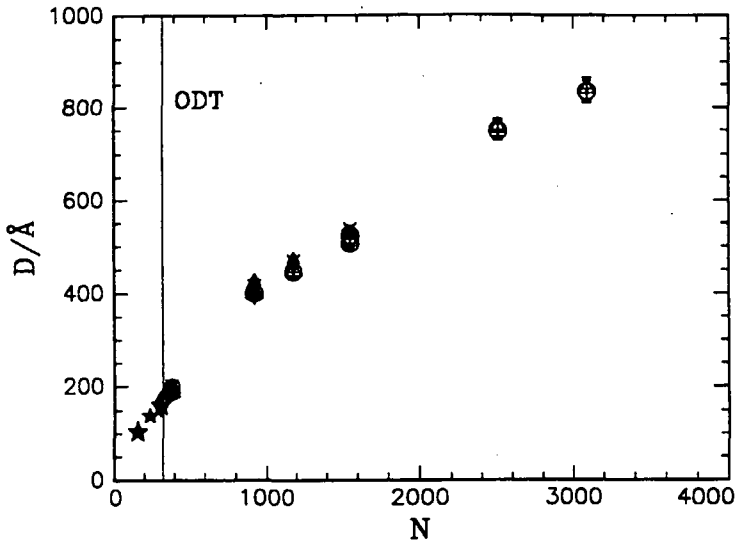

Figure 5.48: *Characteristic lengthscale $D = 2\pi/q^*$ versus chainlength at 150°C as obtained with SAXS and with SANS. Disordered samples: diamonds: SANS, filled stars: SAXS (Kratky-camera), open stars: SAXS (Huxley-Holmes camera). Annealed samples: open circles: SANS, filled circles: SAXS (Kratky-camera). Solvent-cast samples: open triangles: SANS, filled triangles: SAXS (Kratky-camera). Shear aligned samples: plusses: SANS, crosses: SAXS (Kratky-camera). The vertical line indicates the ODT.*

use data from disordered, annealed, solvent-cast (from benzene) and from shear aligned samples for the investigation of the scaling behavior.

We now attempt to establish the scaling behavior of the characteristic lengthscale with chain length, $D = D_o N^{\delta}$. In the following, we will only discuss the exponent δ. The proportionality constant, D_o, is a basic building block length. It is found to vary between 1.4 and 6.1 Å according to the fitting region (Table 5.8). Comparing with the bond lengths of the carbon-carbon bond which is ~ 1.4 Å [10], nearly all values seem to be to small to have a physical interpretation. Only the value found for high molar masses is larger (6.1 Å) and represents a basic building block length.

The fits are all made in log-log-representations of the peak position *vs.* the chain length, because this representation allows to detect changes of the scaling behavior. First, we focus on the disordered region. The peak positions obtained from different instruments are shown in Fig. 5.49[11] as a function of chain length in a log-log-representation. A weighted linear fit[12] gives an exponent $\delta = 0.66 \pm 0.03$ which is considerably higher than the prediction for Gaussian chains, $D \propto N^{1/2}$. For comparison, a line with slope $-1/2$ was force-fitted to data from disordered samples in Fig. 5.49. It clearly does not fit the data. We conclude that the disordered samples are not in the Gaussian regime, but the chains are stretched. A region $\chi N \simeq 5 - 10$ is covered with these samples. In dynamic light scattering experiments in the disordered state, a mode related to chain stretching is

[11]For a description of measurements with the Huxley-Holmes camera see Appendix D.

[12]In all weighted fits, the data points were weighted with the inverse error squared, $(1/\Delta(\ln q^*))^2$. The errors are given in Table 5.7.

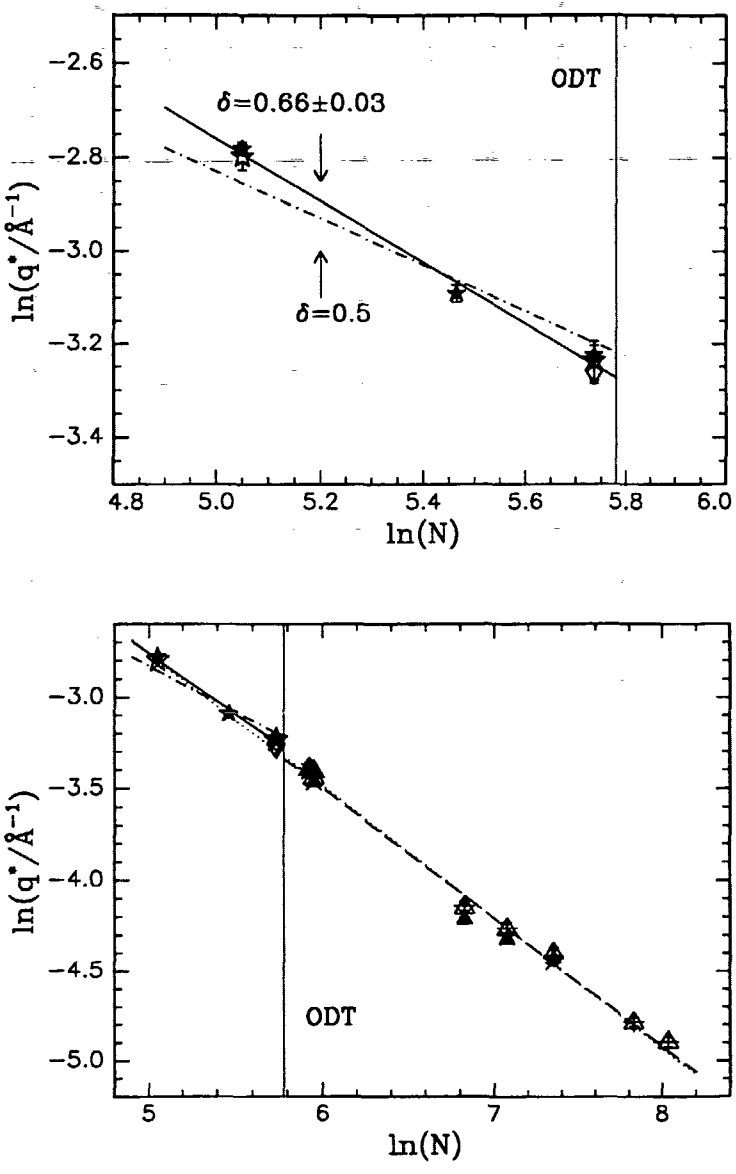

Figure 5.49: *Upper figure: Peak positions of disordered samples as a function of chain length in a log-log-plot. All peak positions were measured at 150°C. Diamonds: SANS, filled stars: Kratky-camera, open stars: Huxley-Holmes camera. The full line is a weighted linear fit. The dash-dotted line is a weighted linear fit with the slope fixed at −0.5. The vertical line indicates the ODT. Lower figure: Peak positions of all samples as a function of chain length at 150°C in a log-log-plot. Same symbols as in Fig. 5.48. The vertical line indicates the ODT. The dotted line is a weighted linear fit to all data, the broken line a fit to data from ordered samples the full line a fit to data from disordered samples, and the dash-dotted line a fit to data from disordered samples keeping the slope fixed to* -0.5.

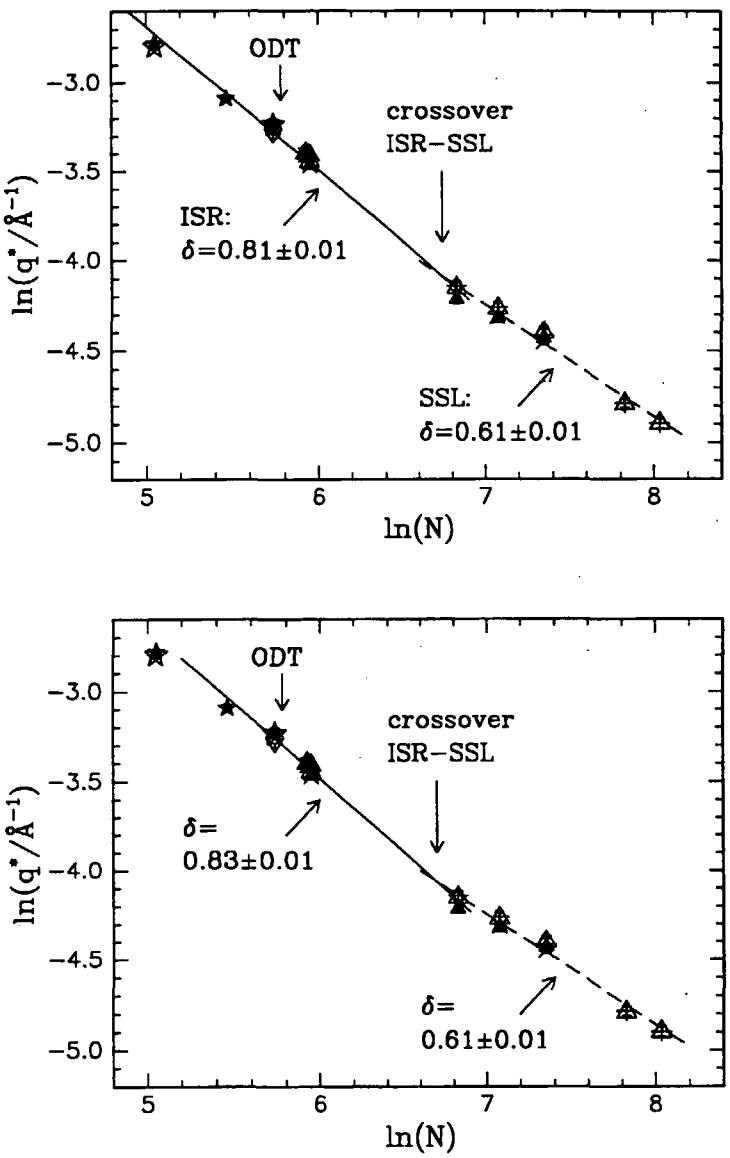

Figure 5.50: *Upper figure: Peak positions as a function of chain length at 150°C in a log-log-plot. Same symbols as in Fig. 5.48. The full line is a weighted linear fit to data from low molar-mass samples ($N = 156 - 921$) and the broken line a weighted linear fit to data from high molar-mass samples ($N = 921 - 3090$). ISR denotes the intermediate-segregation regime and SSL the strong-segregation limit. Lower figure: Same data and same fits as above, but the sample with the lowermost molar mass has been excluded from the fit.*

region	fitting range	D_o/Å	δ
all samples	$N = 156 - 3090$	2.7 ± 0.2	0.72 ± 0.01
disordered samples	$N = 156 - 310$	3.7 ± 0.3	0.66 ± 0.03
ordered samples	$N = 374 - 3090$	2.9 ± 0.2	0.71 ± 0.01
low chain length	$N = 156 - 383$	2.6 ± 0.3	0.72 ± 0.02
	$N = 156 - 921$	1.6 ± 0.2	0.81 ± 0.01
	$N = 236 - 921$	1.4 ± 0.2	0.83 ± 0.01
high chain length	$N = 921 - 3090$	6.1 ± 0.1	0.61 ± 0.01

Table 5.8: *Fitting parameters found in fits of $D = D_o N^{\delta}$ in different regions of the phase diagram. Data from all preparation methods were used.*

observed to vanish at $\chi N \simeq 5$ (Chapter 7). This χN-value is considered the Gaussian- to stretched-coil transition. A similar value has been identified with other block copolymers [8]. We thus conclude that the disordered samples studied are in a stretched configuration.

The data from all samples are shown in a log-log-representation in Fig. 5.49 (lower figure). The exponent found in the ordered state, $\delta = 0.71 \pm 0.01$, is consistent with the mean-field prediction, $\delta = 2/3$ [9], and with a previous experimental study [57]. A more thorough analysis of the scaling behavior in the ordered state is given below. Only a minor difference is thus found between the exponents in the disordered an the ordered state (Table 5.8) which means that there is no drastic change in behavior at the ODT. This is consistent with the findings in a temperature sweep with polystyrene-polybutadiene (Chapter 6) and with the results given in [8] (see Chapter 1).

We now attempt at examining the scaling behavior more closely. In order to identify an intermediate-segregation regime (ISR), lines have been fitted to low ($N = 156 - 921$) and to high molar-mass samples ($N = 921 - 3090$) (Fig. 5.50, upper figure). The following exponents are found:

$$\delta = 0.81 \pm 0.01 \quad \text{for} \quad N = 156 - 921$$
$$\delta = 0.61 \pm 0.01 \quad \text{for} \quad N = 921 - 3090$$

From the crossover points of the fitted lines, the χN-value of the crossover between the ISR and the SSL is estimated: $\ln(N) = 6.7 \Rightarrow \chi N = 27$ where $\chi = 0.033$ at 150°C has been used (Chapter 3). Fitting to the range $N = 156 - 383$ gives an exponent $\delta = 0.72 \pm 0.02$. However, the fit is not consistent with the high molar-mass data (not shown). It will therefore not be used for further investigations. In order to study the influence of the lowermost datapoint ($N = 156$) (which might be in the Gaussian regime) on the scaling behavior, it was omitted from the fit (Fig. 5.50, lower figure). Then, an exponent $\delta = 0.83 \pm 0.01$ is found for $N = 236 - 921$ which is very similar to the values for $N = 156 - 921$. The crossover is found at $(\chi N)_{ISC} = 27$, the same value as above. Below this value, the characteristic lengthscale scales like $D \propto N^{0.82}$ (mean of the two values found) and above like $D \propto N^{0.61}$. These values of the exponent differ significantly from each other.

The latter value of the exponent ($\delta = 0.61$) is somewhat lower than the mean-field predictions $\delta = 0.643$ [23] and $\delta = 2/3$ [9] for the strong-segregation limit (SSL), the reason for this discrepancy being unclear. In spite of this discrepancy, the region $N > 900$ which corresponds to $\chi N > 27$ ($\chi = 0.033$ at 150°C) is considered to be the SSL. Another feature characteristic of the SSL is that the lamellar interfaces are narrow [23]. As established in SAXS-measurements (Section 5.4), the spectra from these high molar-mass samples display up to seventh-order Bragg peaks. The presence of higher order peaks indicates that the lamellar interfaces are narrow and the profile is close to rectangular. For model calculations see Chapter 5.3. The narrow-interphase assumption of the SSL-theories [9, 23] is thus met with these samples.

Below $\chi N \simeq 27$, the characteristic lengthscale scales with chain length like $D \propto N^{0.82}$. The SAXS-spectra from ordered samples in this region display only one peak (Chapter 5.4). This means that the profile is close to sinusoidal as calculated in Chapter 5.3. This regime is identified as the intermediate-segregation regime (ISR) which has the following characteristics: the chain conformation deviates from Gaussian, the chains are stretched, and the density profile is smooth (both in the disordered and in the ordered state). Scaling with an exponent of ca. 0.8 has been observed with chemically different diblock copolymers [8, 68]. We will relate our results to previous measurements below.

To summarize, two regimes were identified where the characteristic lengthscale scales with chain length in different ways:

- the intermediate-segregation regime: $(\chi N)_{GST} < \chi N < (\chi N)_{ISC}$, where $D \propto N^{0.82}$
- the strong-segregation limit: $\chi N > (\chi N)_{ISC}$, where $D \propto N^{0.61}$

The crossover is located at $(\chi N)_{ISC} \simeq 27$.

Comparing this result with the theoretical predictions which were reviewed in Chapter 5.1, the following can be said: In all approaches which describe the ordered state, a crossover has been predicted. The exponent for $\chi N < (\chi N)_{ISC}$ has been predicted to be higher than for $\chi N > (\chi N)_{ISC}$ [71, 72, 73, 74, 75]. The value determined in this study, $(\chi N)_{ISC} \simeq 27$, fits nicely with the theoretical predictions of Tang and Freed, $(\chi N)_{ISC} \simeq 24$ [72][13] and of Sones *et al.* [75], $(\chi N)_{ISC} \simeq 17 - 18$. The values predicted by McMullen [74], $(\chi N)_{cr} \simeq 55$ and by Melenkevitz and Muthukumar [71], $(\chi N)_{cr} \simeq 95$, are higher than the value found in the present study. Vavasour and Whitmore [73] do not give an explicit value for χN at the crossover.

Both the Gaussian- to stretched-coil transition and the intermediate segregation regime are no phase transitions, but smooth changes in chain conformation. These changes are closely related to the shape of the density profile: The Gaussian- to stretched-coil transition occurs in the disordered state. It occurs at the crossover from the fully homogeneous state to a regime, where concentration fluctuations persist. The crossover from the intermediate-segregation regime to the strong-segration limit (in the ordered state) marks the crossing from a sinusoidal density profile to a rectangular profile with narrow interfaces, where pure domains exist.

[13]The authors do not give the value explicitely. It was found by evaluating the expression given for D as a function of N, inserting our value for χ (Chapter 5.1).

We now attempt at comparing our results to experimental data reported in the literature. For this purpose, the data have to be converted to χN-values. As most authors do not give the χ-parameter, this is not straightforward. The data on polystyrene-polyisoprene from Hashimoto *et al.* [57] and from Hadziioannou and Skoulios [68] can be compared with ours only qualitatively. Hashimoto *et al.* [57] report that the exponent 2/3 is consistent with their data. Their samples have molar masses between 21000 and 102000 g/mol, all samples being ordered. Fitting a powerlaw to these data gives $\delta = 0.64 \pm 0.03$. Removing the data point from the sample with the lowest molar mass from the fit, $\delta = 0.59 \pm 0.02$ is found. Omitting the two samples with the highest molar masses (*i.e.* the fitting range is $\bar{M}_N = 21000 - 55000$ g/mol) leads to $\delta = 0.70 \pm 0.05$ which is distinctly different from the high molar-mass result, $\delta = 0.59$. The crossover between these two regimes is located at $\bar{M}_{ISC} \simeq 44000$ g/mol. The data from Hadziioannou *et al.* [68] were also obtained from polystyrene-polyisoprene diblock copolymer samples covering a large range in molar masses: $\bar{M}_N = 8500 - 205000$ g/mol. Samples with $\bar{M}_N < 27000$ g/mol are disordered. Fitting a powerlaw to data from all ordered samples gives an exponent $\delta = 0.79 \pm 0.02$ [68]. A fit to low molar-mass data ($\bar{M}_N = 27000 - 98000$ g/mol) leads to $\delta = 0.80 \pm 0.04$. For long chains ($\bar{M}_N = 114800 - 205000$ g/mol), $\delta = 0.72 \pm 0.08$ is obtained. The crossover is located at $\bar{M}_{ISC} = 109000$ g/mol, thus at a higher value than in Hashimoto's data [57]. However, both crossover values are of the same order of magnitude as the one found in the present study: $\bar{M}_{ISC} \simeq 55000$ g/mol. In both studies, the exponent is higher in the vicinity of the ODT than deeper in the ordered state, which corroborates our findings.

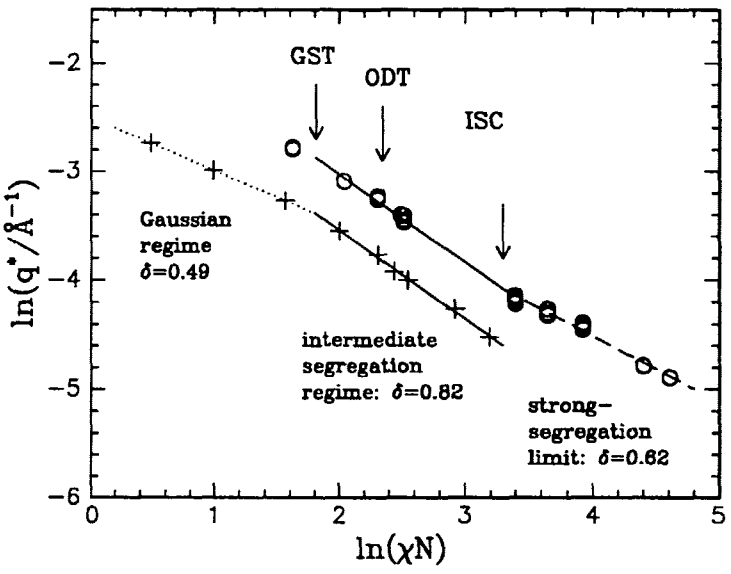

Figure 5.51: *Peak positions as a function of chain length in a log-log-plot. (o) our data, (+) data from PEP-PEE from [8]. The latter data are adjusted such that the ODT is at* $\chi N = 10.5$.

In order to visualize the three regions of the phase diagram: Gaussian regime, intermediate-segregation regime and strong-segregation limit, we attempt to compile our data with data on the Gaussian- to stretched-coil transition (GST) [8]. These data are presented in Chapter 1 (Fig. 1.8). The GST was identified using nearly symmetric ($f_{PEP} = 0.55$)

poly(ethylene propylene)-poly(ethylethylene) (PEP-PEE) diblock copolymers (Chapter 1). In order to bring the data on a χN-scale, the N-values from our data and from the PEP-PEE data are multiplied with the respective χ-parameters (Fig. 5.51). The following values were used: $\chi = 0.033$ for our data measured at 150°C and $\chi = 4.46\text{K}/T + 2.1 \times 10^{-3} = 0.017$ [22] for the measuring temperature, 23°C. The latter value was derived using fluctuation theory. The ODT of the PEP-PEE data is located at $\chi N \simeq 14$ which might be due to the slight asymmetry in composition and to the fact, that the value was derived using fluctuation theory. The χN-values of the PEP-PEE data are adjusted by multiplication with a factor 10.5/14, such that the ODT is located at 10.5 as in our data. Due to the difference in chemical structure, the peak positions of PEP-PEE and polystyrene-polybutadiene are dissimilar. Three regimes are discerned: The Gaussian regime at $\chi N < 6$, the intermediate-segregation regime at $\chi N \simeq 6 - 30$, and the strong-segregation limit at $\chi N > 30$ (Fig. 5.51).

Adding the newly identified crossover between the ISR and the SSL to the phase diagram by Rosedale *et al.* [22] (Chapter 1) results in the diagram shown in Fig. 5.52. Together with the Gaussian- to stretched-coil transition at $(\chi N)_{GST} \sim 5 - 7$ which was identified in dynamic light scattering experiments (Chapter 7 and [110]), the crossover between the ISR and the SSL describes the change in chain conformation.

5.7 Summary and conclusion

In this chapter of the thesis, results from a structural analysis of symmetric polystyrene-polybutadiene diblock copolymers in the bulk were presented. The aim of the study was to establish the scaling behavior of the characteristic lengthscale, D, as a function of chain length, N: $D \propto N^{\delta}$, focusing on the intermediate-segregation regime.

In order to reach the strong-segregation limit, a block copolymer with a relatively high Flory-Huggins segment-segment interaction parameter, χ, was chosen (polystyrene-polybutadiene) and samples covering a large range in molar masses were synthesized. Chain lengths ranged from $N = 156$ to 3090 which allowed a study of the region $\chi N \simeq 5 - 100$. All diblock copolymer samples were close to symmetric, $f_{PS} = 0.5$. For consistency, all sample preparations and measurements were carried out at the same temperature, 150°C. Stabilization was necessary in order to prevent the samples from crosslinking. In order to test the existence of non-equilibrium states, ordered samples were prepared using annealing above the glass temperature, solvent-casting from a good, non-selective solvent, and shear alignment, respectively. In addition, it was studied if the quality of the solvent used for solvent-casting and the width of the molar-mass distribution (*i.e.* the degree of crosslinking in case of polystyrene-polybutadiene) had an influence on the structure.

The characteristic lengthscales were determined in a combined SAXS- and SANS-study. Model calculations for the scattering of lamellar structures were made. They showed that only the first-order Bragg reflection is present in the spectrum of a sample having a sinusoidal density profile. For a sample having a density profile with sharp interfaces, higher-order Bragg reflections appear in the spectrum. In SAXS-experiments, information about the characteristic lengthscale and about the shape of the density profile was gained. The density profile of ordered samples was found to be close to sinusoidal in the vicinity of the ODT whereas it is close to rectangular deep in the ordered state.

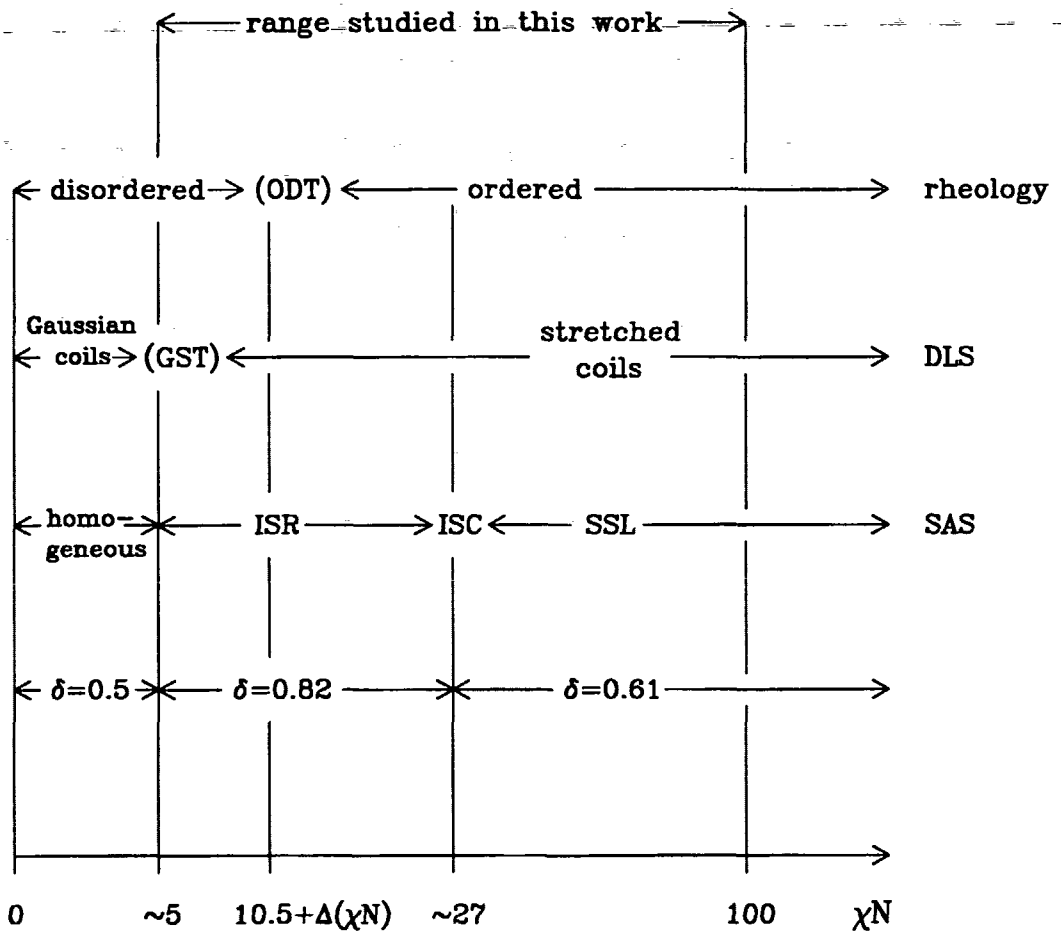

Figure 5.52: *Modified phase diagram. The original diagram is from [22], see Chapter 1. The crossover from the intermediate-segregation regime (ISR) to the strong-segregation limit (SSL) was identified in this study using small-angle scattering (SAS). It was found to be located at* $\chi N \simeq 30$. *GST stands for Gaussian-to-stretched-coil transition which was identified usind dynamic light scattering (DLS). The order-disorder transition (ODT) was determined using rheology. Mean-field theory predicts the ODT to occur at* $\chi N = 10.5$ *for symmetric diblock copolymers [7].* $\Delta(\chi N)$ *denotes the deviation from the value 10.5 as predicted by fluctuation theory [20].*

This was concluded from the absence or presence of higher-order Bragg reflections. No difference in lamellar thickness according to the quality of the solvent used for solvent-casting was observed. However, the lamellar thickness depends slightly on the degree of crosslinking, *i.e.* great care in preventing the samples from crosslinking is prerequisite for an exact determination of the characteristic lengthscale. In SANS-experiments, the peak positions of high molar-mass samples were determined precisely. It was also found that the degree of orientation of shear aligned samples is much higher than for solvent-cast samples under the conditions used in the present work.

The scaling behavior of the characteristic lengthscale with chain length was studied using data from disordered, annealed, solvent-cast and shear-aligned samples, all having narrow molar-mass distributions. No influence of the preparation method on the value of the characteristic lengthscale was observed. The characteristic lengthscales scales with chain length like $D \propto N^{0.82}$ for $\chi N \simeq 5 - 27$ whereas $D \propto N^{0.61}$ was found for $\chi N \simeq 27 - 100$. The first regime ($\chi N < 27$) is interpreted to be the intermediate-segregation regime. Here, no pure domains exist, neither in the disordered nor in the ordered state. The second regime ($\chi N > 27$) is the strong-segregation limit. The exponent found here ($\delta = 0.61$) is slightly lower than the values predicted by mean-field theory [9, 23], the reason being unclear. The density profile is close to rectangular, *i.e.* pure domains are separated by narrow interfaces. It is concluded that the chain conformation is closely related to the shape of the density profile. The existence of a crossover between the intermediate-segregation regime and the strong-segregation limit is in accordance with theories [71, 72, 73, 74, 75]. The value $(\chi N)_{ISC} \simeq 27$ is consistent with the values given in [72] and in [75].

A further perspective of the present study could be to fill the 'hole' in the scaling plot in the region $N = 400 - 900$ in order to determine the position of the crossover more precisely. Expanding the χN-region is not straightforward with polystyrene-polybutadiene diblock copolymers for the following reasons: At the low end of the χN-range, the Gaussian approximation of large chain lengths breaks down. Studying samples with higher molar mass than the ones presented here is difficult using small-angle scattering, because the lower limit of scattering vectors attainable in small-angle scattering experiments is almost reached with our samples. However, synthesis of higher molar-mass samples is feasible. A more precise analysis of the interphase width of our samples could illuminate the relationship between the shape of the density profile and chain conformation, which has been predicted by theory [71, 72, 74, 75].

Chapter 6

Temperature behavior around the ODT

In the previous chapter, the intermediate-segregation regime (ISR) was identified between the homogeneous phase deep in the disordered state and the strong-segregation limit deep in the ordered state. The ISR is located between $\chi N \simeq 5$ and 30 and includes the order-disorder transition (ODT). At a fixed temperature, it has been observed that the characteristic lengthscale, D, does not change discontinuously at the ODT upon varying chain length, N. In the ISR, the same scaling behavior was observed both in the disordered and the ordered state: $D \propto N^{0.82}$. Characteristic for the ISR is the deviation from Gaussian behavior: The chains are stretched. In addition, in the ISR, both in the disordered and in the ordered state, *i.e.* there is a certain degree of mixing of different segments. Two recent publications have focused on the temperature behavior of low molar-mass diblock copolymers around the ODT temperature (*e.g.* [22, 111]). In the present chapter, the behavior of the characteristic lengthscale of one low-molar mass sample upon heating from the lamellar state to the disordered state is discussed. The temperature study was carried out using SANS. Knowledge of the position, height and width of the peak observed in the spectra gives information about the overall structure and the behavior of the characteristic lengthscale. No discontinuous change of the characteristic lengthscale at the ODT temperature is observed; however, the peak height and width change drastically at the ODT. Comparing the variation of the characteristic lengthscale with the prediction for the thermal change of the radius of gyration of the two blocks, information about the chain conformation is obtained. The results are discussed below.

6.1 The background

At temperatures much higher than the ODT temperature, the melt is close to homogeneous. The characteristic lengthscale, $2\pi/q^*$ (defined in terms of a Bragg reflection), is therefore expected to depend on temperature in the same way as the radius of gyration, R_g [111] (Fig. 6.1):

$$\frac{2\pi}{q^*} \propto R_g(T) = R_g(T_{ref}) \exp\left(\frac{\kappa}{2}(T - T_{ref})\right) \tag{6.1}$$

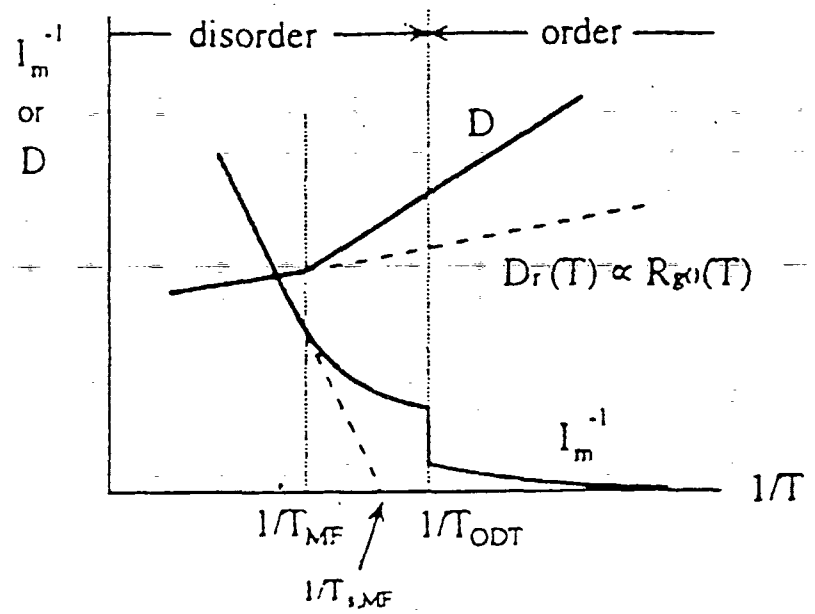

Figure 6.1: *Schematic representation of the ODT and the transition to mean-field (MF) behavior as proposed by Sakamoto et al. [111]. Shown are the inverse peak height, I_m^{-1}, and, schematically, the characteristic lengthscale, D, as a function of the inverse temperature.*

where T_{ref} denotes a reference temperature and $\kappa = d(\ln(R_g(T)^2)/dT$ the thermal expansivity. Here, κ is assumed not to depend on temperature. For the homogeneous melt, it is thus expected that

$$\ln(q^*) = const. - \frac{\kappa}{2}T \tag{6.2}$$

According to the chemical structure of the polymer, the parameter κ takes a positive or a negative value, which is due to a counterbalance of thermal expansion and of the increasing flexibility of the chains with temperature. The behavior according to Eq. 6.1 has been verified experimentally with a low molar-mass polystyrene-polyisoprene diblock copolymer at high temperatures [111]. In the framework of the Leibler theory [7], the structure factor of a diblock copolymer system in the disordered state is given by

$$S(q) = \frac{N}{F(x) - 2\chi N} \tag{6.3}$$

where $F(x)$ is a combination of Debye correlation functions (Chapter 5.1), $x = q^2R_g^2$, χ the Flory-Huggins segment-segment interaction parameter and N the chain length. For symmetric diblock copolymers, the structure factor is predicted to diverge at a certain value of $\chi N = (\chi N)_s$, the spinodal [7]. The spinodal represents the limit of stability; for $\chi N > (\chi N)_s$, the melt demixes locally. For symmetric diblock copolymers, a critical point is predicted. However, the situation is more complicated because of the appearance of ordered structures [7] before the spinodal is reached. The region in the vicinity of the ODT has been studied in more detail by Fredrickson and Helfand [20]. This region is addressed below. In spite of the complications in the vicinity of the ODT, the structure factor given above describes the variation of peak height, $I_o \propto S(q^*)$, with temperature

correctly deep in the disordered state:

$$\left(\frac{I_o}{N}\right)^{-1} \propto \left(\frac{1}{T_s} - \frac{1}{T}\right) N \tag{6.4}$$

where T_s is the spinodal temperature where the peak height is predicted to diverge (Fig. 6.1). Here, it is assumed that the Flory-Huggins interaction parameter is inversely proportional to temperature: $\chi = a/T + b$ and that $F(x)$ is independent of temperature. Plotting the inverse peak height versus inverse temperature (Fig. 6.1), linear behavior far above the ODT has been verified with low molar-mass samples at high temperature [111].

Upon approaching the ODT temperature, deviations from this behavior have been observed. The characteristic lengthscale has been found to depend more strongly on temperature than in the mean-field region which reflects chain stretching [22, 111]. The point where the variation of the characteristic lengthscale deviates from the one given by Eq. 6.1, is the Gaussian- to stretched-coil transition. Fredrickson and Helfand took concentration fluctuations in the disordered state close to the ODT into account and showed (among others), that for symmetric diblock copolymers, the structure factor does not diverge at the ODT [20]. Instead, a finite maximum is reached. A weak first-order phase transition has been predicted for symmetric diblock copolymers.[1] In the vicinity of the ODT, the peak height is thus smaller than predicted by mean-field theory (Eq. 6.4). This has also been observed experimentally (*e.g.* [22, 111]).

At the ODT temperature, different observations have been made in what concerns the characteristic lengthscale, the peak height and the correlation length. A discontinuous drop of the peak height at the ODT temperature has been found with different nearly symmetric diblock copolymers [22, 111, 112, 113, 114, 115]. The discontinuous drop reflects the nature of the phase transition, which is by fluctuation theory predicted to be a weak first-order transition [20]. However, it has not been established unambiguously, how the characteristic lengthscale behaves in the vicinity of the ODT temperature. A slight discontinuity of the peak position has been reported for polystyrene-polyisoprene [112] at the ODT. A continuous rise of the peak position with temperature without any noticeable change of behavior at the ODT was observed with poly(ethylene propylene)-poly(ethylethylene) [115]. With a polyethylene-poly(ethylene propylene) sample, it has recently been found that $\ln(q^*)$ rises more steeply in a narrow region around the ODT temperature than above and below the ODT temperature [22].

In the present work, the temperature behavior of a symmetric low molar-mass polystyrene-polybutadiene sample is studied around the ODT temperature.

6.2 Experimental

The sample (SBI11C) has a chain length $N = 310$ and an ODT temperature of 130°C (Table 4.1). A pill of 1 mm height was pressed and was heated over the ODT temperature before the measurements. The sample was thus in a lamellar, 'polycrystalline' state below the ODT. Measurements were made between 114 and 150°C using SANS. The spectra were measured with the setup and the settings described in Chapter 5.5. The

[1] For asymmetric diblock copolymers, the ODT is also of first order [7].

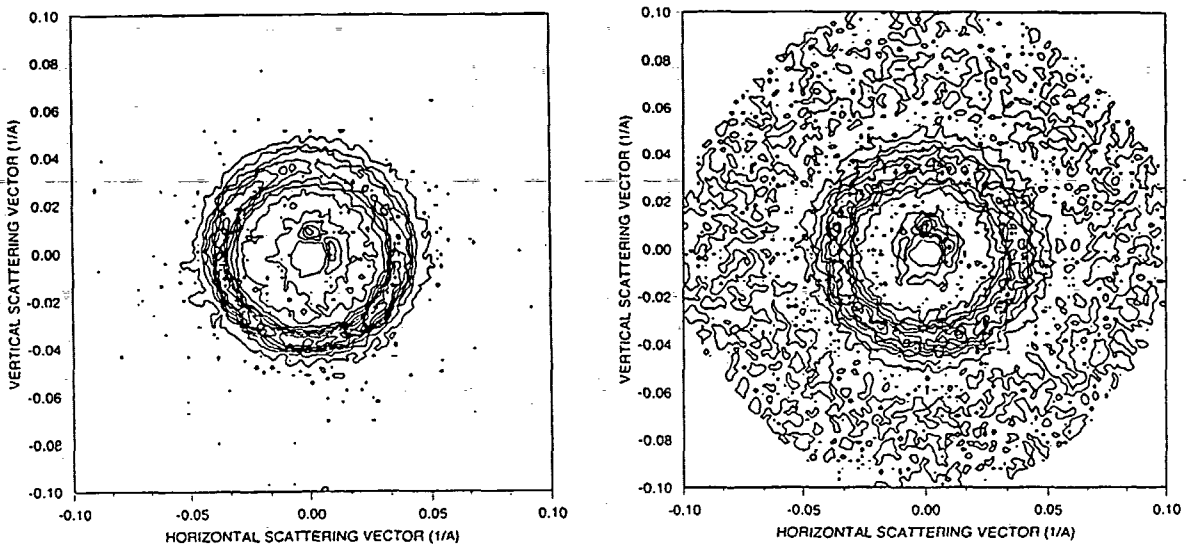

Figure 6.2: *Two-dimensional SANS-spectra of SBI11C at 124 (left figure) and 134°C (right figure). The isointensity lines are spaced linearly.*

two-dimensional spectra were isotropic (Fig. 6.2) both below and above the ODT. The spectra were azimuthally averaged and the background was subtracted. Lorentz-functions

$$I(q) = \frac{I_o}{1 + (q - q^*)^2 \xi^2} + I_{bg} \tag{6.5}$$

were smeared and fitted to the peaks (for the data analysis procedure see Chapter 5.5). In this way, the peak position, q^*, the peak height, I_o, and the correlation length, ξ, were obtained (Table 6.1). I_{bg} denotes a background which is due to incoherent scattering. The correlation length is the inverse half width at half maximum. For consistency, the same fitting range, $q = 0.025 - 0.055 \text{Å}^{-1}$, was chosen for all spectra. Variation of temperature changes the Flory-Huggins segment-segment interaction parameter ($\chi \propto 1/T$). A small χN-region can be studied in detail when varying temperature. In the present study, the range explored is $\chi N = 10.1 - 11.5$.

6.3 Results and Discussion

Narrow peaks are observed below 130°C. Above 130°C, the peaks are much broader and flatter (Fig. 6.3). The temperature where the intensity drops (129 – 130°C) is very close to the ODT temperature determined in dynamic mechanical measurements (130°C), where the elastic modulus drops (Chapter 3). The temperature difference of 1°C is attributed to a mismatch in temperature calibration of the sample holder used during SANS-experiments and the rheometer. As with SAXS (Chapter 5.4), it is observed that the intensity rises towards low q-values, which is attributed to large-scale density fluctuations or to voids. Density fluctuations of a typical size of 500 – 1000 Å have been observed in dynamic light

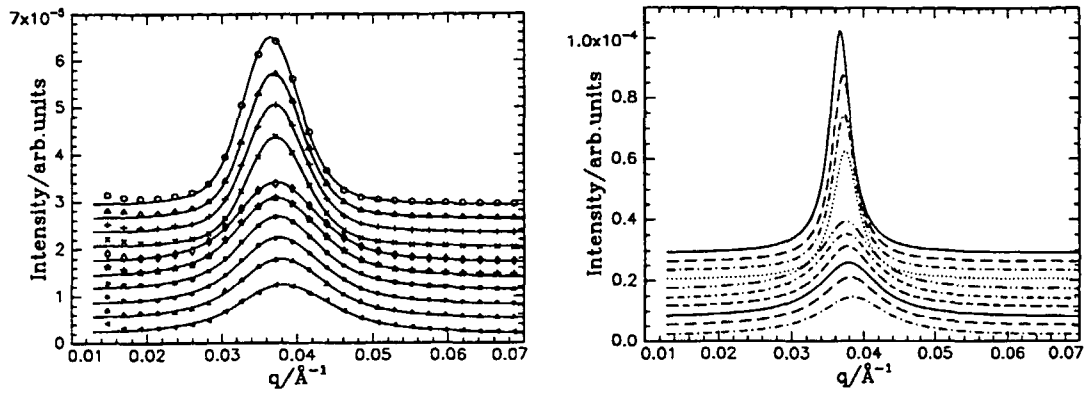

Figure 6.3: *Left figure: Azimuthally averaged SANS-spectra from sample SBI11C at some representative temperatures. From top to bottom: 114, 122, 126, 129, 130, 131, 134, 138, 142, and 150°C. The lines are fits of smeared Lorentz-curves. The curves are shifted. Right figure: The corresponding Lorentz-curves at the same temperatures (also shifted).*

scattering experiments (Chapter 7). However, good fits of Lorentz-functions were obtained in the peak range. The Lorentz-functions are shown in Fig. 6.3 (right figure). A drastic change in peak shape is observed between 129 and 130°C. The peak height decreases and the peak width increases upon heating.

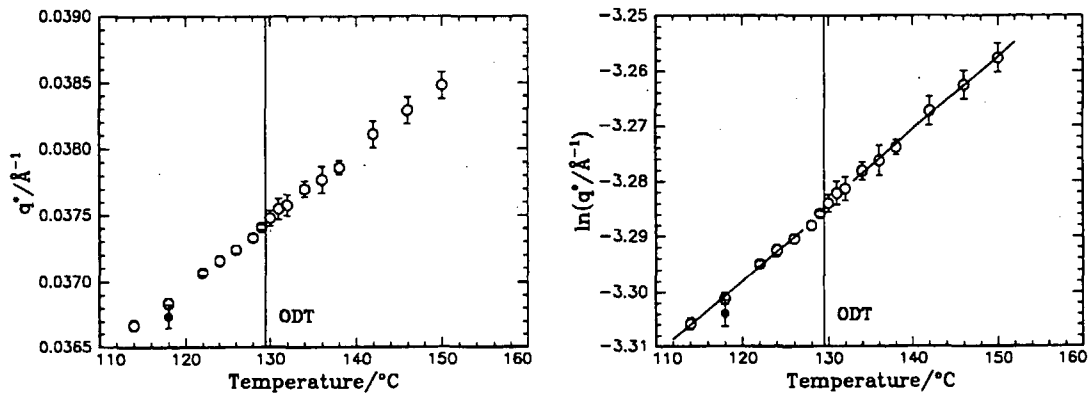

Figure 6.4: *Left figure: Peak position q^* versus temperature for sample SBI11C. The vertical line denotes the ODT temperature as determined from the drop in peak height. (o) heating, (•) cooling. Right figure:* $\ln(q^*)$ *versus temperature. Same symbols as in the left figure. The lines are linear fits.*

Plotting the peak positions, q^*, versus temperature (Fig. 6.4, left figure), a continuous rise of q^* with temperature is observed, *i.e.* the characteristic lengthscale decreases upon heating. Neither a discontinuous change nor a change in slope at the ODT is observed. One spectrum was measured at $\sim$ 118°C when cooling down from high temperatures. A slight mismatch in peak position is observed, which is attributed to temperature instability, the nominal temperature of 118°C being slightly too high. For further investigations, only data from the heating run will be used. In order to compare the variation of the characteristic

T/°C	q^*/Å^{-1}	I_o/arb.units	ξ/Å
114	$(3.667 \pm 0.004)10^{-2}$	$(7.34 \pm 0.24)10^{-5}$	572 ± 25
118	$(3.684 \pm 0.004)10^{-2}$	$(6.74 \pm 0.24)10^{-5}$	557 ± 27
122	$(3.707 \pm 0.002)10^{-2}$	$(6.15 \pm 0.11)10^{-5}$	546 ± 13
124	$(3.716 \pm 0.004)10^{-2}$	$(5.80 \pm 0.17)10^{-5}$	532 ± 22
126	$(3.724 \pm 0.003)10^{-2}$	$(5.15 \pm 0.14)10^{-5}$	503 ± 20
128	$(3.733 \pm 0.003)10^{-2}$	$(4.68 \pm 0.10)10^{-5}$	481 ± 16
129	$(3.741 \pm 0.002)10^{-2}$	$(4.24 \pm 0.07)10^{-5}$	469 ± 12
130	$(3.748 \pm 0.006)10^{-2}$	$(2.25 \pm 0.04)10^{-5}$	234 ± 10
131	$(3.755 \pm 0.008)10^{-2}$	$(2.18 \pm 0.04)10^{-5}$	212 ± 12
132	$(3.758 \pm 0.008)10^{-2}$	$(2.13 \pm 0.05)10^{-5}$	220 ± 13
134	$(3.770 \pm 0.006)10^{-2}$	$(2.04 \pm 0.04)10^{-5}$	222 ± 10
136	$(3.777 \pm 0.010)10^{-2}$	$(1.92 \pm 0.05)10^{-5}$	217 ± 16
138	$(3.786 \pm 0.005)10^{-2}$	$(1.83 \pm 0.02)10^{-5}$	202 ± 7
142	$(3.811 \pm 0.010)10^{-2}$	$(1.62 \pm 0.04)10^{-5}$	197 ± 15
146	$(3.829 \pm 0.010)10^{-2}$	$(1.46 \pm 0.03)10^{-5}$	186 ± 15
150	$(3.848 \pm 0.010)10^{-2}$	$(1.29 \pm 0.03)10^{-5}$	175 ± 13
118	$(3.674 \pm 0.009)10^{-2}$	$(5.96 \pm 0.43)10^{-5}$	538 ± 54

Table 6.1: *Peak positions of sample SBI11C at different temperatures. Given are the peak position, q^*, the peak height, I_o, and the correlation length ξ. The errors given are errors from the fit.*

lengthscale, $2\pi/q^*$, with the variation of the radius of gyration exclusively based on thermal expansivity, $\ln(q^*)$ was plotted versus temperature (Fig. 6.4, right figure). Fitting lines to $\ln(q^*)$, a slope of $(1.32 \pm 0.05) \times 10^{-3}\mathrm{K}^{-1}$ is obtained both in the ordered (fitting range 114 – 126°C) and in the disordered state (fitting range 134 – 150°C). Comparing these slopes to the value of $\kappa/2$ calculated for Gaussian chains, information about the deviations from Gaussian behavior is obtained: For a polystyrene-polybutadiene block copolymer, the average value of κ is calculated following [111]

$$\kappa = \frac{N_{PS}}{N_{PS}+N_{PB}}\kappa_{PS} + \frac{N_{PB}}{N_{PS}+N_{PB}}\kappa_{PB} \tag{6.6}$$

For sample SBI11C, the degrees of polymerization of the two blocks are $N_{PS} = 95$ and $N_{PB} = 155$.[2] The values of the thermal expansivities are $\kappa_{PS} = -1.1 \times 10^{-3}\mathrm{K}^{-1}$ for polystyrene [116] and $\kappa_{PB} = 0\ \mathrm{K}^{-1}$ for polybutadiene [117]. The value of κ_{PS} is negative which is attributed to an increasing flexibility of the coil. Thus, κ for Gaussian symmetric polystyrene-polybutadiene samples is $-4.2 \times 10^{-4}\mathrm{K}^{-1}$, *i.e.* $-\kappa/2 = 2.1 \times 10^{-4}\mathrm{K}^{-1}$. This value is a factor of six lower than the slopes obtained from the fit. This indicates that the chains are not Gaussian, but stretched in the temperature range between 114 and 150°C. Using the χN-value for the Gaussian- to stretched-coil transition, $\chi N \simeq 5$ (Chapter 7), the transition to Gaussian scaling is expected at ~ 350°C. In the temperature range studied here, the sample is thus well in the ISR. Several predictions exist about the scaling of the characteristic lengthscale with χ in the ISR (*e.g.* [71, 72, 73, 75] and Chapter 5.1). Due to the small χN-range covered in the present temperature study, it is not possible

[2]Note that $N_{PS} + N_{PB}$ is not equal to N as defined in Chapter 3.

to test these predictions reliably. It has been reported for polyethylene-poly(ethylene propylene) (PE-PEP) diblock copolymers that the slope in a narrow region around the ODT temperature is higher than below and above the ODT temperature [22]. This change of slope is not present in our data.

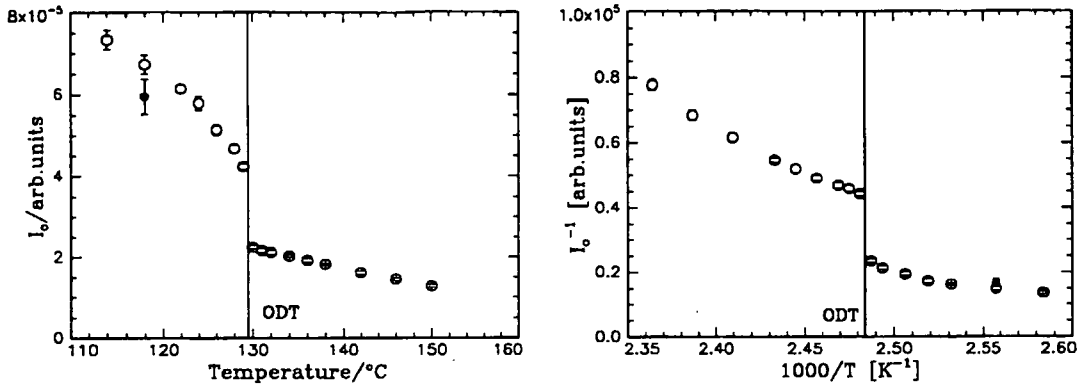

Figure 6.5: *Left figure: Peak height, I_o, versus temperature for sample SBI11C. The vertical line denotes the ODT temperature as determined from the drop in peak height. (o) heating, (•) cooling. Right figure: Inverse peak height versus inverse temperature.*

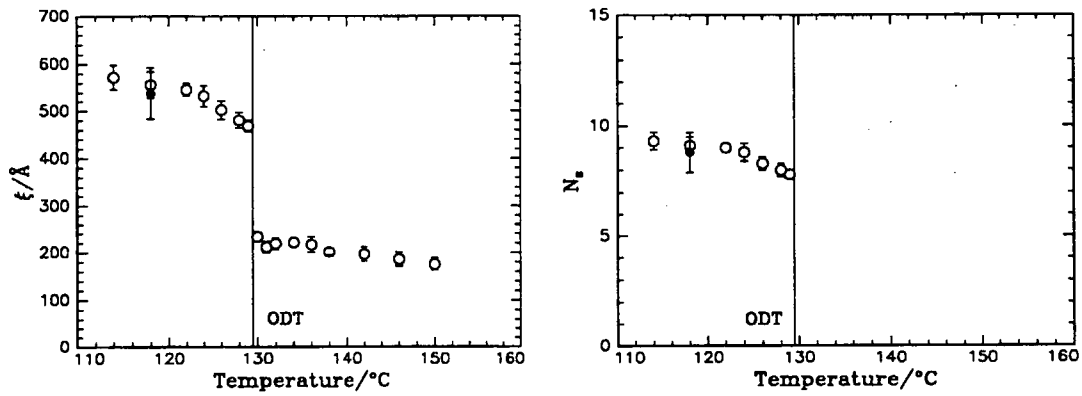

Figure 6.6: *Left figure: Correlation length, ξ, versus temperature for sample SBI11C. The vertical line denotes the ODT temperature as determined from the drop in peak height. (o) heating, (•) cooling. Right figure: Average number of lamellae per stack, N_s, versus temperature.*

The peak height, I_o, as a function of temperature is shown in Fig. 6.5. In the ordered state, the peak height decreases upon heating and eventually drops discontinuously at the ODT (between 129 and 130°C) to ca. half its value. Both SANS-experiments and dynamic mechanical measurements indicate that the phase transition is of weak first order. The peak height measured in the cooling run (at 118°C) is slightly lower than the value obtained in the heating run. This mismatch might be due to loss of sample in the beam. It may also be attributed to a difference in orientation of the lamellar grains in the heating and the cooling run. Plotting the inverse peak height versus the inverse temperature (Fig. 6.5, right figure), the drop between 129 and 130°C is also seen. At high temperatures, the inverse

peak height is predicted to depend linearly on the inverse temperature. This regime is not reached in the present study, as discussed above.

The correlation length, ξ, drops discontinuously at 129°C (Fig. 6.6). This reflects the loss of long-range order upon heating through the ODT. The average number of lamellae per stack in the ordered state, N_s, can be determined from $N_s = 2.783\, q^*\xi/(2\pi)$ (Eq. 5.45). N_s takes values between $N_s = 9$ at 114°C to $N_s = 8$ at 129°C. This value is consistent with the numbers found for other ordered, polycrystalline samples in the vicinity of the ODT (SBI12F and SBI08F at 150°C: $N_s = 10$, Chapter 5.5).

6.4 Summary

With a low molar-mass diblock copolymer, it has been observed that the peak height drops discontinuously at the ODT temperature. The peak width increases discontinuously, which reflects the fact that long-range order persists below the ODT temperature, but not above. The peak position rises continuously with temperature over the whole range studied. No change of behavior is observed at the ODT temperature, as expected from the behavior with chain length at fixed temperature (Chapter 5). The characteristic lengthscale is found to depend more strongly on temperature than is predicted for Gaussian chains. This indicates that the chains are stretched in the region studied ($\chi N \simeq 10.1 - 11.5$). In Chapter 5, it was found that the intermediate-segregation regime extends over a range $\chi N \simeq 5 - 27$. The sample studied here is well in the intermediate-segregation regime. It could be worthwile to test the predictions that exist about the scaling of the characteristic lengthscale with χ. For this purpose, one should choose a sample where a large range in temperature (and thus in χ) is accessible.

Chapter 7

Dynamic processes as observed with dynamic light scattering

(The dynamic light scattering experiments were carried out during my six months stay at the Department of Physical Chemistry at Uppsala University in the group of Prof. Wyn Brown.)

In this chapter, a study of the dynamic processes of three low molar-mass polystyrene-polybutadiene diblock copolymers using dynamic light scattering (DLS) is presented. In DLS experiments, the time-dependence of the fluctuating scattered intensity is recorded. The autocorrelation function of the scattered intensity gives information about the relaxation times of the dynamic processes occuring in the sample. DLS has, among others, been applied to polymer solutions and melts [118]. Due to their complex dynamic behavior, block copolymer melts have only recently been studied using DLS [119], and the field is still under progress. The present study focuses on the influence of the ODT and of the GST on the dynamic processes. For this purpose, the dynamics of a disordered sample was studied just above the ODT temperature. Four dynamic processes were identified: cluster diffusion (long-range heterogeneities), single-chain diffusion, a process related to chain stretching and the segmental reorientational dynamics of the polystyrene blocks. The same sample was studied in the lamellar state just below the ODT temperature. The dynamic processes identified in the disordered state were also observed in measurements on another disordered sample in the vicinity of the ODT. With a sample having lower molar mass, a region deeper in the disordered state was studied and the stretching mode was observed to disappear at $\chi N \simeq 5$, which indicates that the chains become Gaussian.

In the following sections, the background for the present study and the technique of DLS will be presented. As the data analysis was not straightforward, the methods used will be described in some detail. The results concerning the influence of the ODT and of the GST on the dynamics will be discussed. The chapter is an extended version of [110].

7.1 The dynamic processes in block copolymer systems

The dynamics of block copolymers have been intensively studied both in solution and in the bulk. A recent review is given in [119]. The dynamic processes in disordered diblock copolymers in the bulk which have been observed in diblock copolymer systems are schematically shown in Fig. 7.1.

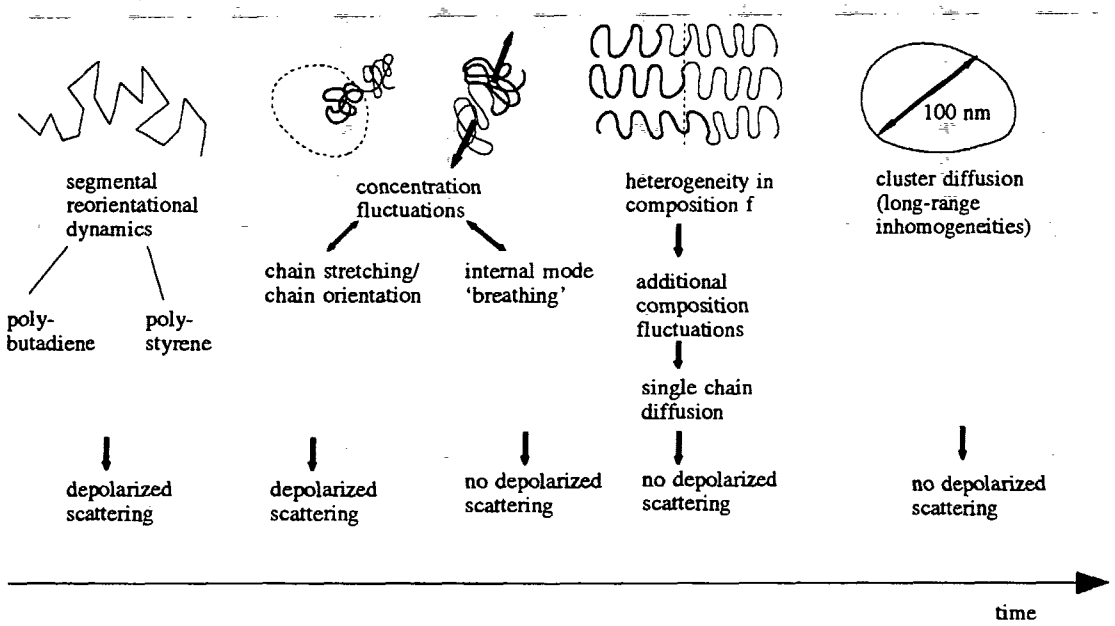

Figure 7.1: *Schematic survey of the dynamic processes in disordered diblock copolymer systems as a function of relaxation time. It is indicated which processes are optically anisotropic and therefore give rise to depolarized scattering.*

The only dynamic process ('mode' in dynamic light scattering jargon) predicted by mean-field theory for diblock copolymer systems in the disordered state is the internal chain mode (or 'breathing' mode) arising from the relative translational motion of the centers of mass of the two blocks [120, 121] (Fig. 7.1). This is the only mode predicted for a melt which is monodisperse both as regards composition and overall molar mass. On the scale of the inverse light scattering vector ($q^{-1} = 20 - 100$ nm), the process is local (for polymers of moderate molar mass), thus, the relaxation time is predicted to be independent of the scattering vector q for small values of q as they are used in dynamic light scattering. The structure factor, $S_I(q)$, is predicted to be q^2-dependent (the notation given in [122] is adopted):

$$S_I(q) \simeq \frac{2}{3} N v f^2 (1-f)^2 (qR_g)^2 \tag{7.1}$$

where N is the chainlength, v the segment volume, f the volume fraction of one block and R_g the overall radius of gyration. As the intensity of this mode is proportional to N^2 for Gaussian chains ($R_g \propto N^{1/2}$), it vanishes for short chains. This mode does not give rise to depolarized scattering (the scattering measured using crossed polarizers which arises from the rotation of anisotropic molecules) because it is essentially a translational and not a rotational motion of the segments (see below). Experiments on block copolymer melts [123, 124] have shown that this internal mode can only be observed for samples of

sufficiently high molar mass. As the polymers studied in the present work were of low molar mass, we did not expect to observe the internal mode.

The theory described above has been extended by Semenov to take into account the fact that real polymers are heterogeneous in composition, *i.e.* that there are variations in f from chain to chain [14]. This led to the prediction of a second mode (the 'polydispersity' mode) referred to here as the heterogeneity mode (Fig. 7.1). The heterogeneity of the chains leads to additional composition fluctuations in the block copolymer melt which causes chain diffusion. The heterogeneity mode is thus related to the self-diffusion coefficient of the block copolymer, D_s.[1] Being diffusive, the relaxation rate of this mode, Γ_H, is q^2-dependent:

$$\Gamma_H = D_H q^2, \qquad \text{where} \qquad D_H = D_s(1 - 2\chi N(\delta f)^2) \tag{7.2}$$

(The notation from [122] is adopted.) D_H is the diffusion coefficient related to the heterogeneity mode. The heterogeneity of the chains is described by the parameter

$$(\delta f)^2 = \frac{\bar{N}_W - \bar{N}_N}{4\bar{N}_W} = \frac{1}{4}\left(1 - \frac{1}{p}\right) \tag{7.3}$$

where $\bar{N}_W$ and $\bar{N}_N$ are the weight and number averaged chain length and $p = \bar{N}_W/\bar{N}_N$ the polydispersity index. Semenov assumed that the molar mass distributions of the two blocks are independent from each other. The intensity of this mode is predicted to be independent of q because $R_g \ll q^{-1}$ for polymers with moderate molar masses (typically a few nanometers), but dependent on the overall chainlength, N [119]:

$$S_H(q) = \frac{N(\delta f)^2}{1 - 2\chi N(\delta f)^2} \tag{7.4}$$

The amplitude thus vanishes if the heterogeneity goes to zero. This mode is not predicted to give rise to depolarized scattering because no segment rotations are involved. A wealth of experimental evidence has accumulated from dynamic light scattering experiments demonstrating the existence of the heterogeneity mode in block copolymer melts [123, 124, 125, 126].

However, the spectrum of relaxation times is often dominated and sometimes almost obscured by a very slow diffusive mode of high amplitude which has not been predicted by theory. This mode has the same characteristics as the 'cluster' mode described in glass-forming liquids [127], in concentrated polymer solutions [128] as well as in melts [129, 130]. It is described as due to cluster formation, long-range density fluctuations or heterogeneities with a characteristic size in the region of 100 nm (Fig. 7.1). This mode has been observed to have a q^2-dependent relaxation rate, *i.e.* it is diffusive. The amplitude was found to decrease strongly with q because the cluster size is comparable with q^{-1}. In addition, the amplitude was observed to be temperature-dependent and to vary strongly between different systems. In the system investigated here, this mode is the dominant feature under all conditions investigated. However, it is not clarified yet what the origin of these heterogeneities on a lengthscale much larger than the radius of gyration of the polymers is. We attribute the cluster mode to the finite compressibility of the polymer

[1] Self- and mutual diffusion are distinguished. Self-diffusion occurs in one-component system, the origin being thermal movement. The origin of mutual diffusion in a mixture is a concentration gradient.

melt. This notion is corroborated by the observation of a rise in scattering intensity towards low values of q in small-angle scattering experiments (Chapters 5.4 and 6)

A dynamic process known from homopolymer melts is the segmental reorientational dynamics (Fig. 7.1) [131]. Segments of the chain backbone or sidegroups move relatively to other segments and change their orientation which leads to depolarized scattering. The former process (*e.g.* the α-relaxation) becomes strongly temperature-dependent as the glass transition of the polymer is approached: the relaxation time of segmental reorientation increases strongly when approaching the glass transition [131]. The time-dependent correlation functions observed using dynamic light scattering are much broader than single-exponential. Usually, they are represented by a Kohlrausch-Williams-Watts (KWW) function

$$g_1(t) = a \exp((-t/\tau)^{\beta}) \tag{7.5}$$

with a stretching exponent β being significantly lower than one. The origin of this particular shape of the decay has not been clarified yet. In disordered block copolymer systems, the glass transition temperature may be shifted according to the degree of mixing (see Chapter 3). Depending on the difference of the glass temperatures of the blocks and on the amplitude of concentration fluctuations, the distribution of the segmental relaxation times has been found to be very broad [13] or bimodal [132, 133].

Depolarized DLS has recently allowed identification of an unexpected additional slow relaxation process in poly(styrene)-poly(isoprene) [134] and in poly(styrene)-poly(methyl phenyl siloxane) [135]. This mode was observed to be close to a single exponential with a q-independent relaxation rate and a strongly temperature-dependent amplitude. This mode was attributed to stretching and orientation of the copolymer blocks in the disordered state close to the ODT where concentration fluctuations are important (Fig. 7.1).

In the present work, three low molar-mass polystyrene-polybutadiene diblock copolymers were studied. With the highest molar-mass sample, the ODT temperature was accessible (130°C), such that the influence of the ODT on the dynamics could be studied. The two other samples were studied in the disordered state. With the lowest molar-mass sample, a region deep in the disordered state could be studied and the GST could be localized at $\chi N \simeq 5$. The time-dependent intensity autocorrelation functions of disordered samples were found to be dominated by a very slow mode which is attributed to cluster diffusion. Analysis of the underlying processes was not straightforward. A new subtraction technique [136] was used in order to reveal the faster dynamic processes which have comparably low amplitudes. The segmental relaxation of the polystyrene blocks is observable at the low limit of the time window. The glass temperature of polybutadiene is much lower than the one of polystyrene (Chapter 3), such that the segmental reorientational dynamics of the polybutadiene block are outside the experimental time window. In addition, two intermediate modes could be identified. One mode is mainly related to chain orientation and stretching and contributes to the depolarized intensity. The other mode is attributed to chain diffusion due to the concentration fluctuations arising from the inherent heterogeneity of the blocks.

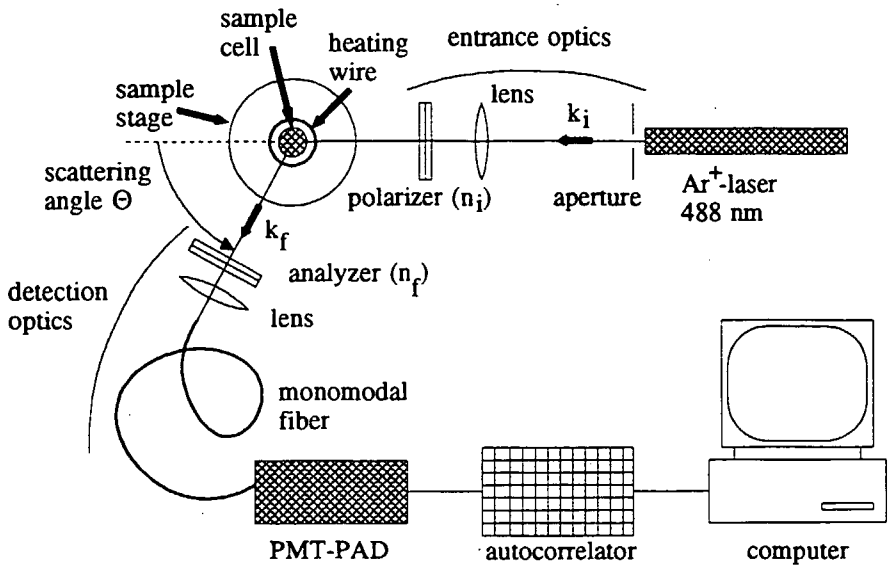

Figure 7.2: *Schematic view of the set-up used for dynamic light scattering.*

7.2 The technique of dynamic light scattering

Static and dynamic light scattering are widely used techniques for studying polymeric systems. Several reviews have been published recently; the books of B. Chu [137], P. Lindner and Th. Zemb [138], and W. Brown [118] provide a survey over the technique and its applications. Traditionally, dynamic light scattering has been used for determination of the translational diffusion coefficients of macromolecules in dilute solution and thereby their hydrodynamic radius ('particle sizing'). Only recently, more complex systems like concentrated polymer solutions, gels, and polymer blends have been studied [118].

Whereas in static light scattering the angular dependence of the time-averaged intensity is monitored and such information about the molar mass and of the shape of the solutes is obtained, in dynamic light scattering, the fluctuations of the scattered signal $I(q,t)$ with time are monitored. In this way, information is gained about the dynamic processes ('modes') in the sample. A schematic view of the set-up used in the present study is shown in Fig. 7.2. In order to determine the relaxation times, the time-dependent autocorrelation function of the fluctuating intensity is calculated. The time range of DLS is between few microseconds and 100 seconds. The technique is complementary to Fabry-Perot interferometry (Brillouin scattering) where smaller time scales can be studied. Dynamic light scattering is often used together with dielectric spectroscopy and dynamic mechanical measurements, which also probe the dynamic response, and with small-angle scattering giving structural information. In what concerns the q-range, the long wavelength of visible light leads to a q-range of $\sim 0.01 - 0.04$ nm^{-1} which is complementary to small-angle X-ray and neutron scattering ($\sim 0.02 - 5$ nm^{-1}).

The theory of light scattering is described in detail in the book of Berne and Pecora [139]. We will briefly review the fundamental theory as far as it is necessary for the

understanding of the results of the present study. Different approaches exist to the theory of light scattering. The most important ones are the theory of Rayleigh, Debye and Gans who described the scattering of particles that are large compared to the wavelength of the incoming beam. However, this approach is only valid for particles having a refractive index close to one. Mie considered particles having a refractive index different from one. The theory of Einstein and Smoluchowski considers a continuous medium where thermal fluctuations lead to local inhomogeneities and thereby to density and/or concentration fluctuations (the latter in mixtures). In what concerns the description of dynamic light scattering, Pecora showed that the frequency distribution of scattered light is related to the diffusion coefficient and to the rotational motions and the flexing of macromolecules.

In a dynamic light scattering experiment, a monochromatic, coherent and polarized laser beam impinges on the sample. The amplitude of the incident electric field may be written as

$$\vec{E}_i(\vec{r},t) = \vec{n}_i E_o \exp(i(\vec{k}_i \cdot \vec{r} - \omega_i t)) \tag{7.6}$$

with $\vec{n}_i$ the direction of polarization (usually chosen to be vertical), E_o the field amplitude, $\vec{k}_i$ the wavevector, and ω_i the angular frequency of the incident beam. In a homodyne experiment, as carried out in the present study, only the scattered radiation is detected as a function of time at a scattering angle θ.[2] The time-dependent intensity autocorrelation function is calculated and used for determination of the relaxation times present in the sample.

The tensor of the dielectric constant in a non-absorbing, isotropic medium can be written as a mean value, ϵ_o, plus local deviations, $\delta\epsilon$ [139]:

$$\epsilon(\vec{r},t) = \epsilon_o \mathbf{I} + \delta\epsilon(\vec{r},t) \tag{7.7}$$

$\mathbf{I}$ is the second-rank unit tensor. The amplitude of the scattered field in a distance R from the sample, $E_s(R,\vec{q},t)$, is related to the amplitude of fluctuations of the dielectric constant by [139]

$$E_s(R,\vec{q},t) = \frac{-k_f^2 E_o}{4\pi R \epsilon_o} \exp(i(k_f R - \omega_i t)) \delta\epsilon_{if}(\vec{q},t) \tag{7.8}$$

where k_f is the magnitude of the wavevector of the scattered ray, and where the scattering process has been assumed to be elastic ($\omega_f = \omega_i$). $\vec{q}$ is the scattering vector

$$\vec{q} = \vec{k}_f - \vec{k}_i, \qquad q = \frac{4\pi n}{\lambda_i} \sin\left(\frac{\theta}{2}\right) \tag{7.9}$$

where $n = \sqrt{\epsilon_o}$ is the refractive index of the sample and λ_i the wavelength of the incoming beam. In contrast to X-ray scattering where n is very close to one, the refractive index of many materials is significantly different from one for the wavelengths of light. The last term in Eq. 7.8, $\delta\epsilon_{if}(\vec{q},t)$, is the projection of the Fourier transformed dielectric fluctuation tensor onto the directions of polarization $\vec{n}_i$ and $\vec{n}_f$. These directions are determined by the directions of the polarizer and the analyzer (Fig. 7.2).

$$\delta\epsilon_{if}(\vec{q},t) = \vec{n}_f \cdot \delta\epsilon(\vec{q},t) \cdot \vec{n}_i \tag{7.10}$$

[2] In heterodyne experiments, the scattered radiation is mixed with the incoming beam, such allowing studies of slow processes [139].

where

$$\delta\epsilon(\vec{q},t) = \int_V d\vec{r}\exp(i\vec{q}\cdot\vec{r})\delta\epsilon(\vec{r},t) \tag{7.11}$$

is the Fourier transform of $\delta\epsilon(\vec{r},t)$. The time-dependent autocorrelation function of the scattered electric field is given by [139]

$$G_1(t) = \langle E_s^*(0)E_s(t)\rangle = \frac{k_f^4|E_o|^2}{16\pi^2R^2\epsilon_o^2}\langle\delta\epsilon_{if}(\vec{q},0)\delta\epsilon_{if}(\vec{q},t)\rangle\exp(-i\omega_i t) \tag{7.12}$$

where the brackets denote a time average. For simplicity, the arguments $\vec{q}$ and R were dropped. The field correlation function is thus related to the correlation function of the fluctuations of the dielectric constant. For very short lag times, there is full correlation, and $G_1(0) = \langle E_s(0)^2\rangle$. For times much larger than the period of fluctuations, the correlation decays and goes to $G_1(t) = \langle E_s\rangle^2$ for infinetely long times. The correlation function of the scattered field is normalized according to

$$g_1(t) = \frac{G_1(t)}{\langle E_s^*(0)E_s(0)\rangle} \tag{7.13}$$

The scattered intensity (which is the quantity measured in a DLS experiment) is given by [139]

$$I_{if}(R,\vec{q},t) = E_s^*(R,\vec{q},t)E_s(R,\vec{q},t) = \frac{|E_o|^2k_f^4}{16\pi^2R^2\epsilon_o^2}|\delta\epsilon_{if}(\vec{q},t)|^2 \tag{7.14}$$

The intensity is thus proportional to the square of the amplitude of the fluctuations of the dielectric constant.

In the present study, two polarization directions were used: In the polarized geometry, $\vec{n}_i$ and $\vec{n}_f$ were both vertical. The resulting intensity will be denoted $I_{VV}(\vec{q},t)$. All rotational and translational processes give rise to polarized scattering. In the depolarized geometry, $\vec{n}_i$ was vertical and $\vec{n}_f$ horizontal. The resulting intensity will be denoted $I_{VH}(\vec{q},t)$. Only those dynamic processes which turn the polarization plane of the incoming light, give rise to depolarized scattering, *e.g.* reorientational processes of anisotropic segments. Information about the relaxation times is obtained by calculating the autocorrelation function of the fluctuating intensity,

$$G_2(t) = \langle I_{if}^*(0)I_{if}(t)\rangle \tag{7.15}$$

If the scattering amplitude is distributed according to a Gaussian distribution[3], $G_2(t)$ is related to $G_1(t)$ by the Siegert relation [139]

$$G_2(t) = \langle I(0)\rangle^2 + |G_1(t)|^2 = \langle I(0)\rangle^2(1 + |g_1(t)|^2) \tag{7.16}$$

In order to account for the geometry of the instrument, the following expression is used:

$$G_2(t) = B(1 + f^*|g_1(t)|^2) \tag{7.17}$$

where f^* is the coherence factor depending on the size of the apertures, for instance (for measurement of f^* see below) and where $B = \langle I\rangle^2$ is the baseline, *i.e.* the level of the time-dependent correlation function for very long times. (At large times, the correlation is zero.) A single-exponential decay is shown schematically in Fig. 7.3.

[3]Cases where the distribution of the scattering amplitude is not Gaussian are very dilute solutions [139] or non-ergodic systems (*e.g.* gels) [140]

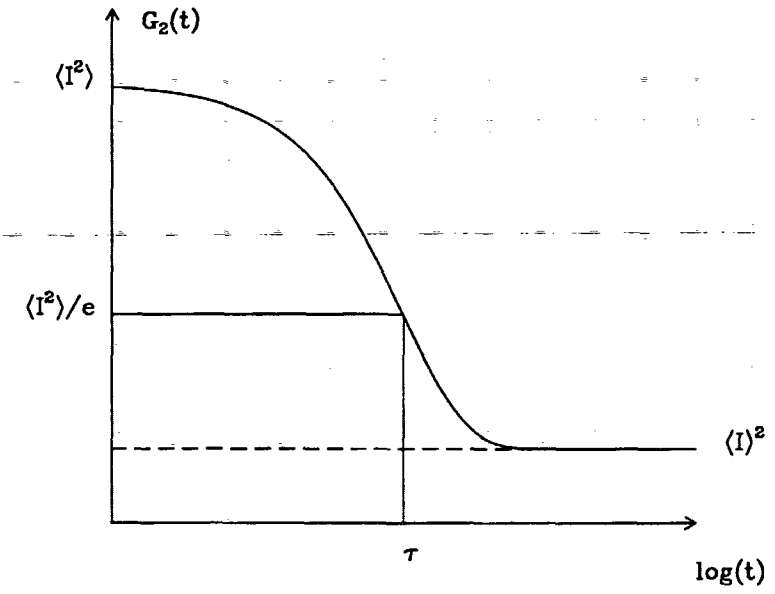

Figure 7.3: *The time-dependent intensity autocorrelation function $G_2(t)$ of a single exponential decay as a function of time in a semi-logarithmic representation. τ is the lag time where the correlation function has decayed to $1/e$ of its intitial value.*

Scattering of the incoming beam is due to fluctuations in the local dielectric constant which, in a binary mixture, is proportional to the amplitude of local concentration fluctuations, $\delta c(\vec{r},t)$ [139, 141]:

$$\delta\epsilon(\vec{q},t) \approx \left(\frac{\delta\epsilon}{\delta c}\right)_{T,p} \delta c(\vec{q},t) \tag{7.18}$$

Here, density fluctuations have been considered negligible compared to concentration fluctuations. The normalized field correlation function then reads

$$g_1(t) = \frac{\langle \delta c(\vec{q},0)\delta c(\vec{q},t)\rangle}{\langle |\delta c(\vec{q},0)|^2\rangle} \tag{7.19}$$

Fick's second law of diffusion describes the time behavior of macroscopic concentration fluctuations

$$\frac{\partial}{\partial t}\delta c(\vec{r},t) = D\nabla^2 \delta c(\vec{r},t) \tag{7.20}$$

where D is the collective diffusion coefficient of the particles and ∇^2 the Laplace operator [141]. If the inverse scattering vector, q^{-1}, is smaller than the size of the diffusing object, the collective diffusion of a group of molecules is probed [141]. Inserting the Fourier transform, $\delta c(\vec{r},t) = \int d\vec{q}\,\delta c(\vec{q},t)\exp(i\vec{q}\cdot\vec{r})$, in Eq. 7.20, it can be seen that $\delta c(\vec{q},t) = \delta c(\vec{q},0)\exp(-q^2Dt)$ is a solution of the diffusion equation. Then,

$$\langle \delta c(\vec{q},0)\delta c(\vec{q},t)\rangle = \langle |\delta c(\vec{q},0)|^2\rangle \exp(-q^2Dt) \tag{7.21}$$

and the autocorrelation function of the scattered field reads

$$g_1(t) = \exp(-q^2Dt) \tag{7.22}$$

which is a single-exponential process with relaxation rate $\Gamma = 1/\tau = Dq^2$. Plotting $\log(\Gamma)$ *vs.* $\log(q)$, a slope of two is obtained and the diffusion constant is obtained from the intersection with the $\log(q)$-axis, b: $D = 10^b$. Using the Stokes-Einstein relation (*e.g.* [4]),

$$D = \frac{k_B T}{6\pi\eta R_h} \tag{7.23}$$

where k_B denotes Boltzmann's constant, η the viscosity of the medium surrounding the diffusing particle, and R_h the hydrodynamic radius. If, on the other hand, the lengthscale of the relaxational process is smaller than q^{-1}, one speaks of local relaxational processes. In this case, the time-dependent field correlation function reads

$$g_1(t) = e^{-t/\tau} \tag{7.24}$$

The corresponding intensity autocorrelation function is shown schematically in Fig. 7.3. One should note that light scattering experiments are not the same as relaxation experiments [139]. In relaxation experiments, a system which, in a first time, is subject to constraints, is left free by removing the constraints and relaxes to a new equilibrium. On contrary, in light scattering, fluctuations around an equilibrium state are probed. However, Onsager predicted that spontaneous fluctuations 'regress' back to equilibrium according to the same relaxation equations that describe macroscopic relaxation processes [139].

To summarize, dynamic light scattering is a technique which allows the determination of diffusion coefficients and of relaxation times, arising from density or concentration fluctuations. In addition, it is possible to detect optically anisotropic dynamic processes by comparison of the depolarized and the polarized intensity.

7.3 The set-up

The set-up used for DLS experiments is shown in Fig. 7.2. The light source is a frequency-stabilized argon-ion laser (Coherent Innova 300) emitting vertically polarized light at a wavelength of 488 nm (single mode), which is in the blue region. The advantage of argon-ion lasers is their high power compared to conventional helium-neon lasers. A power of 300 resp. 500 mW was used in the polarized and in the depolarized geometry, resp., which is a factor 6 – 10 higher than the power of a HeNe-laser (typically 50 mW). An aperture in front of the outlet defines the beam size. The degree of polarization is increased by a Glan-Thompson polarizer which transmits only vertically polarized light. The extinction coefficient, *i.e.* the ratio of transmissions of vertically and horizontally polarized light is larger than 10^6. The polarizer consists of two birefrigent calcite crystals cemented together and is mounted on a gimbal which allows tilting. The polarizer defines the axis of polarization, $\vec{n}_i$. The polarized beam is focused by means of a lens such that a spot of diameter ~ 0.5 mm on the sample is illuminated.

The sample is heated by means of a Philips heating coil wound around the inner part of the sample holder. The heating coil is connected to a temperature controller (Fig. 7.4). The sample temperature is measured using a thermocouple mounted very close to the sample cell. The temperature stability is estimated to be ± 1°C. In the temperature range where measurements were carried out (65 – 160°C), the index matching bath which is

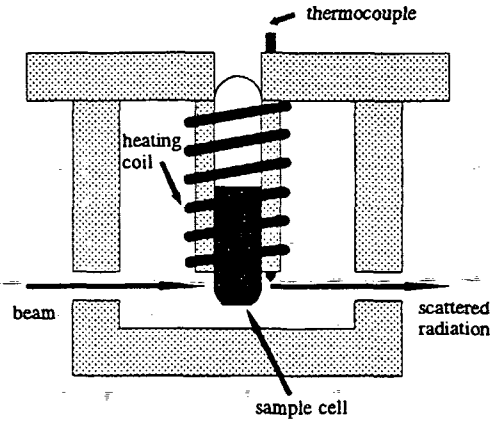

Figure 7.4: *Schematic cross-sectional view of the sample stage showing the sample cell, the heating coil and the thermocouple used for temperature control of the sample.*

normally used had to be removed.[4] However, as the rays diffracted by the walls of the sample cell are not coherent with the scattered, non-diffracted radiation, they are not transmitted by the monomodal fiber used for detection (see below).

Parts of the detection optics, *i.e.* an analyzer, a lens and the monomodal fiber are mounted on a turntable, such that they can be installed at different scattering angles. In order to detect dynamic processes which rotate the plane of polarization of the light (*e.g.* segmental reorientational processes), the scattered radiation is passed through a Glan-Thompson polarizer with an extinction coefficient of $\sim 10^7$ which is installed in the vertical (I_{VV}) or in the horizontal position (I_{VH}). By means of a lens, the scattered radiation is focused onto a monomodal fiber having a diameter of 4 μm. The advantage of monomodal fibers is that they only transmit coherent light due to their small diameter which is comparable to the wavelength of light. This leads to a reduction of the baseline compared to conventional pinhole geometries. In this way, values of the intercept f^* very close to one are obtained, thus significantly higher values than in pinhole geometries. The characteristics of monomodal fibers are discussed in detail in [142]. By means of the fiber, the coherently scattered light is coupled into the photomultiplier (ITT FW130). The output signal is amplified and digitized by an ALV-PM-PD amplifier discriminator. Intensity time correlation functions are obtained online using an ALV-5000 multibit, multitau full digital autocorrelator with 288 channels producing an equidistant spacing of delay times on a logarithmic time axis. The minimum real sampling time is 0.2 μs and the maximum $\sim$ 100 s. The advantage of the 'logarithmic' time spacing is the large span of delay times measured simultaneously. This is especially important when studying concentrated systems, where dynamic processes in a large range of time scales occur.

[4] Usually, the sample cuvette is immersed into an index matching bath having a large diameter ($\sim$ 10 cm) in order to minimize lens effects at the glass walls of the sample cell. The index matching bath is filled with filtered decalin which has approximately the same index of refraction as glass. Decalin degrades at $\sim$ 50°C.

7.4 The experiment

Three low molar-mass samples were studied using dynamic light scattering. Their characteristics are given in Table 7.1.

sample	$\bar{M}_N$/(g/mol)	N	T/°C	η/Pas
SB05	9200	156	72	88
			111	4.3
			129	1.9
			135	1.7[a]
			150	0.89
SB14	13900	236	110	36
SB11	18300	310	135	70

Table 7.1: *Characteristics of the samples used for dynamic light scattering studies. Given are the overall stoichiometric molar mass, $\bar{M}_N$, the chain length based on the polybutadiene segment volume, N, and the zero-shear viscosity, η, at different temperatures. (a) interpolated between 129 and 150 C.*

In dynamic light scattering experiments, it is crucial that the samples are dust-free. As the size of dust particles may be comparable to the wavelength of visible light, they scatter strongly and lead to overflows of the correlator. Therefore, great care was taken to filter the samples and to clean the sample cells. Dust-free samples were prepared in precision-bore NMR tubes (Wilmad Glass Inc., diameter 10 and 12 mm), which were used as sample cells. The tubes were cleaned in sulfochromic acid, filtered ethanol or THF using 0.1 μm Anotop filters. Amounts of 0.9 – 2.0 g polysytrene-polybutadiene were dissolved in benzene and then filtered directly into the tubes, using the same type of filters. The solvent was slowly evaporated under an inert atmosphere at 30 – 60°C for some days. Residual traces of benzene were removed by annealing the samples at 120 – 150°C for 2 days under vacuum. To minimize the risk of cross-linking, the polybutadiene-blocks, the tubes were thoroughly flushed with nitrogen gas prior to flame-sealing. Size exclusion chromatography was carried out when the measurements were finished and showed that no crosslinking had occurred.

The samples were allowed to equilibrate at the measuring temperature for several hours before the measurements. Correlation functions of polystyrene-polybutadiene samples were measured for 1 – 4 h in the polarized geometry and for 10 – 12 h in the depolarized geometry. In order to establish the q-dependence of the different modes, measurements in the polarized geometry were made at several angles between 40 and 150°. Measurements in the depolarized geometry were only made at an angle of 90° because they only served for identification of processes giving rise to depolarized scattering.

In order to determine the light scattering vector, $q = 4\pi n/\lambda \sin(\theta/2)$, knowledge of the refractive index of the polystyrene-polybutadiene samples is prerequisite. The refractive index of polystyrene-polybutadiene is given by [34]

$$n = w_{PS} n_{PS} + (1 - w_{PS}) n_{PB} \tag{7.25}$$

$w_{PS} = 0.55$ is the weight fraction of polystyrene (Chapter 3). n_{PS} and n_{PB} are the refractive indices of polystyrene and polybutadiene, respectively. The following values were used: $n_{PS} = 1.59$ and $n_{PB} = 1.518$ at 20°C [34]. Thermal expansion was taken into account using [34]

$$\frac{dn}{dT} = \alpha \frac{(n^2+2)(n^2-1)}{6n} \tag{7.26}$$

where α denotes the coefficient of thermal expansion. $\alpha = 2.52 \times 10^{-4}\mathrm{K}^{-1}$ was used for polystyrene below 90° and $\alpha = 5.76 \times 10^{-4}\mathrm{K}^{-1}$ above [34]. For polybutadiene, $\alpha = 7.5 \times 10^{-4}\mathrm{K}^{-1}$ was used [34]. At temperatures between 100 and 120°C, $n = 1.52$ was found and $n = 1.50$ at 135°C. As a large part of the measurements was carried out at 110°C, the value of 1.52 was used throughout.

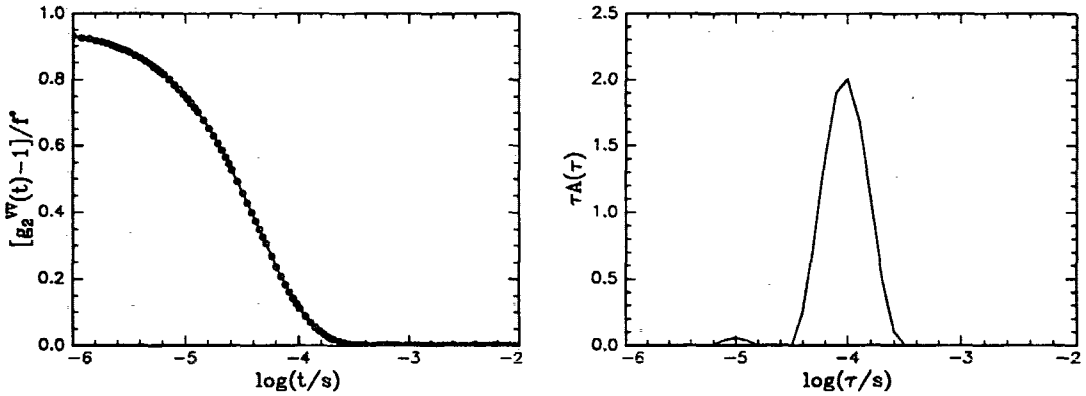

Figure 7.5: *Left figure: Correlation function of a dilute solution of polystyrene in ethylacetate at 22°C and an angle of 90°C. The circles are experimental points and the line is a fit using REPES. Right figure: The corresponding distribution function as determined with REPES.*

For determination of the short-time intercept, f^*, a sample was chosen where dynamic processes having relaxation times shorter than $\sim 10^{-6}$ s are known to be negligible in amplitude, nearly the whole decay being represented in the experimental time window. Dilute polymer solutions, where the dominant decay is due to coil diffusion, meet these requirements. Segmental orientational relaxation processes are known to be too fast to be detected and are negligible in amplitude in the polarized experiment compared to the diffusional mode. In principle, $g_2^{VV}(t) - 1$ should thus go to one for short lag times. Deviations are attributed to instrumental resolution effects. In this study, a dilute solution of high molar-mass polystyrene ($M = 5 \times 10^6$ g/mol) in ethylacetate was used. The difference in refractive index of polystyrene and ethylacetate is relatively high ($\Delta n = 0.22$ [34, 143]), ensuring good contrast. Measurements were made at 90° at 22°C without an index matching bath. The distribution of relaxation times as determined using REPES (see below) displays a dominant peak at ($\tau \simeq 10^{-4}$ s) which is attributed to coil diffusion. In addition, there is a small contribution at $\tau \simeq 10^{-5}$ s which might be due to internal relaxation processes of the chain. Using REPES (see below), the intercept was found to be $f^* = 0.957 \pm 0.003$ which was used for data analysis throughout the study.

For the calculation of the hydrodynamic radius, R_h, knowledge of the zero-shear viscosity of the polystyrene-polybutadiene samples, η, *i.e.* the viscosity at vanishing shear

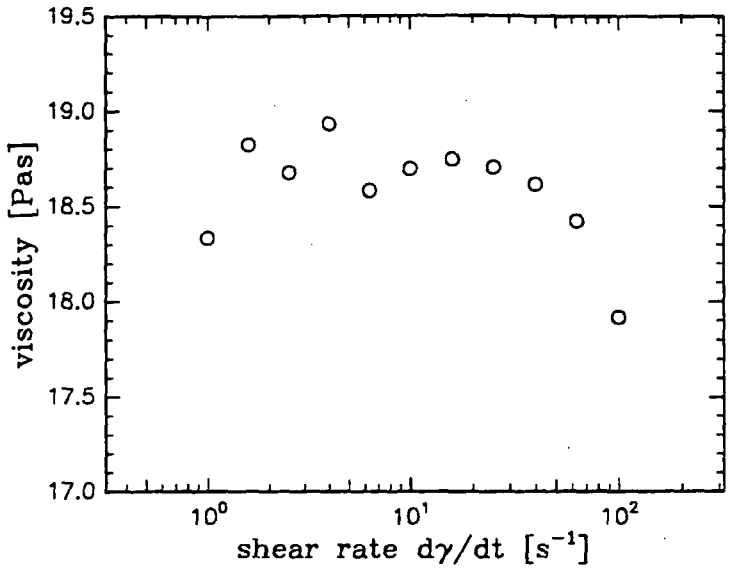

Figure 7.6: *Zero-shear viscosity of sample SB11 at 150°C measured in a cone-and-plate geometry. The average value is 18.7 Pas.*

rate, is prerequisite (Eq. 7.23). Zero-shear viscosities were determined in a Rheometrics RMS-800 rheometer (Chapter 3) operated in the cone-plate geometry (diameter 25 mm) and applying simple shear. At each temperature, the shear rate was varied between 1 and 100 s^{-1}. A typical curve is shown in Fig. 7.6. At high shear rates, the viscosity decreased indicating non-Newtonian behavior. The values obtained from averaging data at low shear rates are given in Table 7.1. The zero-shear viscosity was found to be strongly temperature-dependent.

7.5 Data analysis

Methods for analysis of dynamic light scattering data have recently been reviewed [140]. The quantity measured in a dynamic light scattering experiment, as described above, is the time-dependent intensity autocorrelation function, $g_2(t)$, from which the time-dependent autocorrelation function of the scattered electric field is deduced using Eq. 7.17:

$$g_1(t) = \sqrt{(g_2(t) - 1)/f^*} \tag{7.27}$$

Many dynamic processes are single-exponential (Eqs. 7.22 and 7.24), such that $g_1(t) = \exp(-t/\tau)$ where τ is the relaxation time found at a given scattering vector. However, complex systems (such as block copolymer melts) are known to exhibit distributions of relaxation times, $A(\tau)$, such that the field correlation function is given by the Laplace transform of the distribution

$$g_1(t) = \int d\tau A(\tau) \exp(-t/\tau) \tag{7.28}$$

$$= \int d(\ln(\tau))\, \tau A(\tau) \exp(-t/\tau) \tag{7.29}$$

The so-called 'equal-area representation' $\tau A(\tau)$ *vs.* $\log(\tau)$ is convenient when using a logarithmic time axis. In this way, the ratio of peak areas in a plot of $\tau A(\tau)$ *vs.* $\log(\tau)$ is the same as in the representation $A(\tau)$ *vs.* τ [140]. As the inversion of the Laplace transformation is ill-conditioned, sophisticated numerical methods are necessary to determine the distribution functions. Due to noise, there is no unique solution for the distribution function, *i.e.* different distribution functions can lead to an equally good fit. Thus, in many approaches, *a priori* information is used, *e.g.* the shape of the distribution or the non-negativity constraint $A(\tau) > 0$ [140]. In the present study, two methods were used: a simultaneous fit of two Kohlrausch-Williams-Watts (KWW) functions and the routine REPES (Regularized Positive Exponential Sum). Both routines were implemented in the program GENDIST ('General Distribution') which was developed by the Uppsala group [144].

The KWW-function which is also called 'stretched exponential' reads

$$g_1(t) = a_o + a \exp((-t/\tau)^\beta) \tag{7.30}$$

Fitting parameters are the relaxation time τ, the exponent β, the amplitude a, and the baseline a_o. The smaller β, the broader is the decay. If $\beta = 1$, the decay is single-exponential. No analytic form of the inverse Laplace transform of the KWW-function exists except in the single-exponential case. The expression is often used for describing the correlation functions due to the segmental reorientational dynamics of polymers, where β has been found to be significantly lower than one (*e.g.* [131, 145]). In this study, a fitting routine was used where up to two KWW-functions were fitted simultaneously to the field correlation function, $g_1(t)$:

$$g_1(t) = a_o + a_1 \exp((-t/\tau_1)^{\beta_1} + a_2 \exp((-t/\tau_2)^{\beta_2} \tag{7.31}$$

which constitutes a fit with seven parameters.

REPES [146] is a grid method where the only constraint is the non-negativity of the distribution. No assumptions are made about the shape of the distribution. REPES has formal similarities to CONTIN [147]. A grid which is equidistant on a logarithmic time scale, $\log(\tau_i)$, $i = 1, \ldots, N$ is selected and the solution is set up in a discrete form. The result of the fit to the correlation curve are the amplitudes at the grid points, $a(\tau_i)$, $i = 1, \ldots, N$. The number of independent fitting parameters is thus N, which may be a large number: One typically uses $4 - 10$ points/decade in lag time and performs a fit over up to 10 decades, which gives $40 - 100$ amplitude values that are iterated simultaneously. In order to avoid solutions consisting of many sharp peaks, which might be unphysical, a Lagrange operator is used when minimizing the difference between data points and fitting curve. By means of this Lagrange operator, high second derivatives of the distribution function are penalized. The degree of penalization is related to a smoothing parameter ('probability to reject'), which the user may vary in order to acquire the desired degree of smoothness of the distribution function. It has been found that the values of the relaxation times depend only little on the degree of smoothing, unless the number of peaks changes upon smoothing [140]. In contrast, the peak width is strongly dependent on the degree of smoothing and is therefore not used for further analysis. The routine REPES fits directly to the intensity correlation function, $g_2(t)$. This is different in CONTIN, where $g_1(t)$ is extracted from the measured data, $g_2(t)$, and used for fitting. Using $g_2(t)$ directly has the advantage of avoiding calculation of the square root (which may lead to a poor

determination of the baseline [140]), but requires non-linear fitting:

$$g_2(t) - 1 = f^* \left(\int d(\ln(\tau))\, \tau A(\tau) \exp(-t/\tau) \right)^2 \tag{7.32}$$

Using REPES, one can vary the fitting range, the number of grid points per decade and the probability to reject, *i.e.* the smoothness of the distribution.

In the present study of block copolymer melts, a slow mode with a very high amplitude (typically > 95%) is present, which made the analysis of the other modes having comparably low amplitudes impossible with standard techniques. It was not possible to perform a reasonable fit to the whole correlation function in one run, which was the reason for using a newly developed subtraction routine [136]. Subtraction of single modes was carried out as follows: A fit to the whole correlation function was carried out using REPES. Then, the data points as well as the fitting curve were converted to $g_1(t)$-values. The fit $g_1^{fit}(t)$ reads

$$g_1^{fit}(t) = \sum_i a_i \exp(-t/\tau_i) \tag{7.33}$$

In order to subtract a single decay, $a_k \exp(-t/\tau_k)$, its amplitude was calculated from the area under a histogram bar in the graph $\tau A(\tau)$ *vs.* $\log(\tau)$. Then, the quantity $a_k \exp(-t/\tau_k)$ was subtracted from each experimental $g_1(t)$-value. The such obtained $g_1(t)$-values were then converted to $g_2(t)$-values using the Siegert relation (Eq. 7.17). The remaining curve was then treated as usually.

Alternatively, the routine allowed subtraction of a single fitted KWW-function, $a_1 \exp((-t/\tau_1)^{\beta_1})$ from each experimental $g_1(t)$-value. After subtraction, the remaining $g_1(t)$-values were converted to $g_2(t)$-values and could be treated further.

As will be established below, four modes contribute to the correlation function. Our aim was to characterize each mode by its relaxation time, τ_i, its KWW-exponent, β_i, and its relative amplitude, a_i. The index i increases from 1 to 4 from the slowest to the fastest mode. For illustration of the subtraction procedure, the correlation function of sample SB11 at 135°C (in the disordered state) measured in the polarized geometry is shown in Fig. 7.7a. We will first describe the subtraction procedure and then comment on the difficulties encountered. First, a single KWW-function was fitted to the slowest mode ($i = 1$) such determining τ_1 and β_1. Our experience was that subtraction of this KWW-function often lead to a poorly determined baseline after subtraction. Therefore, the whole correlation curve was analyzed using REPES, leading to a sharp and dominant peak at long relaxation times ($\sim$ 100 s) together with components of very low intensity (Fig. 7.7b). This fit gave the relative intensity of the slow mode, a_1. This slow component was subtracted as described above which gave the correlation function shown in Fig. 7.7c. Analysis of this curve was not straightforward. First, it was interpreted as consisting of two modes, which did not give consistent results (see below). However, analyzing the curve using REPES showed that three components were present, labelled 2, 3 and 4 in Fig. 7.7d. It should be noted that REPES has a tendency to split broad peaks up into several components [146] (as is the case with mode 4), especially when there is a sharp peak adjacent to the broad distribution. We thus interpreted the distribution to consist of 3 modes. In order to analyze mode 2 and 3 in detail, the fast component (4) was subtracted (Fig. 7.8a). A fit of a double KWW-function to the remaining correlation curve gave the relaxation times τ_2 and τ_3, the KWW-exponents β_2 and β_3, and the amplitude ratio

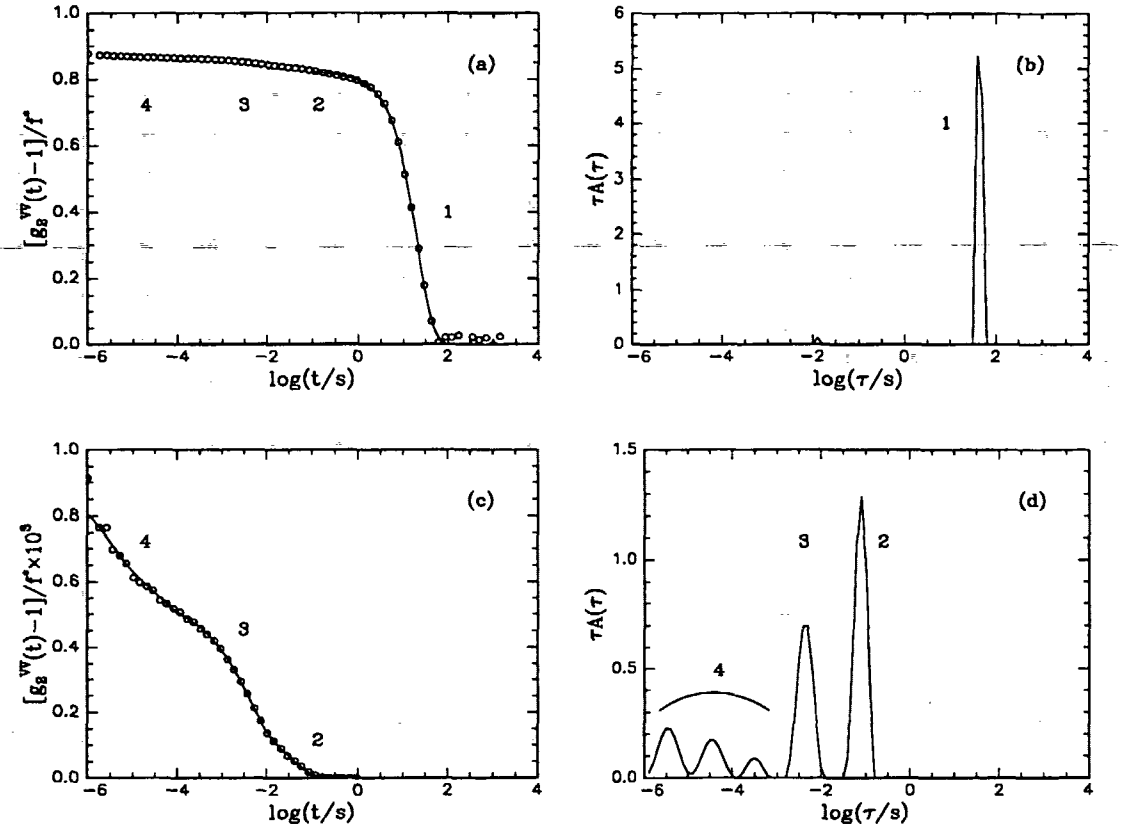

Figure 7.7: *Left side: Correlation functions of SB11 at 135°C in the polarized geometry at an angle of 60°. Right side: The corresponding distribution functions found using REPES. (a) Correlation function before subtraction. For clarity, only every fourth point is show. The line is a fit of a KWW function to the slow mode. (b) Corresponding distribution function. (c) Correlation function after subtraction of the slow mode (1) (see text). The line is a fit using REPES. Every fourth point is shown. (d) Corresponding distribution function.*

$a_2/(a_2 + a_3)$. The corresponding distribution function is shown in Fig. 7.8b. In order to characterize the fastest mode (4), the distribution determined using REPES shown in Fig. 7.7d was used and modes 2 and 3 were subtracted. The remaining correlation function is shown in Fig. 7.8c. A REPES-analysis gave a broad peak characteristic for segmental reorientation processes (Fig. 7.8d). Fitting a single KWW-function to this decay, τ_4 and β_4 were determined. However, as this mode was only partially represented in the time range accessible, τ_4 and β_4 could not be determined precisely.

The analysis of the present kind of correlation functions was not straightforward for different reasons. The slow mode (1) could in many cases not be fitted in a satisfactory way using REPES. It was found to decay steeper than single-exponential. For instance, the KWW-exponent of the correlation curve shown in Fig. 7.7a was found to be $\beta_1 = 1.2$, thus substantially higher than 1.0. The fit of a double KWW-function to a part of the correlation function from sample SB11 at 135°C is shown together with a fit using REPES in Fig. 7.9. In both cases, datapoints up to $\log(\tau/s) = 1.6$ were used. The fit using

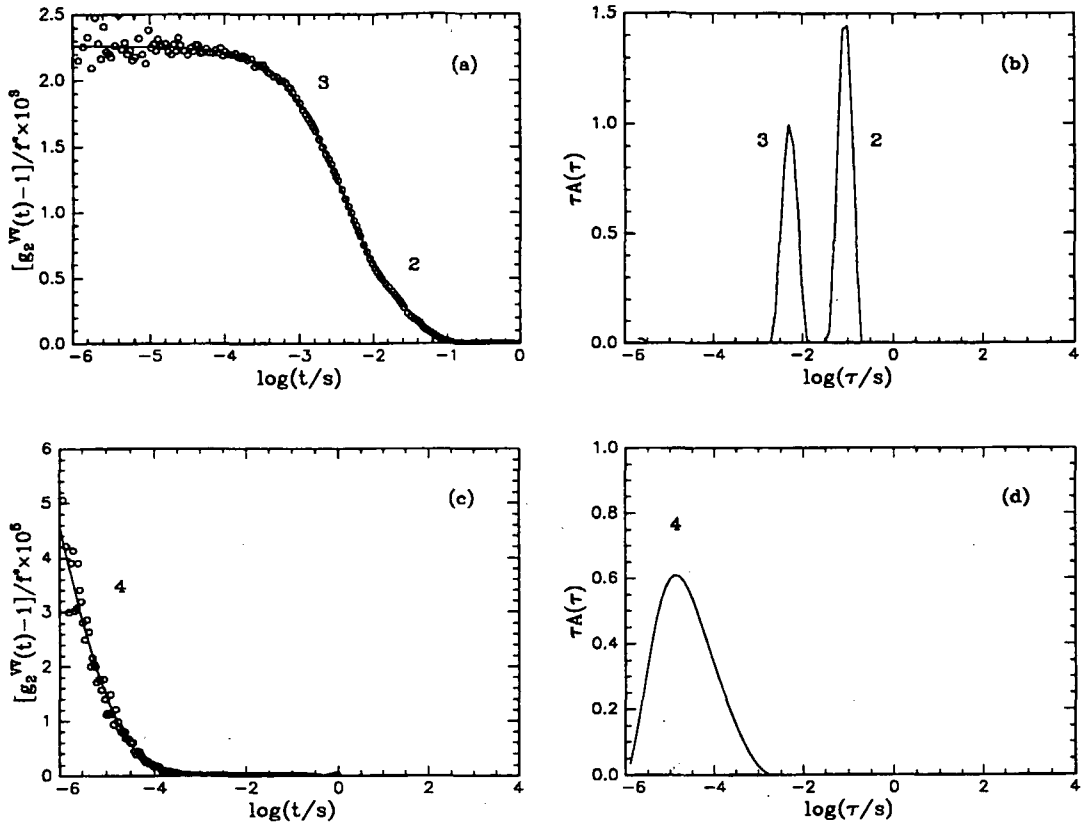

Figure 7.8: *Further treatment of the correlation function from Fig. 7.7. (a) Correlation function after subtraction of mode 4 from the curve shown in Fig. 7.7c. The line is a fit of a double KWW-function. (b) Corresponding distribution function. (c) Correlation function after subtraction of the modes 2 and 3 from the curve shown in Fig. 7.7c. The line is a fit of a single KWW-function. (d) Corresponding distribution function.*

REPES deviates from the experimental data. The reason for this phenomenon could not be established yet. As the relaxation times of the slow mode are at the long-time limit of the correlator ($\tau \simeq 100$ s), it might be that the statistics are not good enough, in spite of measuring times of several hours. It is not clear if there is a physical reason for a relaxation process decaying faster than single-exponential. In order to get a well-defined baseline after subtraction, only the uppermost points of the slow mode (in this case up to $\log(\tau/s) \simeq 0.44$) were used for fits with REPES (the full line in Fig. 7.9). The amplitude of the slow mode was then taken as the baseline (here ~ 0.62) plus the amplitude of the decay given by the program (here ~ 0.23).

Another problem was the large difference in amplitudes of the four modes which made it difficult to establish the number of remaining modes and the q-dependence of their relaxation times reliably. In a first approach, the two middle modes (2 and 3) were treated as being one mode. A fit of a double KWW-function to this middle and to the fast mode after subtraction of the slow mode is shown in Fig. 7.10. It can be seen that the fit deviates slightly from the experimental data. The middle mode identified in this way was found to be approximately diffusive, but it had an average KWW-exponent of

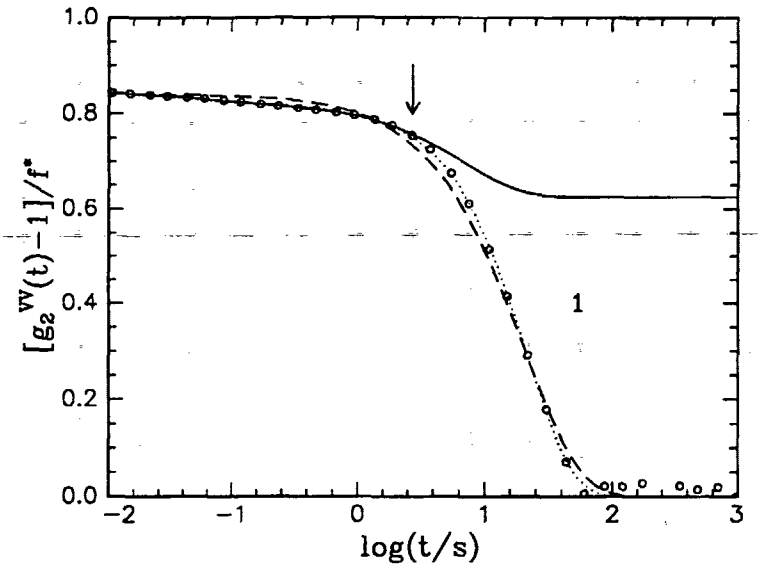

Figure 7.9: *Correlation function of sample SB11 at 135°C at an angle of 60° in the polarized geometry. For clarity, only every fourth datapoint is shown. The dotted line is the fit of a double KWW-function and the broken line a fit using REPES. In both cases all datapoints up to* $\log(t/\mathrm{s}) = 1.6$ *were used. The full line is a fit using REPES using the points up to* $\log(t/\mathrm{s}) = 0.44$ *as indicated by the arrow.*

$0.5-0.6$, which is considered contradictory. Using REPES, it became clear that this mode is a composite (Figs. 7.7d and 7.8b).

In order to calculate the amplitudes $a_1, \ldots, a_4$, the following procedure was applied. From the initial analysis with REPES, the amplitudes A_1 and A_4 of the slow and the fast mode and the baseline B were used. The normalization was such that $\sum_i A_i + B = 1$. Then, the amplitude of mode 1 was set to

$$a_1 = A_1 + B \tag{7.34}$$

(Fig. 7.9) and the amplitude of the fastest mode to

$$a_4 = A_4 \tag{7.35}$$

After subtraction of the slow and the fast mode, the two middle modes (2, 3) were analyzed with better precision using a double KWW function. This fit gave the fraction of mode 2, $f_2 = a_2/(a_2 + a_3)$. The amplitudes of modes 2 and 3 were then calculated using

$$a_2 = [1 - (a_1 + a_4)]f_2 \tag{7.36}$$

and

$$a_3 = [1 - (a_1 + a_4)](1 - f_2) \tag{7.37}$$

The amplitudes $a_1, \ldots, a_4$ were multiplied with the total scattering intensity, I, and with $\sin\theta$ in order to correct for the change of scattering volume with scattering angle, θ:

$$I_i = a_i I \sin\theta, \qquad i = 1, \ldots, 4 \tag{7.38}$$

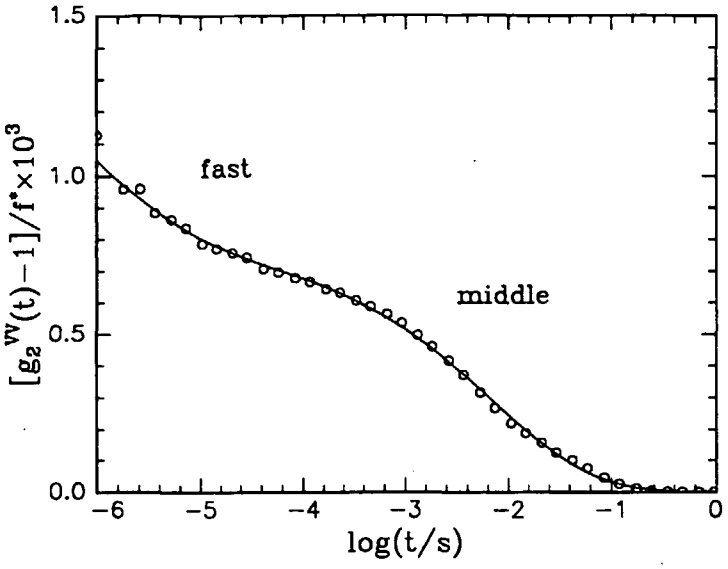

Figure 7.10: *Correlation function of SB11 at 135°C at an angle of 60°C after subtraction of the slow mode. For clarity, only every fourth point is shown. The line is a fit of a double KWW-function to data in the time range shown.*

7.6 The dynamics in the vicinity of the ODT

In order to study the influence of the ODT on the dynamics of block copolymer systems, a sample having an accessible ODT temperature was studied: Sample SB11 ($N = 310$) which has an ODT at 130°C. Measurements were made at 125 and at 135°C. First, the dynamic processes identified at 135°C are described and then their behavior in the ordered state. Results from a sample having an intermediate molar mass (SB14, $N = 236$), which was studied in the disordered state close to the ODT, are presented. They corroborate the findings with sample SB11 at 135°C.

7.6.1 Sample SB11 (*N=310*) just above the ODT temperature

The correlation function of sample SB11 at 135°C at an angle of 60° is shown in Fig. 7.7a. The value of the correlation function at the short time limit is less than one, which is reasonable, since the segmental relaxation is only partially represented in the time window. As will be established below, the polarized and depolarized scattering in the time range faster than about 1 ms reflects the segmental orientational dynamics of the styrene-rich domains. The correlogram is dominated by a slow relaxation mode. Use of conventional analysis methods would preclude a meaningful separation of the remaining components due to their low amplitude. However, the subtraction routine described above made it possible to isolate these modes. It is clear that recovery of low amplitude components from a correlogram dominated by a high amplitude decay in this way has its limitations. On the other hand, subtracting the dominant mode was the only possibility for analyzing the data. In the way described in the previous section, the relaxation rates $\Gamma_i = \tau_i^{-1}$,

$i = 1, \ldots, 4$, the KWW-exponents, β_i, and the intensities, $I_i = a_i I_{VV} \sin\theta$, of the four modes were determined for angles θ between 40 and 140°. The results are presented as a function of scattering vector in Fig. 7.11. The diffusion coefficients and relaxation times together with the amplitude ration of modes 2 and 3 are given in Table 7.2.

sample	N	T/°C	χN	$D_1/(m^2/s)$	$D_2/(m^2/s)$	τ_3/ms	τ_4/μs	$a_3/(a_2+a_3)^a$
SB05	156	70	6.9	1.2×10^{-17}	5.7×10^{-15}	(b)	~ 41	0.2
		110	5.9	4.8×10^{-16}	1.3×10^{-13}	1.1	1.8	0.1
		135	5.4	2.4×10^{-15}	4.0×10^{-13}	0.55	(b)	0.02
SB14	236	90	9.7	1.8×10^{-17}	1.2×10^{-14}	4.3	22	0.4
		110	8.9	1.4×10^{-16}	5.8×10^{-14}	1.1	6.2	0.3
		130	8.3	8.0×10^{-16}	3.7×10^{-13}	0.49	6.0	0.04
SB11	310	125	11.1	(b)	7.6×10^{-15}	1.7	5.7	0.1
		135	10.5	4.7×10^{-17}	2.3×10^{-14}	5.7	6.4	0.3

Table 7.2: *Relaxational characteristics of the samples at different temperatures. N denotes the chain length, T the temperature, χ the Flory-Huggins segment-segment interaction parameter, D_1 and D_2 the diffusion coefficients of mode 1 and 2, τ_3 and τ_4 the relaxation times of mode 3 and 4, and a_2 and a_3 the amplitudes of mode 2 and 3. The χN-parameters were derived using mean-field theory. (see Chapter 3). (a) from a fit of a double KWW-function, (b) determination not possible.*

The slowest mode (1) gives a sharp peak in the distribution function (Fig. 7.7b). The decay is close to single-exponential, but, as discussed above, fits of a KWW-function gave stretching exponents larger than one. It could not be established yet if this feature has a physical origin. As the process is at the upper limit of the correlator ($\sim$ 100 s), we had no means tho study this effect in detail. The polarized intensity of this mode, which was determined as described in the previous section, decreases with rising q (Fig. 7.11). Plots of the inverse total polarized intensity *vs.* q^2 are often used to determine the radius of gyration (*e.g.* [148]). The ratio of the slope to the intercept gives

$$\frac{slope}{intercept} = \frac{16\pi^2 n^2}{3\lambda^2} R_g^2 \tag{7.39}$$

However, the intercept obtained with sample SB11 at 135°C was found to be negative, making a determination of R_g impossible. The reason of this behavior is still unclear. The cluster mode does not give rise to significant depolarized scattering (Fig. 7.12).

In order to determine the hydrodynamic radius, R_h, it was assumed that the Stokes-Einstein equation (Eq. 7.23) can be applied in the melt. The diffusion coefficient, D, is given by $\Gamma = Dq^2$. The relaxation rates as found by fitting a KWW-function to the cluster mode were plotted *vs.* q in a log-log-representation (Fig. 7.11). A line having a slope of two was fitted and the diffusion coefficient was determined from the intercept. As can be seen from the figure, the slope of two fits the data. However, the data scatter which is due to the problems in fitting this mode (see above). The diffusion coefficient of mode 1 was found to be $D_1 = (4.7 \pm 0.3) \times 10^{-17}$ m^2/s (Table 7.2). In conjunction with the measured macroscopic zero-shear viscosity ($\eta = 70$ Pas at 135°C, Table 7.1),

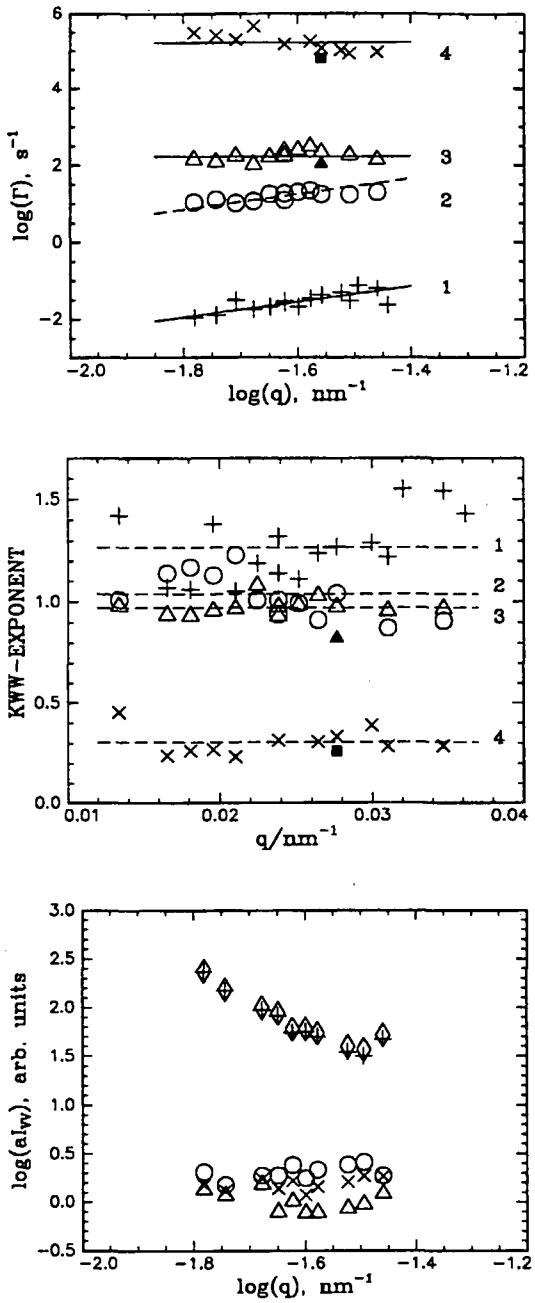

Figure 7.11: *Results from sample SB11 at 135°C. Upper figure: Relaxation rates* Γ *of modes* $1-4$ *as a function of scattering vector,* q*, in a log-log-representation.* $(+)$ *mode 1,* $(\circ)$ *mode 2,* $(\triangle)$ *mode 3,* $(\times)$ *mode 4. Lines are fits of constants (modes 3 and 4) or of lines with slope 2 (modes 1 and 2). Filled symbols are from measurements in the depolarized geometry. Middle figure: KWW-exponents* β *of the four modes as a function of scattering vector. Same symbols as above. Lines are fits of constants. Lower figure: Total intensity and the intensities of the four modes as a function of scattering vector in a log-log-representation.* $(\diamond)$ *total intensity, the other symbols as above.*

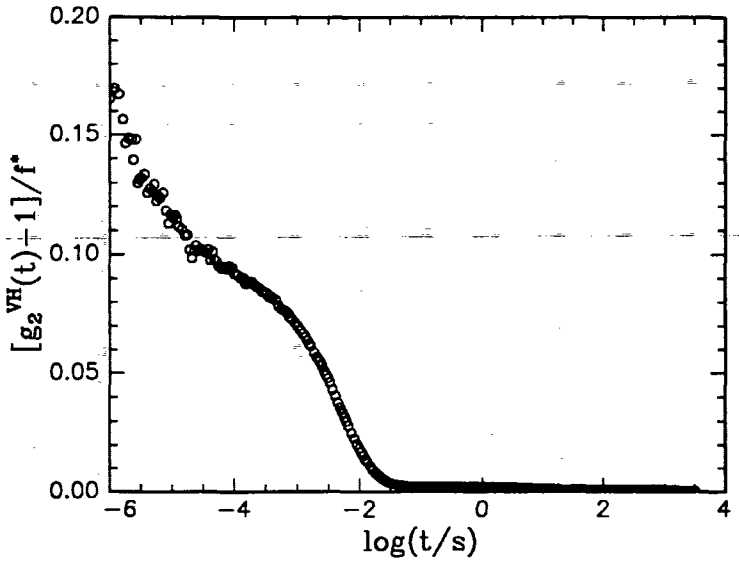

Figure 7.12: *Correlation function of sample SB11 at 135°C at 90° measured in the depolarized geometry.*

the hydrodynamic radius R_h was estimated to 90 nm. This value is much larger than the radius of gyration (R_g = 4.9 nm) which was determined from the peak position in the SAXS-spectrum (Chapter 5.4). This means that many chains are involved in cluster diffusion (Fig. 7.1). The hydrodynamic radius of the clusters decreases with temperature from 90 nm at 135°C to $\sim$ 50 nm at 140 – 160°C. The relative amplitude of the cluster mode in the correlation function remains approximately constant (90 – 96%) between 135 and 160°C.

As described above, a very slow relaxation of high relative intensity which increases strongly as q decreases, and with a relaxation time exceeding 1 s is an important feature of all systems described in the copolymer literature. Clusters have been observed in various diblock copolymer melts [123, 124, 125, 148] with values for $R_h \simeq 50-100$ nm. A dominant amplitude may not always be characteristic of the cluster mode in block copolymer systems above the ODT temperature, as it is for the present system. For the systems poly(ethyl methyl siloxane)-poly(dimethyl siloxane) [123, 124] and polystyrene-poly(methyl phenyl siloxane) [125] above the ODT temperature, the relative amplitude of the cluster peak was found to decrease at higher temperature and eventually disappear. The difference between these polymers and our samples is that polystyrene-polybutadiene has a higher glass temperature and a higher Flory-Huggins segment-segment interaction parameter. There is as yet no general explanation for cluster formation. The phenomenon may be related to the rise of the intensity in small-angle scattering spectra at low values of the scattering vector, which was attributed to the finite compressibility (Chapter 5.4 and 6).

Subtraction of the cluster mode, as described above, results in the correlogram in Fig. 7.7c. The distribution function as obtained using REPES (Fig. 7.7d) showed clearly three modes, two of them being sharp (2 and 3) and the fastest one (4) broad. Fig. 7.13 (upper figure) shows the correlograms in the polarized and in the depolarized geometry

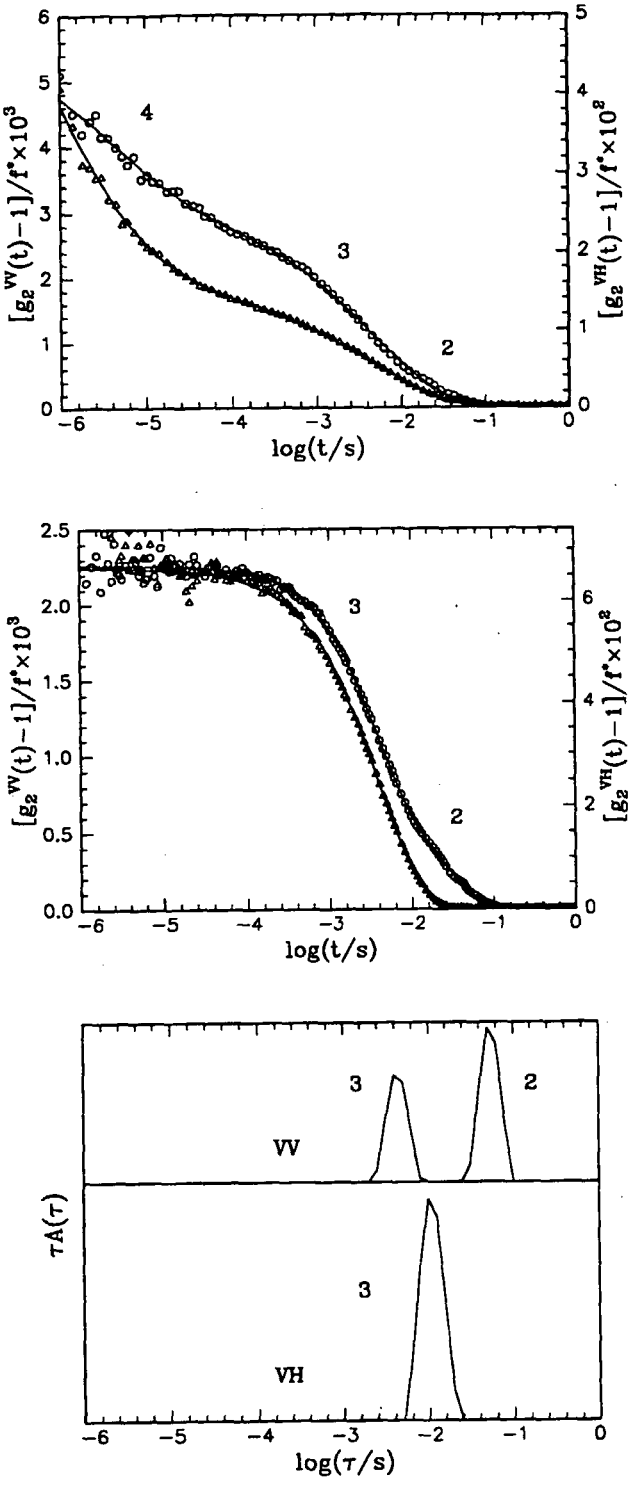

Figure 7.13: *Upper figure: Comparison of correlation functions of sample SB11 at 135°C measured at an angle of 90° in the polarized (o, left axis) and depolarized geometry (△, right axis). The cluster mode was subtracted. For clarity, only every second point is shown. Lines are fits using REPES. Middle figure: Correlation functions from the upper figure with the fast mode (4) subtracted. Same symbols as above. Lines are fits of a double KWW-function to the polarized signal and of a single KWW-function to the depolarized signal. Lower figure: Distribution functions corresponding to the correlation functions shown in the middle figure.*

(mode 1 being subtracted). Additional subtraction of the fast mode leads to the curves in the middle figure. The corresponding distribution function is shown in the lower figure. Modes 2 and 3 are seen in the correlation curve measured in the polarized geometry. Mode 2 is absent in the curve measured in the depolarized geometry. Mode 3 which gives rise to depolarized scattering is close to single exponential and is close to the the peak labelled (3) in the distribution function measured in the polarized geometry. This behavior is also observed in the data on another sample, SB14 (see below). Fitting a single KWW-function to the depolarized signal (Fig. 7.13, middle figure) gives a relaxation time of 9.1 ms and a KWW exponent $\beta = 0.8$ for mode 3. The observed splitting of the compositional fluctuation mode into two parts is important for an understanding of the copolymer dynamics. Although the scatter in relaxation rates is large due to the low amplitudes of modes $2-4$, it is concluded that the relaxation rate for mode 2 is q^2-dependent (*i.e.* diffusive), whereas for mode 3 it is q-independent (Fig. 7.11). The corresponding diffusion coefficient for mode 2 is $D_2 = 2.3 \times 10^{-14}$ m^2/s. An average value for β of mode 2 is 1.0 ± 0.1. The intensity of mode 2 is q-independent within experimental uncertainty. It is considered most probable that the diffusive relaxation (mode 2) corresponds to the heterogeneity mode which is one of the main modes anticipated for a block copolymer melt (Fig. 7.1). The corresponding diffusion coefficient should thus be very similar to the self-diffusion coefficient for the copolymer chain [124]. Using the Stokes-Einstein equation, which has been commonly done (*e.g.* [123]), the dynamic correlation length can be estimated from the diffusion coefficient. This quantity should provide a measure of the range of the hydrodynamic interactions in the system. Using the measured zero-shear viscosity at this temperature, $\eta = 70$ Pas, a correlation length $\xi = 0.16$ nm is found. This value is unphysically small. The reason could be that the local viscosity experienced by the diffusing polymer is different from the macroscopic viscosity, as the viscosities of polystyrene and polybutadiene are very different. As concentration fluctuations persist close to the ODT [20], the friction experienced by each of the blocks may be substantially lower than expected from the macroscopic viscosity. The macroscopically measured value of 70 Pas is thus higher than the local viscosity experienced by a single diffusing chain, because friction between chemically different segments contributes to the macroscopic visosity. Therefore, the value for the correlation length is too low.[5] (Note: the macroscopic viscosity could be used successfully for the determination of the hydrodynamic radius of the cluster mode, because the clusters experience a much larger volume than a single, diffusing copolymer molecule.) The intensity of the heterogeneity mode (mode 2) is expected to be angle-independent as is observed (although the data scatter) because $R_g \ll q^{-1}$ in the light scattering experiment.

Mode 3 has a q-independent relaxation rate ($\tau_3 = 5.7$ ms), a q-independent intensity and a narrow distribution of relaxation times, with a KWW-exponent of approximately unity (Fig. 7.11). This mode is also observed in the depolarized geometry as a slower relaxation than that characterizing the segmental dynamics (Fig. 7.13). Fig. 7.11 includes data from depolarized experiments (the filled points). Several fundamental relaxation processes are possible for a chain in a fluctuating compositional field (concentration fluctuations on the length scale of R_g): The internal mode or processes related to chain orientation and stretching. The internal mode corresponds to the relative translational motion of the centers of mass of the two blocks (Fig. 7.1) and should not give rise to depolarized scattering

[5] In fact, the viscosity should be determined from the loss modulus at the frequency $\omega = 2\pi/\tau_3$, because this frequency is not in the terminal region (Chapter 3).

[124]. It has been found not to have significant amplitude for polymers having low molar mass [119, 123, 124]. Comparing the amplitude of the internal mode (Eq. 7.1) with the amplitude of the heterogeneity mode (Eq. 7.2), the ratio of amplitudes S_I/S_H is found to be 0.05 for SB11 at 135°C at a scattering angle of 90° ($p = 1.05$ and $R_g = 4.9$ nm, Chapter 5.4). Thus, it might be that mode 3 is partly due to the internal mode, *i.e.* breathing around a stretched equilibrium configuration. This process, however, does not give rise to depolarized scattering, although could contribute to the polarized signal. A process related to orientation and stretching has been observed by Hoffmann *et al.* [134] in depolarized DLS measurements on disordered polystyrene-polyisoprene diblock copolymer melts. Close to the ODT, the depolarized spectrum was found to become bimodal. The faster component had $\beta = 0.2$ and derived from the segmental relaxation. The slower relaxation, which was single-exponential, was attributed to orientation and stretching of the copolymer chains in the vicinity of the ODT. Upon heating, the slow depolarized mode disappeared gradually, meaning that the chains become Gaussian as composition fluctuations loose amplitude. Jian *et al.* [135] also reported depolarized DLS experiments on a polystyrene-polyisoprene and on a polystyrene-poly(methylphenylsiloxane) diblock copolymer melt. These authors similarly concluded that a slow depolarized component of narrow distribution derives from orientation and stretching of the copolymer chains in the disordered state near the ODT. Another possible process could be rotation of the stretched chain as a whole. The chain remains stretched but its orientation changes with time. This process could be responsible for the depolarized scattering observed in our experiments. We conclude that the relaxation process seen in our correlation curves, at least partly, is related to chain stretching due to concentration fluctuations in the disordered state close to the ODT. In the following, we refer to this mode as 'stretching mode'.

Mode 4 isolated as described above by subtracting the contributions of modes 1−3 from the correlogram, is depicted in Fig. 7.8c and d. This mode is only partially represented in the time window for SB11 at 135°C. The average relaxation time ($\tau_4 = 6.4$ μs) and the KWW-exponent were obtained by fitting a single KWW-function to the decay. It is typically very broad ($\beta = 0.3$), a value which may be compared with $\beta = 0.39$ for segmental relaxation in the homopolymer polystyrene [145]. As anticipated for a segmental relaxation, the relaxation rate is q-independent, as is also the corresponding intensity shown in Fig. 7.11. The segmental relaxation times depend strongly on the distance from the glass temperature and thus, at 135°C, the segmental relaxation of the polystyrene blocks ($T_g \simeq 90$°C) is slower than the segmental relaxation of the polybutadiene blocks, since polybutadiene has a very low glass temperature (~ -80°C). Therefore, the process seen at the fast end of the time scale probably corresponds to the segmental relaxation of polystyrene. There may be an additional broadening of the polystyrene segmental mode due to mixing with the softer polybutadiene component (as suggested in [133]). The temperature dependence of the segmental mode could not be reliably determined because only a small part of the decay is in the experimental time window.

To summarize, four dynamic processes have been identified with sample SB11 in the disordered state in the vicinity of the ODT (at 135°C). At the slow end of the time scale studied, the cluster mode which has a dominant amplitude, is observed. The clusters are found to have a hydrodynamic radius of 90 nm, thus much larger than the radius of gyration of the polymers. The other three modes could only be analyzed using a new subtraction routine [136]. In this way, a mode related to diffusion of single chains is observed, which is due to heterogeneity in polymer composition. As the heterogeneity mode is very

low in intensity and adjacent to the cluster mode, the q-dependence of the relaxation rate could not be established undoubtedly. However, as the decay is single-exponential, the polarized intensity is approximately constant, and as this mode does not give rise to depolarized scattering, we attribute it as due to single-chain diffusion. A nearly single-exponential mode having a q-independent relaxation rate and approximately constant intensity is attributed to a combination of 'breathing' and stretching. This mode gives rise to depolarized scattering which leads us to conclude that the chains are streched and oriented, which fits to the picture of concentration fluctuations in the vicinity of the ODT. The fastest mode observed is very broad ($\beta = 0.3$) and has a q-independent relaxation rate and intensity. The mode is observed in the depolarized geometry. It is concluded that this mode is due to the segmental reorientational dynamics of the polystyrene segments. However, as only part of the decay is in the experimental time window, its characteristics could not be elaborated in detail.

7.6.2 Sample SB11 (N=310) just below the ODT temperature

Sample SB11 was also studied at 125°C, *i.e.* in the lamellar state, in order to establish the influence of the ODT on the dynamic processes which were identified in the disordered state. The analysis of the correlation curves was not straightforward which, in part, was due to the proximity of the glass transition of the polystyrene block ($\sim$ 90°C). The relaxation times of segmental reorientation increase strongly when approaching the glass transition which leads to overlap with mode 3. For these reasons, analysis of correlation curves measured below 125°C did not give a consistent picture. We will therefore only present results from 125°C.

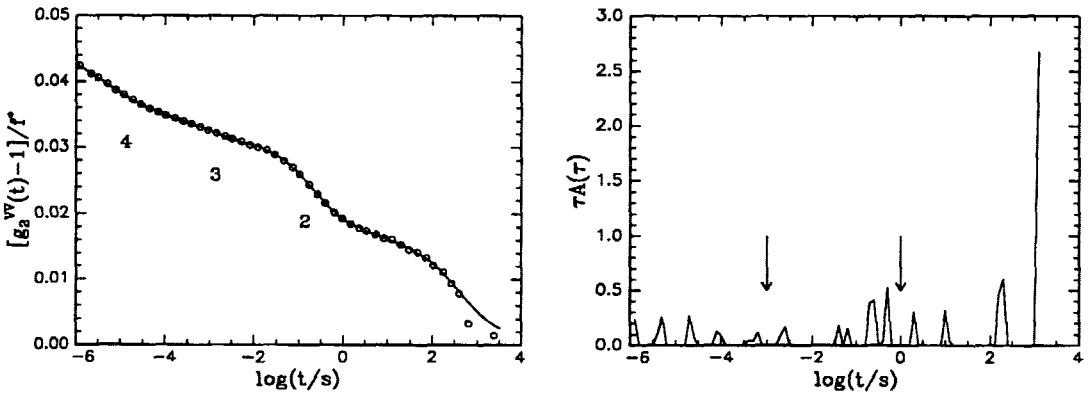

Figure 7.14: *Left figure: Correlation function of sample SB11 at 125°C measured in the polarized geometry at an angle of 70°. For clarity, only every fifth point is shown. The line is a fit using REPES. Right figure: Corresponding distribution function as obtained with REPES. The curve is not smoothed. Arrows indicate the time window chosen for further analysis.*

Experiments in both the polarized and depolarized geometries were made. A typical correlogram is shown in Fig. 7.14. One of the main differences between the correlation functions below the ODT temperature and those above is the shift of mode 1 to much slower relaxation times ($\sim 10^3$ s). This behavior may have different origins: (1) the

clusters (long-range heterogeneities) persist in the ordered state, the phenomenon is thus not related to the block copolymer nature of the samples; (2) mode 1 corresponds to diffusion of lamellar grains in the ordered state or (3) mode 1 corresponds to diffusion of domains rich in one type of segments. The third possibility has recently been proposed [148]. In the present work, mode 1 was not studied further because it was too slow.

After a first fit with REPES to the whole curve (no smoothing was applied), contributions slower than 1 s and faster than 1 ms were subtracted (Fig. 7.14). The choice of these values was somewhat arbitrary because the peaks obtained in the distribution function were not clearly separated, as was the case in the disordered state.

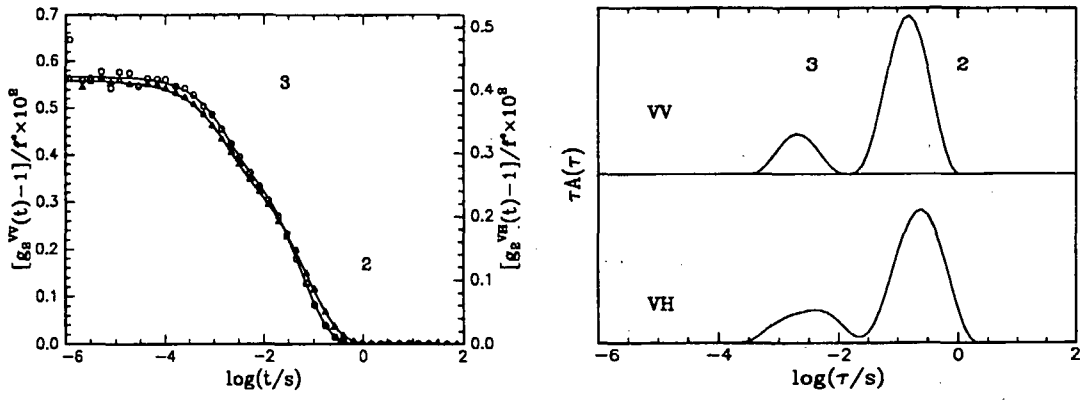

Figure 7.15: *Left figure: Correlation functions of sample SB11 measured at 125°C at an angle of 90° with the slow and the fast mode subtracted (see text). (o) polarized geometry, left axis, (△) depolarized geometry, right axis. For clarity, only every fourth datapoint is shown. Lines are fits of double KWW-functions. Right figure: Corresponding distribution functions as obtained with REPES.*

The result can be seen in Fig. 7.15 where the polarized and the depolarized correlation functions are compared. As can be seen from the distribution functions of these curves, both modes 2 and 3 are present in the polarized as well as in the depolarized correlograms. Two explanations for this behavior are possible. The first is related to the birefringence observed in the lamellar, polycrystalline state [149] which is due to the optical anisotropy of the lamellar structure, the refractive index being different parallel and perpendicular to the lamellar interface [150]. Even for polycrystalline samples, where the grains are randomly oriented, birefringence could be observed. Birefringence may thus be the reason why all modes give rise to depolarized scattering in the ordered state. An alternative explanation is that the chains are stretched perpendicular to the lamellar interface and preferably diffuse along the interface. This type of translation has been established with low molar-mass, only weakly entangled diblock copolymers using field gradient NMR [151] and forced Rayleigh scattering on macroscopically oriented diblock copolymer specimens [15]. In this case, mode 3 would be related to chain stretching as found above the ODT.[6] Thus, modes 2 and 3 together would reflect the lamellar structure and the resulting anisotropy. As above the ODT, segmental reorientational dynamics are observed at a time scale of microseconds.

[6]However, this anisotropic diffusion does not involve rotational motion which is prerequisite for depolarized scattering.

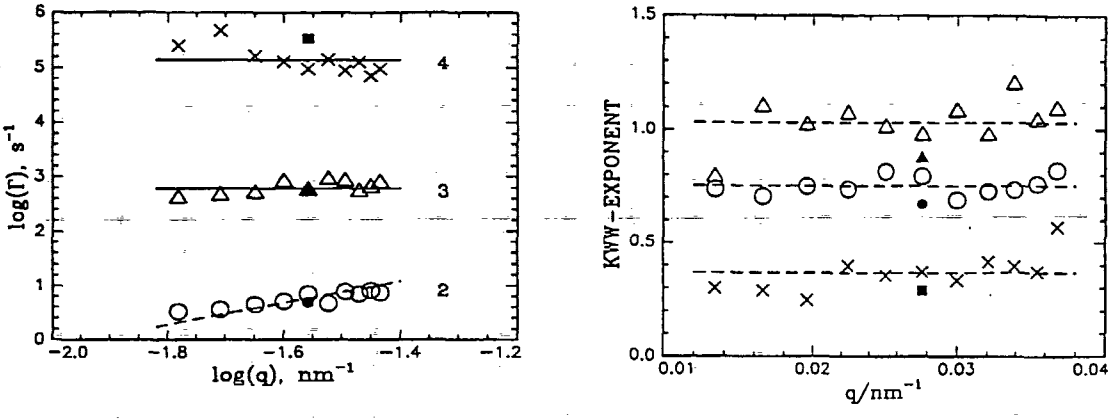

Figure 7.16: *Left figure: Relaxation rates of modes 2 – 4 as a function of scattering vector of sample SB11 at 125°C in a log-log-representation. (o) Mode 2, (Δ) mode 3, (×) mode 4. Filled symbols are from measurements in the depolarized geometry. Full lines are fits of constants, the broken line is a fit of a line with slope two. Right figure: KWW-exponents of modes 2 – 4 as a function of scattering vector. Same symbols as in the left figure. Lines are fits of constants.*

Fig. 7.16 shows the relaxation rates and the KWW-exponents of modes 2 – 4. The values found are given in Table 7.2. The heterogeneity mode (2) at 125°C has a q^2-dependent relaxation rate and an average KWW-exponent of 0.75. This exponent is lower than that above the ODT ($\beta = 1.0$) which is probably due to overlap with the slower modes. The diffusion coefficient is $D_2 = 7.6 \times 10^{-15}\mathrm{m}^2/\mathrm{s}$, *i.e.* a factor 4 lower than at 135°C, which may reflect the hindered diffusion below the ODT due to the lamellar structure. Mode 3 has, as above the ODT, a q-independent relaxation rate ($\tau_3 = 1.7$ ms), and a KWW-exponent of 1.0. It reflects thus, as above the ODT, chain stretching. Mode 4 has a q-independent relaxation rate ($\tau_4 = 5.7$ μs) and a KWW-exponent of 0.37. This mode is assigned to segmental reorientation and has the same characteristics as above the ODT.

To summarize, in the ordered state, the cluster mode becomes very slow (10^3 s). Modes 2–4 give rise to depolarized scattering which may be due to birefringence or to the diffusion of stretched chains along the lamellar interfaces.

7.6.3 Sample SB14 ($N = 236$) in the disordered state

The findings with sample SB11 in the disordered state were corroborated with a sample having an intermediate molar mass thus being slightly deeper in the disordered state. At 110°C, where measurements on SB14 were made, $\chi N = 8.9$, which is lower than the value of $\sim$ 10.5 for SB11 at 135°C. The correlation function for the intermediate molar mass sample measured at 110°C (Fig. 7.17) is similar to that for sample SB11 at 135°C. It is also dominated by the cluster mode. The relative amplitude remains approximately constant (98 – 99%) between 90 and 130°C. The diffusion constant of the cluster mode ($D_1 = 1.4 \times 10^{-16}$ m^2/s at 110°C, see Table 7.2) leads to a hydrodynamic radius of the cluster of $\sim$ 56 nm ($\eta = 36$ Pas). Again, this value is much larger than the radius of

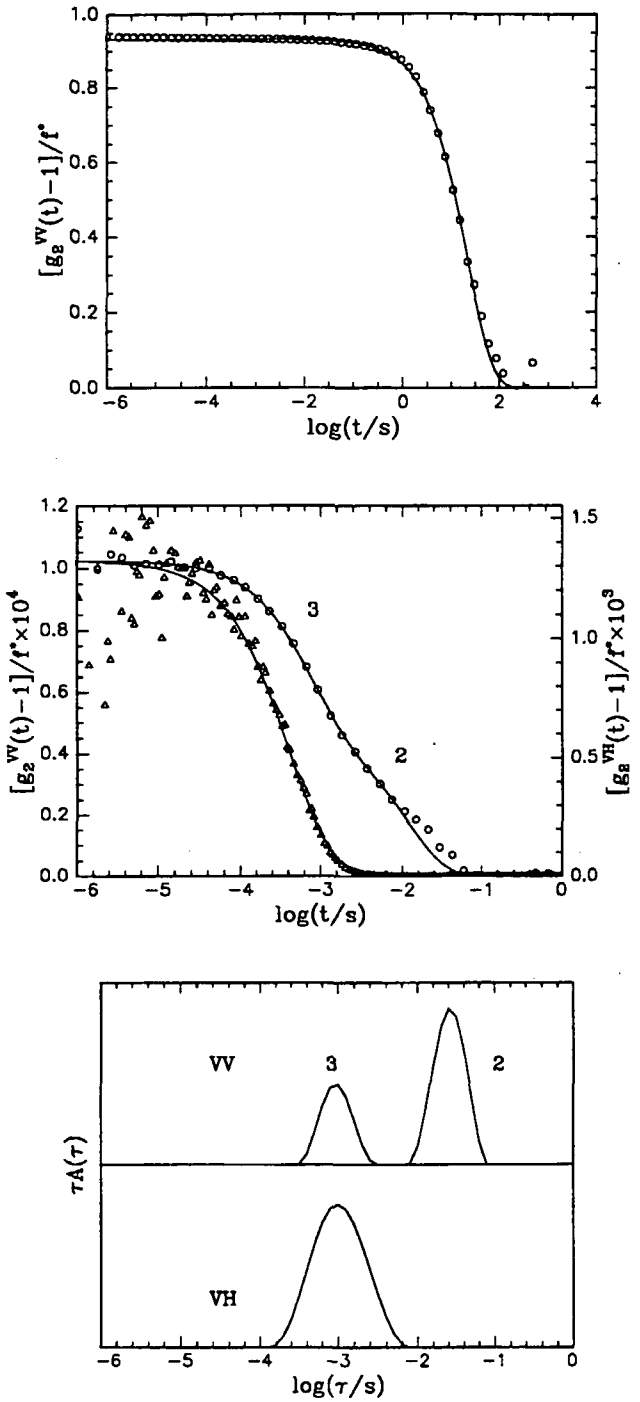

Figure 7.17: *Upper figure: Correlation function of sample SB14 at 110°C measured in the polarized geometry at an angle of 90°C. For clarity, only every fourth point is shown. The line is a fit using REPES. Middle figure: Correlation function of sample SB14 at 110°C at an angle of 90°C with the slow (1) and the fast mode (4) subtracted. (○, left axis) polarized geometry, every fourth point shown, (△, right axis) depolarized geometry. Lines are fits of a double KWW-function to the polarized signal and of a single KWW-function to the depolarized signal. Lower figure: Distribution functions corresponding to the correlation functions shown in the middle figure.*

gyration determined in SAXS measurements (4.3 nm). Correlation functions at 110°C after subtraction of the slow (1) and the fast (4) modes are shown in Fig. 7.17. As with sample SB11, mode 2 is not present in the depolarized geometry as can be seen from the distribution function (Fig. 7.17).

The angular dependences of the relaxation rate, the KWW-exponent and the intensity at 110°C are shown in Fig. 7.18. Mode 2 has a q^2-dependent relaxation rate, a KWW-exponent of about unity and a q-independent intensity within experimental uncertainty. The diffusion constant at 110°C is $D_2 = 5.8 \times 10^{-14}$ m^2/s. This mode thus has the characteristics of the heterogeneity mode. From the diffusion constant and the viscosity (36 Pas), a correlation length of $\xi = 0.13$ nm is obtained. As with sample SB11 at 135°C, this value is unrealistically low, probably because of the difference of macroscopic and local viscosity due to composition fluctuations.

Mode 3 has a constant relaxation rate ($\tau_3 = 1.1$ ms), a KWW-exponent of about one and constant intensity. This mode is identified as the chain stretching mode. The relative intensity of this mode is strongly dependent on temperature: The ratio of amplitudes of modes 3 and 2, $a_3/(a_2+a_3)$, as determined by fits of double KWW-functions to mode 2 and 3 increases when the ODT is approached by lowering the temperature: $a_3/(a_2+a_3) = 0.04$ at 130°C, 0.3 at 110°C and 0.4 at 90°C. This is interpreted to mean that the chain conformation gradually changes from stretched to Gaussian chains, the deeper the sample is in the disordered state. Mode 4 has a constant relaxation time ($\tau_4 = 6.2$ μs) and a KWW-exponent of 0.5. The distribution seems to be a little narrower than for the other sample, but as only a small part of the decay is in the experimental time window, the value of the KWW-exponent is very uncertain. The intensity of this mode is angle-independent as expected for the segmental mode.

To summarize, sample SB14 exhibits the same features as sample SB11 in the disordered state: four modes contribute to the correlation function which are identified as the cluster, heterogeneity, orientation/stretching and segmental modes. The stretching mode has a lower relative intensity with respect to the heterogeneity mode than was the case with sample SB11 at 135°C. We attribute this finding to the fact that sample SB14 at 110°C is deeper in the disordered state, and that the chain conformation is closer to Gaussian than was the case with sample SB11 at 135°C.

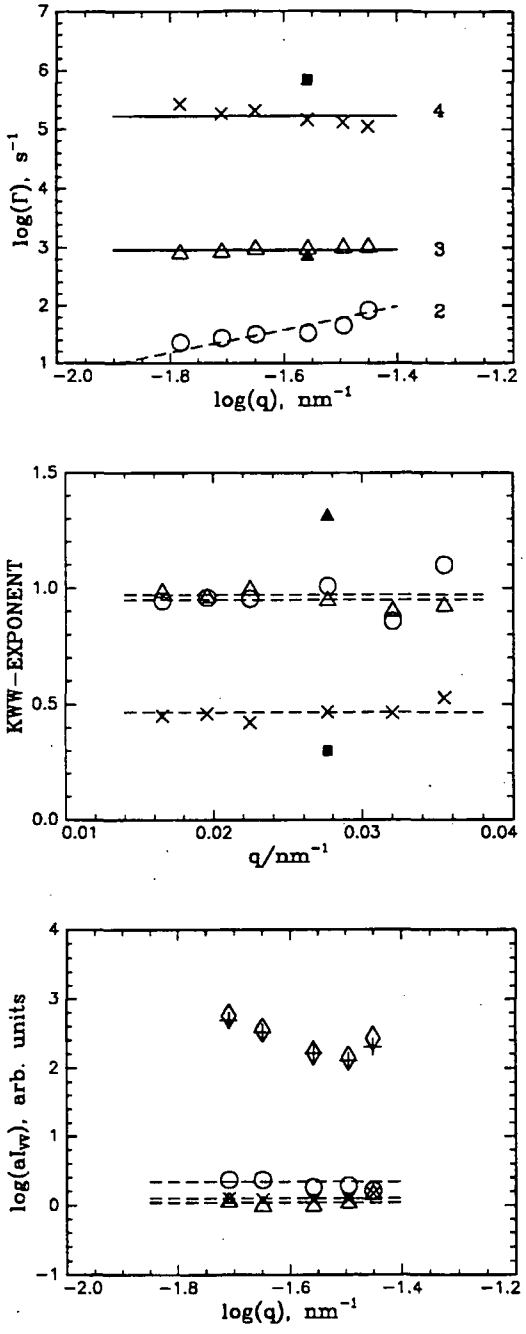

Figure 7.18: *Results from sample SB14 at 110°C. Upper figure: Relaxation rates* Γ *of modes* $2-4$ *as a function of scattering vector,* q*, in a log-log-representation. (*$\circ$*) mode 2, (*$\triangle$*) mode 3, (*$\times$*) mode 4. Filled symbols are from measurements in the depolarized geometry. Full lines are fits of constants, the broken line is a fit of a line with slope two. Middle figure: KWW-exponents* β *of modes* $2-4$ *as a function of scattering vector. Same symbols as above. Lines are fits of constants. Lower figure: Total intensity and the intensities of the four modes as a function of scattering vector in a log-log-representation. (*$\diamond$*) total intensity, (+) mode 1, the other symbols as above. Lines are fits of constants to modes* $2-4$.

7.7 The Gaussian-to-stretched-coil transition

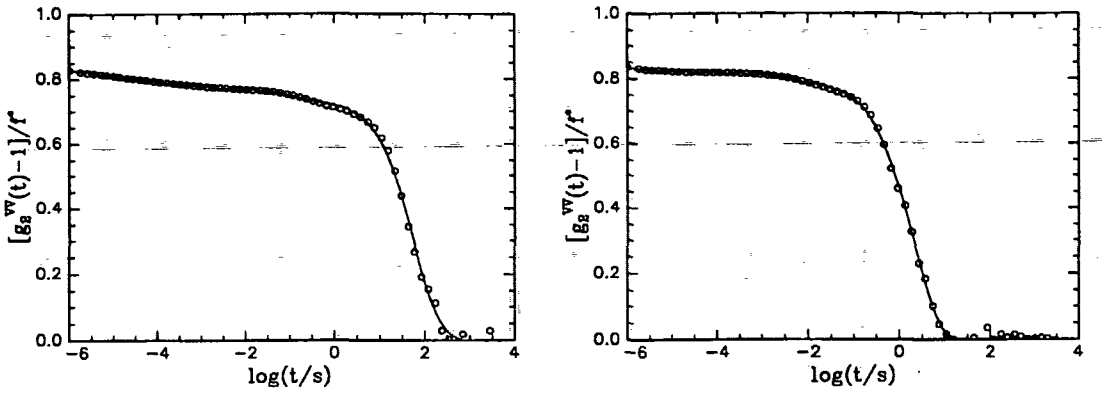

Figure 7.19: *Correlation function of sample SB05 at 70°C (left figure) and at 110°C (right figure). Both curves were measured in the polarized geometry at an angle $\theta = 90°$. For clarity, only every fourth point is shown. Lines are fits using REPES.*

With the lowest molar mass sample (SB05), a region deep in the disordered state could be studied. Measurements were made for this low molar mass sample between 65 and 150°C. These temperatures correspond to $\chi N = 6.9 - 5.0$. χN is thus much smaller than for the other samples (see Table 7.2). The overall pattern of behavior has been found to be the same as for sample SB11 having a higher molar mass studied in the disordered state. Thus, as shown in Fig. 7.19, the correlograms at 70 and at 110°C are dominated by cluster diffusion. From the diffusion coefficient of the cluster mode at 110°C, $D_1 = (4.8 \pm 0.2) \times 10^{-16}$ m^2/s (Fig. 7.20) and the macroscopic viscosity, $\eta = 4.3$ Pas, a value of $R_h = 140$ nm is estimated for the clusters. The radius of gyration of the chains as determined by SAXS is 3.2 nm. The corresponding KWW-exponent for mode 1 is somewhat greater than one, especially for large scattering angles (Fig. 7.20). The reasons are still unclear.

Fig. 7.21 compares the polarized and depolarized correlograms at 70°C at an angle of 90°. Mode 2 is clearly seen in the polarized function, but does not appear in the depolarized correlogram. Mode 3 cannot be investigated without ambiguity at 70°C because, with this sample, it overlaps the segmental mode. (The segmental mode is much slower than at the higher temperature because the sample is close to the glass temperature.). The polarized correlogram at 110°C (Fig. 7.21, middle figure) shows that mode 2 is shifted strongly to shorter relaxation times compared to the correlogram at 70°C. In the distribution function of this correlation curve (Fig. 7.21), mode 2 is of much higher amplitude than mode 3. The depolarized spectrum at 110°C is too weak to reveal the low amplitude mode (3) expected at about 1 ms. In the polarized correlation function, the heterogeneity (2) and the stretching mode (3) are observed as for the higher molar-mass samples. Mode 2 is dominant in intensity: the ratio $a_2/(a_2 + a_3)$ is found to be 0.9. These findings are interpreted to mean that, deep in the disordered state, the melt is more homogeneous than close to the ODT and the chain conformation is close to Gaussian. Therefore, the stretching mode has a very low intensity. Fig. 7.20 shows the dependences of the average relaxation rates, the KWW-exponents and the intensities of modes $2 - 4$ *vs.* scattering

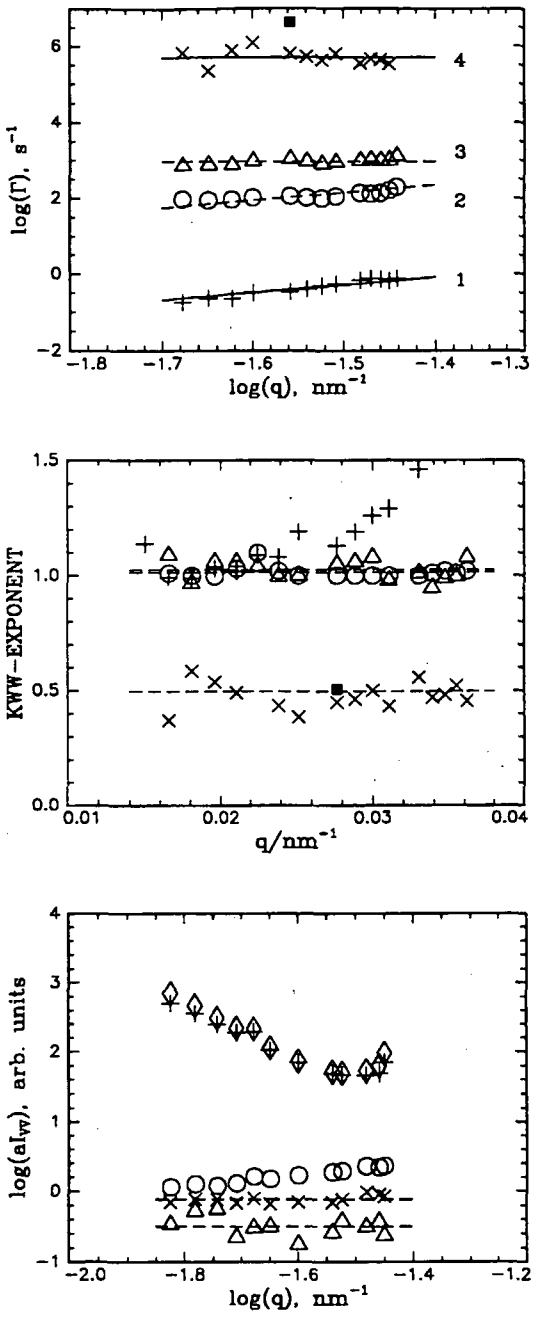

Figure 7.20: *Results from sample SB05 at 110°C. Upper figure: Relaxation rates* Γ *of modes* $1-4$ *as a function of scattering vector,* q*, in a log-log-representation.* $(+)$ *mode 1,* $(\circ)$ *mode 2,* $(\triangle)$ *mode 3,* $(\times)$ *mode 4. Filled symbols are from measurements in the depolarized geometry. The fitted lines have a slope of two for modes 1 and 2 and a slope of zero for modes 3 and 4. Middle figure: KWW-exponents* β *of the four modes as a function of scattering vector. Same symbols as above. Lines are fits of constants to modes* $2-4$*. Lower figure: Total intensity and the intensities of the four modes as a function of scattering vector in a log-log-representation.* $(\diamond)$ *total intensity. Other symbols as above. Lines are fits of constants to modes 3 and 4.*

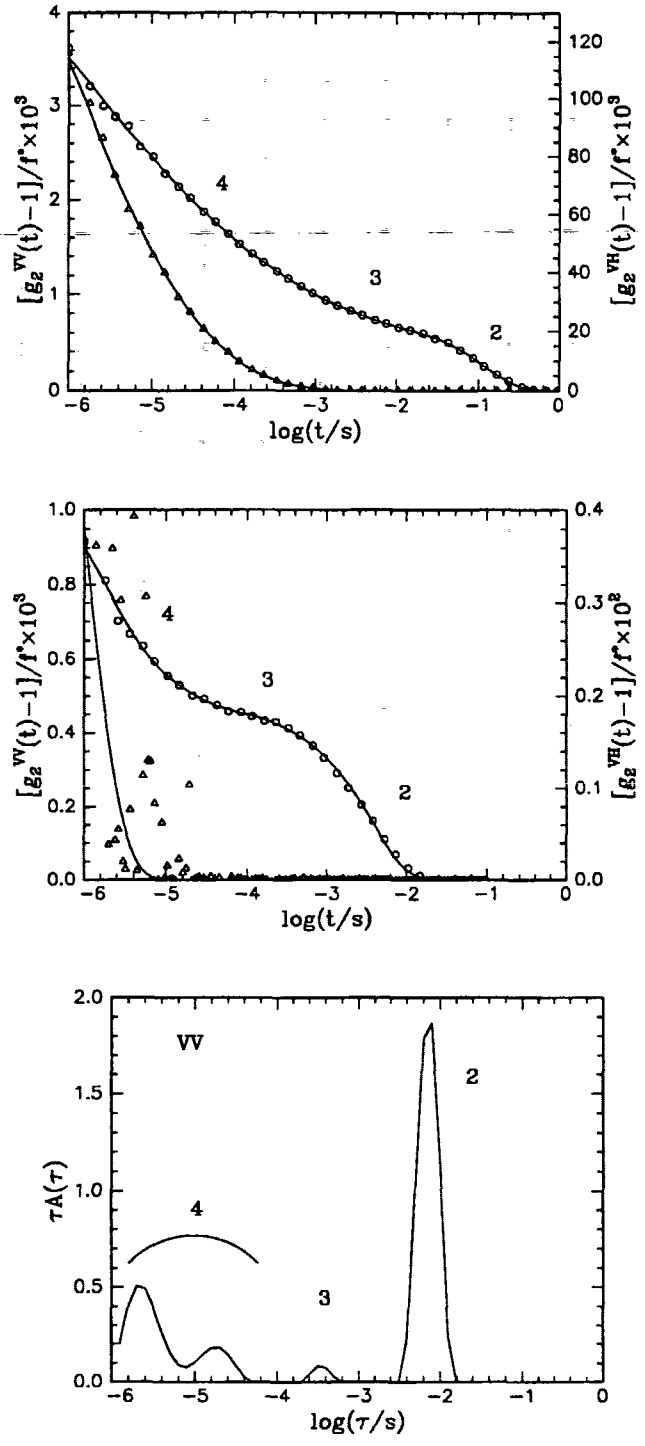

Figure 7.21: *Upper figure: Correlation function of sample SB05 at 70°C measured in the polarized (○, left axis) and depolarized geometry (△, right axis) at an angle of 90°. The cluster mode was subtracted. For clarity, only every fourth point is shown. Lines are fits using REPES. Middle figure: Correlation functions of the same sample at 110°C measured in the polarized and depolarized geometry at an angle of 90°. Same symbols as above. For clarity, only every fourth point of the polarized curve is shown. The lines are fits using REPES. Lower figure: Distribution function corresponding to the polarized correlation function shown in the middle figure.*

vector at 110°C. Mode 2 is close to single-exponential ($\beta = 1.0 \pm 0.1$) and appears to be diffusive with a diffusion coefficient $D_2 = 1.3 \times 10^{-13}$ m^2/s. Using the macroscopic viscosity ($\eta = 4.3$ Pas), a correlation length of 0.51 nm can be deduced. This value is higher than the values obtained with samples SB11 and SB14 (although still unrealistic), possibly because the local viscosity experienced by the diffusing polymer is closer to the macroscopic viscosity than was the case with the other two samples. This could be due to the low χN-parameter of sample SB05 at 110°C ($\chi N \simeq 6$) compared to the other samples (see Table 2), meaning that concentration fluctuations have a lower amplitude. This mode has a weakly q-dependent intensity in the q-range studied, the reasons being unclear.

Mode 3 which is single-exponential ($\beta = 1.0 \pm 0.1$) appears to have a constant relaxation time ($\tau_3 = 1.1$ ms). This value is similar to the value found for SB14 at the same temperature. The intensity of this mode is q-independent and much lower than the intensity of mode 2 as discussed above. This mode is interpreted as the stretching mode. The fastest mode (mode 4) has $\tau_4 = 1.8$ μs, a β-value of about 0.5 and a q-independent intensity. It has thus the same characteristics as the segmental mode seen with the other two samples, but the distribution is slightly narrower.

The temperature behavior of the cluster mode of sample SB05 was studied between 65 and 150°C. The relative amplitude of the cluster mode (94 – 98%) and the hydrodynamic clusterradius (50 – 230 nm) remain approximately constant between 70 and 110°C. The distribution functions of sample SB05 (mode 2 and 3) are shown in Fig. 7.22 for different temperatures between 65 and 135°C. The relative intensity of mode 3 decreases with increasing temperature. This is illustrated by the plot of the ratio $a_3/(a_2 + a_3)$ versus temperature (Fig. 7.22). The relative amount of the stretching mode decreases with increasing temperature, which is consistent with the picture of increasing homogeneity at higher temperature. At 150°C, where the stretching mode disappears, the χN-value is 5 ± 2. This value is consistent with the value of $\chi N \simeq 6$ given in [8, 22] for the Gaussian- to stretched-coil transition in PEP-PEE diblock copolymers. A possible explanation is that the chains are oriented and stretched in the disordered state for $\chi N > 5$, but are Gaussian at $\chi N < 5$. In this case, DLS allows to study the Gaussian- to stretched-coil transition.

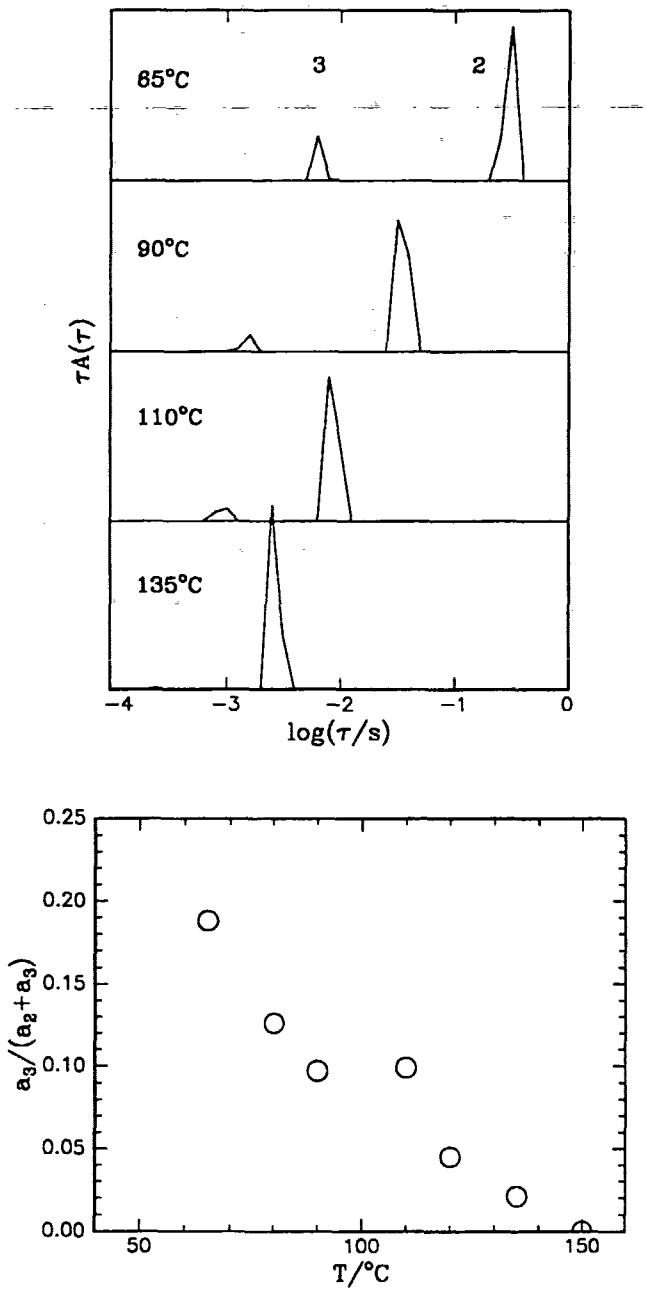

Figure 7.22: *Upper figure: Distribution functions of sample SB05 at various temperatures (mode 2 and 3). Lower figure: Relative intensity of mode 3 of sample SB05 as a function of temperature (corresponding to the upper figure).*

7.8 Conclusion

Three symmetric low molar-mass polystyrene-polybutadiene diblock copolymers have been studied in the disordered and in the ordered state using dynamic light scattering. As the correlation functions are dominated by a mode of very high intensity, a newly developed subtraction routine was applied [136].

In the disordered state, four dynamic processes are identified which reflect the non-homogeneity of the system. In the depolarized geometry, two modes are observed: a broad decay related to the segmental reorientational dynamics of the polystyrene blocks, and a slower, nearly single-exponential mode. The latter is interpreted to be due to chain orientation and stretching in the compositional fluctuation field. However, it might partly derive from an internal mode which could contribute to the polarized scattering. In the polarized experiments, two additional diffusive processes are observed: the heterogeneity mode related to self-diffusion of individual copolymer chains and to the polydispersity in polymer composition, and a very slow mode due to translational diffusion of large clusters ('long-range density fluctuations'), giving the dominant intensity.

Just below the ODT temperature, the slowest mode is shifted to very long times ($\sim$ 1000 s), which might be related to cluster diffusion as in the disordered state or to diffusion of lamellar grains. The segmental reorientation mode is partially observed at the fast end of the experimental time window. The stretching mode is well represented. The heterogeneity mode gives rise to depolarized scattering, which is interpreted in terms of birefringence of the lamellar, polycrystalline sample or in terms of the orientation of the diffusing chains below the ODT.

With the middle and the lowest molar-mass copolymer, the behavior deeper in the disordered state was studied. The chain-stretching mode has a lower relative amplitude than for the higher molar-mass samples, because the chain conformation is closer to Gaussian than in the vicinity of the ODT. When the temperature is increased, the relative amplitude of the stretching mode compared to the heterogeneity mode decreases. With the lowest molar-mass sample, the stretching mode vanishes at 150°C, corresponding to a χN-value of ~ 5. This is interpreted to reflect the fact that, deep in the disordered state, the concentration fluctuations are lower in amplitude than close to the ODT and the chains become Gaussian, which corresponds to the Gaussian- to stretched-coil transition. The finding is consistent with the non-Gaussian scaling of the characteristic lengthscale with chainlength observed in the disordered state close to the ODT using small-angle X-ray and neutron scattering (Chapter 5 and [29]). The value $\chi N \simeq 5$ corresponds to the low χN-limit of the intermediate-segregation regime. In addition, the value $\chi N \simeq 5$ corresponds nicely with the value of $(\chi N)_{GST} \simeq 6$ reported for poly(ethylene propylene)-poly(ethyl ethylene) [8, 22].

Future work on the dynamics of diblock copolymer melts could focus on the stretching mode which could give valuable information on chain conformation. However, a sample should be chosen where the cluster mode is lower in amplitude than was the case with the present sample.

Conclusion

The structure and dynamics of symmetric diblock copolymers have been studied focusing on the chain conformation in different regions in phase space.

A homologous series of eleven symmetric polystyrene-polybutadiene diblock copolymers having narrow molar-mass distributions was synthesized using anionic polymerization. The samples were characterized using various techniques (SEC, NMR, DSC, and dynamic mechanical measurements). The Flory-Huggins segment-segment interaction parameter was estimated from the order-disorder transition (ODT) temperatures determined in dynamic mechanical measurements. As the interaction parameter is relatively high, studies deep in the ordered state are possible.

One part of the thesis dealt with the scaling of the characteristic lengthscale with chain length. A homologous series of symmetric polystyrene-polybutadiene diblock copolymers in the bulk was prepared using various techniques: melting, annealing, solvent-casting and shear alignment. In this way, the existence of non-equilibrium states could be tested. The characteristic lengthscale was not observed to depend on the preparation method used which indicates that the samples are in thermal equilibrium. The scaling of the characteristic lengthscale with chain length was determined in a combined SAXS-and SANS-study. It was found that the characteristic lengthscale scales with chain length like $D \propto N^{0.6}$ for $\chi N > 27$. This regime is identified as the strong-segregation limit. In this region, the lamellar interfaces are narrow. For $\chi N < 27$, the characteristic lengthscale scales with chain length like $D \propto N^{0.8}$. This regime is the intermediate-segregation regime which links the Gaussian regime and the strong-segregation limit. In the intermediate-segregation regime, the density profile is smooth, both in the disordered and the ordered state. The crossover between the intermediate- and the strong-segregation regime in the ordered state is identified at $\chi N \simeq 30$ in consistency with theoretical approaches.

In a temperature study with one sample in a region around the ODT, it could be verified that the characteristic lengthscale does not change discontinuously at the ODT. The variation of the characteristic lengthscale with temperature is stronger than expected for Gaussian chains, indicating that the chains are stretched at the ODT temperature. The peak intensity decreases discontinuously at the ODT temperature and the peak width increases. This is consistent with the prediction that the ODT is a first-order phase transition.

A dynamic light scattering study on three low molar-mass samples focused on the dynamics of disordered samples in the bulk. Four dynamic processes were identified in the disordered state close to the ODT: cluster diffusion (long-range heterogeneities on a lengthscale of $\sim$ 100 nm), single-chain diffusion due to heterogeneity in polymer compo-

sition, a process attributed to chain stretching and orientation related to concentration fluctuations and the segmental reorientation of polystyrene. The two latter processes give rise to depolarized scattering. In the ordered state, the cluster mode is shifted to very long times and all processes give rise to depolarized scattering, which reflects the anisotropy of the lamellar state. With two samples having lower molar mass, the stretching mode was observed to decrease in intensity, the deeper the samples are in the disordered state. This mode vanishes at $\chi N \simeq 5$, which is attributed to the Gaussian- to-stretched-coil transition.

In summary, we have identified the intermediate-segregation regime between the Gaussian regime and the strong-segregation limit. It is located between $\chi N \simeq 5$ and 30. In this regime, the chains are stretched. The density profile is smooth, both in the disordered and the ordered state.

The present thesis shows that, in spite of their simple architecture, diblock copolymers in the bulk display complex structural and dynamic properties.

Appendix A

A vacuum oven for sample preparation

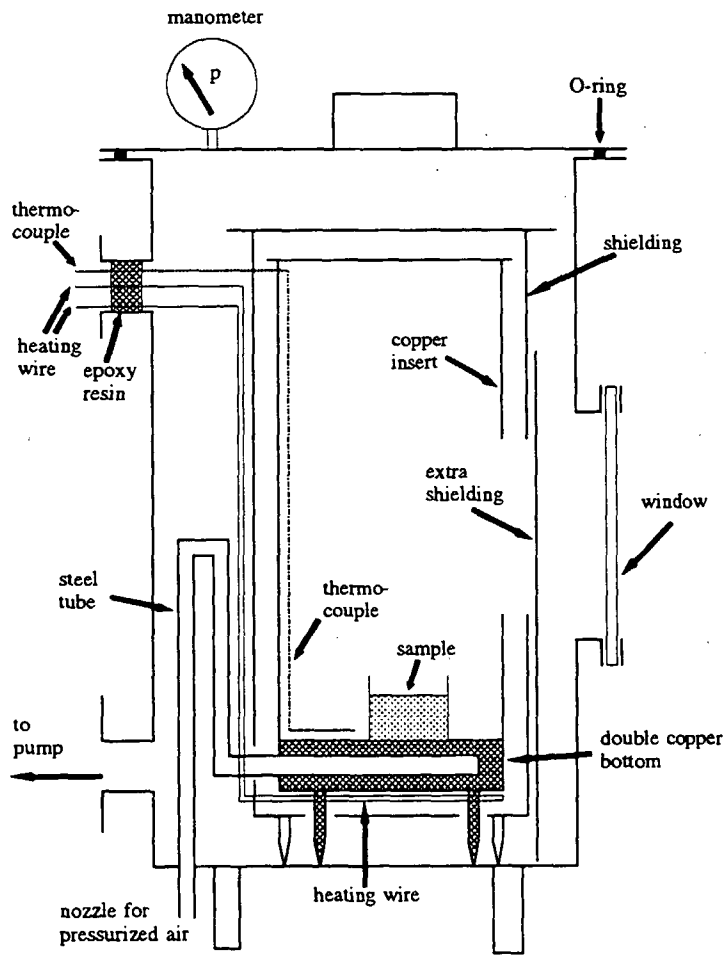

Figure A.1: *Schematic drawing of the vacuum oven for sample preparation (cross-section).*

A vacuum oven for sample preparation (Chapter 4) was designed. It should meet the following requirements:

- Temperatures of up to 200°C should be attainable.
- The temperature gradients should be small.
- The base pressure should be below 1 mbar.
- The oven should be fast to cool down. This was especially important during sample preparation, because the polystyrene-polybutadiene samples may not be exposed to air while they are at high temperature.
- The oven should have a window.

The oven is shown in Fig. A.1. It is cylindric, $\sim$ 20 cm high and has a diameter of $\sim$ 10 cm. The housing is made of stainless steel. A window is installed on one side. It is made from hardened glass (Euro-Glass) and has a diameter of 10 cm.

The oven contains a copper inset which consists of a thick copper bottom, copper walls, and a copper lid on top. It is constructed in this way in order to avoid temperature gradients. The copper wall has a hole which is nearly as large as the window and which can be shielded (see below), when good temperature stability is required. The bottom is heated by means of a Thermocoax heating element. This heating element is $\sim$ 1 mm thick and has a middle section where it becomes hot upon applying a voltage. This section is mounted to the bottom of the copper inset. The temperature in the inset is measured by means of a thermocouple (Type K). The thermocouple is mounted to the inner side of the copper inset, close to the sample. The heating wire and the thermocouple are connected to a temperature controller (Omron E5CW). The temperature stability is assumed to be $\pm$0.5°C. Temperatures of 250°C can be reached within one hour.

Around the copper inset, a shielding made of a stainless-steel sheet, having a hole at the window side, is installed. An extra stainless-steel shielding can be inserted in front of the window.

The oven can be rapidly cooled down by means of pressurized air which is passed through the copper bottom. The copper bottom consists of two plates. A groove is milled into one of the plates. The two plates are welded together and two stainless-steel tubes are welded to the outlets of the groove (only one of the tubes is shown in Fig. A.1). The tubes are lead out of the vacuum oven. In order to avoid a heat leakage from the copper bottom to the outer wall of the oven, the tubes are bent as shown in Fig. A.1. Passing pressurized air through the copper bottom is very effective in cooling the oven down to room temperature: In less than one hour, the oven is cooled from 150 to 30°C. Without the use of pressurized air, it takes at least 6 hours.

The oven is connected to an Edwards double-stage pump. A foreline trap is installed in order to prevent pump oil from diffusing into the oven. If necessary, a cold trap can be installed between the oven and the pump. The pressure is measured using a Pirani 501 gauge. The base pressure of the system is 0.03 mbar.

The oven is used for drying, annealing and solvent-casting of polymer samples (Chapter 4).

Appendix B

Calculation of the scattering intensity

In Chapter 5.3, the scattering intensity of a lamellar structure having sharp interfaces has been presented. The intensity was calculated as the product of the form- and the structure factor. The scattering intensity can also be written as the modulus squared of the scattering amplitude, which is a more straightforward way of calculating the intensity. The results from Chapter 5.3 are recovered.

Consider a sample which has a lamellar density profile $\rho(z)$ in z-direction and is isotropic in x- and y-direction (Fig. 5.7). This corresponds to a single crystal. The scattering amplitude of such a sample is given by the Fourier transform of the density:

$$A(q) = \int_0^{(N-1)D} dz\, \rho(z) e^{iqz} . \tag{B.1}$$

which, for lamellae, gives (Eq. 5.32):

$$A(q) = \sum_{n=0}^{N-1} \left\{ \int_{(n+\phi)D}^{(n+1)D} dz\, \rho_1 e^{iqz} + \int_{nD}^{(n+\phi)D} dz\, \rho_2 e^{iqz} \right\} \tag{B.2}$$

$$= \frac{1}{iq} \left[\rho_1 (e^{iqD} - e^{iq\phi D}) + \rho_2 (e^{iq\phi D} - 1) \right] \sum_{n=0}^{N-1} e^{iqDn} \tag{B.3}$$

Using Eq. 5.37, the scattering intensity, $I(q)$, is given by

$$I(q) = A(q)A^*(q) \tag{B.4}$$

$$= \frac{2}{q^2} \times \frac{\sin^2(qDN/2)}{\sin^2(qD/2)} \tag{B.5}$$

$$\times \{ \rho_1^2 [1 - \cos(q(1-\phi)D)] + \rho_2^2 [1 - \cos(q\phi D)] \} \tag{B.6}$$

$$+ \rho_1 \rho_2 [-1 + \cos(q(1-\phi)D) + \cos(qD) + \cos(qD\phi)] \} \tag{B.7}$$

which is rearranged:

$$I(q) = \frac{2}{q^2} \times \frac{\sin^2(qDN/2)}{\sin^2(qD/2)} \tag{B.8}$$

$$\times\{(\rho_2 - \rho_1)^2 + \rho_1\rho_2[1 - \cos(qD)] \tag{B.9}$$

$$+(\rho_2 - \rho_1)[\rho_1 \cos(q(1-\phi)D) + \rho_2 \cos(q\phi D)]\} \tag{B.10}$$

The result from Eq. 5.38 is thus recovered, setting $\rho_2 - \rho_1 = \Delta\rho$ and $\rho_1 = 0$ (Fig. 5.8). In the calculation presented in Chapter 5.3, the intensity is written as the product of the formfactor of one lamella and the structure factor of the one-dimensional lattice. The density profile of one lamella is written relatively to the density ρ_1 and only the difference $\Delta\rho = \rho_2 - \rho_1$ enters the calculations. In the approach presented here, the densities ρ_2 and ρ_1 enter explicitely.

For symmetric lamellae ($\phi = 0.5$), Eq. B.10 reads

$$I(q) = \frac{4}{q^2} \times \frac{\sin^2(qDN/2)}{\sin^2(qD/2)} \tag{B.11}$$

$$\times\left\{(\rho_2 - \rho_1)^2 \sin^2\left(\frac{qD}{4}\right) + \rho_1\rho_2 \sin^2\left(\frac{qD}{2}\right)\right\} \tag{B.12}$$

In the general case, the peak height is found setting $q = 2\pi k/D$, where k is an integer. According to l'Hospital's rule, the term $\sin^2(qDN/2)/\sin^2(qD/2)$ converges to N^2 for $q = 2\pi k/D$. Thus, the peak height is given by

$$I\left(\frac{2\pi}{D}k\right) = \frac{(ND)^2}{2\pi^2k^2}\{(\rho_2 - \rho_1)^2 + (\rho_2 - \rho_1)[\rho_1 \cos(2\pi k(1-\phi)) - \rho_2 \cos(2\pi k\phi)]\} \tag{B.13}$$

which, in case of symmetric lamellae, becomes

$$I\left(\frac{2\pi}{D}k\right) = \frac{(ND)^2}{\pi^2k^2}(\rho_2 - \rho_1)^2 \sin^2\left(\frac{\pi k}{2}\right) \tag{B.14}$$

and Eq. 5.39 is recovered.

Appendix C

A sledge for measuring the beam length profile

In order to measure the beam length profile, a sledge for sidewards movement of the TPF filter unit together with the detector was designed. The sledge should meet the following specifications:

- The total travel path should be ± 2.5 cm around the middle position.
- The sidewards position should be reproducible within 0.2 mm.
- Movement of the filter and detector should be possible with the camera main body and the filter unit evacuated.
- The construction should be easy to mount and easy to demount.

The sledge is shown schematically in Fig. C.1. It consists of two brass plates connected by means of a rail/carriage system. One plate (the 'fixed plate') is attached to the camera main body. The hole for the beam in this plate is 5 cm wide and 5 cm high. The other plate is screwed onto the filter unit and is referred to as the 'movable plate'. The hole for the beam in this plate is 13 cm wide and 5 cm high, such allowing the beam to pass also in the off-center positions. A well-greased O-ring around the hole assures vacuum in the camera and filter unit. It is possible to move the filter without breaking the vacuum. The overall thickness of the sledge is 1.8 cm, such increasing the sample-detector distance from 26.7 to 28.5 cm.

The rails are mounted above and below the camera main body. The U-shaped design of the fixed plate allows to save weight by using plates which are only 8 mm thick. The rail-carriage system KUME 9 from INA-lejer A/S (Fig. C.2) has been chosen because of the small size of the carriages and the rail: The absolute height of the carriage mounted on the rail amounts only to 10 mm. This system has low friction, which facilitates gliding, but can bear a high load (several kilograms).

The ball-screw allows positioning of the filter unit. A miniature screw SHBO 10×2R from SKF A/S has been chosen. The diameter of the spindle is 10 mm and the diameter of the screw 19.5 mm. One turn corresponds to a displacement of 2 mm. The maximum

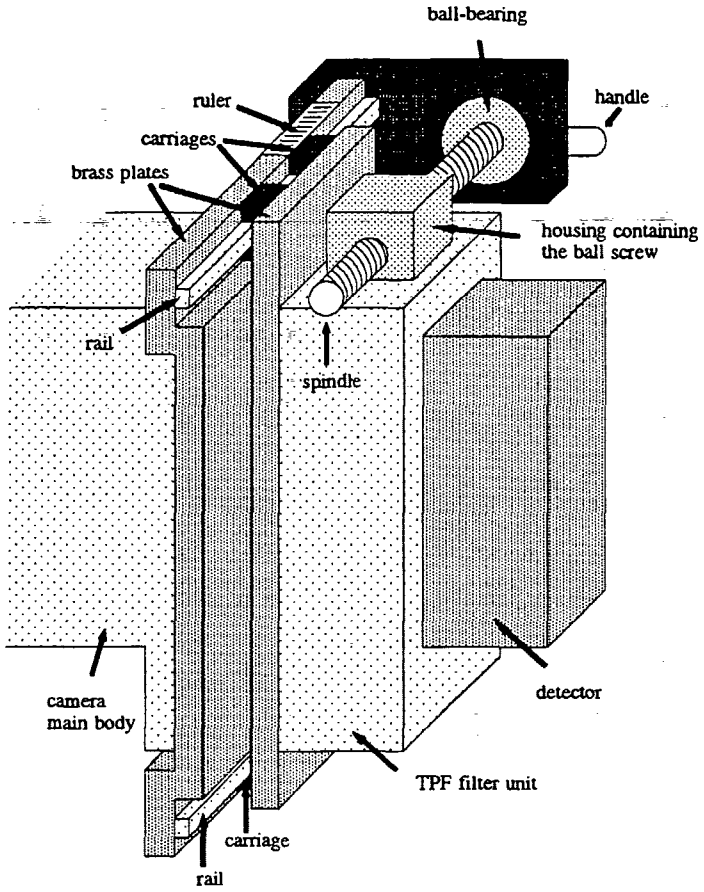

Figure C.1: *Schematic drawing of the sledge mounted between the camera main body and the TPF filter unit. Shown are the two plates and the rail/carriage system. On top of the filter unit, a ball screw is mounted in a housing, the spindle being fitted to a ball-bearing. A handle allows positioning. The position of the movable plate is read off using a ruler. For details see text.*

axial play is specified to be 0.03 mm. The screw is mounted in a housing on top of the filter and the end of the spindle is fitted into a ball-bearing (model 3200A-2ZTN9 from SKF which has a very small axial play). The ball-bearing is fitted into a brass stripe, which is attached to the fixed plate. A handle mounted on the end of the spindle allows positioning. Turning the handle by 10° corresponds to a displacement of ~ 0.06 mm.

The position of the movable plate is controlled using a ruler, which is glued on top of the fixed plate. The position of the edge of one of the carriages can be read off within ± 0.5mm, which is considered sufficiently precise.

A beam profile measured with a beam length of 10 mm and a beam width of 15 μm is shown in Fig. C.3. A brass absorber of 0.5 mm thickness was mounted in front of the

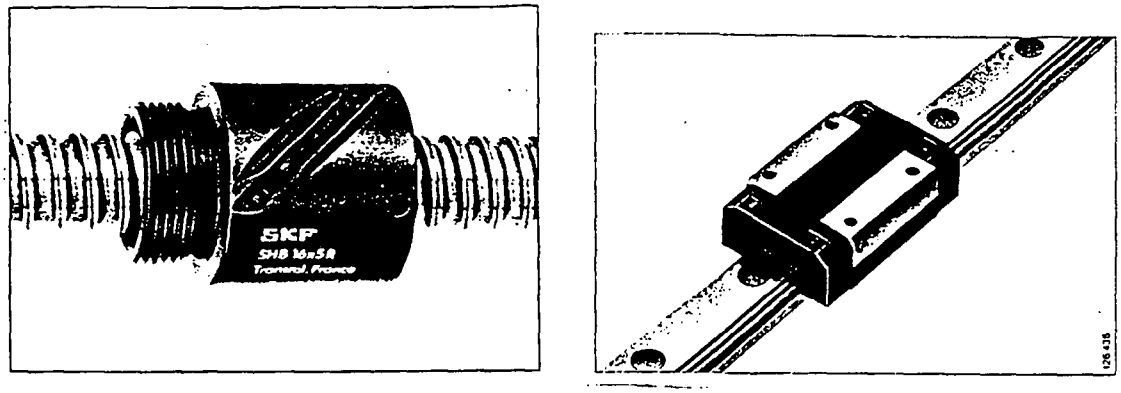

Figure C.2: *Left figure: The design of the ball screw. From [152]. Right figure: The rail/carriage system KUME. From [153].*

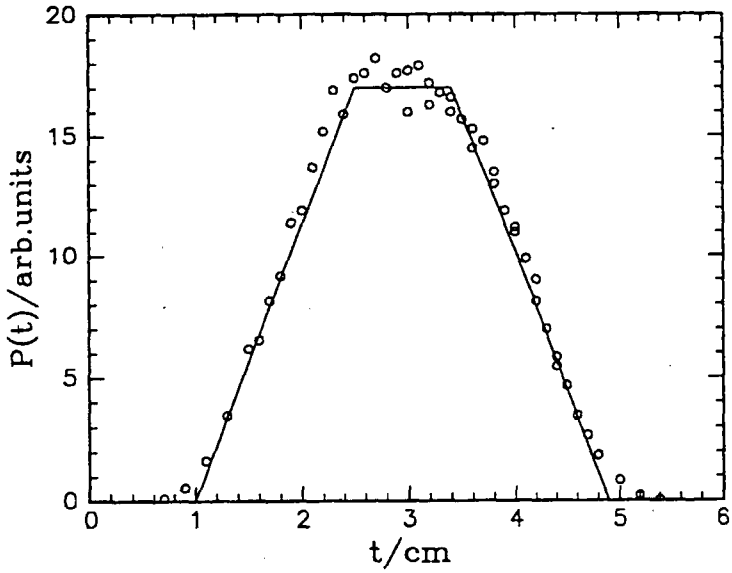

Figure C.3: *Beam length profile measured using the slege. The beam length was 10 mm.*

collimation block. A flat sample holder covered with lead was installed in the camera, such that the beam could freely pass through the camera. The filter in the TPF filter unit was installed at the lowermost position, such that it was not in the beam. Spectra were taken in each position. The data plotted were obtained by integrating over the width of the direct beam (10 channels). The measured profile can be nicely approximated by a trapezoid, as expected from geometrical considerations.

Appendix D

SAXS-measurements using a Huxley-Holmes camera

(SAXS-study in collaboration with Didier Gazeau, 'Service de Chimie Moléculaire', Centre de l'Energie Atomique, Saclay, France, Lise Arleth and Dorthe Posselt, IMFUFA. The experiments were carried out at the 'Service de Chimie Moléculaire' in the laboratory of Thomas Zemb.)

The Huxley-Holmes-camera used in the present study is a pinhole setup with a monochromatized beam. Two low molar-mass samples were studied in order to compare the spectra with data obtained with the Kratky-camera. One sample was disordered at the temperature chosen (150°C), the other sample was shear aligned and measurements were made in the shear aligned, in the disordered and the quenched, polycrystalline state. As will be established below, the measurements using the Huxley-Holmes camera corroborate the values of the peak positions as determined with SANS using the instrument at Risø and with SAXS using the Kratky-camera.

Sample preparation

sample	N	ODT/ °C	preparation method
SB05F	156	-21 ± 10	pressed at 100°C under a nitrogen atmosphere
SB11B	310	130 ± 1	heated to 130°C shear aligned at 119°C for 155 min with 1.0 rad/s and 50 – 200%

Table D.1: *Sample preparation. Given are the chain length, N, the ODT temperature and the preparation method. In case of shear alignment, temperature, duration, shear rate and shear amplitude are given. Details of the preparation methods are given in the text.*

The parameters used for the preparation of samples SB05F and SB11B are given in Table D.1. The samples were not stabilized. However, we consider the effect of crosslink-

ing of the polybutadiene blocks on the structure negligible, firstly, because the samples were not kept at high temperatures longer than some hours, and secondly, because our experience is that crosslinking only has a minor effect on the characteristic lengthscale (Chapter 5.4 and 5.5).

The pills used for scattering experiments were prepared in an RMS-800 rheometer in the parallel-plate geometry (Fig. 3.6). Pills having a diameter of 50 mm and a height of ca. 1 mm were pressed and inserted between the plates. Sample SB05F was heated to 100°C and pressed under a stream of nitrogen gas. Sample SB11B was shear aligned as described in Chapter 4.

The setup

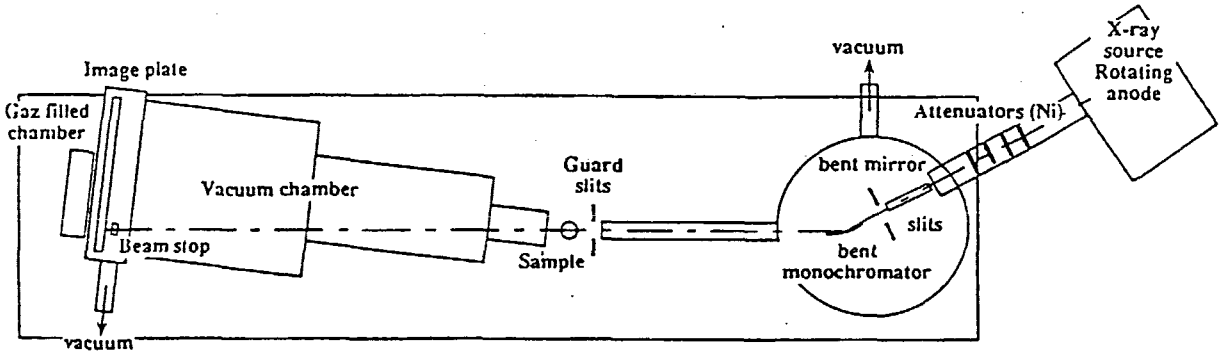

Figure D.1: *Schematic drawing of the Huxley-Holmes camera at Saclay. From [154].*

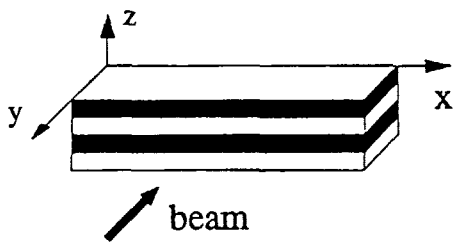

Figure D.2: *The way of mounting samples in the Huxley-Holmes camera. The shear direction is x and the shear gradient is parallel to y. A sample oriented perpendicular to the shear plane is shown (see Fig. 4.3).*

The camera used at Saclay was a Huxley-Holmes camera [155] (Fig. D.1) which is described in detail in [105, 154]. It is characterized by a collimation section which leads to a well-

focused, pointlike, monochromatic beam of high flux. The X-ray source is a rotating Cu-anode ($\lambda = 1.54$ Å) operated at 15 kW. The beam is collimated and monochromatized by a bent glass mirror, covered with nickel, together with a bent germanium crystal and two slits. The tube containing the collimation system as well as the detector tank are evacuated in order to minimize parasitic scattering. The sample stage is kept in air. In the experiments described her, samples were mounted between kapton foil in the same sample holder as used in the Kratky-camera (Fig. 5.14). In order to minimize crosslinking of the polymers, a shielding was mounted around the sample holder which was flushed with nitrogen during the experiments at high temperatures. The shielding had windows for the beam. Kapton tape was glued onto these windows. Samples were mounted such that the beam impinged perpendicular to the pill surface. With shear aligned samples, the vertical axis of the detector corresponds thus to q_z and the horizontal axis to q_x (Figs. D.2 and D.3). The sample-detector distance is 2.15 m. The detector is a multiwire area detector having a diameter of 30 cm and a pixel size of $(1.8\text{mm})^2$. The length of one pixel side thus corresponds to ca. $3.4 \times 10^{-3}\text{Å}^{-1}$. In order to increase the q-range, the detector is positioned such that the direct beam hits off-center. The q-range of the instrument is $0.01 - 0.7$ Å^{-1}. q-calibration was performed measuring the pixel size in real space units (1.8 mm) and transforming pixels into q-values. The calibration was verified using various samples such as collagen fibers from kangaroo tails [105]. A semi-transparent beamstop is mounted in front of the detector, allowing the simultaneous determination of the position and the intensity of the direct beam. In the present study, the integrated intensity of the image of the direct beam behind the beamstop was also used as a measure of the transmission. The transmission of the empty holder with kapton together with the kapton windows of the shielding was found to be 0.67. Measuring times were between 1500 and 4000 sec.

Data analysis

Data analysis was performed using standard Saclay software [156]. Isotropic spectra were azimuthally averaged using masks covering the beamstop and regions of the detector where the sensitivity was reduced or where parasitic scattering occured. The spectrum of the shear aligned sample was anisotropic. It was analyzed using stripes of 5 pixels width in the four directions in order to get information about the degree of alignment (Fig. D.3). The azimuthally averaged intensity was normalized according to [105, 156]

$$I_{norm} = \frac{I_{count}}{\phi_o d\, T_s \epsilon\, \Delta\Omega} \tag{D.1}$$

where I_{norm} denotes the normalized intensity, I_{count} the measured intensity, ϕ_o the flux incident on the sample, d the sample thickness, T_s the sample transmission, ϵ the detector efficiency, and $\Delta\Omega$ the solid angle for detection. The solid angle of one pixel is given by $\Delta\Omega = a^2/D^2$ where a is the pixel size of the detector and D the sample-detector distance. Furthermore, the flux of non-scattered photons through the sample per unit of time is given by $\phi_o T_s = MK/(t\epsilon)$, where M denotes the monitor (the number of photons counted behind the beamstop during the time t) and $K = 131327$ the attenuation factor of the beamstop. Compiling all expressions, one finds [105]

$$I_{norm} = I_{count}(q) \times \frac{D^2/a^2}{MKd} \tag{D.2}$$

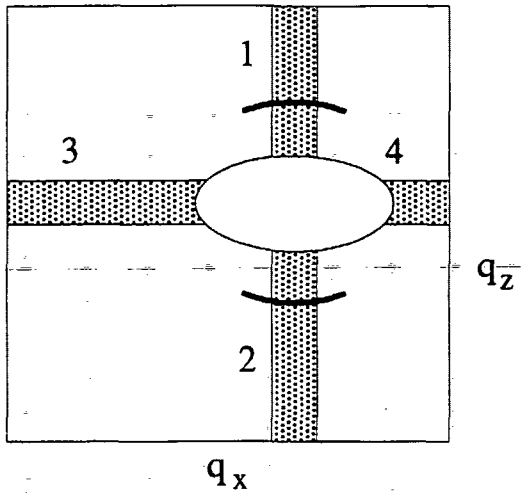

Figure D.3: *Rectangular areas* $(1-4)$ *used for azimuthal averaging of anisotropic spectra. The white ellipse is the beamstop. The shear aligned sample (SB11B) was mounted such that the vertical direction corresponded to* q_z *and the horizontal direction to* q_x*. The arcs indicate the the diffraction peaks from shear aligned samples.*

Background spectra from the empty sample holder were treated in the same way and were subtracted as follows

$$I(q) = I^{s+bg}_{norm} - I^{bg}_{norm} \tag{D.3}$$

where s and bg stand for sample and background. $I(q)$ is given on an absolute scale [156]. Lorentz-functions

$$I(q) = \frac{I_o}{1+(q-q^*)^2\xi^2} + I_{bg} \tag{D.4}$$

were fitted to the peaks in the azimuthally averaged and normalized spectra. I_o, q^*, ξ, and I_{bg} denote the peak intensity, the peak position, the correlation length and the background. $1/\xi$ is the half width at half maximum of the peak. As the spectra are subject to smearing due to the beam size, the peak width can only be evaluated qualitatively.

Results and Discussion

The two-dimensional spectrum of sample SB05F at 150°C (Fig. D.4) shows an isotropic broad ring of scattering as expected for a disordered sample. The azimuthally averaged spectrum displays a broad peak (Fig. D.5). A Lorentz-function was fitted to the range of $0.04-0.3$ Å^{-1} yielding a good fit over the whole range. The fitting parameters are given in Table D.2. A peak position $q^* = (6.10 \pm 0.17) \times 10^{-2}$Å^{-1} is found which coincides nicely with the peak position found using the Kratky-camera ($q^* = (6.20 \pm 0.09) \times 10^{-2}$Å^{-1}, Chapter 5.4). The correlation length is $\xi = (29.8 \pm 0.4)$ Å which is lower than $2\pi/q^* = 103$ Å. The latter value represents the characteristic lengthscale of fluctuations, defined in terms of a Bragg reflection. The correlation length should thus be equal to or larger than this value. The discrepancy is attributed to the fact that the spectrum was not desmeared for the beam size effect.

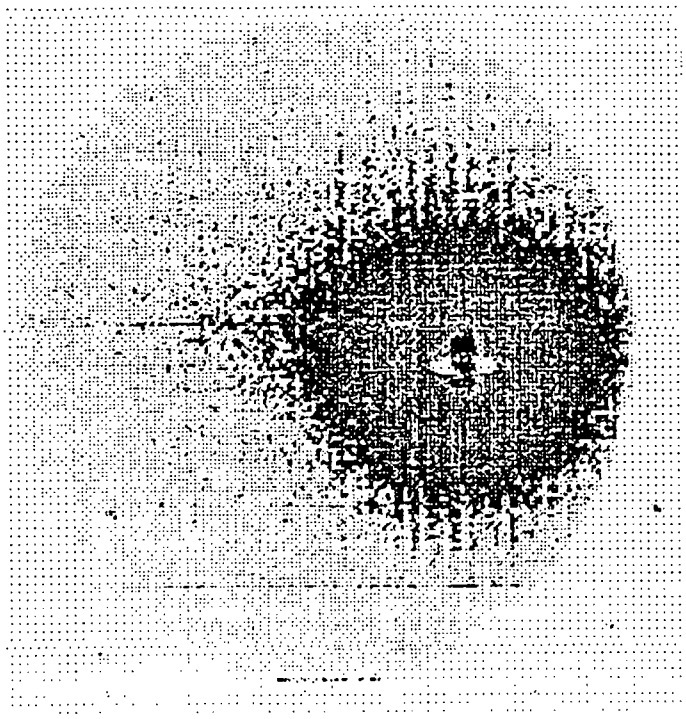

Figure D.4: *Two-dimensional spectrum of SB05F at 150°C.*

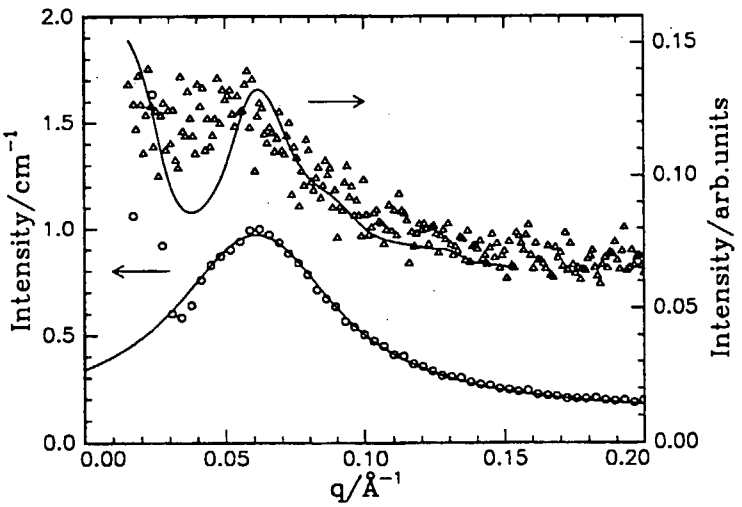

Figure D.5: *(o) Spectrum of SB05F at 150°C measured using the Huxley-Holmes camera. The line is a fit of a Lorentz-function. (△) Spectrum of SBI05B at 150°C measured using the Kratky-camera. For clarity, only every second point is shown. The line is the curve desmeared for the beam length and width effect. For clarity, the Kratky-spectra are shifted upwards by 0.05.*

sample	d/mm	state	T/°C	T_s	q^*/Å^{-1}	I_o/cm^{-1}	ξ/Å
SB05F	0.8	molten	155	0.34	$(6.10 \pm 0.17)10^{-2}$	0.833 ± 0.004	29.8 ± 0.4
SB11B	1.05	shear aligned	120	0.31	$(3.90 \pm 0.17)10^{-2}$	373 ± 52	680 ± 110
	1.25	molten	150	0.25	$(3.93 \pm 0.17)10^{-2}$	8.15 ± 0.07	122 ± 2
	1.25	quenched	120	0.25	$(3.73 \pm 0.17)10^{-2}$	31.6 ± 1.6	268 ± 20
		(a)			$(3.82 \pm 0.17)10^{-2}$	0.542 ± 0.015	280 ± 12

Table D.2: *Results from the measurements using the Huxley-Holmes camera. Given are sample thickness, measuring temperature, sample transmission, peak position, q^*, peak height, I_o, and correlation length, ξ. The errors on q^* are assumed to be 0.5 pixels. (a) Results from the quenched sample after multiplication with the Lorentz-factor $4\pi q^2$.*

In order to compare the azimuthally averaged spectrum of SB05F with the spectrum obtained using the Kratky camera, a slit-smeared Kratky-spectrum together with the corresponding desmeared curve is shown in Fig. D.5. Desmearing of the Kratky-spectrum for the beam length and width effect reveals the peak position, but the peak shape is different from the pinhole spectrum which is attributed to the smearing effect in the pinhole spectrum. In both the Kratky- and the Huxley-Holmes-spectrum, a rise of the intensity towards low values of the scattering vectors ($q < q^*$) is observed. It might be due to a non-vanishing compressibility and the corresponding density fluctuations on a large scale which were also observed with dynamic light scattering [110] (Chapter 7). Another reason might be voids or other inhomogeneities.

The spectrum of a shear aligned sample (SB11B) at 120°C is shown in Fig. D.6. Two diffraction peaks are seen above and below the beamstop, which indicates that the sample was oriented such that the lamellar interfaces were perpendicular to the shear plane (Fig. 4.3b). The azimuthally averaged and normalized spectrum is shown in Fig. D.7. Spectra in q_z-direction (stripe 1 in Fig. D.3) and in q_x-direction (stripe 3) are shown. Unfortunately, the beamstop is wider than high such that scattering in q_x-direction cannot be resolved properly. However, it can be seen that the sample is oriented to a high degree. The parameters found from fitting a Lorentz-function to the q_z-data are given in Table D.2. As the diffraction peak in q_z-direction is as narrow as the direct beam, the value of the correlation length ξ has to be taken as a lower limit. Estimating the average number of lamellae (Eq. 5.45) gives $N_s = 2.783\,\xi q^*/(2\pi) = 12 \pm 2$. As ξ is underestimated due to the smearing effect, the value of N_s has to be taken as a lower limit.

The sample was subsequently heated over the ODT temperature and a spectrum was measured at 150°C. The two-dimensional spectrum shows diffuse isotropic scattering similar to sample SB05F (Fig. D.6). Azimuthal averaging over all directions, normalization and background subtraction gives the spectrum shown in Fig. D.7. As with sample SB05F, a broad peak is observed together with a rise in intensity at low q-values. The intensity found by fitting a Lorentz-curve to the peak is a factor 46 lower than the intensity of the diffraction peaks of the shear aligned sample (Table D.2). The peak position has not changed within the error bars. The correlation length is estimated to be (122 ± 2) Å, thus a factor of six lower than in the shear aligned state.

After melting, the sample was cooled down to 120°C. The obtained spectrum is also

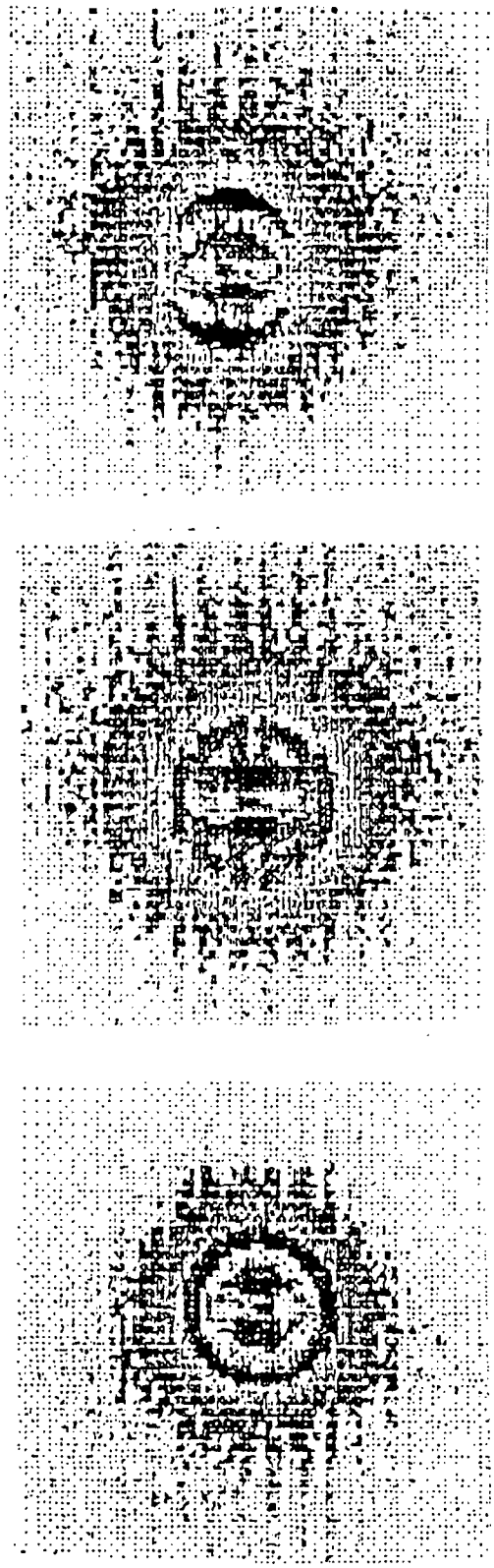

Figure D.6: From top to bottom: *Two-dimensional spectra of shear aligned SB11 at 120°C (oriented), 150°C (disordered) and 120°C (quenched). Only parts of the spectra are shown (around the beamstop).*

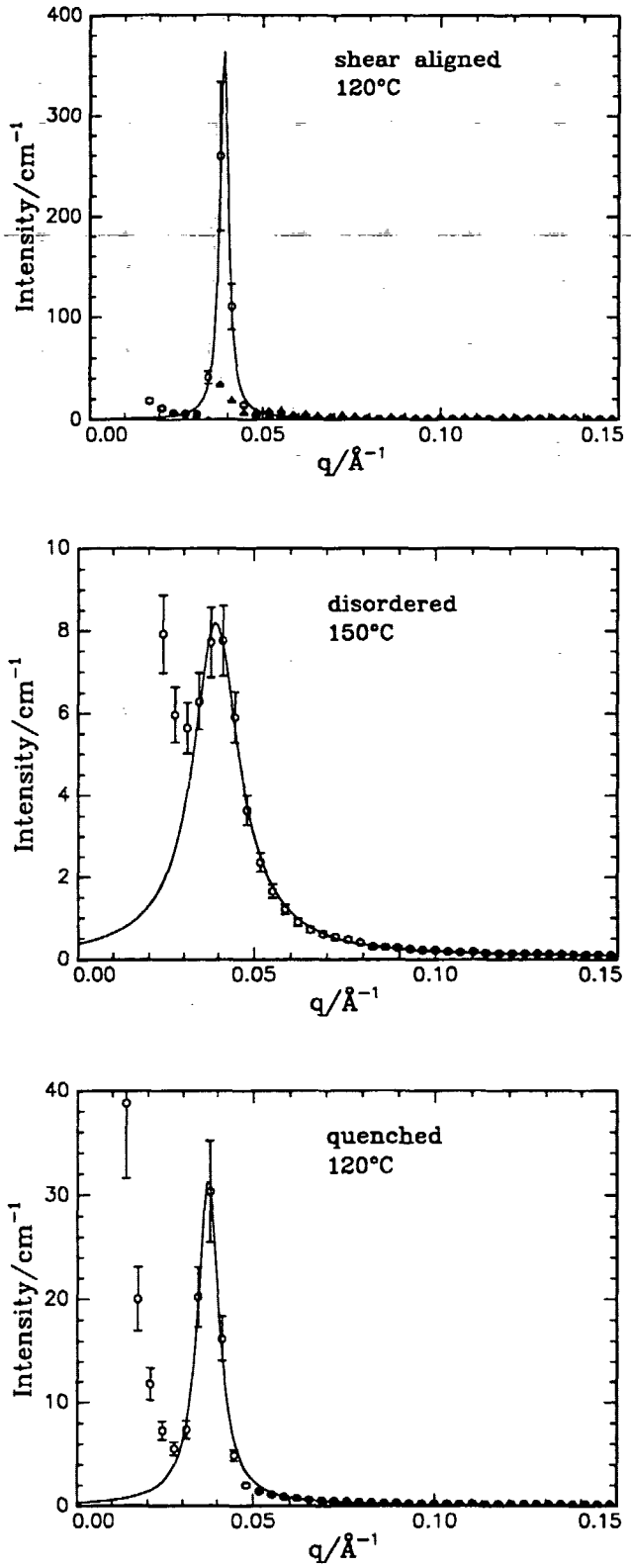

Figure D.7: *Spectra of SB11B measured using the Huxley-Holmes camera. Upper figure: Shear aligned SB11B sample at 120°C. (o) q_z-direction. The line is a fit of a Lorentz-function to the q_z-spectrum. ($\triangle$) q_x-direction. The intensity of the q_x-spectrum is multiplied by a factor of 10. Middle figure: Molten SB11B sample (150°C). (o) experimental data. The line is a fit of a Lorentz-function. Lower figure: Quenched SB11B sample (120°C). (o) experimental data. The line is a fit of a Lorentz-function.*

isotropic, but the ring is much sharper, indicating that the sample is ordered with the lamellar domains oriented randomly (Fig. D.6). Azimuthal averaging using the whole angular range, normalization and background subtraction results in the spectrum shown in Fig. D.7. The upturn of the intensity is attributed to scattering from the domains. This upturn was absent in the spectrum from the shear aligned sample. Fitting a Lorentz-funtion to the peak yields a somewhat lower peak position than before ($q^* = (3.73 \pm 0.17) \times 10^{-2}\text{Å}^{-1}$). However, because of the low q-resolution, the difference cannot be elaborated in detail. Multiplying the intensity with the Lorentz-factor for polycrystalline samples, $4\pi q^2$, and fitting a Lorentz-function to the resulting curve yields a slightly higher peak position: $(3.82 \pm 0.17) \times 10^{-2}\text{Å}^{-1}$ (Table D.2). It should be noted that multiplication with a Lorentz-factor is only appropriate after desmearing, which means that the present calculation is only valid if the smearing effect of the instrument is negligible. This is probably not the case here. However, with the resolution present it is not possible to decide whether the difference in peak position between a shear aligned and a quenched sample is real.

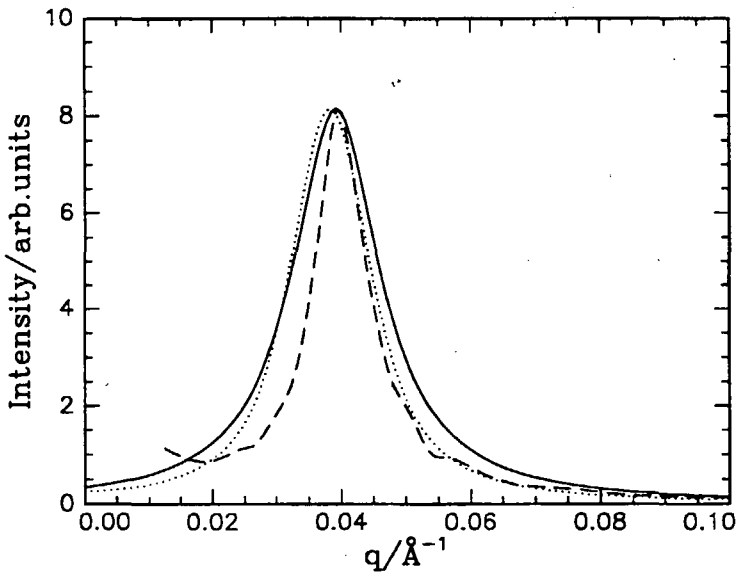

Figure D.8: *Spectra from SB11 samples at 150°C. Full line: Lorentz-function fitted to the Huxley-Holmes-spectrum. Dashed line: spectrum measured with the Kratky-camera which was desmeared for the beam width and length effect. Dotted line: Lorentz-function (not smeared) fitted to the SANS-spectrum measured at Risø. The spectra are scaled such that they coincide in the top point. Before scaling, a background was subtracted from the SANS- and the Huxley-Holmes-spectrum.*

In Fig. D.8, spectra of sample SB11 measured at 150°C with the Huxley-Holmes-camera, the Kratky-camera and the SANS-instrument at Risø are shown. The peak positions are equal within 3% (Table D.3). The values of the correlation length as determined from desmeared SANS- and Kratky-spectra are very similar. This can be seen from Fig. D.8: the larger the correlation length, the narrower the peak. The ξ-value determined with the Huxley-Holmes camera is somewhat lower which is attributed to the smearing of the Huxley-Holmes-spectrum.

instrument	$q^*/\text{Å}^{-1}$	$\xi/\text{Å}$
Huxley-Holmes	$(3.93 \pm 0.17)10^{-2}$	122 ± 2
Kratky	$(3.98 \pm 0.09)10^{-2}$	200 ± 3
SANS	$(3.85 \pm 0.11)10^{-2}$	180 ± 10

Table D.3: *Results from the measurements of sample SB11 at 150°C using the Huxley-Holmes camera, the Kratky camera and the SANS instrument. Given are the peak position and the correlation length.*

Conclusion

The measurements using the Huxley-Holmes corroborate the results from measurements with the Kratky-camera and those found using SANS. The peak positions are equal within 3 %. However, as the Huxley-Holmes spectra are subject to smearing due to the beam size, no quantitative conclusions can be drawn from the peak width. Sample SB05F is disordered at 150°C and displays a broad peak, as expected. With sample SB11 which has an ODT temperature of 130°C, it was qualitatively possible to study the peak shape in the oriented, the disordered and the quenched, polycrystalline state. The two-dimensional spectrum of the oriented sample displays two sharp peaks. In the disordered state, the two-dimensional spectrum is isotropic and displays a broad peak. In the quenched state, the two-dimensional spectrum is isotropic, but the peak is sharper than in the disordered state. This shows that the sample is 'polycrystalline'. The spectra measured at 150°C corroborate the values of the peak positions found with the Kratky-camera and with SANS (Chapters 5.4 and 5.5).

Bibliography

[1] F. S. Bates and G. H. Fredrickson. Block copolymer thermodynamics: Theory and experiment. *Annual Review of Physical Chemistry*, 41:525–557, 1990.

[2] T. A. Witten. Structured fluids. *Physics today*, pages 21–28, July 1990.

[3] M. A. Hillmyer, F. S. Bates, K. Almdal, K. Mortensen, A. J. Ryan, and J. P. A. Fairclough. Complex phase behavior in solvent-free nonionic surfactants. *Science*, 271:976–978, 1996.

[4] P. W. Atkins. *Physical Chemistry.* Oxford University Press, Oxford, 4th edition, 1990.

[5] P. J. Flory. *Statistical Mechanics of Chain Molecules.* Interscience Publishers, New York, 1969.

[6] P.-G. de Gennes. *Scaling concepts in polymer physics.* Cornell University Press, 1979.

[7] L. Leibler. Theory of microphase separation in block copolymers. *Macromolecules*, 13(6):1602–1617, 1980.

[8] K. Almdal, J. H. Rosedale, F. S. Bates, G. D. Wignall, and G. H. Fredrickson. Gaussian- to stretched-coil transition in block copolymer melts. *Physical Review Letters*, 65(9):1112–1115, 1990.

[9] A. N. Semenov. Contribution to the theory of microphase layering in block-copolymer melts. *Sov. Phys. JETP*, 61(4):733–742, 1985. Zh. Eksp. Teor. Fiz. **88**, 1242–1256 (1985).

[10] C. E. Mortimer. *Chemie. Das Basiswissen der Chemie in Schwerpunkten.* Georg Thieme Verlag, 1983.

[11] M. Doi and S. F. Edwards. *The theory of polymer dynamics.* Oxford University Press, 1986.

[12] P.-G. de Gennes. Entangled polymers. *Physics today*, pages 33–39, June 1983.

[13] J. Kanetakis and G. Fytas. Relaxation processes in a homogeneous diblock copolymer at low and high temperatures by means of dynamic light scattering. *Journal of Non-Crystalline Solids*, 131–133:823–826, 1991.

[14] A. N. Semenov, G. Fytas, and S. H. Anastasiadis. Dynamics of composition fluctuations in block-copolymer systems. *Polymer Preprints (Am. Chem. Soc., Div. Polym. Chem.*, 35(1):618–619, 1994.

[15] M. C. Dalvi and T. P. Lodge. Parallel and perpendicular chain diffusion in a lamellar block copolymer. *Macromolecules*, 26(4):859–861, 1993.

[16] A. K. Khandpur, S. Förster, F. S. Bates, I. W. Hamley, A. J. Ryan, W. Bras, K. Almdal, and K. Mortensen. Polyisoprene-polystyrene diblock copolymer phase diagram near the order-disorder transition. *Macromolecules*, 28(26):8796–8806, 1995.

[17] F. S. Bates. Polymer-polymer phase behavior. *Science*, 251:898–905, February 1991.

[18] E. Helfand and Z. R. Wasserman. Microdomain structure and the interface in block copolymers. In I. Goodman, editor, *Developments in Block Copolymers*, volume 1, chapter 4, pages 99–125. Applied Science Publishers, London, 1982.

[19] J. N. Israelachvili. *Intermolecular and surface forces.* Academic Press, 1985.

[20] G. H. Fredrickson and E. Helfand. Fluctuation effects in the theory of microphase separation in block copolymers. *Journal of Chemical Physics*, 87(1):697–705, 1987.

[21] T. Lodge. Characterization of polymer materials by scattering techniques, with applications to block copolymers. *Microchimica Acta*, 116:1–31, 1994.

[22] J. H. Rosedale, F. S. Bates, K. Almdal, K. Mortensen, and G. D. Wignall. Order and disorder in symmetric diblock copolymer melts. *Macromolecules*, 28(5):1429–1443, 1995.

[23] E. Helfand and Z. R. Wasserman. Block copolymer theory. 4. Narrow interphase approximation. *Macromolecules*, 9(6):879–888, 1976.

[24] B. Minchau, B. Dünweg, and K. Binder. Microphase separation transition in block copolymers: A test of Leibler's theory by Monte Carlo simulation. *Polymer Communcations*, 31(9):348–350, 1990.

[25] H. Fried and K. Binder. The microphase separation transition in symmetric diblock copolymer melts: A Monte Carlo study. *Journal of Chemical Physics*, 94(12):8349–8366, 1991.

[26] A. Weyersberg and T. A. Vilgis. Phase transitions in diblock copolymers: theory and Monte Carlo simulations. *Physical Review E*, 48(1):377–390, 1993.

[27] J.-L. Barrat and G. H. Fredrickson. Collective and single-chain correlations near the block copolymer order-disorder transition. *Journal of Chemical Physics*, 95(2):1281–1289, 1991.

[28] S. Ndoni, C. M. Papadakis, F. S. Bates, and K. Almdal. Laboratory-scale setup for anionic polymerization under inert atmosphere. *Review of Scientific Instruments*, 66(2):1090–1095, 1995.

[29] C. M. Papadakis, K. Almdal, and D. Posselt. Molar-mass dependence of the lamellar thickness in symmetric diblock copolymers. *Il Nuovo Cimento*, 16D(7):835–842, 1994.

[30] M. Morton. *Anionic Polymerization: Principles and Practice.* Academic Press, New York, 1983.

[31] K. Almdal. *Absolute Molar Mass Distribution Determination by Size Exclusion Chromatography. Synthesis of Narrow Molar Mass Distribution Polymers. Anionic Polymerization under High Vacuum Conditions. A Manual for Synthesis of High Molar Mass Polyisoprene, Polybutadiene and Polystyrene. II.* PhD thesis, Risø National Laboratory, Roskilde, Denmark, May 1989.

[32] L. J. Fetters, N. P. Balsara, J. S. Huang, H. S. Jeon, K. Almdal, and M. Y. Lin. Aggregation in living polymer solutions by light and neutron scattering: A study of model ionomers. *Macromolecules*, 28(14):4996–5005, 1995.

[33] K. Almdal. Private communication.

[34] J. Brandrup and E. H. Immergut, editors. *Polymer Handbook.* Wiley-Interscience, New York, 1975.

[35] C. R. McIlwrick and C. S. G. Philips. The removal of oxygen from gas streams: application in catalysis and gas chromatography. *Journal of Physics E: Scientific Instruments*, 6:1208–1210, 1973.

[36] H. Gilman and A. H. Haubein. The quantitative analysis of alkyllithium compounds. *Journal of the American Chemical Society*, 66:1515–1516, 1944.

[37] H. Gilman and F. K. Cartledge. The analysis of organolithium compounds. *Journal of Organometallic Chemistry*, 2:447–454, 1964.

[38] S. Ndoni. *Rubber networks with controlled viscoelastic properties.* PhD thesis, Department of Chemistry, University of Copenhagen, Denmark, December 1994.

[39] D. J. Pollock and R. F. Kratz. *Methods of experimental physics. Vol 16: Polymers, Part A: Molecular structure and dynamics.* Academic Press, 1980.

[40] F. W. Billmeyer. *Textbook of polymer science.* John Wiley & Sons, New York, 1984.

[41] A. E. Tonelli. *NMR spectroscopy and Polymer Microstructure: The Conformational Connection.* VCH, 1989.

[42] J. LaMonte Adams, W. W. Graessley, and R. A. Register. Rheology and the microphase separation transition in styrene-isoprene block copolymers. *Macromolecules*, 27(21):6026–6032, 1994.

[43] C. D. Han, D. M. Baek, and J. K. Kim. Effects of molecular weight and block length ratio on the rheological behavior of low molecular weight polystyrene-*block*-polyisoprene copolymers in the disordered state. *Macromolecules*, 28(17):5886–5896, 1995.

[44] J. D. Ferry. *Viscoelastic properties of polymers.* John Wiley and Sons, 1980.

[45] P. J. Flory. *Principles of Polymer Chemistry.* Cornell University Press, Ithaca, New York, 1953.

[46] *RMS-800 owners' manual*, 1986.

[47] J. H. Rosedale and F. S. Bates. Rheology of ordered and disordered symmetric poly(ethylenepropylene)–poly(ethylethylene) diblock copolymers. *Macromolecules*, 23(8):2329–2338, 1990.

[48] N. P. Balsara, H. J. Dai, P. K. Kesani, B. A. Garetz, and B. Hammouda. Influence of imperfections on the disordering of block copolymer cylinders. *Macromolecules*, 27(25):7406–7409, 1994.

[49] P. Munk. *Introduction to macromolecular science.* John Wiley & Sons, New York, 1989.

[50] M. E. Brown. *Introduction to Thermal Analysis*, chapter 4. Chapman & Hall, London, 1988.

[51] R. J. Spontak, M. C. Williams, and D. A. Agard. Interphase composition profile in SB/SBS block copolymers, measured with electron microscopy, and microstructural implications. *Macromolecules*, 21(5):1377–1387, 1988.

[52] F. S. Bates, J. H. Rosedale, H. E. Bair, and T. P. Russell. Synthesis and characterization of a model saturated hydrocarbon diblock copolymer. *Macromolecules*, 22(6):2557–2564, 1989.

[53] N. S. Allen and M. Edge. *Fundamentals of polymer degradation and stabilisation.* Elsevier Applied Science, 1992.

[54] J. Pospíšil. Chain-breaking antioxidants in polymer stabilisation. In G. Scott, editor, *Developments in Polymer Stabilisation*, volume 1. Applied Science Publishers, 1979.

[55] S. Förster, A. K. Khandpur, J. Zhao, F.-S. Bates, I. W. Hamley, A. J. Ryan, and W. Bras. Complex phase behavior of polyisoprene-polystyrene diblock copolymers near the order-disorder transition. *Macromolecules*, 27(23):6922–6935, 1994.

[56] T. Inoue, T. Soen, T. Hashimoto, and H. Kawai. Thermodynamic interpretation of domain structure in solvent-cast films of A-B type block copolymers of styrene and isoprene. *Journal of Polymer Science: Part A-2*, 7:1283–1302, 1969.

[57] T. Hashimoto, M. Shibayama, and H. Kawai. Domain-boundary structure of styrene–isoprene block copolymer films cast from solution. 4. Molecular weight dependence of lamellar microdomains. *Macromolecules*, 13(5):1237–1247, 1980.

[58] Y. Matsushita, K. Mori, R. Saguchi, Y. Nakao, I. Noda, and M. Nagasawa. Molecular weight dependence of lamellar domain spacing of diblock copolymers in bulk. *Macromolecules*, 23(19):4313–4316, 1990.

[59] R. W. Richards and J. L. Thomason. Small-angle neutron scattering study of block copolymer morphology. *Macromolecules*, 16(6):982–992, 1983.

[60] G. Hadziioannou, A. Mathis, and A. Skoulios. Obtention de monocristaux de copolymères triséquencés styrène/isoprène/styrène par cisaillement plan. *Colloid and Polymer Science*, 257(2):136–139, 1979.

[61] Y. Zhang and U. Wiesner. Symmetric diblock copolymers under large amplitude oscillatory shear flow: Entanglement effect. *Journal of Chemical Physics*, 103(11):4784–4793, 1995.

[62] K. A. Koppi, M. Tirrell, F. S. Bates, K. Almdal, and R. H. Colby. Lamellae orientation in dynamically sheared diblock copolymer melts. *Journal de Physique II*, 2(11):1941–1959, 1992.

[63] K. I. Winey, S. S. Patel, R. G. Larson, and H. Watanabe. Interdependence of shear deformation and block copolymer morphology. *Macromolecules*, 26(10):2542–2549, 1993.

[64] V. K. Gupta, R. Krishnamoorti, J. A. Kornfield, and S. D. Smith. Evolution of microstructure during shear alignment in a polystyrene-polyisoprene lamellar diblock copolymer. *Macromolecules*, 28(13):4464–4474, 1995.

[65] K. Almdal, K. A. Koppi, F. S. Bates, and K. Mortensen. Multiple ordered phases in a block copolymer melt. *Macromolecules*, 25(6):1743–1751, 1992.

[66] I. W. Hamley, M. D. Gehlsen, A. K. Khandpur, K. A. Koppi J. H.Rosedale, M. F. Schulz, F. S. Bates, K. Almdal, and K. Mortensen. Complex layered phases in asymmetric diblock copolymers. *Journal de Physique II*, 4(12):2161–2186, 1994.

[67] K. A. Koppi, M. Tirrell, F. S. Bates, K. Almdal, and K. Mortensen. Epitaxial growth and shearing of the body centered cubic phase in diblock copolymer melts. *J. Rheol.*, 38(4):999–1027, 1994.

[68] G. Hadziioannou and A. Skoulios. Molecular weight dependence of lamellar structure in styrene/isoprene two- and three-block copolymers. *Macromolecules*, 15(2):258–262, 1982.

[69] *RSA II owners' manual*, 1991.

[70] A. N. Semenov. Microphase separation in diblock-copolymer melts: Ordering of micelles. *Macromolecules*, 22(6):2849–2851, 1989.

[71] J. Melenkevitz and M. Muthukumar. Density functional theory of lamellar ordering in diblock copolymers. *Macromolecules*, 24(14):4199–4205, 1991.

[72] H. Tang and K. F. Freed. Immiscibility induced chain stretching, local segregation, and formation of locally ordered domains in diblock copolymers. *Journal of Chemical Physics*, 96(11):8621–8623, 1992.

[73] J. D. Vavasour and M. D. Whitmore. Self-consistent mean field theory of the microphases of diblock copolymers. *Macromolecules*, 25(20):5477–5486, 1992.

[74] W. E. McMullen. A fourth-order, density-functional, random-phase approximation study of monomer segregation in phase-separated, lamellar, diblock-copolymer melts. *Macromolecules*, 26(5):1027–1036, 1993.

[75] R. A. Sones, E. M. Terentjev, and R. G. Petschek. Lamellar ordering in symmetric diblock copolymers. *Macromolecules*, 26(13):3344–3350, 1993.

[76] F. S. Bates, S. B. Dierker, and G. D. Wignall. Phase behavior of amorphous binary mixtures of perdeuterated and normal 1,4-polybutadienes. *Macromolecules*, 19(7):1938–1945, 1986.

[77] B. Holzer, A. Lehmann, B. Stühn, and M. Kowalski. Asymmetric diblock copolymers near the microphase separation: limitations of mean field theory. *Polymer*, 32(11):1935–1942, 1991.

[78] T. Ohta and K. Kawasaki. Equilibrium morphology of block copolymer melts. *Macromolecules*, 19(10):2621–2632, 1986.

[79] W. E. McMullen and K. F. Freed. Static structure factors of compressible polymer blends and diblock copymer melts. *Macromolecules*, 23(1):255–262, 1990.

[80] H. Tang and K. F. Freed. Static structure factors of compressible polymer blends and diblock copolymer melts. 2. Constraints on density fluctuations. *Macromolecules*, 24(4):958–966, 1991.

[81] S. A. Brazovskiĭ. Phase transition of an isotropic system to a nonuniform state. *Sov. Phys.-JETP*, 41(1):85–89, 1975.

[82] O. Glatter and O. Kratky, editors. *Small-Angle X-Ray Scattering.* Academic Press, New York, 1982.

[83] O. Kratky and P. Laggner. X-ray small-angle scattering. *Encyclopedia of Physical Science and Technology*, 14:693–742, 1987.

[84] D. Posselt. *Structural and thermal studies of silica aerogel. A mass-fractal model system.* PhD thesis, Risø National Laboratory, Roskilde, Denmark, 1991.

[85] H. Brumberger, editor. *Modern aspects of small-angle scattering.* NATO ASI, Kluwer Academic Publishers, 1995.

[86] R. Hosemann and S. N. Bagchi. *Direct analysis of diffraction by matter.* North-Holland Publishing Company, 1962.

[87] O. Glatter. Evaluation of small-angle scattering data from lamellar and cylindrical particles by the indirect transformation method. *Journal of Applied Crystallography*, 13:577–584, 1980.

[88] L. Gråbæk. *X-ray diffraction studies of Kr, Xe and Pb inclusions in aluminum.* PhD thesis, Risø National Laboratory, Roskilde, Denmark, July 1990.

[89] C. G. Vonk. Synthetic polymers in the solid state. In O. Glatter and O. Kratky, editors, *Small angle X-ray scattering*, pages 433–466. Academic Press, 1982.

[90] P. W. Schmidt. Some fundamental concepts and techniques useful in small-angle scattering studies of disordered solids. In H. Brumberger, editor, *Modern aspects of small-angle scattering*, NATO ASI Series, pages 1–56. Kluwer Academic Publishers, 1995.

[91] J. T. Koberstein, B. Morra, and R. S. Stein. The determination of diffuse-boundary thicknesses of polymers by small-angle x-ray scattering. *Journal of Applied Crystallography*, 13:34–45, 1980.

[92] L. Leibler and H. Benoit. Theory of correlations in partly labelled homopolymer melts. *Polymer*, 22:195–201, 1981.

[93] O. Kratky. Neues Verfahren zur Herstellung von blendenstreuungsfreien Röntgen-Kleinwinkelaufnahmen. *Zeitschrift für Elektrochemie*, 58(1):49–53, 1954.

[94] O. Kratky and A. Sekora. Neues Verfahren zur Herstellung von blendenstreuungsfreien Röntgenkleinwinkelaufnahmen. II. *Monatshefte für Chemie*, 85(3):660–672, 1954.

[95] O. Kratky. Neues Verfahren zur Herstellung von blendenstreuungsfreien Röntgen-Kleinwinkelaufnahmen III. *Kolloid-Zeitschrift*, 144:110–120, 1955.

[96] O. Kratky. Neues Verfahren zur Herstellung von blendenstreuungsfreien Röntgen-Kleinwinkelaufnahmen. IV. *Zeitschrift für Elektrochemie*, 62(1):66–77, 1958.

[97] O. Kratky and H. Stabinger. X-ray small angle camera with block-collimation system an instrument of colloid research. *Colloid and Polymer Science*, 262(5):345–360, 1984.

[98] S. Bøggild, M. H. Nielsen, and B. W. Petersen. Røntgendiffraktion af blandinger af symmetriske diblokcopolymerer. Report, IMFUFA (Institut for Mathematics and Physics), Roskilde University, 1996.

[99] R. Allemand and G. Thomas. Nouveau détecteur de localisation. *Nuclear Instruments and Methods*, 137:141–149, 1976.

[100] T. C. Huang, H. Toraya, T. N. Blanton, and Y. Wu. X-ray powder diffraction analysis of silver behenate, a possible low-angle diffraction standard. *Journal of Applied Crystallography*, 26:180–184, 1993.

[101] O. Glatter and K. Gruber. Indirect transformation in reciprocal space: desmearing of small-angle scattering data from partially ordered systems. *Journal of Applied Crystallography*, 26:512–518, 1993.

[102] O. Glatter. Modern methods of data analysis in small-angle scattering and light scattering. In H. Brumberger, editor, *Modern aspects of small-angle scattering*, NATO ASI Series, pages 107–180. Kluwer Academic Publishers, 1995.

[103] D. G. H. Ballard, G. D. Wignall, and J. Schelten. Measurement of molecular dimensions of polystyrene chains in the bulk polymer by low angle neutron diffraction. *European Polymer Journal*, 9:965–969, 1973.

[104] O. Glatter. Data treatment. In O. Glatter and O. Kratky, editors, *Small-Angle X-Ray Scattering*, chapter 4. Academic Press, New York, 1982.

[105] L. Arleth. Characterization of tetraaza-AC8 — a surfactant with cation complexing potential. Master's thesis, IMFUFA, Roskilde University, 1995.

[106] K. Mortensen. Small-angle scattering on soft materials. *Nukleonika*, 39(1–2):169–184, 1994.

[107] J. S. Pedersen, D. Posselt, and K. Mortensen. Analytical treatment of the resolution function for small-angle scattering. *Journal of Applied Crystallography*, 23:321–333, 1990.

[108] K. Mortensen. Private communication.

[109] T. Hashimoto, K. Nagatoshi, A. Todo, H. Hasegawa, and H. Kawai. Domain-boundary structure of styrene-isoprene block copolymer films cast from toluene solutions. *Macromolecules*, 7(3):364–373, 1974.

[110] C. M. Papadakis, W. Brown, R. M. Johnsen, D. Posselt, and K. Almdal. The dynamics of symmetric polystyrene-polybutadiene diblock copolymer melts studied above and below the order-disorder transition using dynamic light scattering. *Journal of Chemical Physics*, 104(4):1611–1625, 1996.

[111] N. Sakamoto and T. Hashimoto. Order-disorder transition of low molecular weight polystyrene-*block*-polyisoprene. 1. SAXS analysis of two characteristic temperatures. *Macromolecules*, 28(20):6825–6834, 1995.

[112] B. Stühn, R. Mutter, and T. Albrecht. Direct observation of structure formation at the temperature-driven order-to-disorder transition in diblock copolymers. *Europhysics Letters*, 18(5):427–432, 1992.

[113] T. Wolff, C. Burger, and W. Ruland. Synchrotron SAXS study of the microphase separation transition in diblock copolymers. *Macromolecules*, 26(7):1707–1711, 1993.

[114] G. Floudas, S. Vogt, T. Pakula, and E. W. Fischer. Density and concentration fluctuations in poly(styrene-*b*-phenylmethylsiloxane) copolymers. *Macromolecules*, 26(26):7210–7213, 1993.

[115] F. S. Bates, J. H. Rosedale, and G. H. Fredrickson. Fluctuation effects in a symmetric diblock copolymer near the order-disorder transition. *Journal of Chemical Physics*, 92(10):6255–6270, 1990.

[116] J. W. Mays, N. Hadjichristidis, and L. J. Fetters. Solvent and temperature influences on polystyrene unperturbed dimensions. *Macromolecules*, 18(11):2231–2236, 1985.

[117] L. J. Fetters, D. J. Lohse, D. Richter, T. A. Witten, and A. Zirkel. Connection between polymer molecular weight, density, chain dimensions, and melt viscoelastic properties. *Macromolecules*, 27(17):4639–4647, 1994.

[118] W. Brown, editor. *Dynamic light scattering. The method and some applications.* Oxford University Press, 1993.

[119] P. Štěpánek and T. P. Lodge. Light scattering by block copolymer liquids in the disordered and ordered state. In W. Brown, editor, *Dynamic light scattering. Principles and development.* Oxford University Press, 1996.

[120] A. Z. Akcasu and M. Tombakoglu. Dynamics of copolymer and homopolymer mixtures in bulk and in solution via the random phase approximation. *Macromolecules*, 23(2):607–612, 1990.

[121] R. Borsali and T. A. Vilgis. Dynamics of copolymer and homopolymer blends in strong solutions and bulk: The Edwards Hamiltonian approach. *Journal of Chemical Physics*, 93(5):3610–3613, 1990.

[122] G. Fytas, S. H. Anastasiadis, and A. N. Semenov. Diffusive relaxation mode in diblock copolymer melts. *Macromol. Symp.*, 79:117–124, 1994.

[123] S. H. Anastasiadis, G. Fytas, S. Vogt, and E. W. Fischer. Breathing and composition pattern relaxation in "homogeneous" diblock copolymers. *Physical Review Letters*, 70(16):2415–2418, 1993.

[124] S. Vogt, S. H. Anastasiadis, G. Fytas, and E. W. Fischer. Dynamics of composition fluctuations in diblock copolymer melts above the ordering transition. *Macromolecules*, 27(15):4335–4343, 1994.

[125] S. H. Anastasiadis, G. Fytas, S. Vogt, B. Gerharz, and E. W. Fischer. Diffusive composition pattern relaxation in disordered diblock copolymer melts. *Europhysics Letters*, 22(8):619–624, 1993.

[126] S. Vogt, T. Jian, S. H. Anastasiadis, G. Fytas, and E. W. Fischer. Diffusive relaxation mode in poly(styrene-*b*-methylphenylsiloxane) copolymer melts above and below the order-disorder transition. *Macromolecules*, 26(13):3357–3362, 1993.

[127] B. Gerharz, G. Meier, and E. W. Fischer. The dynamics of binary mixtures of nonpolymeric viscoelastic liquids as studied by quasielastic light scattering. *Journal of Chemical Physics*, 92(12):7110–7122, 1990.

[128] W. Brown and P. Štěpánek. Distribution of relaxation times from dynamic light scattering on semidilute solutions: Polystyrene in ethyl acetate as a function of temperature from good to Θ conditions. *Macromolecules*, 21(6):1791–1798, 1988.

[129] T. Kanaya, A. Patkowski, E. W. Fischer, J. Seils, H. Gläser, and K. Kaji. Light scattering studies on long-range density fluctuations in a glass-forming polymer. *Acta Polymer*, 45:137–142, 1994.

[130] T. Bremner and A. Rudin. Persistence of regions with high segment density in polyethylene melts. *Journal of Polymer Science: Part B: Polymer Physics*, 30:1247–1260, 1992.

[131] G. D. Patterson. Photon correlation spectroscopy of bulk polymers. *Advances in Polymer Science*, 48:125–167, 1983.

[132] J. Kanetakis, G. Fytas, F. Kremer, and T. Pakula. Segmental dynamics in homogeneous 1,4-polyisoprene-1,2-polybutadiene diblock copolymers. *Macromolecules*, 25(13):3484–3491, 1992.

[133] A. K. Rizos, G. Fytas, and J. E. L. Roovers. Segmental motion in poly(styrene-*b*-1,4-isoprene) block copolymers in the disordered state. *Journal of Chemical Physics*, 97(9):6925–6932, 1992.

[134] A. Hoffmann, T. Koch, and B. Stühn. Effect of the disorder-to-order transition in diblock copolymers on the segmental dynamics: A study using depolarized photon correlation spectroscopy. *Macromolecules*, 26(26):7288–7294, 1993.

[135] T. Jian, A. N. Semenov, S. H. Anastasiadis, G. Fytas, F.-J. Yeh, B. Chu, S. Vogt, F. Wang, and J. E. L. Roovers. Composition fluctuation induced depolarized Rayleigh scattering from diblock copolymer melts. *Journal of Chemical Physics*, 100(4):3286–3296, 1994.

[136] P. Štěpánek and R. M. Johnsen. Dynamic light scattering from polymer solutions: The subtraction technique. *Collect. Czech. Chem. Commun.*, 60:1941–1949, 1995.

[137] B. Chu. *Laser light scattering. Basic principles and practice.* Academic Press, 1991.

[138] P. Lindner and T. Zemb, editors. *Neutron, X-ray and light scattering.* Elsevier Science Publishers, 1991.

[139] B. J. Berne and R. Pecora. *Dynamic Light Scattering. With Applications to Chemistry, Biology, and Physics.* Wiley-Interscience, 1976.

[140] P. Štěpánek. Data analysis in dynamic light scattering. In W. Brown, editor, *Dynamic light scattering. The method and some applications*, chapter 4, pages 177–241. Oxford University Press, 1993.

[141] K. Schillén. *Solution properties of block copolymers studied using light scattering.* PhD thesis, Uppsala University, 1994.

[142] J. Rička. Dynamic light scattering with single-mode and multimode recivers. *Applied Optics*, 32(15):2860–2875, 1993.

[143] D. R. Lide, editor. *CRC Handbook of chemistry and physics.* CRC Press, 1993.

[144] K. Schillén, W. Brown, and R. M. Johnsen. Micellar sphere-to-rod transition in an aqueous triblock copolymer system. A dynamic light scattering study of translational and rotational diffusion. *Macromolecules*, 27(17):4825–4832, 1994.

[145] W. Brown and T. Nicolai. Polarized and depolarized light scattering of concentrated polystyrene solutions. *Macromolecules*, 27(9):2470–2480, 1994.

[146] J. Jakeš. Testing of the constrained regularization method of inverting Laplace transform on simulated very wide quasielastic light scattering autocorrelation functions. *Czechoslovak Journal of Physics*, B38:1305–1316, 1988.

[147] S. W. Provencher. Inverse problems in polymer characterization: Direct analysis of polydispersity with photon correlation spectroscopy. *Die makromolekulare Chemie*, 180:201–209, 1979.

[148] P. Štěpánek and T. P. Lodge. Dynamic light scattering from block copolymer melts near the order-disorder transition. *Macromolecules*, 29(4):1244–1251, 1996.

[149] N. P. Balsara, D. Perahia, C. R. Safinya, M. Tirrell, and T. P. Lodge. Birefringence detection of the order-to-disorder transition in block copolymer liquids. *Macromolecules*, 25(15):3896–3901, 1992.

[150] N. P. Balsara, B. A. Garetz, and H. J. Dai. Relationship between birefringence and the structure of ordered block copolymer materials. *Macromolecules*, 25(22):6072–6074, 1992.

[151] G. Fleischer, F. Fujara, and B. Stühn. Restricted diffusion in the regime of the order-to-disorder transition in diblock copolymers: a field gradient NMR study. *Macromolecules*, 26(9):2340–2345, 1993.

[152] SKF Danmark A/S. Booklet SKF precision ball screws, 1993.

[153] INA-Lejer A/S. Booklet Miniatur-Kugelumlaufeinheiten, 1992.

[154] V. Le Flanchec, D. Gazeau, J. Taboury, and Th. Zemb. Two-dimensional desmearing of small angle X-ray scattering diffraction patterns. *J. Appl. Cryst.*, 29:110, 1996.

[155] H. E. Huxley and W. Brown. The low-angle X-ray diagram of vertebrate striated muscle and its behavior during contraction and rigor. *Journal of Molecular Biology*, 30:383–434, 1967.

[156] F. Né, D. Gazeau, J. Lambard, P. Lesieur, T. Zemb, and A. Gabriel. Characterization of an image-plate detector used for quantitative small-angle-scattering studies. *Journal of Applied Crystallography*, 26:763–773, 1993.

Liste over tidligere udkomne tekster tilsendes gerne. Henvendelse herom kan ske til IMFUFA's sekretariat tlf. 46 75 77 11 lokal 2263

217/92 "Two papers on APPLICATIONS AND MODELLING IN THE MATHEMATICS CURRICULUM"

by: Mogens Niss

218/92 "A Three-Square Theorem"

by: Lars Kadison

219/92 "RUPNOK - stationær strømning i elastiske rør"

af: Anja Boisen, Karen Birkelund, Mette Olufsen

Vejleder: Jesper Larsen

220/92 "Automatisk diagnosticering i digitale kredsløb"

af: Bjørn Christensen, Ole Møller Nielsen

Vejleder: Stig Andur Pedersen

221/92 "A BUNDLE VALUED RADON TRANSFORM, WITH APPLICATIONS TO INVARIANT WAVE EQUATIONS"

by: Thomas P. Branson, Gestur Olafsson and Henrik Schlichtkrull

222/92 On the Representations of some Infinite Dimensional Groups and Algebras Related to Quantum Physics

by: Johnny T. Ottesen

223/92 THE FUNCTIONAL DETERMINANT

by: Thomas P. Branson

224/92 UNIVERSAL AC CONDUCTIVITY OF NON-METALLIC SOLIDS AT LOW TEMPERATURES

by: Jeppe C. Dyre

225/92 "HATMODELLEN" Impedansspektroskopi i ultrarent en-krystallinsk silicium

af: Anja Boisen, Anders Gorm Larsen, Jesper Varmer, Johannes K. Nielsen, Kit R. Hansen, Peter Bøggild og Thomas Hougaard

Vejleder: Petr Viscor

226/92 "METHODS AND MODELS FOR ESTIMATING THE GLOBAL CIRCULATION OF SELECTED EMISSIONS FROM ENERGY CONVERSION"

by: Bent Sørensen

227/92 "Computersimulering og fysik"

af: Per M.Hansen, Steffen Holm, Peter Maibom, Mads K. Dall Petersen, Pernille Postgaard, Thomas B.Schrøder, Ivar P. Zeck

Vejleder: Peder Voetmann Christiansen

228/92 "Teknologi og historie"

Fire artikler af:

Mogens Niss, Jens Høyrup, Ib Thiersen, Hans Hedal

229/92 "Masser af information uden betydning"

En diskussion af informationsteorien i Tor Nørretranders' "Mærk Verden" og en skitse til et alternativ bassereet på andenordens kybernetik og semiotik.

af: Søren Brier

230/92 "Vinklens tredeling - et klassisk problem"

et matematisk projekt af

Karen Birkelund, Bjørn Christensen

Vejleder: Johnny Ottesen

231A/92 "Elektrondiffusion i silicium - en matematisk model"

af: Jesper Voetmann, Karen Birkelund, Mette Olufsen, Ole Møller Nielsen

Vejledere: Johnny Ottesen, H.B.Hansen

231B/92 "Elektrondiffusion i silicium - en matematisk model" Kildetekster

af: Jesper Voetmann, Karen Birkelund, Mette Olufsen, Ole Møller Nielsen

Vejledere: Johnny Ottesen, H.B.Hansen

232/92 "Undersøgelse om den simultane opdagelse af energiens bevarelse og især eles om de af Mayer, Colding, Joule og Helmholtz udførte arbejder"

af: L.Arleth, G.I.Dybkjær, M.T.Østergård

Vejleder: Dorthe Posselt

233/92 "The effect of age-dependent host mortality on the dynamics of an endemic disease and
Instability in an SIR-model with age-dependent susceptibility

by: Viggo Andreasen

234/92 "THE FUNCTIONAL DETERMINANT OF A FOUR-DIMENSIONAL BOUNDARY VALUE PROBLEM"

by: Thomas P. Branson and Peter B. Gilkey

235/92 OVERFLADESTRUKTUR OG POREUDVIKLING AF KOKS

- Modul 3 fysik projekt -

af: Thomas Jessen

236a/93 INTRODUKTION TIL KVANTE HALL EFFEKTEN

af: Anja Boisen, Peter Bøggild

Vejleder: Peder Voetmann Christiansen
Erland Brun Hansen

236b/93 STRØMSSAMMENBRUD AF KVANTE HALL EFFEKTEN

af: Anja Boisen, Peter Bøggild

Vejleder: Peder Voetmann Christiansen
Erland Brun Hansen

237/93 The Wedderburn principal theorem and Shukla cohomology

af: Lars Kadison

238/93 SEMIOTIK OG SYSTEMEGENSKABER (2)

Vektorbånd og tensorer

af: Peder Voetmann Christiansen

239/93 Valgsystemer - Modelbygning og analyse

Matematik 2. modul

af: Charlotte Gjerrild, Jane Hansen, Maria Hermannsson, Allan Jørgensen, Ragna Clauson-Kaas, Poul Lützen

Vejleder: Mogens Niss

240/93 Patologiske eksempler.
Om sære matematiske fisks betydning for den matematiske udvikling

af: Claus Dræby, Jørn Skov Hansen, Runa Ulsøe Johansen, Peter Meibom, Johannes Kristoffer Nielsen

Vejleder: Mogens Niss

241/93 FOTOVOLTAISK STATUSNOTAT 1

af: Bent Sørensen

242/93 Brovedligeholdelse - bevar mig vel

Analyse af Vejdirektoratets model for optimering af broreparationer

af: Linda Kyndlev, Kare Fundal, Kamma Tulinius, Ivar Zeck

Vejleder: Jesper Larsen

243/93 TANKEEKSPERIMENTER I FYSIKKEN

Et 1.modul fysikprojekt

af: Karen Birkelund, Stine Sofia Korremann

Vejleder: Dorthe Posselt

244/93 RADONTRANSFORMATIONEN og dens anvendelse i CT-scanning

Projektrapport

af: Trine Andreasen, Tine Guldager Christiansen, Nina Skov Hansen og Christine Iversen

Vejledere: Gestur Olafsson og Jesper Larsen

245a+b /93 Time-Of-Flight målinger på krystallinske halvledere
Specialerapport

af: Linda Szkotak Jensen og Lise Odgaard Gade

Vejledere: Petr Viscor og Niels Boye Olsen

246/93 HVERDAGSVIDEN OG MATEMATIK
- LÆREPROCESSER I SKOLEN

af: Lena Lindenskov, Statens Humanistiske Forskningsråd, RUC, IMFUFA

247/93 UNIVERSAL LOW TEMPERATURE AC CONDUCTIVITY OF MACROSCOPICALLY DISORDERED NON-METALS

by: Jeppe C. Dyre

248/93 DIRAC OPERATORS AND MANIFOLDS WITH BOUNDARY

by: B. Booss-Bavnbek, K.P.Wojciechowski

249/93 Perspectives on Teichmüller and the Jahresbericht Addendum to Schappacher, Scholz, et al.

by: B. Booss-Bavnbek

With comments by W.Abikoff, L.Ahlfors, J.Cerf, P.J.Davis, W.Fuchs, F.P.Gardiner, J.Jost, J.-P.Kahane, R.Lohan, L.Lorch, J.Radkau and T.Söderqvist

250/93 EULER OG BOLZANO - MATEMATISK ANALYSE SET I ET VIDENSKABSTEORETISK PERSPEKTIV

Projektrapport af: Anja Juul, Lone Michelsen, Tomas Højgård Jensen

Vejleder: Stig Andur Pedersen

251/93 Genotypic Proportions in Hybrid Zones

by: Freddy Bugge Christiansen, Viggo Andreasen and Ebbe Thue Poulsen

252/93 MODELLERING AF TILFÆLDIGE FÆNOMENER

Projektrapport af: Birthe Friis, Lisbeth Helmgaard, Kristina Charlotte Jakobsen, Marina Mosbæk Johannessen, Lotte Ludvigsen, Mette Hass Nielsen

253/93 Kuglepakning

Teori og model

af: Lise Arleth, Kåre Fundal, Nils Kruse

Vejleder: Mogens Niss

254/93 Regressionsanalyse

Materiale til et statistikkursus

af: Jørgen Larsen

255/93 TID & BETINGET UAFHÆNGIGHED

af: Peter Harremoës

256/93 Determination of the Frequency Dependent Bulk Modulus of Liquids Using a Piezoelectric Spherical Shell (Preprint)

by: T. Christensen and N.B.Olsen

257/93 Modellering af dispersion i piezoelektriske keramikker

af: Pernille Postgaard, Jannik Rasmussen, Christina Specht, Mikko Østergård

Vejleder: Tage Christensen

258/93 Supplerende kursusmateriale til "Lineære strukturer fra algebra og analyse"

af: Mogens Brun Heefelt

259/93 STUDIES OF AC HOPPING CONDUCTION AT LOW TEMPERATURES

by: Jeppe C. Dyre

260/93 PARTITIONED MANIFOLDS AND INVARIANTS IN DIMENSIONS 2, 3, AND 4

by: B. Booss-Bavnbek, K.P.Wojciechowski

261/93 OPGAVESAMLING
Bredde-kursus i Fysik
Eksamensopgaver fra 1976-93

262/93 Separability and the Jones Polynomial
by: Lars Kadison

263/93 Supplerende kursusmateriale til "Lineære strukturer fra algebra og analyse" II
af: Mogens Brun Heefelt

264/93 FOTOVOLTAISK STATUSNOTAT 2
af: Bent Sørensen

265/94 SPHERICAL FUNCTIONS ON ORDERED SYMMETRIC SPACES
To Sigurdur Helgason on his sixtyfifth birthday
by: Jacques Faraut, Joachim Hilgert and Gestur Olafsson

266/94 Kommensurabilitets-oscillationer i laterale supergitre
Fysikspeciale af: Anja Boisen, Peter Bøggild, Karen Birkelund
Vejledere: Rafael Taboryski, Poul Erik Lindelof, Peder Voetmann Christiansen

267/94 Kom til kort med matematik på Eksperimentarium - Et forslag til en opstilling
af: Charlotte Gjerrild, Jane Hansen
Vejleder: Bernhelm Booss-Bavnbek

268/94 Life is like a sewer ...
Et projekt om modellering af aorta via en model for strømning i kloakrør
af: Anders Marcussen, Anne C. Nilsson, Lone Michelsen, Per M. Hansen
Vejleder: Jesper Larsen

269/94 Dimensionsanalyse en introduktion
metaprojekt, fysik
af: Tine Guldager Christiansen, Ken Andersen, Nikolaj Hermann, Jannik Rasmussen
Vejleder: Jens Højgaard Jensen

270/94 THE IMAGE OF THE ENVELOPING ALGEBRA AND IRREDUCIBILITY OF INDUCED REPRESENTATIONS OF EXPONENTIAL LIE GROUPS
by: Jacob Jacobsen

271/94 Matematikken i Fysikken.
Opdaget eller opfundet
NAT-BAS-projekt
vejleder: Jens Højgaard Jensen

272/94 Tradition og fornyelse
Det praktiske elevarbejde i gymnasiets fysikundervisning, 1907-1988
af: Kristian Hoppe og Jeppe Guldager
Vejledning: Karin Beyer og Nils Hybel

273/94 Model for kort- og mellemdistanceløb
Verifikation af model
af: Lise Fabricius Christensen, Helle Pilemann, Bettina Sørensen
Vejleder: Mette Olufsen

274/94 MODEL 10 - en matematisk model af intravenøse anæstetikas farmakokinetik
3. modul matematik, forår 1994
af: Trine Andreasen, Bjørn Christensen, Christine Green, Anja Skjoldborg Hansen. Lisbeth Helmgaard
Vejledere: Viggo Andreasen & Jesper Larsen

275/94 Perspectives on Teichmüller and the Jahresbericht
2nd Edition
by: Bernhelm Booss-Bavnbek

276/94 Dispersionsmodellering
Projektrapport 1. modul
af: Gitte Andersen, Rehannah Borup, Lisbeth Friis, Per Gregersen, Kristina Vejrø
Vejleder: Bernhelm Booss-Bavnbek

277/94 PROJEKTARBEJDSPÆDAGOGIK - Om tre tolkninger af problemorienteret projektarbejde
af: Claus Flensted Behrens, Frederik Voetmann Christiansen, Jørn Skov Hansen, Thomas Thingstrup
Vejleder: Jens Højgaard Jensen

278/94 The Models Underlying the Anaesthesia Simulator Sophus
by: Mette Olufsen(Math-Tech), Finn Nielsen (RISØ National Laboratory), Per Føge Jensen (Herlev University Hospital), Stig Andur Pedersen (Roskilde University)

279/94 Description of a method of measuring the shear modulus of supercooled liquids and a comparison of their thermal and mechanical response functions.
af: Tage Christensen

280/94 A Course in Projective Geometry
by Lars Kadison and Matthias T. Kromann

281/94 Modellering af Det Cardiovaskulære System med Neural Pulskontrol
Projektrapport udarbejdet af:
Stefan Frello, Runa Ulsøe Johansen, Michael Poul Curt Hansen, Klaus Dahl Jensen
Vejleder: Viggo Andreasen

282/94 Parallelle algoritmer
af: Erwin Dan Nielsen, Jan Danielsen, Niels Bo Johansen

283/94 Grænser for tilfældighed
(en kaotisk talgenerator)
af: Erwin Dan Nielsen og Niels Bo Johansen

284/94 Det er ikke til at se det, hvis man ikke lige ve' det!
Gymnasiematematikkens begrundelsesproblem
En specialerapport af Peter Hauge Jensen og Linda Kyndlev
Vejleder: Mogens Niss

285/94 Slow coevolution of a viral pathogen and its diploid host
by: Viggo Andreasen and Freddy B. Christiansen

286/94 The energy master equation: A low-temperature approximation to Bässler's random walk model
by: Jeppe C. Dyre

287/94 A Statistical Mechanical Approximation for the Calculation of Time Auto-Correlation Functions
by: Jeppe C. Dyre

288/95 PROGRESS IN WIND ENERGY UTILIZATION
by: Bent Sørensen

289/95 Universal Time-Dependence of the Mean-Square Displacement in Extremely Rugged Energy Landscapes with Equal Minima
by: Jeppe C. Dyre and Jacob Jacobsen

290/95 Modellering af uregelmæssige bølger
Et 3.modul matematik projekt
af: Anders Marcussen, Anne Charlotte Nilsson, Lone Michelsen, Per Mørkegaard Hansen
Vejleder: Jesper Larsen

291/95 1st Annual Report from the project
LIFE-CYCLE ANALYSIS OF THE TOTAL DANISH ENERGY SYSTEM
an example of using methods developed for the OECD/IEA and the US/EU fuel cycle externality study
by: Bent Sørensen

292/95 Fotovoltaisk Statusnotat 3
af: Bent Sørensen

293/95 Geometridiskussionen - hvor blev den af?
af: Lotte Ludvigsen & Jens Frandsen
Vejleder: Anders Madsen

294/95 Universets udvidelse - et metaprojekt
Af: Jesper Duelund og Birthe Friis
Vejleder: Ib Lundgaard Rasmussen

295/95 A Review of Mathematical Modeling of the Controled Cardiovascular System
By: Johnny T. Ottesen

296/95 RETIKULER den klassiske mekanik
af: Peder Voetmann Christiansen

297/95 A fluid-dynamical model of the aorta with bifurcations
by: Mette Olufsen and Johnny Ottesen

298/95 Mordet på Schrödingers kat - et metaprojekt om to fortolkninger af kvantemekanikken
af: Maria Hermannsson, Sebastian Horst, Christina Specht
Vejledere: Jeppe Dyre og Peder Voetmann Christiansen

299/95 ADAM under figenbladet - et kig på en samfundsvidenskabelig matematisk model
Et matematisk modelprojekt
af: Claus Dræby, Michael Hansen, Tomas Højgård Jensen
Vejleder: Jørgen Larsen

300/95 Scenarios for Greenhouse Warming Mitigation
by: Bent Sørensen

301/95 TOK Modellering af træers vækst under påvirkning af ozon
af: Glenn Møller-Holst, Marina Johannessen, Birthe Nielsen og Bettina Sørensen
Vejleder: Jesper Larsen

302/95 KOMPRESSORER - Analyse af en matematisk model for aksialkompressorer
Projektrapport af: Stine Bøggild, Jakob Hilmer, Pernille Postgaard
Vejleder: Viggo Andreasen

303/95 Masterlignings-modeller af Glasovergangen
Termisk-Mekanisk Relaksation
Specialerapport udarbejdet af:
Johannes K. Nielsen, Klaus Dahl Jensen
Vejledere: Jeppe C. Dyre, Jørgen Larsen

304a/95 STATISTIKNOTER Simple binomialfordelingsmodeller
af: Jørgen Larsen

304b/95 STATISTIKNOTER Simple normalfordelingsmodeller
af: Jørgen Larsen

304c/95 STATISTIKNOTER Simple Poissonfordelingsmodeller
af: Jørgen Larsen

304d/95 STATISTIKNOTER Simple multinomialfordelingsmodeller
af: Jørgen Larsen

304e/95 STATISTIKNOTER Mindre matematisk-statistisk opslagsvær
indeholdende bl.a. ordforklaringer, resuméer og tabeller
af: Jørgen Larsen

305/95 The Maslov Index:
A Functional Analytical Definition
And The Spectral Flow Formula

By: B. Booss-Bavnbek, K. Furutani

306/95 Goals of mathematics teaching

Preprint of a chapter for the forth-comming International Handbook of Mathematics Education (Alan J.Bishop, ed)

By: Mogens Niss

307/95 Habit Formation and the Thirdness of Signs

Presented at the semiotic symposium

The Emergence of Codes and Intensions as a Basis of Sign Processes

By: Peder Voetmann Christiansen

308/95 Metaforer i Fysikken

af: Marianne Wilcken Bjerregaard, Frederik Voetmann Christiansen, Jørn Skov Hansen, Klaus Dahl Jensen Ole Schmidt

Vejledere: Peder Voetmann Christiansen og Petr Viscor

309/95 Tiden og Tanken
En undersøgelse af begrebsverdenen Matematik udført ved hjælp af en analogi med tid

af: Anita Stark og Randi Petersen

Vejleder: Bernhelm Booss-Bavnbek

310/96 Kursusmateriale til "Lineære strukturer fra algebra og analyse" (E1)

af: Mogens Brun Heefelt

311/96 2nd Annual Report from the project
LIFE-CYCLE ANALYSIS OF THE TOTAL DANISH ENERGY SYSTEM

by: Hélène Connor-Lajambe, Bernd Kuemmel, Stefan Krüger Nielsen, Bent Sørensen

312/96 Grassmannian and Chiral Anomaly

by: B. Booss-Bavnbek, K.P.Wojciechowski

313/96 THE IRREDUCIBILITY OF CHANCE AND THE OPENNESS OF THE FUTURE
The Logical Function of Idealism in Peirce's Philosophy of Nature

By: Helmut Pape, University of Hannover

314/96 *Feedback Regulation of Mammalian* Cardiovascular System

By: Johnny T. Ottesen

315/96 a + b "Rejsen til tidens indre" - Udarbejdelse af et manuskript til en fjernsynsudsendelse + manuskript

af: Gunhild Hune og Karina Goyle

Vejledere: Peder Voetmann Christiansen og Bruno Ingemann

316/96 Plasmaoscillation i natriumklynger

Specialerapport af: Peter Meibom, Mikko Østergård

Vejledere: Jeppe Dyre & Jørn Borggreen

317/96 Poincaré og symplektiske algoritmer

af: Ulla Rasmussen

Vejleder: Anders Madsen

318/96 Modelling the Respiratory System

by: Tine Guldager Christiansen, Claus Dræby

Supervisors: Viggo Andreasen, Michael Danielsen

319/96 Externality Estimation of Greenhouse Warming Impacts

by: Bent Sørensen